

Innovative front contact systems for a-Si:H/ μ c-Si:H solar cells based on thermally treated zinc oxide

vorgelegt von
Diplom-Physiker
Sebastian Neubert
geb. in Marienberg

von der Fakultät IV - Elektrotechnik und Informatik
der Technischen Universität Berlin
zur Erlangung des akademischen Grades

Doktor der Naturwissenschaften
- *Dr. rer. nat.* -

genehmigte Dissertation

Promotionsausschuss:

Vorsitzender: Prof. Dr. Bernd Szyszka

Berichter: Prof. Dr. Bernd Rech

Berichter: Prof. Dr. Mario Dähne

Berichter: Prof. Dr. Christophe Ballif

Tag der wissenschaftlichen Aussprache: 12. November 2014

BERLIN 2015

Kurzbeschreibung

Diese Arbeit beschreibt die Verwendung von thermisch nachbehandeltem Aluminium-dotiertem Zinkoxid (ZnO:Al) als Frontkontakt in Tandem-Dünnschichtsolarzellen, welche auf amorphem Silizium (a-Si:H) und mikrokristallinem Silizium ($\mu\text{c-Si}$) basieren. In vorangegangenen Studien wurde entdeckt, dass sich die opto-elektronischen Eigenschaften von ZnO:Al (insbesondere die Mobilität) durch Tempern unter einer Deckschicht aus a-Si:H bei Temperaturen von bis zu 650 °C wesentlich verbessern lassen. Zunächst wurde dieser Prozess auf die Solarzellenentwicklung am PVcomB übertragen. Darüber hinaus wurde der Effekt in einer systematischen Studie mit Hinblick auf die Anwendung in Tandem-Solarzellen weitergehend untersucht. Hierfür wurde sowohl von einem Industriepartner bereitgestelltes, als auch in unserem Haus entwickeltes, DC-Magnetron gesputtertes ZnO:Al verwendet. Es wurden prinzipiell zwei Vorgehensweisen etabliert: (1) Eine Verbesserung der Transparenz des ZnO:Al's bei konstanter Schichtdicke und gleichbleibendem Schichtwiderstand und (2) eine Minimierung der ZnO:Al-Schichtdicke bei gleichbleibendem Wirkungsgrad. Mit dem ersteren Ansatz konnten Zell-Wirkungsgrade von bis zu 12.1 % (nach Lichtalterung) erreicht werden. Darüber hinaus konnten serienverschaltete Mini-Module mit einem Wirkungsgrad von 11.6 % (nach Lichtalterung, apert. area) gezeigt werden. Der zweite Ansatz erlaubte vorerst eine Verringerung der ZnO:Al Schichtdicke von 820 auf 550 nm ohne Wirkungsgradeinbußen. Für dünnere ZnO:Al Schichten wurden mikro-texturierte Glassubstrate verwendend, da die geringe ZnO:Al Schichtdicke keine ausreichende Texturierung durch Ätzen erlaubt. Das Licht-Management in Tandem-Solarzellen, welche auf solchen Substraten basieren, wurde detailliert untersucht. Mit diesem Ansatz konnte anhand von Mini-Modulen gezeigt werden, dass die Verwendung von thermisch nachbehandeltem ZnO:Al selbst für 100 nm dünne Schichten keinen signifikanten Wirkungsgradverlust im Vergleich zu einer Referenz verursacht.

Abstract

This thesis describes the implementation of thermally treated aluminum-doped zinc oxide (ZnO:Al) as front electrode (transparent conducting oxide, TCO) in thin-film silicon tandem solar cells based on amorphous silicon (a-Si:H) and microcrystalline silicon (μ c-Si:H). In previous studies it was found that the opto-electronic properties of ZnO:Al (i.e. mobility) are fundamentally improved upon annealing at temperatures up to 650 °C when capped with an a-Si:H layer. First of all, this process was scaled and technologically implemented in the solar cell development at PVcomB. Afterwards, this phenomenon was further investigated in a systematic study with focus on application in tandem solar cells. DC-sputtered ZnO:Al both from an industrial supplier and in-house developed have been used. Generally, two routes were identified: (1) Improving the transparence of the ZnO:Al while maintaining the thickness and sheet resistance and, (2), minimizing the TCO thickness, thereby, maintaining cell efficiency. The first approach led to tandem cells with highest conversion efficiency, reaching 12.1 % (after light soaking). Moreover, series connected mini modules with 11.6 % (after light soaking, apert. area) were demonstrated. The second approach first allowed to reduce the ZnO:Al layer thickness from 820 to 550 nm while maintaining efficiency. For thinner ZnO:Al layers micro-textured glass was used as substrate, since small ZnO:Al thickness did not allow to sufficiently texture the surface by etching. Light management in tandem solar cells based on such front electrode systems was investigated in detail. With this approach it was demonstrated in mini modules that an annealed ZnO:Al layer as thin as 100 nm did not result in significant efficiency loss compared to the reference.

Contents

Kurzbeschreibung	i
Abstract	ii
List of Figures	v
List of Tables	viii
1 Introduction	1
2 Fundamentals	4
2.1 Transparent Conductive Zinc Oxide	4
2.1.1 Crystallographic Structure	4
2.1.2 Doping	5
2.1.3 Electronic Transport	6
2.1.4 Charge Carrier Scattering Processes	8
2.1.5 Optical Properties	12
2.2 Si-based Thin-film Solar Cells	18
2.2.1 Si based Materials for Thin-film Solar Cells	20
2.2.2 Basic Description of opto-electric Solar Cell Properties	22
2.2.3 Light Trapping in Si-based Thin-film Solar Cells	25
2.2.4 Advanced Device Concepts	29
3 Experimental Details	31
3.1 Sample Preparation	31
3.1.1 The Glass Substrates	31
3.1.2 Reactive MF-Magnetron Sputtering of SiO_xN_y Layers	31
3.1.3 DC-Magnetron Sputtering of ZnO:Al Layers	33
3.1.4 Wet-chemical Texture-Etching	35
3.1.5 Thermal post-Deposition Treatment	37
3.1.6 PECVD Processing of Si-based Thin-film Cells	38
3.1.7 Laser Scribing, Back Contact Deposition and Device Annealing	40
3.2 Characterization Techniques	41
3.2.1 Electronic Characterization of ZnO:Al	42
3.2.2 Optical Measurements	43
3.2.3 Atomic Force Microscopy	45
3.2.4 Solar Cell Analysis	46

4	Post-deposition Thermal Treatment of sputtered ZnO:Al	50
4.1	State of the Art	50
4.2	Systematic Variation of Film Thickness and Annealing Conditions	51
4.2.1	Characterization of the ZnO:Al Layers in the as-deposited State	51
4.2.2	Electronic Properties after Thermal Treatment	55
4.2.3	Mechanism of Thermal Treatment	57
4.2.4	Optical Properties after Thermal Treatment	58
4.2.5	Technological Evaluation of the Results	62
4.3	Interdependence of Annealing and Texture Formation	67
5	Analysis of a Light Coupling related Artifact in EQE Data	72
5.1	Description of the Discrepancy	72
5.2	Considerations on the Root Cause	72
5.3	The Concentric Cell Experiment	74
5.4	The Large Area Setup	77
6	Application of annealed ZnO:Al to a-Si:H/μc-Si:H Solar Cells	80
6.1	Annealing and the ZnO:Al/p-layer contact	80
6.2	Improving the opto-electronic Properties of conventional ZnO:Al Layers	85
6.3	Thin, highly conductive ZnO:Al Electrodes	90
6.4	Limitations for textured ZnO:Al	92
6.5	Utilization of micro-textured Glass Substrates	94
6.5.1	Surface morphology and ZnO:Al film growth	95
6.5.2	Light scattering and opto-electronic properties of the ZnO:Al	100
6.5.3	Application to solar cells	103
6.6	Application of a textured Front Cover	119
7	Achievements in Si-based Thin-film Cells and Modules	125
7.1	High Efficiency Tandem Cells and Modules	125
7.2	Mini Modules on very thin, cap-annealed ZnO:Al layers	126
8	Conclusions and Outlook	128
	References	I
	List of Publications	X
	Acknowledgements	XII

List of Figures

2.1	Crystallographic structure of ZnO	5
2.2	Exemplary transmittance, reflectance and absorptance of a typical ZnO:Al film on glass	13
2.3	Schematic band structure of a degenerate semiconductor	14
2.4	Schematic drawing of an a-Si:H/ μ c-Si:H-based thin film cell	19
2.5	Absorption coefficient and penetration depth of c-Si, a-Si:H and μ c-Si:H	20
2.6	Equivalent circuit for the one-diode model	23
2.7	Illuminated J - V characteristic of a representative a-Si:H/ μ c-Si:H tandem cell	24
2.8	External quantum efficiency and total absorption of a representative a-Si:H/ μ c-Si:H tandem cell	26
2.9	Haze and total transmittance for ZnO:Al layers on glass with moderate and rather strong texture.	27
2.10	TEM image of a μ c-SiO _x layer grown on top of a-Si:H.	29
3.1	Transmittance of the glass types used as substrates.	32
3.2	Schematic drawing of the sputter process.	34
3.3	Optical properties of the two types of ZnO:Al commonly used	36
3.4	Haze of the two types of ZnO:Al commonly used	37
3.5	Schematic cross section of a PECVD chamber.	39
3.6	Stepwise illustration of the monolithically interconnection	41
3.7	Measurement configurations of the photo spectrometer	44
3.8	Spectral distribution of solar irradiance	47
3.9	Light induced degradation as a function of light soaking time for several a-Si:H-based devices.	48
4.1	Transmittance, reflectance and absorptance of ZnO:Al films with different thickness on SiO _x N _y coated glass.	52
4.2	Electronic properties of ZnO:Al layers in the as-deposited state as a function of layer thickness.	52
4.3	XRD data ($\theta - 2\theta$ spectra) of 358 and 692 nm thick ZnO:Al films on SiO _x N _y coated glass	54
4.4	XRD derived position and FWHM of the ZnO (002)-reflex for different film thickness before and after annealing	54
4.5	Mobility as a function of charge carrier density for ZnO:Al films of different thickness and for different thermal treatments	55
4.6	Absorptance of characteristic ZnO:Al films with respect to their annealing procedure.	59

4.7	Absorptance of characteristic annealed ZnO:Al films with respect to their sheet resistance.	62
4.8	Conductivity of annealed ZnO:Al films on SiO _x N _y coated glass as a function of their solar weighted effective absorption coefficient.	64
4.9	Implied photo current density loss in an a-Si:H/ μ c-Si:H tandem cell due to absorption in the front contact	66
4.10	SEM images and AFM topography scans of annealed, textured ZnO:Al for different sequences according to tab. 4.1.	69
4.11	Height and inclination distribution of surface topography of textured ZnO:Al achieved by different sequencing	69
5.1	Correlation of tandem cell current density obtained from <i>EQE</i> and <i>J-V</i> measurements.	73
5.2	Illustration of the optical collection losses related to small spot illumination	74
5.3	<i>EQE</i> of concentric a-Si:H/ μ c-Si:H tandem cells illustrating the lateral light scattering	75
5.4	<i>EQE</i> derived current density of concentric a-Si:H/ μ c-Si:H tandem cells as a function of cell width	76
5.5	<i>EQE</i> data of 1×1 cm ² -sized a-Si:H/ μ c-Si:H tandem cells derived from a small beam and a large area setup for different front textures	78
6.1	Influence of the capping/decapping process on the <i>EQE</i> data of a-Si:H/ μ c-Si:H tandem cells.	82
6.2	Influence of different ZnO:AL surface treatments on the <i>EQE</i> data of a-Si:H/ μ c-Si:H tandem cells.	84
6.3	Transmittance, reflectance and absorptance of ZnO:Al layers with and without 2-step annealing.	86
6.4	<i>EQE</i> and $1 - R$ of cells, and transmittance and absorptance of the corresponding flat ZnO:Al layer with and without 2-step annealing.	88
6.5	<i>EQE</i> and $1 - R$ of an a-Si:H/ μ c-Si:H tandem cell on thin textured, cap-annealed ZnO:Al	91
6.6	Statistical analysis of the surface topography of wet-chemically etched ZnO:Al films with different initial film thickness.	92
6.7	Surface topography of micro-textured glass.	96
6.8	Exemplary line profile of surface topography of micro-textured glass.	97
6.9	Height and inclination distribution of surface topography of micro-textured glass.	98
6.10	Haze and total transmittance of micro-textured glass and textured ZnO:Al layers on planar glass.	100

6.11	<i>EQE</i> and $1 - R$ of an a-Si:H/ μ c-Si:H tandem cell on micro-textured and planar glass, and on textured ZnO:Al.	104
6.12	<i>IQE</i> and diffuse and specular reflectance of an a-Si:H/ μ c-Si:H tandem cell on micro-textured glass.	106
6.13	<i>EQE</i> and $1 - R$ of an a-Si:H/ μ c-Si:H tandem cell on micro-textured glass and on similarly textured ZnO:Al.	109
6.14	Schematic drawing indicating the impact of using textured glass on the light coupling	111
6.15	<i>EQE</i> , $1 - R$ and <i>IQE</i> for a-Si:H/ μ c-Si:H tandem cells with differing intermediate reflector layer thickness.	113
6.16	Quantitative analysis of optical changes introduced by the intermediate reflector layer for different front texture/electrode types expressed in terms of photo current density.	115
6.17	<i>J-V</i> data of a-Si:H/ μ c-Si:H tandem cells with different front texture/electrode types and varying IRL thickness before and after 1 week of light soaking . . .	117
6.18	Photo current densities of a-Si:H/ μ c-Si:H tandem cells with different front texture/electrode types and varying IRL thickness as derived from <i>J-V</i> and <i>EQE</i> measurements.	117
6.19	Photograph of a model of a surface element of the textured front cover illustrating retro-reflective light trapping	120
6.20	<i>EQE</i> and $1 - R$ of an a-Si:H/ μ c-Si:H tandem cell on micro-textured glass with and without textured front cover.	122
6.21	Internal quantum efficiency of an a-Si:H/ μ c-Si:H tandem cell on micro-textured glass with and without textured front cover.	122
6.22	<i>EQE</i> derived photo current densities of a-Si:H/ μ c-Si:H tandem cells with different front texture/electrode types and varying IRL thickness with and without front texture.	123
7.1	External quantum efficiency and <i>J-V</i> curve of the a-Si:H/ μ c-Si:H tandem cell with the highest stabilized efficiency among all cells made at PVcomB so far.	126

List of Tables

3.1	Basic properties of the glass types used as substrate.	32
3.2	Main features of the sputter processes commonly used for ZnO:Al deposition	35
3.3	Electronic properties of the two types of ZnO:Al commonly used	36
3.4	PECVD sequence and main process parameters for standard a-Si:H/ μ c-Si:H device.	40
4.1	Processing sequences used for etching and annealing of ZnO:Al	68
4.2	J - V data of a-Si:H/ μ c-Si:H tandem cells deposited on textured, 2-step annealed ZnO:Al achieved by different sequences	71
6.1	Influence of the capping/decapping process on the J - V -data of a-Si:H/ μ c-Si:H tandem cells.	82
6.2	Influence of different ZnO:AL surface treatments on the J - V -data of a-Si:H/ μ c-Si:H tandem cells.	84
6.3	Electronic properties, derived from Hall-measurements, of 816 nm thick, non-texturized industrial ZnO:Al for different annealing states.	86
6.4	J - V parameters for cells on as-deposited and 2-step annealed, textured ZnO:Al films.	89
6.5	J - V parameters of an a-Si:H/ μ c-Si:H tandem cell on thin, textured, cap-annealed ZnO:Al and on standard textured ZnO:Al.	91
6.6	Electronic properties of thin ZnO:Al layers on micro-textured and planar glass before and after cap-annealing.	102
7.1	J - V parameters of the particular a-Si:H/ μ c-Si:H tandem devices with the highest stabilized efficiency.	126
7.2	ZnO:Al layer properties, cell width and J - V parameters of single cells for a-Si:H/ μ c-Si:H tandem mini modules on micro-textured glass.	127

1 Introduction

Over the past 30 years thin film silicon solar cells have been widely used in various applications from consumer electronics to large power plants. They have been very attractive due to the mature manufacturing process and equipment as well as the use of silicon as material, which is well known, available and eco-compatible. Low production costs have been the major driver to develop this technology further. The limited conversion efficiency, however, is a severe drawback, hindering this development. Particular in the case of Si-based thin-film solar cells, high efficiencies are closely related to innovative light management concepts. This thesis deals with processes and materials to improve the light management and facilitate to increase conversion efficiency.

In 1969 Chittick was the first, who deposited hydrogenated amorphous silicon a-Si:H layers in a glow discharge process using silane [1]. Six years later Spear and Le Comber observed that such layers can be effectively doped n-type and p-type by, respectively, blending small portions of phosphine and diborane to the silane [2,3]. These results pioneered the application of such layers to semi-conductor devices. The first p-i-n type a-Si:H solar cells was presented by Carlson *et al.*, in 1977 [4]. A similar history can also be found for hydrogenated micro-crystalline silicon (see ref. [5]).

Around the same time that Carlson showed the first a-Si:H p-i-n cell Redfield [6] proposed a design for thin film cells that makes use of light trapping. Experimental validation of such concepts followed soon [7,8]. For the introduction of light scattering into Si-based thin-film cells transparent conducting oxides (*TCO*) with a rough surface have been established. In 1999 Löffl and Kluth presented a way to introduce texture to sputter deposited Al-doped zinc oxide (*ZnO:Al*) layers by wet-chemical etching [9,10]. Such textures showed good light trapping properties, when used as a substrate in a-Si:H and $\mu\text{-Si:H}$ solar cells. In 2007 Berginski *et al.* [11] showed that the photo current density of $\mu\text{-Si:H}$ solar cells can be significantly increased by a reduction of the charge carrier density within the textured ZnO:Al layer used as front electrode. This is a direct consequence of lower free carrier absorption. But, it also led to an increased resistive loss in the ZnO:Al layers. This demonstrates the transparency-conductivity trade-off, which is always present in TCOs, when applied to solar cells.

In the same year Lee and Ruske *et al.* [12] reported on an improvement of the *charge carrier mobility* of a ZnO:Al layer that was capped with an intrinsic a-Si layer and subsequently annealed for 24 h at 600 °C. Further experiments demonstrated that this effect can be used to achieve significant increase in mobility from around $40 \frac{\text{cm}^2}{\text{Vs}}$ (initial) up to $67 \frac{\text{cm}^2}{\text{Vs}}$ after treatment [13]. Later on, a preceding annealing without capping layer was added to the procedure [14]. This allowed to tune the charge carrier density while the mobility remained at high levels. In other words: This 2-step annealing relaxes the transparency-conductivity

trade-off and allows to tune the balancing of this two quantities to different needs. With respect to Si-based thin film cells, it seems that this treatment of ZnO:Al layers provides a versatile tool to improve cell performance. This needs to be proven and further developed.

The aim of this thesis is to evaluate the benefits of ZnO:Al annealing by applying it to ZnO:Al based front electrodes for a-Si:H/ μ c-Si:H tandem cells. For this purpose we will focus on the following aspects.

Annealing and texture formation Up to now the annealing procedure was only applied to non-textured ZnO:Al layers. But for application to cells the presence of a light scattering texture is crucial. Therefore, we will investigate how the annealing can be combined with the wet-chemical etching used for texture formation. This point is addressed in sec. 4.3.

Annealing and the ZnO:Al/p-layer contact The TCO/p-layer contact is known to be a crucial interface in a-Si:H based solar cells. In sec. 6.1 the reasons for this will be briefly introduced and discussed in the context of ZnO:Al annealing. First, the influence of the capping/decapping process will be experimentally observed based on cell results. Afterwards, different surface treatments will be applied to cap-annealed ZnO:Al layers prior to cell deposition.

Application to conventional ZnO:Al layers In sec. 6.2 the results of our first successful utilization of 2-step annealed ZnO:Al to a-Si:H/ μ c-Si:H tandem cells are presented and discussed.

Variation of ZnO:Al layer thickness and annealing conditions In sec. 4.2 the results of a systematic variation in ZnO:Al layer thickness and annealing conditions are presented. One aim of this experiment was to study a comprehensive set of data for the application in solar cells and modules. For this purpose the data was presented and discussed in terms of two different figures of merit. The variety of data was also used to identify general trends with respect to the annealing conditions. This provides valuable indications on the underlying doping mechanisms.

Cells on thin, highly conductive ZnO:Al layers In sec. 6.3 we utilize the high conductivity achieved by annealing to reduce the ZnO:Al layer thickness. With further reduction of the ZnO:Al film thickness we observed a limitation to this approach, which was due to lower light scattering for thinner ZnO:Al layers. The results of this observation are presented in sec. 6.4.

Micro-textured glass substrates In sec. 6.5 an alternative way to introduce light scattering by a textured glass is evaluated.

2 Fundamentals

In this section the theoretical and physical fundamentals of this work are presented. In sec. 2.1 the basic properties of transparent conductive zinc oxide are introduced with a scope on its opto-electronic application. The crystallographic structure, doping, electronic transport and its limitation by various charge carrier scattering mechanisms as well as the optical properties and its relation to the electronic properties via the dielectric function, ϵ , are described. Section 2.2 is dedicated to the properties and working principle of thin film solar cells based on hydrogenated amorphous silicon (a-Si:H) and hydrogenated microcrystalline silicon ($\mu\text{c-Si:H}$). A short introduction to the general description and rating of a solar cell is provided. Afterwards, the introduction of light management concepts in Si-based thin film cells is motivated and common ways for its realization are presented. In a last section the state of the art and some advanced concepts related to this thesis are presented.

2.1 Transparent Conductive Zinc Oxide

Most transparent materials are electric insulators. Conversely, metals commonly show high conductivity, but at the same time practically have no transparency. However, *transparent conducting oxide* (TCO) materials can be very transparent in the visible (and near infrared) spectral range and at the same time show an excellent conductivity. For comparison, the room temperature resistivity of Ag is $1.6 \cdot 10^{-6} \Omega\text{cm}$ [15] whereas the lowest reported values for TCO films are in the order of $10^{-4} \Omega\text{cm}$ [16]¹. These combined opto-electronic properties made TCOs highly interesting for various applications, such as flat panel displays, touch screens and solar cells. Beside some bulk single crystals used in basic research, poly-crystalline thin films of TCO are best investigated and by far mostly used in technical applications. An overview on different thin film TCOs can for example be found in the review of Exarhos and Zhou [16] and the references therein.

2.1.1 Crystallographic Structure

Generally ZnO exhibits the hexagonal wurtzite structure, which consists of two interpenetrating hexagonal close-packed structures one occupied by zinc and the other by oxygen atoms. The according unit cell is depicted in fig. 2.1. Each atom is bound in tetrahedral configuration to four atoms of the respectively converse kind. The wurtzite structure has polar character, i.e. it lacks inversion symmetry, in [001]-direction. In consequence ZnO shows piezo- and pyro-electric activity and comprises polar surfaces, i.e. it is Zn-terminated on (001)-surfaces

¹To be precise the lowest resistivity published so far for a ZnO:Al-film is $\rho = 8.5410^{-5} \Omega\text{cm}$ ($\mu = 47.6 \frac{\text{cm}^2}{\text{Vs}}$ and $n_e = 1.54 \cdot 10^{21} \text{ cm}^{-3}$) and was obtained by magnetic field assisted pulsed laser deposition (PLD) from a ceramic ZnO target with an effective Al_2O_3 -doping of 1.8 at.% [17].

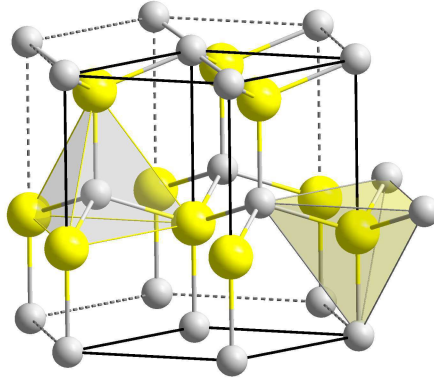


Figure 2.1: Schematic drawing of the common ZnO crystal structure (wurtzite structure). Zn- and oxygen-atoms are depicted in grey and yellow, respectively. The grey and yellow shaded are as depict the tetrahedral coordination of zinc (by oxygen) and oxygen (by zinc), respectively. Note the opposite orientation of the corresponding tetrahedrons (a consequence of the polarity along $[00\bar{1}]$ -direction).

and O-terminated on $(00\bar{1})$ -surfaces. The lattice constants of ZnO are $a = 0.325$ nm and $c = 0.5207$ nm [18].

2.1.2 Doping

In TCOs the presence of a high energetic band gap ($E_g \gtrsim 3.2$ eV) leads to transparency in the visible to near infrared (*NIR*) spectral region. At the same time TCOs can be heavily doped, hence exhibit a high charge carrier concentration up to $1.5 \cdot 10^{21} \text{ cm}^{-3}$ [19]². The doping can be realized by intrinsic point defects (*intrinsic doping*) or the admixture of dopants (*extrinsic doping*). In the case of zinc oxide the intrinsic doping is realized via the formation of unoccupied oxygen sites (*oxygen vacancies*) or zinc atoms located in between regular lattice sites (*metal interstitials*). Both point defects contribute two electrons to the valence band, thus introduce n-conduction. The intrinsic doping level can be adjusted by controlling the sub-stoichiometry of oxygen³. This can be achieved either by tuning the oxygen partial pressure during the material preparation or by a post-deposition reduction of the oxide, e.g. annealing in vacuum or a hydrogen containing atmosphere [19]. With this doping method resistivities below $5 \cdot 10^{-4} \Omega\text{cm}$ have been achieved in RF-sputtered poly-crystalline ZnO-films [22]. With respect to technical application the intrinsic doping exhibits two major drawbacks. First, the typically achieved conductivity is several times lower compared to that obtained by extrinsic doping. Furthermore, the intrinsic doping is only metastable. This is due to the reversibility of the oxygen sub-stoichiometry especially at elevated temperatures [19,23]. Therefore, extrinsic

²A carrier concentration of $1.5 \cdot 10^{21} \text{ cm}^{-3}$ corresponds to dopant concentration of 3.6 at.% with respect to the metallic cations in the case of ZnO:Al. Higher dopant concentrations gradually lead to formation of Al-sub oxides, which act as scattering centers and hence hinder the carrier transport [20,21].

³Zinc oxide tends to grow in a sub stoichiometric regime with respect to oxygen.

doping is preferred in nowadays application of zinc oxide (as for other TCOs, like indium and tin oxide). For ZnO typical dopants are Group III elements, like boron, aluminum, gallium and indium. Built in on zinc sites they act as a shallow defect contributing one electron to the valence band⁴. The role of hydrogen in acting as a dopant has also been widely discussed in literature [25, 26].

2.1.3 Electronic Transport

The generally high density of donor states in n-type TCOs like doped ZnO leads to a shift of the FERMI level towards the conduction band. For very high doping levels the FERMI level lies within the conduction band and the TCO becomes a *degenerate semiconductor*. In this case no additional activation energy is needed to excite electrons into the conduction band. The carrier concentration needed for degeneracy (n_{deg}) can be estimated with the MOTT-criterion [27]

$$n_{\text{deg}}^{1/3} a_0 \approx 0.25$$

where a_0 is the effective BOHR radius

$$a_0 = \frac{4\pi\epsilon_r\epsilon_0\hbar^2}{m^*e^2}.$$

This yields $n_{\text{deg}} \approx 3.5 \cdot 10^{18} \text{ cm}^{-3}$ in the case of ZnO ($m^* = 0.28 \cdot m_e$ and $\epsilon_r = 8.75$ taken from ref. [21]). Thus, n_{deg} is one to two orders lower than n_e in typical doped ZnO films for opto-electronic application and hence such films are degenerate. In other words the electrons can be treated as *free*⁵ and the DRUDE theory [28], commonly used to describe the interaction of free electrons with electric fields in metals, can also be applied to those (degenerate) ZnOs.

In the DRUDE model the interaction of the ensemble of free electrons with an external electric field $\vec{E} = \vec{e}_x E_0$ is described by the equation of motion

$$m^* \frac{d^2x}{dt^2} + \frac{m^*}{\tau} \frac{dx}{dt} = -e\vec{E} \quad (2.1)$$

for a single charge carrier, where τ is the mean time between two scattering events or *relaxation time*. The movement of the charge carrier in the electric field is hindered by the scattering events. For constant electric fields eq. (2.1) can be solved for the stationary case⁶,

⁴There are also other dopants leading to carrier concentrations in the order of 10^{20} cm^{-3} . An overview is given by Minami in [24]

⁵The term "free" points at the parabolic dispersion relation ($E \propto k^2$) of the electrons at the lower edge of the conduction band. All effects of the crystal structure on the electrons are accounted for in the effective electron mass approximation.

⁶The scattering term in eq. (2.1) can be interpreted as a classical friction term with the friction coefficient $\frac{m^*}{\tau}$. In the stationary case the friction force just cancels out the COULOMB force introduced by the electric field. Hence, no net force is applied to the electron and it conserves its actual state of movement, i.e. $\frac{d^2x}{dt^2} = 0$.

which yields the constant drift velocity

$$\vec{v}_d = \frac{dx}{dt} = \frac{e\tau}{m^*} \vec{E} = \mu \vec{E} . \quad (2.2)$$

The factor of proportionality between \vec{E} and \vec{v}_d is called charge carrier mobility

$$\mu = \frac{e\tau}{m^*} . \quad (2.3)$$

Based on eq. (2.2) and taking into account the density of charge carriers n_e and their respective charge the current density \vec{j} caused by the ensemble of free charge carriers can be calculated via

$$\vec{j} = -n_e e \vec{v}_d = n_e e \mu \vec{E} = \sigma \vec{E} . \quad (2.4)$$

Equation (2.4) represents OHM's law and the factor of proportionality σ between \vec{j} and \vec{E} is called *conductivity*,

$$\sigma = n_e e \mu . \quad (2.5)$$

In the literature the use of resistivity

$$\rho = \frac{1}{\sigma} = \frac{1}{n_e e \mu} \quad (2.6)$$

is also very common. For technical application the sheet resistance

$$R_{\text{sh}} = \frac{\rho}{d} , \quad (2.7)$$

where d denotes the thickness of the film, is of great interest. It is sometimes also denoted as R_{\square} and can be derived from

$$R = \rho \frac{l}{b \cdot d} , \quad (2.8)$$

where l denotes the distance between two straight and parallel contacts (ranging over the whole sample width) and b denotes the width of the rectangular shaped sample. In the case of a square-shaped sample ($l = b$) the right sides of eq. (2.8) and eq. (2.7) become equal and

$$R_{\text{sh}} = R|_{l=b} .$$

The definition of R_{sh} assumes that ρ and d are uniformly distributed over the whole sample.

Combining eq. (2.6) and (2.7) yields

$$R_{\text{sh}} = \frac{1}{n_e e \mu d}. \quad (2.9)$$

From eq. (2.9) it can be seen that there are three possibilities to decrease the sheet resistance. Either charge carrier density, their mobility or the film thickness has to be increased. With respect to the optical properties of a TCO these approaches have very different consequences, as we will discuss later.

2.1.4 Charge Carrier Scattering Processes

In the following the different scattering processes, relevant for heavily doped poly-crystalline ZnO:Al films at room temperature are briefly introduced. Each of these scattering processes can be represented by an individual relaxation time τ_i . If the individual scattering mechanisms are independent of each other, the total relaxation time τ_{total} results from MATTHIESEN'S rule

$$\frac{1}{\tau_{\text{total}}} = \sum_i \frac{1}{\tau_i} \quad (2.10)$$

and according to eq. (2.3) the total mobility is calculated in analogy

$$\frac{1}{\mu_{\text{total}}} = \sum_i \frac{1}{\mu_i}. \quad (2.11)$$

Ionized impurity scattering In literature it is widely agreed that ionized impurity scattering (IIS) is the most important scattering mechanism in heavily doped TCOs [19,29–31], as commonly used for technological application. This is due to the fact that IIS generally leads to a considerable reduction in μ with increasing n_e (i.e. density of ionized impurities, n_{ii}) and hence is the limiting process with respect to achievable conductivity (cf. eq. (2.5)). In literature several analytical expressions can be found for describing the IIS related dependence of μ on n_{ii} . Ellmer compared different approaches with experimental data obtained for ZnO (and Si) [19]. He found that, among the theoretical expressions, the model based on the works of Brooks, Herring and Dingle (*B-H-D*) [32,33]⁷ including a refinement for non-parabolic bands by Pisarkiewicz *et al.* [35] showed the best agreement to the experimental data. However, even this (best) fit could not explain the strong decrease of μ for $n_e > 10^{20} \text{ cm}^{-3}$. A possible explanation was given by taking into account impurity clustering as a statistical effect at very high doping levels. This would yield clusters with a high charge number, Z , and therefore a

⁷The model of Brooks and Herring is based on an expression by Conwell and Weisskopf [34] describing IIS in non-degenerate semiconductors using truncated Coulomb potentials of the ionized impurities. This approach underestimated the mobilities. Brooks and Herring modified the expression for screening of the Coulomb potentials by the ensemble of charge carriers and later Dingle adapted it for degenerate semiconductors.

stronger scattering effect (cf. eq. (2.12)) [19]. In its general form the B-H-D expression can be written as

$$\mu_{ii}(n_e, n_{ii}) = \mu_{ii0}(n_e) \frac{n_e}{Z^2 n_{ii}} \quad (2.12)$$

with Z being the charge number of the ionized impurity and

$$\mu_{ii0}(n_e) = \frac{3(\varepsilon_0 \varepsilon_r)^2 \hbar^3}{e^3 m^{*2}} \cdot \frac{1}{F_{ii}^{\text{BHD}}(n_e)} \quad (2.13)$$

and the screening function

$$F_{ii}^{\text{BHD}}(n_e) = \ln(1 + \xi_0(n_e)) - \frac{\xi_0(n_e)}{1 + \xi_0(n_e)} \quad (2.14)$$

where

$$\xi_0(n_e) = (3\pi^2)^{1/3} \frac{\varepsilon_0 \varepsilon_r \hbar^2 n_e^{1/3}}{e^2 m^*} . \quad (2.15)$$

The refinement of Pisarkiewicz [35] accounting for the non-parabolicity of the conduction band is based on an electron dispersion

$$\frac{\hbar^2 k^2}{2m_0^*} = E + CE^2$$

with m_0^* , the effective mass at the bottom of the conduction band and C , the non-parabolicity coefficient, yielding

$$m^* = m_0^*(1 + 2CE)$$

and by applying the FERMI-DIRAC distribution

$$m^* = m_0^* \left[1 + 2C \frac{\hbar^2}{m_0^*} (3\pi^2 n_e)^{2/3} \right]^{1/2} .$$

For the B-H-D formalism the non-parabolicity refinement leads to an expansion of the screening function eq. (2.14)⁸

$$F_{ii}^{\text{np}} = \left[1 + \frac{4\xi_{\text{np}}}{\xi_0} \left(1 - \frac{\xi_{\text{np}}}{8} \right) \right] \ln(1 + \xi_0) - \frac{\xi_0}{1 + \xi_0} - 2\xi_{\text{np}} \left(1 - \frac{5\xi_{\text{np}}}{16} \right) \quad (2.16)$$

with

$$\xi_{\text{np}} = 1 - \frac{m_0^*}{m^*} .$$

⁸Note that eq. (2.16) equals eq. (2.14) for $\xi_{\text{np}} = 0$, i.e. conserved parabolicity.

From eq. (2.12) it can be seen that for a given charge carrier density the highest mobility (with respect to IIS) is reached for donors with $Z = 1$, as for instance in the case of Al_{Zn} . The presence of any compensating acceptor states leads to a reduction of n_e (trapping) along with an increase in n_{ii} according to

$$n_e = Z_d n_d - Z_a n_a \quad \text{and} \quad n_{\text{ii}} = n_d + n_a \quad (2.17)$$

and hence also lowers the mobility. This points out the detrimental nature of compensation with respect to conductivity. Like other TCOs, ZnO shows a high tendency for self-compensation. Therefore, the presence of compensating acceptors always needs to be regarded⁹.

In ZnO Zn-vacancies and O-interstitials are the dominating acceptors. Both defects exhibit $Z = 2$. Unfortunately, the B-H-D formalism, as presented in eq. (2.12) does not account for multiple species of ionized impurities having different Z . However, Look *et al.* derived a notation essentially based on eq. (2.17) and MATTHIESEN's rule [29]:

$$\mu_{\text{ii}}^{-1} = \mu_{\text{ii}0}^{-1} \frac{\sum_i Z_{\text{d},i}^2 n_{\text{d},i} + \sum_i Z_{\text{a},i}^2 n_{\text{a},i}}{n_e} = \mu_{\text{ii}0}^{-1} \frac{\sum_i Z_{\text{d},i}^2 n_{\text{d},i} + \sum_i Z_{\text{a},i}^2 n_{\text{a},i}}{\sum_i Z_{\text{d},i} n_{\text{d},i} - \sum_i Z_{\text{a},i} n_{\text{a},i}}. \quad (2.18)$$

This modified expression allows the application also to (partly) compensated TCOs regardless of number and charge of ionized impurity species.

Grain boundary scattering Like most TCO films used for opto-electronic application, ZnO films commonly exhibit a poly-crystalline morphology. This already implies the presence of grain boundaries (GB). In the context of electronic transport a GB represents a quasi-two dimensional disruption of the atomic structure accompanied by a corresponding change in the local electronic configuration commonly described by the formation of a potential barrier. In 1975 Seto proposed a one dimensional model describing the electronic transport through GBs¹⁰ [36]. He assumed a geometry built up of grains with a constant lateral grain size, l , interspersed by narrow regions, the GBs, having a considerable amount of trap states (defects), represented by an interface density Q_t . Charge carriers originating from the intra-grain regions are trapped at the GBs. Due to band bending a potential barrier, Φ_{gb} , accompanied by a depletion zone of width $w = Q_t/n_d$ is formed. For low doping level (i.e. $n_d < Q_t/l$) the whole grain is depleted. The barrier gets higher with increasing doping before reaching a maximum at $n_d = Q_t/l$. After passing that point all trap states are occupied and

⁹At this point it is noteworthy that Ellmer disregarded the effect of compensating acceptors in his investigations [19], while it could also give a reasonable explanation for the mobility breakdown at high charge carrier densities.

¹⁰Seto originally derived the model for Boron-doped p-type silicon.

the depletion width and hence Φ_{gb} reduces for further doping:

$$\begin{aligned}\Phi_{\text{gb}} &= \frac{e}{8\varepsilon_0\varepsilon_r} \cdot n_d l^2 & \text{for } n_d \leq Q_t/l \\ &= \frac{e}{8\varepsilon_0\varepsilon_r} \cdot \frac{Q_t^2}{n_d} & \text{for } n_d \geq Q_t/l\end{aligned}\quad (2.19)$$

In the case of ZnO, the interpretation of n_d with respect to Seto's model is not straight forward. Due to its high tendency for self-compensation n_d , the density of *non-compensated, ionized* donor states or even more correctly the density of charge carries, whether trapped at the GBs or not, is experimentally hard to obtain. Therefore, authors commonly refer to n_e as derived from Hall-effect measurements, instead (see for instance [37–39]). Since carriers are trapped at the GBs, this approximation is strictly limited to $n_d \gg Q_t/l$. A fact sometimes ignored by the authors. Moreover, the influence of additional intra-grain acceptor states on n_d depends on their energetic positions relative to that of the GB defect states and is hence hard to estimate. In summary the Seto-model provides a simple quantitative description of GB scattering, but care needs to be taken in its application to ZnO.

For thermionic emission the model yields a mobility,

$$\mu_{\text{gb}} = \frac{e \cdot l}{(2\pi m^* kT)^{1/2}} e^{-\frac{e\Phi_{\text{gb}}}{kT}}, \quad (2.20)$$

for carrier transport across grain boundaries. For narrow barriers the probability for the carriers tunneling through the barrier also becomes reasonable. However, since both the width and height of the barrier scale with $1/n_d$, tunneling (field emission) was neglected by Seto in application to p-type Si. Beside that there are some works on LPCVD-grown ZnO also accounting for the contribution of tunneling with respect of transport across grain boundaries [39–42]. This is of particular necessity when conducting temperature dependent measurements of the electronic transport. In the room temperature regime it was found that tunneling becomes the predominant effect for carrier transport across GBs for high boron-doping ($n_e \geq 1 \cdot 10^{20} \text{ cm}^{-3}$) in ZnO:B [40]. However, since electronic transport is no longer limited by GB scattering but by IIS for such high doping levels, tunneling is not considered in this work¹¹. Thus, μ_{gb} as defined in eq. (2.20) has to be interpreted as a lower limit of the GB contribution to μ_{tot} .

Phonon scattering At room temperature interaction of charge carriers with vibrational modes of the crystal lattice (phonons) has to be considered both in polycrystalline material and single crystals. In ZnO three phonon-related scattering terms are commonly accounted [18, 29]: (i) polar optical mode scattering, (ii) acoustic mode scattering and (iii) piezoelectric

¹¹The presence of intra-grain compensating acceptors (not regarded in the aforementioned publications) is believed to have a more dominant effect on the mobility - carrier density relation.

mode scattering. Whereas (i) is related to interacting with vibrational polarization effects, a specialty of polar semiconductors with partially ionic bonding, (ii) is due to scattering at lattice deformations accompanied by a local shift of the band edges, caused by acoustical phonons and (iii) is an interaction with the electric fields induced by acoustical phonons in piezoelectric materials [18]. For ZnO the contribution of (ii) is minor compared to (i) and (iii). All of these scattering mechanisms show temperature dependence and hence need to be considered when temperature is varied. In contrast to that there is no (or little¹².) dependence on charge carrier density for phonon scattering. As all transport measurements presented here are conducted at room temperature the approach of Ellmer [19] is adapted who accounted for phonon related scattering by the constant contribution

$$\mu_{\text{ph}}(T = 300 \text{ K}) = 210 \frac{\text{cm}^2}{\text{Vs}} . \quad (2.21)$$

Additional scattering mechanisms, like neutral impurity scattering and dislocation scattering, are rarely regarded as they are believed to have a minor impact in heavily doped ZnO [37]. Therefore, with eq. (2.11) we get

$$\frac{1}{\mu_{\text{tot}}} = \frac{1}{\mu_{\text{ii}}} + \frac{1}{\mu_{\text{gb}}} + \frac{1}{\mu_{\text{ph}}} \quad (2.22)$$

expressing the theoretical mobility limit.

2.1.5 Optical Properties

When matter is exposed to an electro-magnetic field generally some interaction occurs. On a phenomenological scale the interaction can lead to transmission and reflection at the interface and absorption within the volume. All three phenomena are wavelength dependent and commonly take place simultaneously to a certain extent. This extent is represented by the transmittance (T), the reflectance (R), and the absorptance (A) defined as the ratio of transmitted, reflected and absorbed light intensity to the intensity of incident light, respectively¹³ Following from the principal of energy conservation

$$1 = A(\lambda) + R(\lambda) + T(\lambda) \quad (2.23)$$

¹²The models taken in [18] don't exhibit a dependence on n_e , whereas the expressions used by Look *et al.* [29] to describe acoustic and piezoelectric mode scattering show a moderate dependence on n_e

¹³In the context of TCOs and its application to solar cells we are interested in a region of the electromagnetic spectrum which is commonly referred to as *optical* part containing the ultra-violet (*UV*), visible (*vis*) and near infra-red (*NIR*) light regime (altogether ranging approximately $200 \text{ nm} < \lambda < 3000 \text{ nm}$ or $4 \text{ eV} > h\nu > 0.41 \text{ eV}$). Therefore the term *light* is used equivalent to *electro-magnetic wave* in this work.

must be fulfilled. The absorption of light propagating through a medium can be described by the LAMBERT-BEER-law

$$A_{\text{int}}(x, \lambda) = 1 - e^{-\alpha(\lambda)x} \quad \longleftrightarrow \quad \alpha(\lambda) = -\frac{1}{x} \ln(1 - A_{\text{int}}(x, \lambda)), \quad (2.24)$$

where x is the distance passed by the light within the medium and α is the absorption coefficient of the specific material. For a layer with thickness d the absorption coefficient can be calculated from reflectance and transmittance by

$$\alpha(\lambda) = -\frac{1}{d} \ln \left(\frac{T(\lambda)}{1 - R(\lambda)} \right). \quad (2.25)$$

This expression also accounts for reflection at the interfaces of the layer and is thus more relevant for practical use. It is equivalent to the right hand side of eq. (2.24) for $x = d$ and $A_{\text{int}} = A/(1 - R)$.

Figure 2.2 depicts the transmittance (T), reflectance (R) and absorptance (A) of a representative ZnO:Al film on glass. The film thickness of the ZnO:Al was determined by fitting the optical model described in the course of this section to the T and R data measured by a photo-spectrometer (cf. sec. 3.2.2) whereas A was derived from eq. (2.23). An obvious feature are the oscillations in T and R between 350 nm and 1600 nm. They occur due to

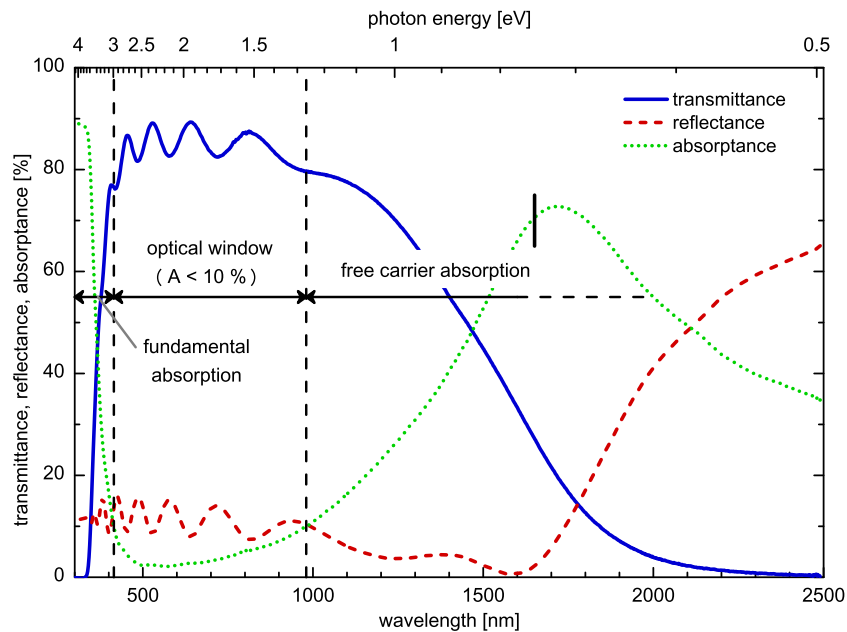


Figure 2.2: Transmittance (T), reflectance (R) and absorptance ($A = 1 - R - T$) of a representative ZnO:Al film of 668 nm thickness on glass as a function of wavelength. The spectral regions of fundamental absorption ($\lambda < 415$ nm) and free carrier absorption ($\lambda > 980$ nm) as well as the optical window region in-between, where $A < 10\%$, are indicated and separated by the horizontal dashed lines. For orientation the top axis shows the corresponding photon energy scale.

interference effects within the ZnO:Al film. In contrast to that the absorptance shows no oscillations. Except for long wavelengths (> 1700 nm) the reflectance stays below $\approx 12\%$. Regarding A (and T) three regions can be distinguished (separated by the dashed lines). Below 415 nm A raises for shorter wavelengths within few 10 nm from 10 to more than 85%. This is the absorption due to excitation of electrons from the valence band into the conduction band, the so called fundamental or band-to-band absorption. Accordingly the position of this edge (on the photon energy scale) represents the optical band gap energy. In fig. 2.3 the corresponding band structure is depicted. For degenerate semiconductors the bottom of the conduction band is filled with charge carriers. Hence, as electrons can only be excited to empty states the optical band gap energy evolves with the charge carrier density. This effect is known as BURSTEIN-MOSS-shift (fig. 2.3(b)). It is counteracted by a band gap narrowing due to exchange interaction of the electron ensemble and due to ionized impurity scattering (fig. 2.3(c)). However, in the case of degenerate ZnO:Al the BURSTEIN-MOSS-shift is predominant and the optical band gap energy increases with increasing charge carrier density [43]. Coming back to fig. 2.2, above 415 nm the ZnO:Al film exhibits an absorptance well below 10% and a transmittance above 80%. This region of high transmittance is called the optical window and is a feature of interest with respect to the application of TCOs. In the NIR region above 980 nm the absorptance increases (transmittance decreases) again until a maximum is reached at approximately 1700 nm. This is related to collective oscillations of the free carrier ensemble, which are referred as so called plasmons. This type of absorption is accordingly referred to as free carrier absorption (FCA). For even longer wavelengths A decreases again while R raises and T approaches 0%.

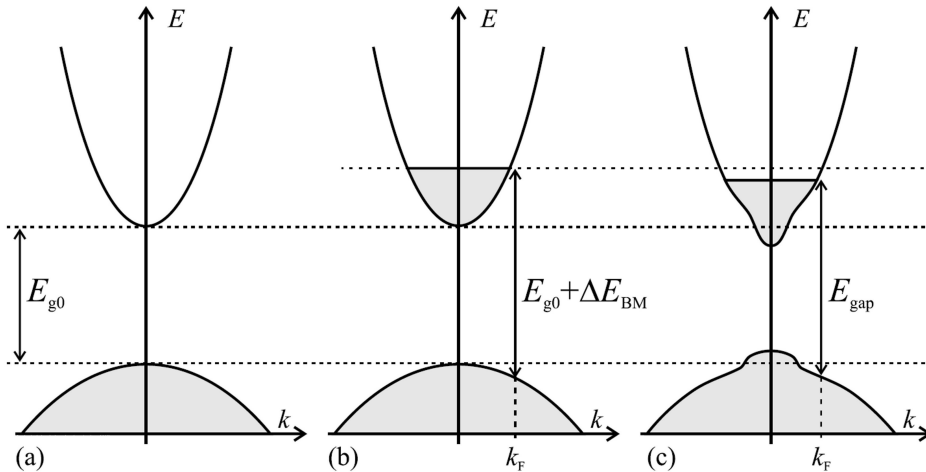


Figure 2.3: Schematic band structure according to Sernelius *et al.* [43] for (a) an undoped semiconductor, (b) a degenerate semiconductor including the BURSTEIN-MOSS-effect and (c) the same with additional band gap narrowing (see text). Figure taken from Berginski [44].

A theoretical description of the propagation of electro-magnetic waves (including the interaction with matter) is provided by MAXWELL's equations. For the purpose of describing

the interaction of light, (i.e. an electro-magnetic wave in the optical regime) with a TCO some simplifying assumptions can be made. First, in the optical regime magnetic interaction and hence current induction can be neglected ($j = 0$). Further, the material can be regarded as isotropic. Under this circumstances the interaction of an electromagnetic plane wave

$$\vec{E}(t) = \vec{e}_x E(t) = \vec{e}_x E_0 e^{-i\omega t} \quad (2.26)$$

with matter yields the displacement field

$$\vec{D} = \varepsilon \varepsilon_0 \vec{E} = \varepsilon_0 \vec{E} + \vec{P} , \quad (2.27)$$

where ε_0 is the electric field constant, \vec{P} is the polarization of the material and ε is the dielectric function of the material. In other words, the presence of the material (instead of vacuum) is regarded by introducing ε , which is a complex number¹⁴ and generally exhibits a frequency dependence

$$\varepsilon(\omega) = \varepsilon_1(\omega) + i\varepsilon_2(\omega) \quad (2.28)$$

and is related to the complex index of refraction, \tilde{n} , by

$$\tilde{n} = n + i\kappa = \sqrt{\varepsilon} , \quad (2.29)$$

where n denotes the real-valued index of refraction, i.e. $n = c/v_{\text{medium}}$, and κ is called extinction coefficient accounting for the absorptive loss. Thereby, the absorption coefficient, α , used in eq. (2.25) can be expressed as

$$\alpha = \frac{2\kappa\omega}{c} . \quad (2.30)$$

In order to describe the optical properties of ZnO:Al over a wide spectral range (typically 300 to 2500 nm as presented in fig. 2.2) we need to handle the particular contributions of the different effects to ε . This can be easily done by introducing the concept of susceptibility χ

$$\varepsilon = (1 + \chi) . \quad (2.31)$$

With that eq. (2.27) can be written as

$$\vec{D} = \varepsilon_0 \vec{E}(1 + \chi) \quad \text{and} \quad \vec{P} = \varepsilon_0 \chi \vec{E} . \quad (2.32)$$

¹⁴Generally the dielectric constant is a tensor, but as we assumed isotropy it can be treated as a scalar.

For the purpose of this work the expression

$$\varepsilon = \varepsilon_{\infty} + \chi_{\text{BG}} + \chi_{\text{FC}} , \quad (2.33)$$

with the contribution of the band gap (χ_{BG}) and the free carriers (χ_{FC}) is sufficient [45]. ε_{∞} is a constant positive real number containing contributions related to higher energies (shorter wavelengths)¹⁵ [46]. For the description of the band gap and the free carrier contributions we will follow the approach of Pflug *et al.* [45]. A very detailed derivation and description of this optical model, also in the context of sputtered poly-crystalline ZnO(:Al) films on foreign substrates, is given by Greiner [47]. A LENG-oscillator [48] is used to describe χ_{BG} . Despite its abstract nature, this oscillator provides good fit results and its calculation is very time saving with respect to numerical fitting¹⁶. The free carrier contribution χ_{FC} is represented by a modified DRUDE term. The DRUDE-model already used to describe the interaction of stationary electric fields with the free charge carriers (sec. 2.1.3) can also be solved for electro-magnetic plane waves as defined in eq. (2.26). Setting

$$x(t) = x_0 e^{i\omega t} \quad (2.34)$$

Equation (2.1) can be rewritten as

$$-m^* \omega^2 x_0 e^{i\omega t} - i\omega m^* \tau x_0 e^{i\omega t} = -e E_0 e^{i\vec{k}\vec{x} - i\omega t} . \quad (2.35)$$

The resulting oscillation of a single electron shows the amplitude

$$x_0 = \frac{e E_0}{m^* \omega^2 + i\omega \frac{m^*}{\tau}} \quad (2.36)$$

and introduces the dipole moment

$$p(t) = -ex(t) .$$

Together with eq. (2.26) and (2.36) the polarization resulting from the collective oscillation of the ensemble of electrons is

$$P(t) = n_e p(t) = -\frac{e^2 n_e}{m^*} \cdot \frac{1}{\omega^2 + i\frac{1}{\tau}\omega} E(t) . \quad (2.37)$$

¹⁵The susceptibility of an oscillator approaches a constant positive real number far away from the resonance [38].

¹⁶Details on the Leng-formalism and its application to χ_{BG} for ZnO can be found, e.g. in [38, 47].

Comparing this to eq. (2.32) we can write

$$\chi_{\text{FC}} = -\frac{\omega_{\text{p}}^2}{\omega^2 + i\omega\omega_{\tau}}, \quad (2.38)$$

with ω_{p} and ω_{τ} being the plasma frequency and the damping frequency, respectively:

$$\omega_{\text{p}}^2 = \frac{e^2 n_{\text{e}}}{\varepsilon_0 m^*} \quad \text{and} \quad (2.39)$$

$$\omega_{\tau} = \frac{1}{\tau} = \frac{e}{m^* \mu} \quad (\text{with eq. (2.3)}). \quad (2.40)$$

It is known, that this classical DRUDE formalism is not sufficient for the description of heavily doped TCOs. This was for instance discussed by Hamberg and Granqvist in the case of ITO [49]. They observed a reduction of ω_{τ} for $\omega > \omega_{\text{p}}$. This is in accordance with a theoretical work by Gerlach [50] utilizing the energy-loss method to describe the IIS of electrons. This theory was applied to ITO in [49] and later on also to ZnO:Al [46].

To circumvent the rather complex numerical nature of these formalisms, Pflug *et al.* suggested a simple and hence, easy computable empirical approximation [45]:

$$\omega_{\tau}(\omega) = f(\omega)\omega_{\tau 0} + (1 - f(\omega))\omega_{\tau 1} \left(\frac{\omega}{\omega_{\text{tr}}}\right)^s \quad (2.41)$$

with

$$f(\omega) = \left[1 + e^{\frac{\omega - \omega_{\text{tr}}}{\gamma_{\text{tr}}}}\right]^{-1}.$$

This extended *Drude* model exhibits the additional parameters $\omega_{\tau 1}$, ω_{tr} , γ_{tr} and s representing the damping frequency in the frequency dependent regime, transition frequency, transition band width and scattering exponent, respectively. For low frequencies, this model approximates the classical *Drude* model. The scattering exponent is related to the predominant scattering mechanism and generally set to $-3/2$ in this work, representing IIS.

The whole model is implemented in the software environment *RIG-VM*, which was used for fitting the optical properties of the ZnO:Al layers to the measured reflectance and transmittance data. The algorithm is based on the transfer matrix method. In order to extract the above mentioned parameters for the ZnO:Al film, the complete sample stack (cf. sec. 3.1) needs to be modelled. This was realized by assuming half-space of air ($\tilde{n}_{\text{air}} = 1$), the glass substrate with its known thickness and experimentally determined values of \tilde{n} in tabulated form, the SiO_xN_y layer with variable thickness and experimental determined values of \tilde{n} represented by a third order CAUCHY-term, the ZnO:Al described by the above described model

(eq. (2.33)) and again half-space of air. The layers have been treated as coherent, whereas the glass (and the air) were assumed to be incoherent. Moreover, a surface roughness with variable thickness at the ZnO:Al/air interface was allowed. Its physical description is based on the effective medium approach suggested by Bruggeman [51].

2.2 Si-based Thin-film Solar Cells

The term *thin-film solar cells* already points at the low thickness of these devices being only 0.5 to 5 μm compared to $\approx 160 \mu\text{m}$ for conventional wafer-based crystalline Si-solar cells. Si-based thin film solar cells can be divided into two groups.

One group is based on poly-crystalline silicon on glass (poly-Si). As this cell type is not discussed within this work, only a very brief introduction is given in the following. The basic idea behind these cells is to use cheap and fast techniques for depositing a precursor material (usually comprising poor device quality) and convert it via post-deposition processing into a poly-crystalline phase with high device quality comparable to that of Si-wafers used in conventional solar cells. Despite the potential for high conversion efficiencies, there are still some challenges to overcome with that concept. Depending on the specific processes involved those issues are mainly attributed to high temperatures, interface passivation and implementation of a device structures. With that concept the devices are usually prepared in p-n (or n-p) configuration. Several contributions giving an overview on the technological realization as well as the status and potential of this approach were recently published [52–54].

The approach used within this work is based on hydrogenated amorphous and/or hydrogenated microcrystalline silicon. Thereby, the materials are deposited in device quality, directly. For this purpose, chemical vapor deposition (CVD) techniques are predominantly used. By using silane (SiH_4) assisted by adding H_2 as the fundamental precursor gases, CVD allows the essential incorporation of atomic hydrogen (cf. sec. 2.2.1) during the growth process even at rather low substrate temperatures. The energy needed to decompose the precursors is supplied rather by a plasma (plasma enhanced CVD, PECVD) or by a heated filament (hot wire CVD, HWCVD). Among those two techniques only PECVD has reached industrial relevance, up to now. An introduction to the particular PECVD processes used for growing the cells presented in this thesis is given in sec. 3.1.6.

These directly grown cell types are usually configured as a p-i-n or n-i-p structure (with respect to the deposition sequence), where the doped layers introduce an internal field across the intrinsic absorber layer in order to increase the carrier collection. This is also often referred to as a *drift driven device*. Stacking two or more of such devices with different band gaps of the particular i-layer allows a better utilization of the solar spectrum [55]. For instance, it is a common technique to use a top cell and a bottom cell based on hydrogenated amorphous silicon (*a-Si:H*) and hydrogenated micro-crystalline silicon ($\mu\text{c-Si:H}$), respectively [56].

Figure 2.4 shows the schematic structure of such a tandem device. The sun light enters the cell through the glass. The transparent front TCO (≈ 500 nm of ZnO:Al, in our case) contacts the cell and exhibits a texture that introduces light scattering (sec. 2.2.3). The short wavelength light ($\lambda \lesssim 600$ nm) is mainly absorbed in the top cell. For longer wavelengths the a-Si:H gets increasingly transparent and hence allows absorption of the remaining light in the bottom cell. A back reflector is placed at the back of the cell which reflects the light which is not absorbed during the first pass through the cell and at the same time constitutes the back side electrode (back contact). In our case, the back reflector was built up of a double layer of 80 nm ZnO:Al and 200 nm Ag. The typical thickness of the particular silicon layers is 10 to 30 nm for the doped (p and n) layers, and 250 and 2000 nm for the intrinsic layer of the a-Si:H top cell and the μ c-Si:H bottom cell, respectively. Since the light absorbed in the doped layers does not contribute to the photo current generation, they are kept as thin as possible, whereas the i-layer thicknesses have to be mutually adjusted in order to generate a similar photo current density (*current matching*). The intention of the intermediate reflector layer (IRL), also depicted in the scheme, will be explained in sec. 2.2.4.

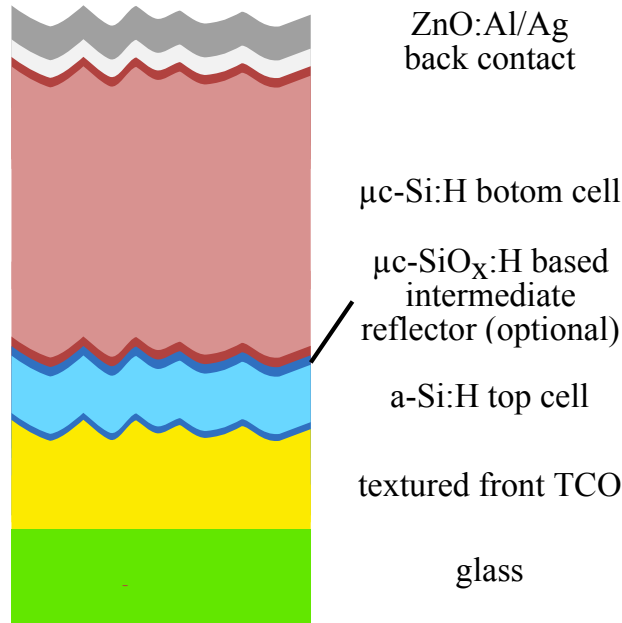


Figure 2.4: Schematic drawing of an a-Si:H/ μ c-Si:H-based thin film cell

Compared to conventional wafer based c-Si solar cells, a-Si:H/ μ c-Si:H cells can be processed at low temperatures ($T_{\text{dep}} \lesssim 200$ °C). On the other hand, the conversion efficiency is lower and a-Si:H based cells exhibit a light induced degradation (cf. sec. 2.2.1). In the following, the fundamental requirements and properties of this device type and the materials involved will be explained.

2.2.1 Si based Materials for Thin-film Solar Cells

Figure 2.5 shows the absorption coefficient and the penetration depth for wafer-type crystalline silicon and typical device quality hydrogenated amorphous silicon and hydrogenated microcrystalline silicon. Crystalline silicon exhibits a direct band gap of 3.4 eV and an indirect band gap of 1.12 eV [57]. The absorption of photons with energies in the range 1.1 to 3.4 eV requires the incorporation of at least one phonon in order to conserve the momentum. As indirect processes are less probable than the direct band-to-band transition the absorption coefficient is accordingly lower. Below 1.1 eV absorption can occur due to shallow and deep defects as well as due to free charge carriers (in doped silicon or at high temperatures). In contrast to band-band transitions, the latter absorption mechanisms do not contribute to the creation of excitons. However, spectroscopic investigation of the sub-band gap absorption can reveal information, e.g. on material quality, defect levels and charge carrier scattering mechanisms.

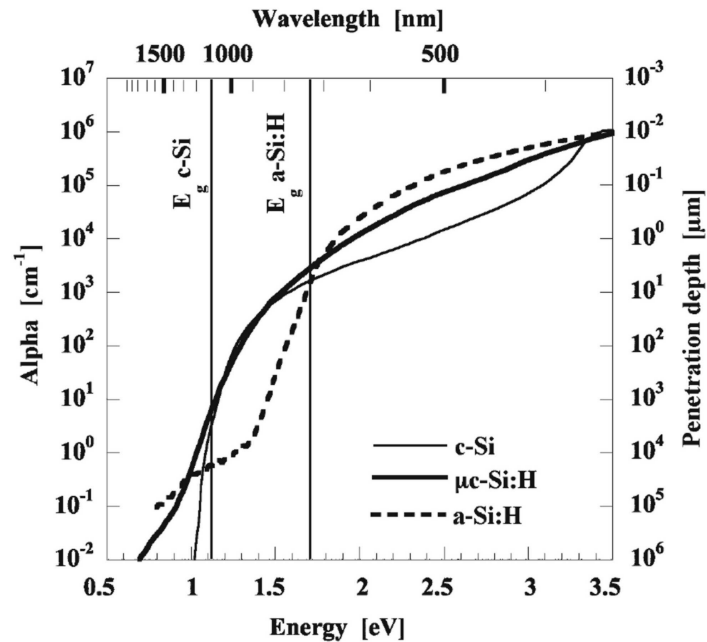


Figure 2.5: Optical absorption coefficient, α and penetration depth, $d_\lambda = 1/\alpha$, as function of the photon energy and the wavelength for wafer-type crystalline silicon (c-Si) and typical device quality hydrogenated amorphous silicon (a-Si:H) and hydrogenated microcrystalline silicon ($\mu\text{c-Si:H}$; corrected for light scattering due to surface roughness [58]) layers on glass. Graph taken from [5]. Original data from [58, 59].

Due to the similar short range order, i.e. average bond length, average bond angle and number of neighbors (*coordination*) amorphous silicon in general shows the same material properties as crystalline silicon, i.e. it has similar electronic structure and hence is a semiconductor as well. But, in contrast to crystalline silicon, it shows no translational periodicity (i.e. long range order). For the electronic properties, this has the following consequences [60]:

- The band structure becomes isotropic in \vec{k} -space. Hence, the concept of dispersion relation $E(\vec{k})$ is commonly replaced by that of density of states distribution $N(E)$. The formalism of direct and indirect band-to-band transitions is no longer valid.
- Deviations in the length and angle of bonds lead to significant electron scattering. This reduces the charge carrier mobility for the extended states within the bands. Moreover, the presence of the bonding disorder introduces localized tail states at the band edges. These states are of importance since electronic transport takes place at the band edges.
- Structural deviations lead to defect states deep within the band gap. Effects like trapping and recombination are mainly related to these states.

The latter is the main reason why a-Si is commonly doped with hydrogen (a-Si:H) for application as a semiconductor in electronic devices. The hydrogen terminates open bonds in the silicon network (*dangling bonds*) and therefore reduces the defect density. The band gap energy (E_g) of a-Si:H is not well defined and depends on the hydrogen content. For its determination the TAUC-definition [61] is often used and hence referred to as optical gap. Typical values range from 1.6 to 1.9 eV. Due to the missing long range order there are no momentum selection rules anymore. Hence, the probability for absorbing photons, i.e. the absorption coefficient, is increased for photon energies between the optical gap and 3.4 eV compared to crystalline silicon.

In 1977, Staebler and Wronski reported on a *light induced degradation* (LID) in photo- and dark-conductivity of a-Si:H films [62]. They also found that the effect was fully reversible by annealing the samples for few hours at temperatures $T \gtrsim 150^\circ\text{C}$. Nowadays, the phenomenon is also referred to as *Staebler-Wronski-effect* (SWE). Despite many activities and publications on the nature of defects in a-Si:H and their influence on the electronic material properties [63–69] up to now there is no commonly accepted picture of the microscopic mechanism behind the SWE. However, most authors ascribe it to the light induced formation and thermal H-passivation of (additional) dangling bonds [60]. The SWE limits the i-layer thickness of efficient a-Si:H based thin-film cells to about < 400 nm. Otherwise, recombination would dramatically increase after few hours of light exposure and hence conversion efficiency would break down.

Thanks to the H-termination of dangling bonds, a-Si:H can be doped n-type (phosphorus) or p-type (boron) by adding phosphine (PH_3) or trimethylboron (TMB, $\text{B}(\text{CH}_3)_3$) / diborane (B_2H_6) to the precursor gas, respectively. This was first done by Spear and Le Comber in 1975 [2]. However, due to the presence of localized states within the band tails and due to the formation of additional dangling bonds by incorporating dopants, the doping efficiency in a-Si:H is rather low compared to c-Si and even decreases with increasing doping level [2]. As a consequence, the maximum achievable conductivity is limited to $\sigma \lesssim 10^{-1}$ and

$\lesssim 10^{-2} (\Omega\text{cm})^{-1}$ for n- and p-type doping, respectively. The difference is due to the steeper conduction band tail compared to the valence band tail [60].

Hydrogenated microcrystalline silicon ($\mu\text{c-Si:H}$) can easily be obtained by varying the deposition conditions, otherwise used for producing a-Si:H. This includes parameters such as process pressure, gas flow rate, excitation power, excitation frequency, temperature and so on, but predominantly the silane/hydrogen ratio (see sec. 3.1.6). The latter is commonly expressed as the silane concentration

$$SC = \frac{Q_{\text{SiH}_4}}{Q_{\text{SiH}_4+\text{H}_2}}, \quad (2.42)$$

or the hydrogen dilution

$$R = \frac{Q_{\text{H}_2}}{Q_{\text{SiH}_4}} \quad (2.43)$$

where Q denotes the standard volume flow rate for the particular gas.

According to Vetterl *et al.* [70], $\mu\text{c-Si:H}$ consists of columnar crystallites more or less embedded in a matrix of a-Si:H and interspersed by defective regions (also referred to as voids, cracks or porous zones). Generally, increasing hydrogen dilution leads to higher crystalline volume fraction, an important material property with respect to application in solar cells. The best cell performance is obtained close to the transition to the a-Si:H material as the amorphous matrix acts as a passivation layer to the crystallites.

Similar to c-Si, $\mu\text{c-Si:H}$ exhibits an indirect band gap with $E_g = 1.1$ eV. Between 1.5 and 3.3 eV, the absorption coefficient of $\mu\text{c-Si}$ lies in-between that of a-Si and c-Si (see fig. 2.5), a direct consequence of the mixed phase nature. Below 1.5 eV, the absorption coefficient of $\mu\text{c-Si:H}$ is similar to that of c-Si. This makes $\mu\text{c-Si:H}$ an appropriate absorber material for solar cells, especially when combined with a-Si:H in a tandem cell.

2.2.2 Basic Description of opto-electric Solar Cell Properties

In order to describe the ideal J - V -characteristic of a solar cell, the so-called *one-diode model* is usually used. Its equivalent circuit model is presented in fig. 2.6. It consists of a diode representing the dark characteristic of the junction, J_{dark} , a current source accounting for the photo-generated current density, J_{ph} , a series resistance, R_S , accounting for ohmic losses either within the device or external and a parallel resistance, R_P , considering ohmic shunts. The corresponding J - V -characteristic is written as

$$J(V) = J_{\text{ph}} - \underbrace{J_0 \left[\exp \left(\frac{e(V - J(V) \cdot R_S)}{nkT} \right) - 1 \right]}_{J_{\text{dark}}(V)} - \frac{V - J(V) \cdot R_S}{R_P}, \quad (2.44)$$

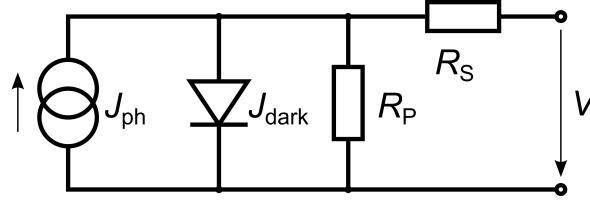


Figure 2.6: Equivalent circuit for the one-diode model universally used to describe the fundamental J - V characteristic of solar cells.

where J_0 and n are the reverse saturation current and the ideality factor of the diode, respectively. In the basic case of a p-n junction, we have $n = 1$ when the diffusion current is predominant and $n = 2$ when generation and recombination in the depletion zone of the p-n junction dominates. According to Shah [71] this picture can be coarsely approximated for p-i-n junctions by assuming the i-layer as being inserted into a p-n junction, representing a kind of extended depletion zone. Consequently the ideality factor of a high quality p-i-n device, i.e. with recombination predominantly in the i-layer, should be $n = 2$. Besides that maybe the most marked difference compared to a p/n junction is the dependence of the recombination on J_{ph} . This is commonly accounted for by introducing a voltage dependence to the photo current [72], $J_{ph} = f(V)$, or by inserting an additional photocurrent dependent current sink in the equivalent circuit of the one-diode model [73]. In the case of multiple monolithically stacked junctions, the situation even gets more complicated, since each single junction needs to be represented by a separate diode according to eq. (2.44). However, in this work, the analysis of the illuminated J - V characteristics, as will be described in the following paragraph is sufficient. From an electrical point of view, all these junctions are connected in series. Thus, the flowing current density in all single junctions is always the same and the individual voltages (at a given current density) add up to the total voltage at the contacts. This principle directly implies the need for balancing the (potential) photo current densities of all single junctions in order to achieve the full potential of such a device. Otherwise, the current density of the whole device is predominantly determined by the junction with the lowest photo current density.

In fig. 2.7 an illuminated J - V curve of a representative a:Si-H/ μ c-Si:H based tandem cell is presented together with the J - V parameters, short circuit current density, $J_{SC} = j(V = 0)$, open circuit voltage, $V_{OC} = V(j = 0)$, maximum power point where $j \cdot V = P_{out}$ reaches its maximum value, P_{MPP} , as well as the corresponding current density, j_{MPP} , and voltage, V_{MPP} . Additionally, the power density curve, $p(V)$ (red line, $p = P/A$) is presented. Another important illuminated J - V parameter is the *fill factor*,

$$FF = \frac{j_{MPP} \cdot V_{MPP}}{J_{SC} \cdot V_{OC}} = \frac{p_{MPP}}{J_{SC} \cdot V_{OC}}. \quad (2.45)$$

It can be interpreted as a measure of collection efficiency under load. For standard test

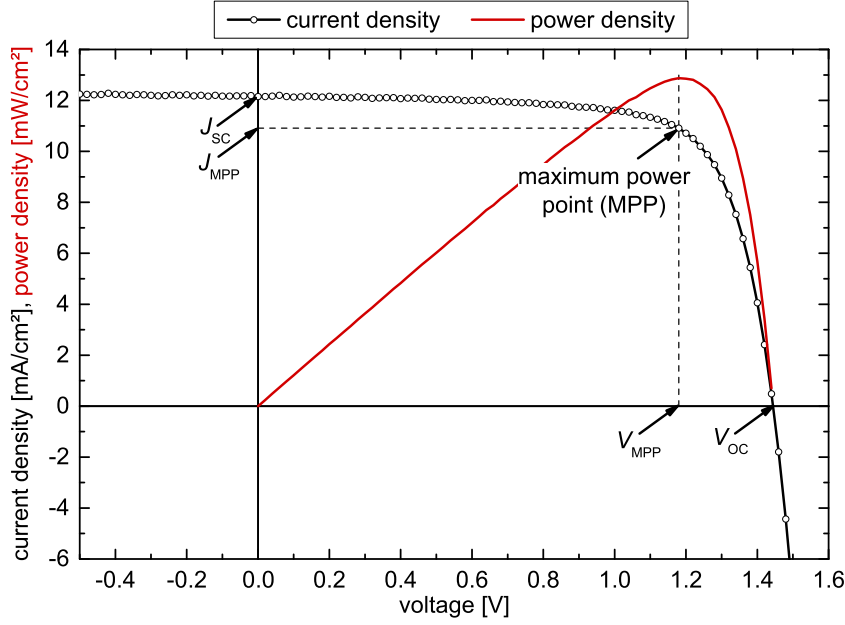


Figure 2.7: Illuminated J - V characteristic of a representative a-Si:H/ μ c-Si:H tandem cell

conditions (i.e. an irradiance of $E_{\text{STC}} = 1000 \text{ W/m}^2$ and a spectral distribution according to AM1.5g; cf. sec. 3.2.4) the conversion efficiency is determined as

$$\eta = \frac{P_{\text{out}}}{P_{\text{in}}} = \frac{p_{\text{out}}}{E_{\text{STC}}} = \frac{p_{\text{MPP}}}{1000 \text{ W/m}^2} = \frac{J_{\text{SC}} \cdot V_{\text{OC}} \cdot FF}{1000 \text{ W/m}^2}. \quad (2.46)$$

Another important quantity for the characterization of solar cells is the *quantum efficiency*, QE . It represents the statistical probability of collecting a photo-generated charge carrier per incoming photon and is usually interpreted as a function of wavelength (i.e. photon energy). The QE can also be expressed as *spectral response*, SR , by the relation

$$SR = QE \cdot \frac{\lambda \cdot e}{h \cdot c}. \quad (2.47)$$

Thus, by accounting for the charge of the collected carriers and the energy of the incoming photons, the SR represents the collected current density per irradiance. There are two common ways to account for the incoming photons: (i) referring to the total photon flux impinging the solar cell - *external quantum efficiency* (EQE) or (ii) referring to the photon flux absorbed in the cell structure (i.e. correcting for reflection and transmission, if any) - *internal quantum efficiency* (IQE). Due to the metallic back reflector transmission through the cell is virtually zero, and IQE can thus be written as

$$IQE(\lambda) = \frac{EQE(\lambda)}{1 - R(\lambda)}, \quad (2.48)$$

where $R(\lambda)$ is the total cell reflection, i.e. including specular and diffuse reflection. Accordingly, $1 - R(\lambda)$ will be referred to as total cell absorptance. In the case of multi junction devices, the EQE is measured separately for each single junction. This is a valuable opportunity, since it allows the determination of the potential photo current density of each single junction separately. Figure 2.8 depicts $EQE(\lambda)$ and $1 - R(\lambda)$ of a representative a-Si:H/ μ c-Si:H tandem cell. The $1 - R$ curve separates the reflective losses (red shaded area) from the total cell absorption (green and blue shaded area). The parasitic absorption (green shaded area) accounts for absorption within layers not contributing charge carriers to the photo current, whereas the EQE (blue shaded area) represents the fraction of photons absorbed within the intrinsic absorber layers that yield an collected electron-hole pair at the contacts. According to the J - V characteristic, the QE generally is also a function of the applied voltage, but is commonly measured and interpreted under short circuit conditions. Thus, for cells comprising reasonable device quality, collection losses can be neglected and the EQE hence approximates the actual optical absorption in the intrinsic absorber layer(s). From EQE , i.e. SR , the actually collected current density, J , for given irradiance, $E(\lambda)$, can be calculated by

$$J_{EQE} = e \int EQE(\lambda) \cdot \Phi_{ph}(\lambda) d\lambda = \int SR(\lambda) \cdot E(\lambda) d\lambda , \quad (2.49)$$

where Φ_{ph} is the photon flux. The irradiance is usually set to E_{STC} and referred to as "one sun" or "AM1.5g". In analogy this calculation was also applied to the other optical quantities, reflective loss and parasitic absorption, in order to determine (implied) current densities. The values corresponding to the different fractions under one sun are also added to fig. 2.8. The integration was generally carried out for $\lambda = 300 \dots 1100$ nm.

2.2.3 Light Trapping in Si-based Thin-film Solar Cells

In order to obtain high efficiencies the light absorption within the intrinsic absorber layer has to be maximized. This is especially crucial in these devices due to the rather low absorption coefficients at long wavelengths (compare fig. 2.5). In fact, this could be realized by simply increasing the i-layer thickness, but this would also lead to a decreased collection efficiency due to a lowered electric field strength and is of course economically undesirable with respect to deposition time and material consumption. Therefore, in practice a high absorption is realized by introducing so-called light-trapping concepts which prolong the effective path of the light within the device. The common basic approach is to apply light scattering textures and a reflective backside. In the case of p-i-n cells, the light scattering is usually implemented by incorporating a front-TCO with a random textured surface with typical lateral feature size $l \approx 0.2 \dots 2 \mu\text{m}$. For this purpose, either sputtered ZnO:Al [9, 74], ZnO:B grown by low

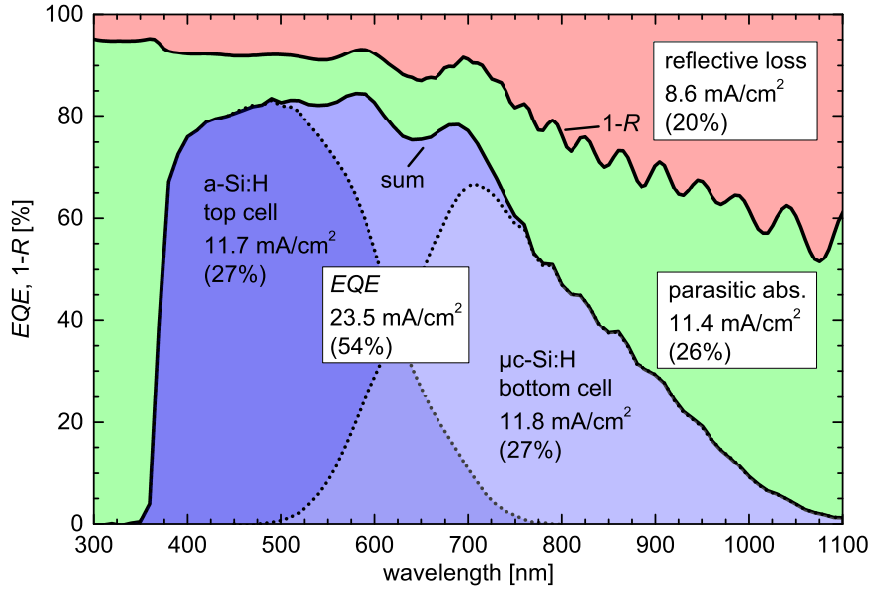


Figure 2.8: External quantum efficiency (blue shaded area) and total absorption of a representative a-Si:H/ μ c-Si:H tandem cell. The *EQE* is shown for the top and the bottom cell separately, as well as in total. The red shaded area represents the loss due to reflection. The green shaded area depicts the fraction of light absorbed in layers, which does not contribute charge carriers to the photo current. The numbers indicate the particular effective current densities in mA/cm² and, in parenthesis, the relative fraction of the totally available effective current density between 300 and 1100 nm under one sun (43.5 mA/cm²).

pressure chemical vapor deposition (LPCVD) [75] or SnO₂:F [76, 77] grown by atmospheric pressure chemical vapor deposition (APCVD) is used. In the case of sputtered ZnO:Al, a crater-like texture is achieved by post-deposition wet-chemical etching in diluted hydrochloric acid whereas the LPCVD-ZnO:B and the APCVD-SnO₂:F exhibit an as-grown pyramid-like texture. In all cases, the actual surface topography is closely related to the growth conditions of the TCO films [44, 78–84]. The light trapping capability strongly depends on the specific topography of the interface and needs to be adapted to the absorber material. Moreover, the device quality of the silicon is very sensitive to the surface texture [85–87]. From this fact, a trade-off between good light trapping, i.e. high short circuit current densities, and good electric device quality, i.e. high fill factor and open circuit voltage, arises.

In order to quantify the light scattering capability of a given texture, various methods have been established. A very common technique is to determine the *haze* in transmission as a function of wavelength,

$$H_T(\lambda) = \frac{T_{\text{diffuse}}(\lambda)}{T_{\text{total}}(\lambda)}, \quad (2.50)$$

where T_{diffuse} and T_{total} are the diffuse and total transmittance, respectively. Hence, haze defines the fraction of scattered light intensity (in transmittance). Figure 2.9 depicts typical

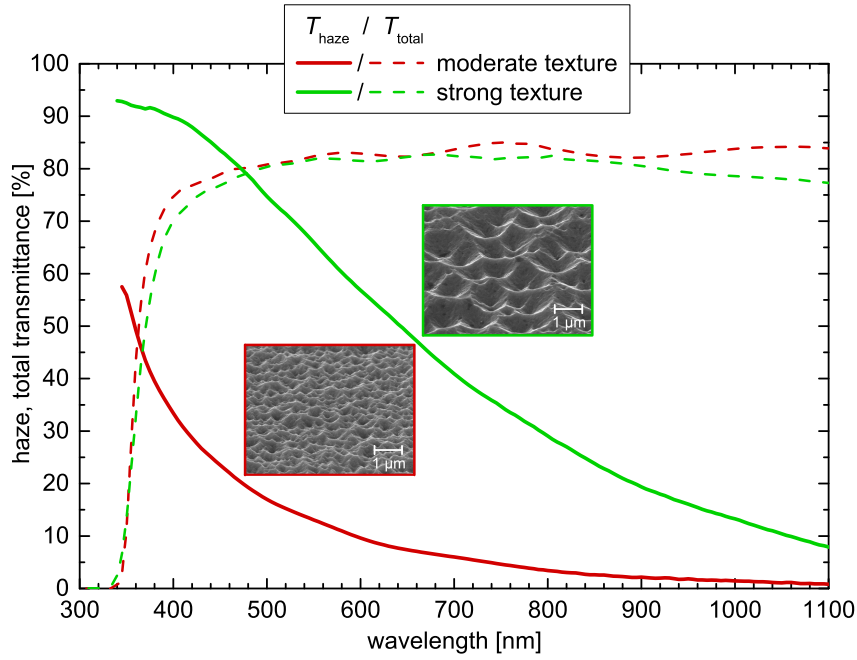


Figure 2.9: Haze (solid lines) and total transmittance (dashed lines) for ZnO:Al layers on glass with moderate (red) and rather strong texture (green). Tilted-view SEM images of the particular surface topography are also added. The images have the same magnification.

haze curves together with T_{total} and a SEM image for ZnO:Al layers on glass with moderate and rather strong texture. From the SEM images it can be seen that both surfaces exhibit the crater-like topography, typical for sputter-etched ZnO:Al layers. The moderate texture comprises a smaller feature size compared to the stronger textured sample. In both cases, haze decreases for longer wavelength, a direct consequence of the underlying scattering mechanism [88,89], whereas the stronger texture obviously yields higher haze, hence indicating stronger light trapping. However, care must be taken in rating the light trapping ability of different textures based on their haze spectra [90,91]. This is due to the fact that haze is an optical property determined in the far-field regime and for the TCO/air interface whereas the light trapping within a real thin-film solar cell is a near-field effect and takes place at the TCO/Si interface. Moreover, haze contains no information on the angular distribution of the scattered light intensity. This is of particular importance, since scattering into larger angles is preferable for good light trapping. Thus, the angular distribution can strongly determine the resulting light trapping.

There are several approaches to predict the light trapping of a given texture, at best in terms of photo current density or its increase in comparison to the case of a flat interface. These methods are commonly based on the knowledge of the particular surface texture as well as the optical constants of the materials incorporated, and application of scalar scattering theory [92–95], or rigorous solution of MAXWELL’s equations [96–99]. However, for two reasons we will not make use of such rather complex determinations within this thesis. First,

as will be shown in sec. 4.3, applying various annealings to textured ZnO:Al layers will not affect the particular morphology. Hence the light trapping capability will not change upon annealing. Second, all these approaches only deal with the optical influence of rough surfaces, whereas the consequences on the electrical quality of the cell, generally counteracting the optical improvements obtained by better light scattering, are not regarded. Instead, the light trapping ability of different front contact systems will be evaluated directly from *EQE* and photo current density values of thin-film solar cells.

At this point, we define the light path enhancement factor

$$m = \frac{l_{\text{light}}}{d_{\text{absorber}}} \quad (2.51)$$

as a measure for light trapping effectivity. For instance, the incorporation of a (perfect, flat) back reflector corresponds to $m = 2$, i.e. a doubling of the light path, l_{light} , with respect to the absorber layer thickness, d_{absorber} . In the ideal case, light trapping would lead to multiple internal reflections. A thin-film solar cell design making use of light path enhancement by an inclined back reflector was already proposed by Redfield in 1974 [6]. First experimental investigations on light trapping textures for thin-film a-Si:H can be traced back to 1983 [7,8]. In 1982 Yablonovitch and Cody postulated an upper limit of $m_{\text{max}} = 4 \cdot n_{\text{absorber}}^2$ for light path enhancement [100]. Thus, assuming $n_{\text{Si}} \lesssim 4$ we get $m_{\text{max}} \lesssim 64$ as an theoretical upper limit for light path enhancement in the case of silicon.

Experimental maximum values for the light path enhancement factor have been determined to be $m = 16$ and $m = 15.2$ in the case of $\mu\text{c-Si:H}$ single junction cells on sputter-etched ZnO:Al by Berginski [11,44] and the bottom cell of a-Si:H/ $\mu\text{c-Si:H}$ tandem cells on LPCVD-grown ZnO:B by Dominé [101], respectively. Obviously, these values are well below the theoretical limit. A reasonable portion of the difference can be ascribed to the ideal assumptions made by Yablonovitch and Cody in their model. In particular, the weak absorption approximation is violated in the case of Si within the wavelength region where light trapping takes place. Therefore, Tiedje *et al.* proposed an extension of the model accounting for absorption in the silicon [102]. Deckman *et al.* introduced further corrections with respect to non-ideal back reflection and parasitic absorption [8]. A nice description and comparison of those models to experimental data for $\mu\text{c-Si:H}$ single junction cells (1 μm intrinsic layer thickness) was done by Berginski *et al.* [103]. They showed that light trapping is already on a good level for the state-of-the-art textures used and that most of the potential current gain can be achieved by reducing parasitic absorption, particular in the front-TCO and at the back reflector (surface-plasmon absorption at the Ag-interface), and by improving light coupling, i.e. minimizing primary reflection losses.

2.2.4 Advanced Device Concepts

Beside the basic structure of a-Si:H/ μ c-Si:H based tandem cells, as depicted in fig. 2.4, in recent years there have been various adaptations and advances to this basic concept. Most of them aim at a higher photo current generation, while others focus on improved electrical device quality. In the following, two of these advances, relevant for this thesis will be briefly introduced.

Silicon-(sub)-oxide based layers In the context of present day a-Si:H based thin film technology, the term *hydrogenated micro-crystalline silicon oxide*, μ c-SiO_x commonly refers to a layer of a two phase material consisting of nano-scaled μ c-Si:H filaments embedded in an a-SiO_x:H matrix [104]. Such layers can be achieved in a PECVD process similar to that used for μ c-Si:H deposition. This makes such films highly compatible with the common deposition of a-Si:H/ μ c-Si:H based solar cells. Figure 2.10 shows a transmission electron microscopic image of such a layer on a-Si:H with element specific coloration. The two phase character of the material gets obvious from the image. The benefit of this material is its tunable refractive index ($n \approx 1.7 \dots 2.6$) and its rather low absorption coefficient. Furthermore, like a-Si:H and μ c-Si:H, it can be doped n- or p-type. Therefore, it is appropriate for use as p- or n-layer and it at the same time provides low parasitic absorption.

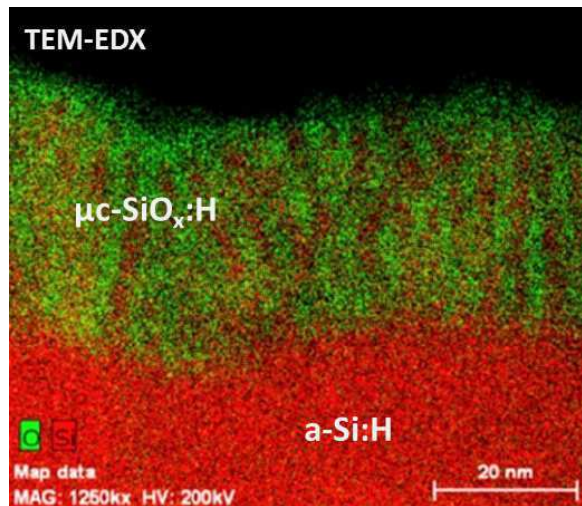


Figure 2.10: TEM image of a μ c-SiO_x layer grown on top of a-Si:H. Red correspond to Si-rich (i.e. O-free) sites and green to O-containing sites. Hence the μ c-Si:H filaments and the a-SiO_x matrix correspond to the red and green regions inside the μ c-SiO_x layer, respectively. The color contrast was achieved by electron dispersive X-ray spectroscopy. The picture was taken by Max Klingsporn.

When used as top cell p-layer, it additionally provides an anti-reflective effect due to index grading [105], whereas when applied in-between the top and the bottom cell of a tandem device it acts as an intermediate reflective layer (*IRL*) [106]. The latter allows an increase in the portion of light absorbed in the top cell (at the expense of the bottom cell) and hence the

tuning of the current matching between top and bottom cell. This effect can also be used to generate the same current density in a thinner a-Si:H absorber layer, which helps to mitigate its light induced degradation (cf. sec. 2.2.1). Beside these optical benefits, its incorporation also improves the electrical device quality, particular when grown on rough substrates [87]. The development of such layers and their implementation to solar cells made in our group was one of the main topics of the PhD thesis of Kirner [107,108]. Actually all cells that will be presented in this thesis comprise $\mu\text{-SiO}_x$ layers (cf. sec. 3.1.6).

Alternative front textures As already pointed out, the common approach to introduce light scattering in p-i-n type cells is the utilization of textured front TCOs. An appropriate texture is hence inherently related to certain requirements for the deposition process for both as-grown textured TCOs like LPCVD-grown ZnO:B or post-deposition textured ones like sputter-etched ZnO:Al. This constitutes a trade-off between texture formation and opto-electronic properties of the particular TCO. Hence, introducing light scattering by alternative approaches or at least ways to relax this trade-off are highly desired.

An obvious way is to grow the whole device, i.e. including the front TCO, on a transparent textured substrate. This can be achieved either by texturing the glass surface itself [109–112], or by coating with a textured transparent material. For the latter UV nano-imprint-lithography (UV-NIL) is a prominent technique [113–115]. Both approaches have already been used in application to Si-based thin film solar cells. For instance Bailat *et al.* demonstrated a confirmed efficiency of 11.91 % after 1000 h of light soaking for a-Si:H/ $\mu\text{-Si:H}$ tandem cells incorporating textured glass [116], which was the world record at this time (in 2010). The utilization of micro-textured glass will also be part of this thesis (cf. sec. 6.5).

3 Experimental Details

In this section the experimental methods used for sample preparation and characterization are described. The samples consist either of ZnO:Al films deposited on SiO_xN_y coated glass substrates or a-Si:H/ $\mu\text{c-Si:H}$ tandem devices grown on top of those. The former is used for characterizing the opto-electronic and morphologic properties of the ZnO:Al layers on glass, whereas the latter is used to directly investigate how different treatments and substrates affect the device performance.

3.1 Sample Preparation

The sample preparation always started with a proper cleaning procedure. For this purpose, the substrates were first cleaned in an ultra-sonic bath for 20 min. This was carried out either in deionized water containing a basic detergent (*Mucasol* by *Brand GmbH + Co. KG*) at 80 °C in the case of bare glass substrates or in pure deionized water at room temperature to prevent etching in the case of substrates already coated with a ZnO:Al layer. Subsequently, all substrates were washed and dried in a flat glass washing machine (by *buxtrup GmbH*). At this stage all substrates had a size of $300 \times 300 \text{ mm}^2$.

3.1.1 The Glass Substrates

Table 3.1 lists all glass types used as substrate. Due to its high strain point, the Corning Eagle XG (“Corning”) is appropriate for the investigation of ZnO:Al annealing. Temperatures up to 650 °C were applied to samples on Corning glass. On low iron soda lime glass (“white glass”) and the borosilicate glass (“borofloat”) the annealing temperature was restricted to 500 °C. However, with industrial application in mind the utilization of the rather thin and expensive Corning glass is no option. Figure 3.1 shows the transmittance of the three glass types. Among the three glass types, the borofloat glass shows the highest transmittance. This is due to both low absorption but primarily the rather low refractive index, i.e. low reflectance. At photon energies around 3.7 eV all glasses start absorbing and hence exhibit a drop in transmittance. With respect to the typical band gap energy of 3.4...3.7 eV for the ZnO:Al layers used here this is no issue. The slight decrease in transmittance for lower photon energies visible in the data of the white glass is due to absorption at residual iron impurities. Altogether all glass types are generally well suited as a transparent substrate for solar cells.

3.1.2 Reactive MF-Magnetron Sputtering of SiO_xN_y Layers

The SiO_xN_y films inserted as anti-reflection and surface conditioning layer between the glass and the ZnO:Al layer were deposited in a reactive mid-frequency(MF)-twin-magnetron

Table 3.1: The different types of glass used as substrate. The strain point temperature defines the upper limit for reversible mechanical properties. n denotes the refractive index at a wavelength of 600 nm. Different trade names of white glass have been used. However, due to their characteristic composition and processing they all show very similar properties.

type/ trade name	d [mm]	strain point [°C]	n (600 nm)	composition & key features
white glass (div.)	3.2	≈ 510	1.52	low iron soda lime; float glass; inexpensive; available on large scale
Schott boro-float 33	3.3	518	1.48	borosilicate; float glass; low thermal expansion (similar to Si); good optical properties; excellent thermal shock resistance; high chemical durability
Corning Eagle XG	1.1	669	1.51	alkaline earth boro-aluminosilicate; fusion drawn glass; low thermal expansion (similar to Si); excellent chemical durability; outstanding surface quality

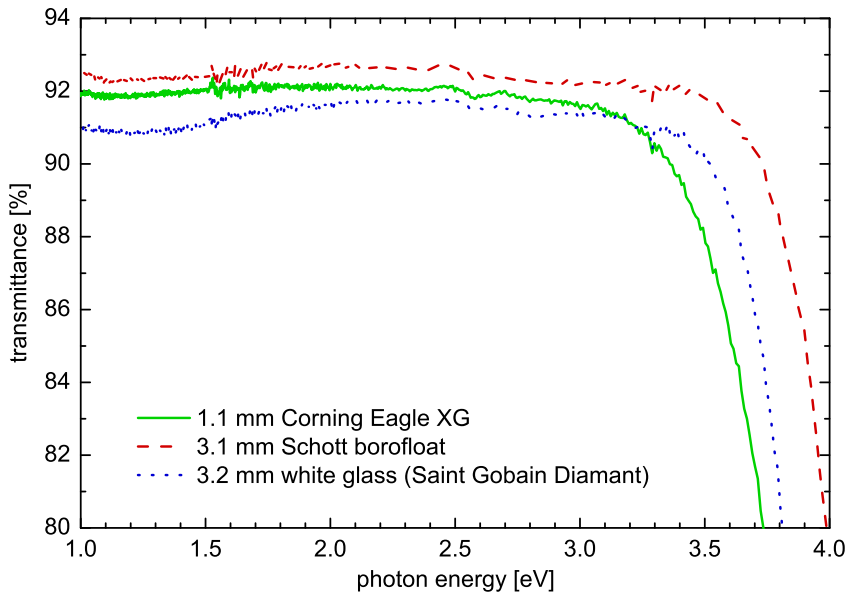


Figure 3.1: Transmittance of the different glass types used as substrates as a function of photon energy. The respective glass thickness is added to the legend. White glass is represented by the brand *Diamant* by *Saint Gobain*.

sputter process, which is rather complex. Since this layer is not in the focus of this work, only a brief description of the used parameters will be given in the following. For a more general introduction to magnetron sputtering refer to sec. 3.1.3. A more detailed description of the process and its application can for instance be found in refs. [117–119].

The process uses a pair of Si:Al(0.1 wt.%) tube targets ($l = 600$ mm, by GfE) which are arranged in a special configuration. The Al-doping provides a reasonable conductivity, needed to maintain the process stable. The system is driven by a MF-generator that reverses the polarity of the particular targets with a fixed frequency of 40 kHz. This technique prevents the accumulation of electrons at the target surface, which would otherwise not allow a reliable sputtering. Since it is a reactive sputter process the sputter gas (argon) exhibits an admixture of nitrogen and oxygen, which is dissociated in the plasma and hence is incorporated in the growing layer. The process parameters are as follows: MF-power 6.9 kW, working pressure $1.3 \cdot 10^{-3}$ mbar, Ar-flow rate typical 28 sccm (controled via total pressure), O₂-flow rate typical 30 sccm (controled via MF-voltage), N₂-flow rate fixed at 70 sccm. The process is nominally carried out at room temperature. The dynamic deposition rate is ≈ 100 nm \cdot m⁻¹min. The resulting SiO_xN_y layer has a thickness of ≈ 60 nm and a refractive index of $n = 1.7$ at $\lambda = 500$ nm. It comprises low dispersion as well as low absorption.

3.1.3 DC-Magnetron Sputtering of ZnO:Al Layers

Sputtering refers to the major principle used with this deposition technique: High energetic ions hit the surface of a target, where they release particles (or small compounds) of the target material, which subsequently condenses inside the process chamber, i.e. also on the substrate intended to be coated. All ZnO:Al films presented within this thesis were produced by non-reactive DC-magnetron sputtering.

Figure 3.2 shows a schematic view of a DC-magnetron sputtering system using tube targets. The volume in-between two electrodes is filled with the sputter gas Ar¹⁷. Due to cosmic radiation some of the Ar-atoms are ionized spontaneously. When a voltage is applied between the electrodes (typically a few hundred volts) the charged particles are accelerated in the electric field leading to ionization of additional Ar-atoms. For appropriate pressure and electric field strength, a stable plasma containing neutral and charged species is generated. As these conditions are only reached for a rather large mean free path length, i.e. low gas pressure, sputtering generally is a vacuum process.

The target is placed just in front of the cathode (or it comprises the cathode in the case of metallic targets). Ar-Ions (positively charged) are accelerated towards the cathode and hit the target surface with rather high kinetic energies. This leads to emission of secondary electrons which support the gas ionization and particles or clusters of the target material

¹⁷Ar is usually used as sputter gas due to its inert character and availability.

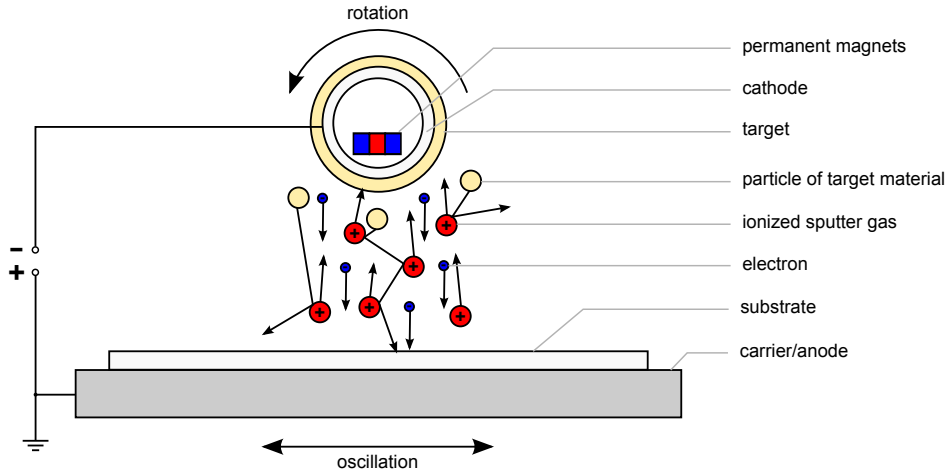


Figure 3.2: Schematic drawing of the sputter process.

which condense inside the sputter chamber, particularly onto the substrate. Thereby, the mean free path length of the target material, hence the deposition rate is reduced by the presence of the ionized sputter gas. Lower sputter pressure could mitigate this issue but at the same time would lead to a breakdown of the plasma due to a reduced collision rate.

A solution to this dilemma is provided by magnetron sputtering. A specific configuration of strong permanent magnets just behind the cathode introduces strong magnetic fields close to the target surface. The electrons are forced on cycloid trajectories leading to higher residence times and hence increased ionization efficiency. This allows a reduction in the sputter pressure without plasma breakdown, therefore, allowing higher deposition rates. A disadvantage of magnetron sputtering is the reduced target utilization. The target erosion becomes non-uniform as it is increased in the vicinity of the cycloid trajectories of the electrons. This can be reduced e.g. by using cylindrical rotating targets (so called *tube targets*) as it was the case for the system used here.

The first experiments were based on ZnO:Al films provided by a project partner. They have been fabricated in an industrial large area process (in the following referred to as *industrial ZnO:Al*) whereas later on an in-house process was established and mainly used. The development of the in-house process is not in the focus of this thesis and will therefore not be explained here. In order to serve as a stable reference no significant changes have been made to that process. The main process parameters for both ZnO:Al types are listed in tab. 3.2.

The two types of ZnO:Al were quite similar with respect to their opto-electronic and light trapping properties. Figure 3.3 shows the transmittance, reflectance and absorptance of the industrial and the in-house ZnO:Al for the different annealing states (ref. to sec. 3.1.5 (a) as-deposited, (b) cap-annealed, (c) thermally degraded and (d) 2-step annealed. Note that the in-house ZnO:Al is slightly thinner (725 nm compared to 816 nm for the industrial ZnO:Al). Despite that, the general trends and characteristic features are very similar for the

Table 3.2: Main features of the sputter processes used to deposit the particular types of ZnO:Al. For the industrial zinc oxide, some process parameters have to be treated as confidential.

ZnO:Al type	industrial	in-house
SiO _X N _Y -layer neath	under- yes	yes (optional)
target type	sintered ceramic tube target	sintered ceramic tube target ($l = 600$ mm; by GfE)
target doping level	1 wt.% Al ₂ O ₃	1 wt.% Al ₂ O ₃
process type	DC-magnetron sputtering (non-reactive)	DC-magnetron sputtering (non-reactive)
deposition type	dynamic (single pass/multiple targets)	dynamic (multiple pass/single target)
substrate temperature	> 250 °C	330 °C
sputter power	-	2 kW
sputter pressure	-	$5.1 \cdot 10^{-3}$ mbar
Argon flow rate	-	550 sccm
target-substrate distance	-	80 mm
dynamic deposition rate	-	≈ 85 nm · m ⁻¹ min

two ZnO:Al types. This general observation is even true for the three different annealing states, which points to the similar sensitivity to the particular mechanisms acting during thermal treatments. The electronic properties of the samples presented in fig. 3.3 were derived from HALL-effect measurements and are summarized in tab. 3.3. As expected the similar optical properties are linked to similar electronic properties. The general behavior due to different annealing will be discussed in sec. 4.

Besides the opto-electronic properties of the non-textured ZnO:Al films also the texture formation upon wet-chemical etching was compared between the two ZnO:Al types. The haze after appropriate wet-chemical etching in 0.5 wt.% HCl is shown in fig. 3.4. As can be seen, also the haze curves for the two ZnO:Al types are rather similar, whereas the haze of the in-house ZnO:Al in comparison to the industrial one is a bit higher for shorter wavelength, but gradually approaches the latter with increasing wavelength.

3.1.4 Wet-chemical Texture-Etching

The wet-chemical etching of the ZnO:Al films, used to introduce a light scattering texture was done by immersing the samples in 0.5 % HCl at room temperature. The applied etch durations depend on the specific ZnO:Al material and its thickness. Unless otherwise stated,

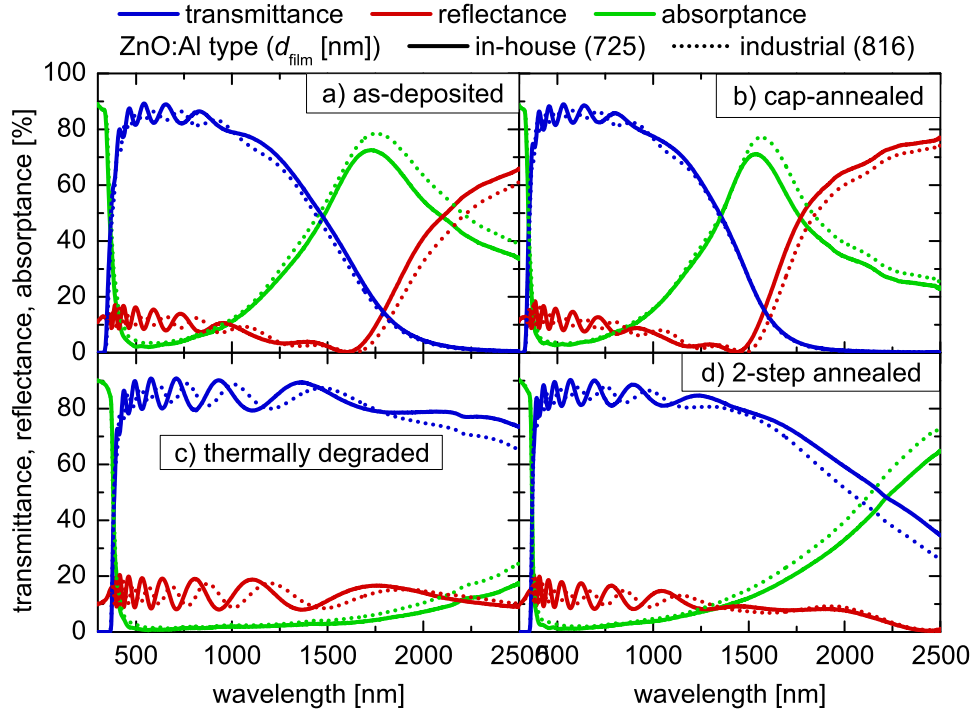


Figure 3.3: Transmittance, reflectance and absorptance of non-textured in-house (solid line) and industrial (dotted line) ZnO:Al in the (a) as-deposited, (b) cap-annealed, (c) thermally degraded and (d) 2-step annealed state. All annealing was done at 500 °C with 6 h plateau time.

Table 3.3: Electronic properties of non-textured in-house and industrial ZnO:Al in different annealing states. All annealing was done at 500 °C with 6 h plateau time.

annealing state	ZnO:Al type	$n_{e,Hall}$ 10^{20} cm^{-3}	μ_{Hall} $\frac{\text{cm}^2}{\text{Vs}}$	ρ_{Hall} $10^{-4} \Omega\text{cm}$
as-deposited	in-house	3.3	35	5.42
	industrial	3.1	30	6.58
cap-annealed	in-house	5.0	54	2.33
	industrial	4.6	54	2.49
thermally degraded	in-house	0.32	8.8	219
	industrial	0.30	8.1	260
2-step annealed	in-house	1.4	62	7.00
	industrial	1.4	60	7.34

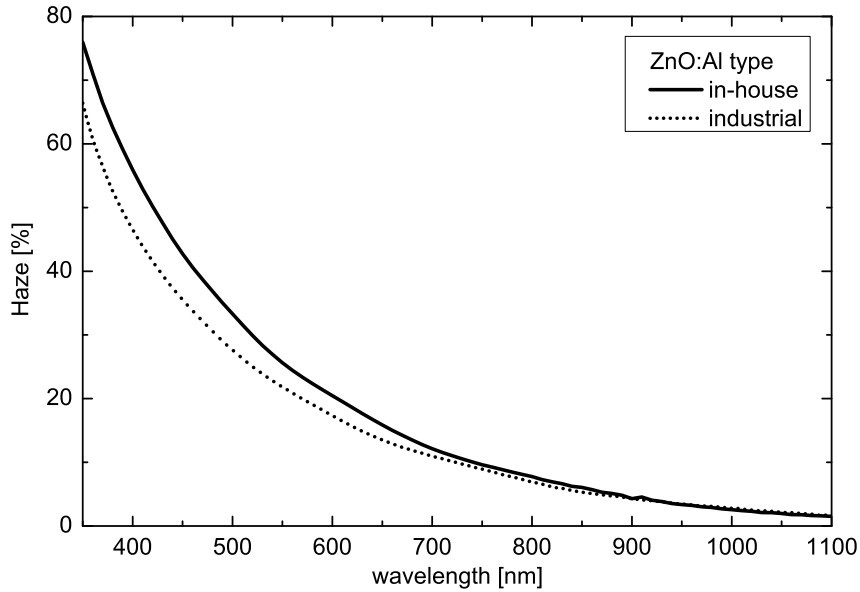


Figure 3.4: Haze in transmission for wet-chemically textured in-house (solid line) and industrial (dotted) ZnO:Al on glass. The duration for wet-chemical texturing was adapted to achieve a similar sheet resistance for the two samples, $R_{sh} \approx 11 \Omega$, leading to $t_{text} = 40$ s and 75 s for in-house and industrial ZnO:Al, respectively.

the standard etch time of 50 and 75 s for the in-house and industrial ZnO:Al, as listed in tab. 3.2 was applied, respectively.

The short HCl-dip, used to refresh the ZnO:Al surface after cap-annealing was carried out in the same way, but the concentration of the HCl and the duration was 0.1 % and 10 s, respectively.

The wet-chemical treatment was generally stopped by immediately immersing the samples in de-ionized water followed by either washing and drying in the glass washer (for $30 \times 30 \text{ cm}^2$ samples) or rinsing with de-ionized water and drying with a nitrogen pistol (smaller samples).

3.1.5 Thermal post-Deposition Treatment

The thermal post-deposition treatment (for convenience referred to as *annealing*) of sputtered ZnO:Al layers occupies the central position in this thesis. Despite its technological importance, in practice it is a simple process. A brief introduction to the history and state of the art of post deposition annealing of ZnO in general and ZnO:Al in particular is given in sec. 4.1.

For now, it is sufficient to distinguish between annealing of bare ZnO:Al layers on glass, referred to as *thermal degradation*, which is due to its deteriorating impact on electronic properties of the ZnO:Al, and annealing of ZnO:Al layers that were coated with a capping layer, hence referred to as *cap-annealing*. In our case the capping comprises an intrinsic a-Si:H

layer with a thickness of about 100 nm. It is deposited in the same PECVD tool that is also used for cell deposition (cf. sec. 3.1.6). The deposition parameters were actually adapted from an older version of our intrinsic a-Si:H absorber layer. Note, that we increased the thickness of the capping layer compared to the 50 nm, typically used in the original publication [13]. This was decided to assure a dense capping also on textured ZnO:Al layers, which were not subjected to cap-annealing prior to this thesis.

Regarding the annealing itself, there is no fundamental difference between thermal degradation and cap-annealing. The annealing is carried out in a muffle furnace (customized, by *HTM Reetz GmbH*, Germany). It can seize up to six samples with a sample size of up to $30 \times 30 \text{ cm}^2$. The samples are placed on ceramic substrates which are stacked in slots inside the muffle chamber. The furnace exhibits a gas tied design and an internal fan assures a homogeneous temperature distribution inside the chamber. During operation a continuous nitrogen-flow ($\approx 1700 \text{ sccm}$) is applied. To prevent glass breaking due to thermal shocks, the samples are heated up and cooled down at rates not larger than 2.5 K/min . The furnace is designed for a maximum temperature of 700°C . More details on the layout and processing can be found in ref. [120].

The process parameters of the annealing were actually adapted from a tube furnace, that was originally used for ZnO:Al annealing of small samples.

After cap-annealing the cap needs to be removed again, since it is no longer suited for device implementation. Moreover, removing the cap eases characterization of the annealed ZnO:Al films. For this purpose an NF_3 based plasma etching process, that is originally used to clean the process chambers of our PECVD system, was adapted. This process is very selective to Si. The ZnO:Al is not attacked, as it was evidenced from an experiment presented in sec. 6.1.

Thus, all processes needed to carry out ZnO:Al annealing on $30 \times 30 \text{ cm}^2$ -sized samples were available. At this point we want to note, that we experienced a minor deformation of float glass based samples after annealing for several hours at 500°C . This deformation led to problems in the alignment of the P1 laser pattern and the subsequent P2 and P3 pattern (cf. sec. 3.1.7), when the P1 patterning was carried out prior to annealing and was hence also subjected to the annealing-induced deformation.

3.1.6 PECVD Processing of Si-based Thin-film Cells

All Si-based layers used in this thesis were deposited in an *Applied Materials AKT 1600A* cluster tool. It is equipped with 3 process chambers (A, B and D) that are connected to a central transfer chamber. Up to six $30 \times 30 \text{ cm}^2$ -sized substrates can be loaded to the system. An automated substrate mover handles the transfer of the substrates to the different process chambers. Figure 3.5 shows a schematic cross section of a process chamber. The substrate

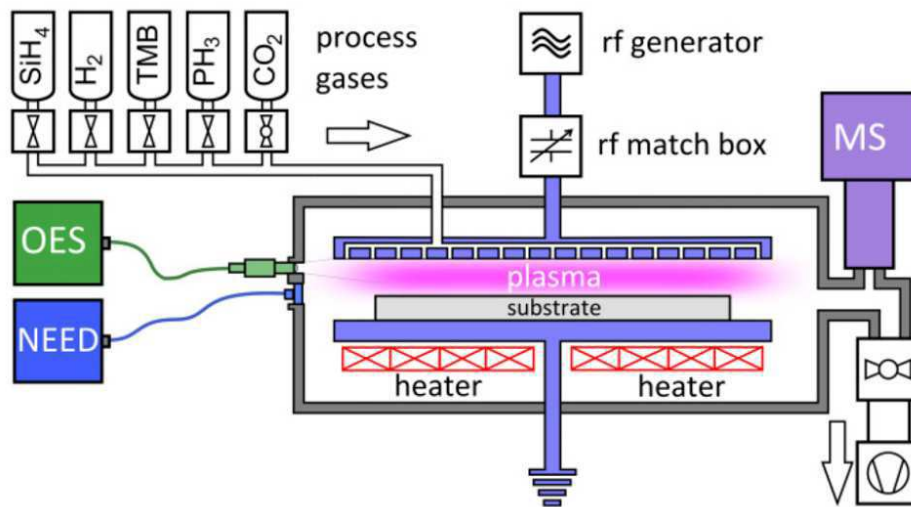


Figure 3.5: Schematic cross section of a PECVD chamber. Taken from [121]

is located on a grounded electrode which is heated up to typically 200°C . The shower head electrode located right above the substrate is capacitively coupled to a 13.56 MHz radio frequency (RF) generator. The shower head electrode also serves as the gas inlet for all process gases. The process gases flow into the chamber where a glow discharge is initiated and sustained by the RF generator. This yields decomposition of the process gases and the formation of molecules, neutral radicals and ionized species. The film growth basically occurs due to neutral radicals that stick to the substrate surface. In reality the chemistry inside such plasmas is much more complex. For the purpose of monitoring the plasma conditions and hence the film growth we have three plasma diagnostic tools, which are also depicted in fig. 3.5. Further information on the system, the process optimization and the application of the plasma diagnostic tools can be found in refs. [121–123].

Table 3.4 lists the process sequence and main parameters used for the standard a-Si:H/ $\mu\text{-Si:H}$ device on ZnO:AL front electrodes. Note, that the chambers are dedicated to particular doping types. The sequence also contains a seasoning of chamber A prior to any p-layer deposition. Moreover chamber A and D were cleaned by means of a NF_3/Ar plasma and subsequently seasoned after deposition of the top cell p- and bottom cell i-layer, respectively. This avoids a memory effect related to accumulation of residual layers inside the process chambers.

Some of the cells presented in this thesis were based on an older version of our standard process, which had a different top cell p-layer design, a thicker top cell i-layer, a thinner and less effective IRL and a thinner bottom cell i layer thickness. Since these cells will only be used for direct comparison, this should be no issue.

Table 3.4: PECVD sequence and main process parameters for deposition of the standard a-Si:H/ μ c-Si:H device. The comments for the i-layers include the silane concentration and the deposition rate. All p- and n-layer thicknesses given were determined for thick layers (typ. 200 nm) and scaled by assuming constant deposition rate.

step	chamber	T °C	layer	thickness nm	comments
1	A	205	TC-p	20	p- μ cSiO _x , 3 sub-layers , based on ref. [124]
2	A	205	TC-i	275	SiH ₄ /H ₂ =1/10; 0.22 nm/min
3	B	185	TC-n	88 (18+60)	incl. 60 nm IRL
4	A	205	BC-p	30	p- μ cSiO _x
5	D	190	BC-i	2200	SiH ₄ /H ₂ \approx 1/120; 0.45 nm/min
6	B	185	BC-n	25	n- μ cSiO _x

3.1.7 Laser Scribing, Back Contact Deposition and Device Annealing

This section describes the final steps needed to achieve a working device after the Si-stack was deposited.

Laser Scribing For the definition of particular device layouts, pulsed laser scribing is generally used at PVcomB. Figure 3.6 depicts the single steps needed for monolithically interconnection. For the P1 scribe, used to open the front TCO a picosecond laser with a wavelength of 1064 nm was used. The P2 and P3 scribe both use a picosecond laser with 532 nm wavelength. The depicted process yields a series connection of neighboring cells. This layout is commonly used to define interconnected modules. For our single cell process yielding 180 (9 × 20) 1 × 1 cm²-sized cells per substrate, the P1 scribe is not needed.

Back Contact Deposition The standard back contact for our cells is based on a ZnO:Al/Ag bilayer (80/200 nm) and was used for all devices presented in this thesis. The intermediate ZnO:Al increases the reflectivity of the back reflector and mitigates plasmonic absorption at the nano-rough Ag interface [125]. The Ag serves as combined back electrode/back reflector. Both layers were deposited by non-reactive DC-magnetron sputtering.

The back contact ZnO:Al layer is sputtered from the same target as the front ZnO:Al film (cf. tab. 3.2). Compared to the latter the process is done at room temperature and 20 sccm of Ar:O₂ (90:10) are added to the sputter gas resulting in 0.35 % of O₂. This reduces the parasitic absorption in the ZnO:Al and improves the adhesion of the Ag. The latter is of particular importance for the laser patterning. A weak adhesion results in small flakes of Ag near the laser scribe that tend to form local shunts within the laser scribe.

The Ag was sputtered from a metallic planar target (600 × 125 mm²; by *GfE*, Germany)

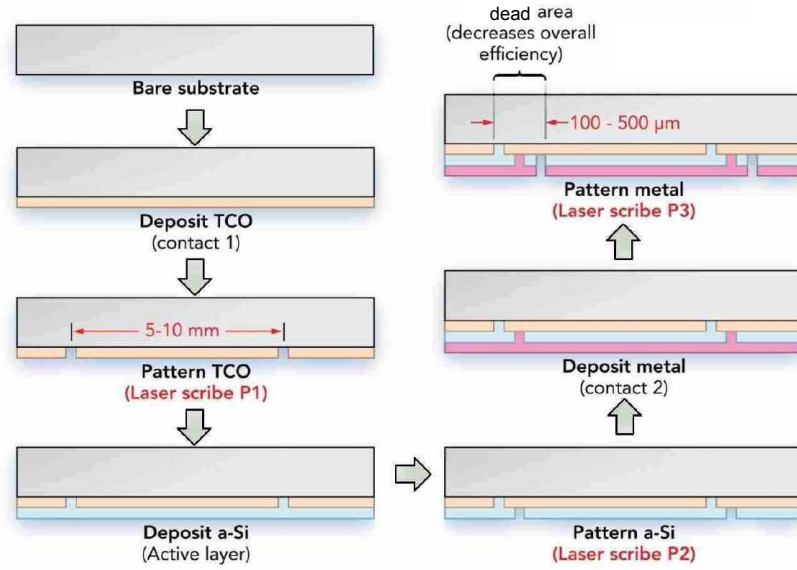


Figure 3.6: Stepwise illustration of the monolithically interconnection. Taken from ref. [120].

at room temperature. The sputter conditions were 1 kW sputter power, 380 sccm Ar flow rate and $50 \text{ nm} \cdot \text{m}^{-1} \text{min}$ dynamic deposition rate.

Device Annealing In a final step the device was annealed at 160°C for 50 min at ambient conditions, which mainly improves the back contact.

3.2 Characterization Techniques

In this section the different measurement methods and devices that were extensively used in this thesis are briefly described.

Additional methods, that are rather common or were not used that extensively were:

Four Point Probe (4pp) In a 4pp measurement 4 contact needles are arranged equidistant in a line and connected to a source/sensing unit in 4-wire configuration. The particular arrangement allows to directly determine the sheet resistance of a conductive layer (provided uniform and extended layers). The method was used to determine the sheet resistance of ZnO:Al layers. Compared to the method of VAN DER PAUW (sec. 3.2.1), this method is fast and can be applied to large samples. It requires no sample preparation. With this method the sheet resistance of a $30 \times 30 \text{ cm}^2$ sample was commonly measured in a 3×3 mesh after deposition, texture etching, any annealing and HCl-dip. The measurements were done at a *RM3000* by *Jandel*.

Step Profiler In a step profiler a tip ($2.5\ \mu\text{m}$ tip radius in our case) scans the surface of a sample and records a height profile. It was used to determine the thickness of ZnO:Al layers when they were grown on textured substrates or have been textured by itself. For that purpose a step was prepared by drawing a small circle with a waterproof pen and subsequent etching of the ZnO:Al layer inside this mark by means of a droplet of 10 % HCl. After waiting for about 1 min the sample was rinsed with de-ionized water and dried with a nitrogen pistol. The ink served as an etch mask, which could be easily removed with IPA and resulted in a well-defined step in the ZnO:Al layer. Two of such steps were commonly prepared at different corners of the same sample and three thickness measurements were done per step. The average value of these six measurements was taken as film thickness. The measurements were done at a *D-120* by *KLA Tencor*, USA.

Scanning Electron Microscopy (SEM) This method was used to examine the surface topography and cross section of ZnO-Al layers. In contrast to atomic force microscopy it does not provide a quantitative depth information. But it exhibits a very plastic visual impression. The measurements were conducted by Dr. Florian Ruske. A *S-4100* by *Hitachi* (Japan) was used. The sample preparation was analog to that described for the AFM measurements.

X-ray Diffraction (XRD) This method was used to evidence the predominant $\langle 001 \rangle$ -orientation of the ZnO:Al layers perpendicular to the substrate surface. A *D8* system by *Bruker*, working with a Copper anode was used in BRAGG-BENTANO configuration. The measurements were guided by Dr. Sonya Calnan. The samples were cut to a size of $2 \times 2\ \text{cm}^2$.

3.2.1 Electronic Characterization of ZnO:Al

A common technique to determine the electronic properties of degenerate TCOs (among many other materials) is the method of VAN DER PAUW [126, 127]. In a first step it allows to determine the resistivity of the material (provided that the film thickness is known). This is basically achieved by contacting the sample at four distinct points. Thereby two contacts are used to inject a current and the corresponding voltage is measured via the other two contacts. This configuration is then varied in a special order including the polarity of the individual contacts. Since there are many detailed step by step descriptions available in recent publications [47, 128, 129] we will not go into detail with that. In a second step a similar contacting scheme is used and the sample is exposed to a permanent magnetic field oriented normal to the layer surface in order to utilize the HALL effect. This step is then repeated with altered polarity of the magnetic field. All in all, this allows to determine the HALL

coefficient, R_H which is related to the charge carrier concentration via

$$R_H = -\frac{r_H}{n_e \cdot e} . \quad (3.1)$$

Note, that a negative value of R_H corresponds to n-type doping. The quantity r_H is the HALL factor. It is defined between 1 and 2 and its particular value commonly depends on the charge carrier scattering mechanisms occurring in the sample. However, in the case of degenerate ZnO:Al it is commonly set to unity [47, 128]. Therefore, we will also assume $r_H = 1$. Finally by applying eq. (2.6) the mobility can be extracted from the measurement.

A major advantage of the method of VAN DER PAUW is that no knowledge of the explicit lateral sample dimensions is needed. Despite that, there are four requirements on the sample and the measurement layout: the sample (i) has a homogeneous film thickness, (ii) exhibits no cracks, wholes, etc. in its inner area and (iii) is contacted close to its edges, and (iv) the contacts are small compared to the lateral sample dimensions.

For the measurements made in this work a system of type *HMS3000* by *Ecopia* was used. For this purpose the samples were cut to a size of about $8 \times 8 \text{ mm}^2$. The contacting was realized by four spring loaded manipulators with Au-coated tips. Prior to each measurement the contacts were checked by a simple I - V measurement. The system is equipped with a permanent magnet providing a magnetic field strength of 0.56 T. Prior to each measurement series a reference sample provided with permanent contacts was measured. Note, that, despite the mobility, the accuracy of this method explicitly relies on a proper determination of the particular film thickness.

3.2.2 Optical Measurements

For the optical characterization of the samples a dual beam photo spectrometer of type *Lambda 1050* by *Perkin Elmer* was used. The system is equipped with a deuterium/halogen dual light source and a 150 mm diameter integrating sphere with $0^\circ/8^\circ$ port configuration. The two detectors of the system, namely a photomultiplier tube and an InGaAs detector allow a measurement range of $\lambda = 250 \dots 2500 \text{ nm}$. Figure 3.7 illustrates the different configuration used for measuring (a) the total and diffuse transmittance, (b) the total reflectance and (c) the specular reflectance.

For textured ZnO:Al films on glass the total and diffuse transmittance was measured for $\lambda = 250 \dots 1500 \text{ nm}$ with a step width of 5 nm and later on used to calculate the haze according to eq. (2.50). When the reflective plug is inserted in the integrating sphere, the total transmittance is obtained. When it is removed, the specular part of the transmittance gets lost for detection and hence the diffuse transmittance is directly measured. The opening angle, that discriminates between specular and diffuse transmission (red dash dotted line

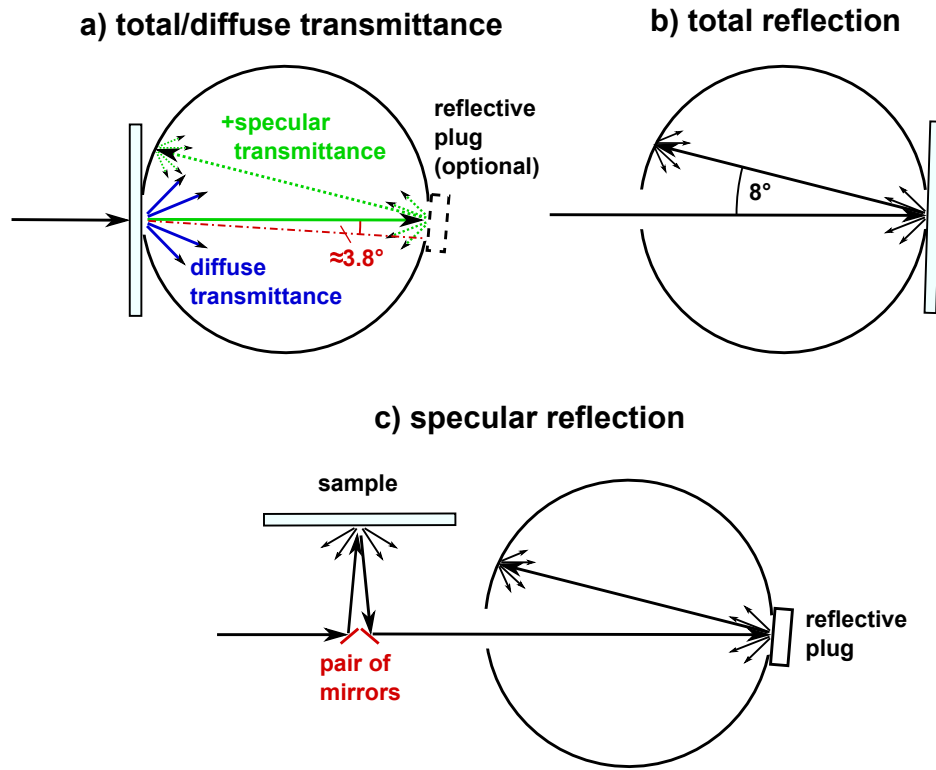


Figure 3.7: Measurement configurations of the photo spectrometer

in (a)) accounts to $\approx 3.8^\circ$ in the present setup. It is defined by the ratio of port opening diameter to total diameter of the integrating sphere. During the measurement the samples have been oriented with the film side towards the integrating sphere. This reduces unwanted light trapping within the sample, which would otherwise lead to underestimation of the diffuse transmittance. Moreover, it is closer to the situation within a working solar cell (light enters through the glass).

For optical characterization and modelling (cf. sec. 2.1.5) of planar ZnO:Al films on glass total transmittance (a) and total reflectance ((b) were subsequently obtained. Thereby, the measurement range was increased to $\lambda = 250 \dots 2500$ nm and a step width of 2 nm was used. For these measurements the samples were oriented with the film side towards the incident beam.

The total absorptance of solar cells was derived from total reflectance measurements (b). Thereby a focusing optic was inserted in the path of the incident beam. This allowed to illuminate distinct 1 cm^2 -cells with a beam of ≈ 3 mm in diameter, similar to that of our *EQE* setup. The samples were illuminated through the front glass. The metallic back reflector allows to assume zero transmittance and hence $A = 1 - R$ (cf. eq. (2.23)). The wavelength range and step width were the same as used for the haze determination.

The last measurement configuration, depicted in fig. 3.7 (c) was used to determine the specular reflectance of cells. For that purpose the samples were placed on an accessory, which

was placed outside the integrating sphere. Only light being specular reflected by the sample is detected in this case. Again, the scan-settings used for haze determination were used.

The system was generally calibrated prior to each measurement series. All measurements were taken with respect to a back ground correction and a reference measurement either without any sample (transmittance mode) or a known standard with high reflectance (reflectance mode).

3.2.3 Atomic Force Microscopy

The knowledge of the explicit surface topography of textured surfaces is an essential key to understanding their light scattering properties and impact on the properties of materials grown on top of them. Atomic force microscopy (AFM) is an appropriate method for recording the three dimensional surface topography. The basic working principle of this technique is to scan a nano-scaled tip, located at the end of a cantilever, over the surface of the sample. Due to the high accuracy needed, this is commonly achieved by piezo-electric drivers. The particular interaction of the tip and the surface depends, among other quantities, on the distance between them. For short distances (< 1 nm typical) the repulsive COULOMB interaction is predominant. For larger distances (1...10 nm typical) the attractive VAN DER WAALS interaction is predominant.

The interaction of the tip and the sample surface yields a deflection of the cantilever, which is recorded by a photo diode as elongation of the reflection of a laser beam that aims at the reflecting top site of the cantilever. This signal is either just recorded (*constant height mode*) or routed to a closed-loop, that controls the height for constant signal (*constant force mode*). For our purpose the latter is more common. In general, there are three modes of operation for topographical surface observation: (i) In *contact mode* the tip is driven in the repulsive regime close to the sample - in *contact* to it. This yields good resolution, but also strong erosion of the tip. (ii) In *non-contact mode* the cantilever is brought in to resonant vibration by an external source. A variation of the tip-to-sample distance yields a shift of the resonant frequency, which is hence providing information on the topography of the sample. Since the non-contact mode relies on rather weak tip-surface interaction, it shows virtually no erosion of the tip, but, on the other hand, commonly requires operation in vacuum. (iii) the *intermittent contact mode* is quite similar to the non-contact mode. It also makes use of a vibrating cantilever. In contrast to non-contact mode, the excitation is commonly not resonant and a change in the amplitude or the phase of the cantilever oscillation is used as indicator for the tip-to-sample distance. As the naming already tells, this mode is operated at intermittent tip-to-sample distances. In comparison to the non-contact mode, this increases the tip-to-sample interaction and hence allows operation also in ambient atmosphere. Compared to the contact-mode the intermittent mode provides still reasonable sensitivity, but significantly reduces tip erosion.

The AFM measurements used in this work were all done in intermittent contact mode using constant force mode. They were carried out in ambient atmosphere on a *XE-70* system by *Park Systems*. Prior to measurement the samples have been rinsed with IPA and de-ionized water. A scan area of $10\ \mu\text{m}^2$ and a resolution of 512×512 pixel were used. This yields a pixel size of around 20×20 nm. The scan rate was typically set to 0.2 lines per second, resulting in a total scan time of about 45 min. For data analysis the open access software *Gwyddion* [130] was used.

3.2.4 Solar Cell Analysis

This section introduces the characterization techniques used for solar cells. Additionally the light soaking procedure, used to quantify the light induced degradation of the cell performance, is explained. Some cells were also subjected to optical measurements, which are explained in sec. 3.2.2.

J-V-measurement Like for other energy converting devices, the most important parameter of a photovoltaic cell or module, is its conversion efficiency, η , particular with respect to application and benchmarking. As it depends on external parameters such as device temperature, irradiance and spectral distribution of the insolation, the rating of η must be related to the particular conditions during measurement. Moreover, for practical reasons the conditions during measurement should be close to those during outdoor operation of the photovoltaic device. For that purpose, the standard test conditions (STC) for rating terrestrial photovoltaic devices have been established world wide . They comprise the device temperature, $T = 25\ ^\circ\text{C}$, the irradiance, $E = 1000\ \text{W}/\text{m}^2$ and the spectral distribution of the AM1.5g ("air mass 1.5 global") reference spectrum, according to the international standard IEC 60904-3 [131]. The term AM1.5g denotes the spectral distribution of the global (diffuse and direct) sun light at sea level after traversing 1.5 times the atmosphere, i.e. under a solar zenith angle of 48° . It reasonably represents the over-all yearly average spectral distribution for regions of mid-latitude.

In practice, solar simulators are commonly used to realize an AM1.5g-like insolation. Figure 3.8 shows the AM1.5g reference spectrum together with a representative spectrum of the dual source solar simulator used at PVcomB (type *WXS-155S-L2* by *Wacom* (Japan)). The system is rated class AAA according to international standard IEC 60904-9 [132]. It operates in steady state mode (i.e. exhibits continuous irradiation) and consists of two individual light sources, a short arc Xenon lamp and a halogen lamp working in the visual and red-to-NIR part of the spectrum, respectively. The two light sources are superimposed into one optical axis by a dichroic mirror. The dual source concept provides the opportunity to balance the spectral distribution in terms of "blue-" or "red-rich". This is of special interest when

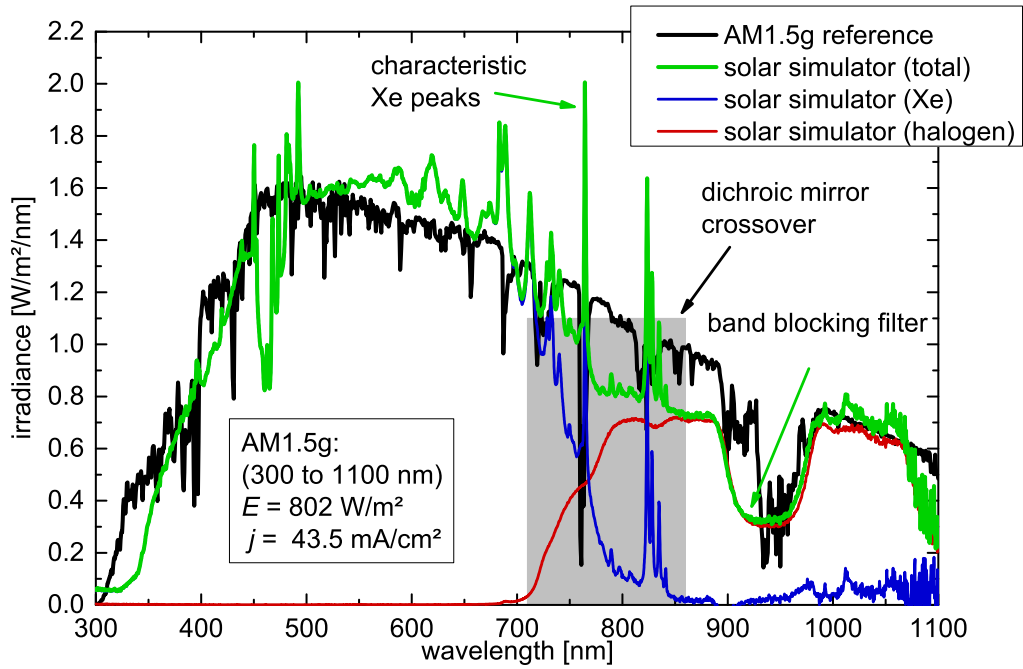


Figure 3.8: Spectral distribution of solar irradiance. The black line shows the AM1.5g reference spectrum according to the international standard IEC 60904-3:2008. The green line represents the measured spectral distribution of the irradiance of the dual source solar simulator used at PVcomB. It consists of two sub-spectra originating from a Xe-lamp (blue line) and a halogen lamp (red line), which are superimposed by a dichroic mirror.

measuring tandem cells, as it allows the elimination of the spectral mismatch between the reference spectrum and the simulator spectrum with respect to the top and the bottom cell, individually. Actually, this adjustment is an essential part of our solar simulators calibration routine. To ensure a certain temperature (25°C in the case of STC), the device under test is fixed on a temperature controlled copper-chuck (electrically isolated by a Kapton sheet). Each single solar cell is subsequently connected in four-wire mode to a source-measure-unit by an automated switching device. The measurement of the current density - voltage (J - V) characteristic is realized by a voltage-sweep while the corresponding current is measured step-by-step.

External Quantum Efficiency The external quantum efficiency of the cells is measured in a home-built system. The basic working principle is as follows: The cell is illuminated by a chopped monochromatic probe beam and a constant bias light. The latter is needed for measuring multi-junction devices, i.e. $\text{a-Si:H}/\mu\text{-Si:H}$ tandem cells. The resulting total photo-current, filtered at the chopper frequency, is recorded by a lock-in amplifier. This technique has a much better signal-to-noise ratio than a direct measurement of the cell current. Moreover, it allows the separation of the DC current part induced by the bias-light. The

system also offers the possibility to apply a defined bias-voltage across the cell. Details on the particular setup can be found elsewhere [133]. Illustrative and detailed descriptions of the special situation of determining the EQE of multi-junction devices were made, e.g., by Pravettoni *et al.* [134] and Shah [135].

Light Soaking In sec. 2.2.1 it was mentioned that a-Si:H-based solar cells exhibit a light induced degradation due to the Staebler-Wronski effect. For rating the performance of such devices it is hence crucial to consider this effect. The amount of this degradation depends on the light intensity and the device temperature during degradation [63]. To allow a quantitative interpretation of the effect a standardized procedure is commonly applied. It comprises an irradiance of $\approx 1000 \text{ W/m}^2$ and a device temperature of 50°C . The samples are commonly subjected to this conditions for 1000 h and are afterwards often referred to as “stable” or “stabilized”. Due to the reversability of the effect, this is somehow misleading. We will refer to the process as *light soaking*. 1000 h is a rather long periode, particular when feedback for further device adaption is needed. Therefore, we got used to reduce the light soaking duration to 168 h (1 week), unless we were not interested in the ultimate result. Figure 3.9 shows the efficiency of different devices containing an a-Si:H based cell as function of the light soaking time. As can be seen, in all cases the majority of the effect as observed after 1000 h of light soaking did already occur after 168 h. We take this as legitimation for our approach.

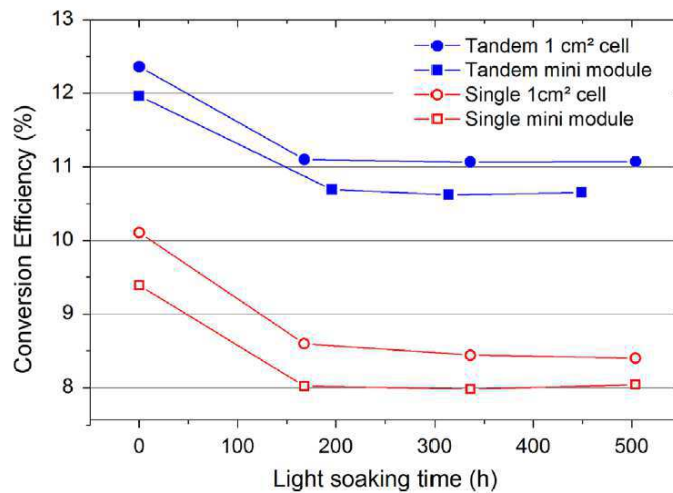


Figure 3.9: Light induced degradation as a function of light soaking time for several a-Si:H-based devices. Red refers to a-Si:H single junctions and blue to a-Si:H/ $\mu\text{c-Si:H}$ tandem devices. The data for $1 \times 1 \text{ cm}^2$ -sized cells (circles) and mini modules (squares; cf. sec. 7.1) are shown. The graph is taken from one of our publications [136].

The light soaking itself is carried out either in a large system by *Hönle UV Technology* using air cooling to maintain the sample temperature or a small home-built system equipped with a water cooling. The latter is preserved to long term investigations and also allows to vary the irradiance and sample temperature over a wider range (see ref. [137] for further

information). Both systems make use of the same light source type, namely a metal-halide lamp and use a closed-loop to regulate the sample temperature, which is measured directly at the back contact of the devices under test. The spectral distribution of the irradiance is in accordance with class C according to international standard IEC 60904-9 [132]. The light intensity is set for to have an implied photo current density in the top cell of a representative a-Si:H/ μ c-Si:H cell that equals that under AM1.5g. We refer to this as *1 sun equivalent*. For all samples presented in this thesis the light soaking conditions were fixed at 50 °C sample temperature and 1 sun irradiance.

4 Post-deposition Thermal Treatment of sputtered ZnO:Al

In this section, the post-deposition thermal treatment of sputtered ZnO:Al is discussed from a material point of view. First, a brief review of earlier works is given in sec. 4.1. Section 4.2 presents a systematic study on the interdependence of the ZnO:Al film thickness and variations of annealing time and temperature in the post-deposition thermal treatment. We suggest a model which allows a comprehensive interpretation of the changes found in charge carrier density and mobility upon the different ZnO:Al annealings. The technological relevance of the results is evaluated in terms of two different figures of merit. As texture formation of the ZnO:Al is crucial to introduce light trapping in thin film Si solar cells the influence of the post-deposition annealing procedure on the wet-chemical texturization was studied for different sequencings. The results are presented in sec. 4.3.

4.1 State of the Art

There are many publications on post-deposition thermal treatment of ZnO in different atmospheres. Different findings were made concerning the influence of the annealing on the (opto-) electronic properties. Increased conductivity was mainly observed for annealing at moderate temperatures ($T \leq 350^\circ\text{C}$) in inert atmospheres [138]. At higher temperatures, this was only achieved by some groups for annealing in hydrogen (containing) atmospheres [139–141] or vacuum ($T \leq 500^\circ\text{C}$) [142, 143] whereas e.g. Minami reported a decreased conductivity after annealing in hydrogen atmosphere or vacuum [23]. The use of oxygen (containing) atmospheres or nitrogen [139, 141, 144] generally led to a decrease in conductivity. The degradation was found to be reversible by subsequent annealing in hydrogen [23, 145]. Looking at all these findings it becomes obvious that the presence of (even small amounts of) oxygen during annealing is the main driver for decreased conductivity. Minami [23] and Takata [145] explained this by chemisorption of oxygen at the grain boundaries (and the film surface). This would lead to the formation of additional acceptor-like defects, hence a stronger grain boundary scattering lowering the charge carrier mobility. Additionally, the formation of compensating point defects, like oxygen interstitials and zinc vacancies as well as the inactivation of Al-donors would yield a decrease in charge carrier concentration.

Berginski used vacuum annealing to reduce the carrier concentration (i.e. to increase the transparency at the expense of sheet resistance) of ZnO:Al films used as front electrode in (a-Si:H)/ $\mu\text{c-Si:H}$ based solar cells [44, 146]. In 2007 Lee *et al.* found the beneficial effect of a Si-capping during annealing on the carrier mobility of ZnO:Al [12]. Based on this work, a systematic study on the influence of the capping layer material and thickness as well as the annealing duration and temperature was conducted [13, 147]. Wimmer *et al.* combined annealing without and with a protective a-Si:H-capping layer in a 2-step post deposition

treatment procedure [14, 128]. With this approach the charge carrier concentration could be adjusted while, at the same time the mobility was generally improved. Therefore, tailoring the (generally improved) opto-electronic properties of ZnO:Al in terms of balancing high transparency and low sheet resistance was possible. The implementation of such annealed ZnO:Al as a front-electrode in a-Si:H/ μ c-Si:H based thin-film solar cells is the main scope of this thesis.

4.2 Systematic Variation of Film Thickness and Annealing Conditions

The data presented in this section are based on a systematic study addressing the influence of varying thermal treatment conditions and layer thicknesses on the opto-electronic properties of ZnO:Al films. The original experimental work was conducted by Welker as part of his master thesis [120] which was supervised by the author of the present work. The ZnO:Al films were deposited on Corning Eagle XG glass substrates with a thickness of 1.1 mm using the in-house process including a SiO_xN_y-layer. The ZnO:Al film thickness was varied between 360 and 720 nm (nominal thickness). Moreover, different plateau temperatures and durations were applied for the thermal degradation as well as the subsequent annealing under Si-capping. In the following the specific heat treatments are referred to by the notation $T_{\text{ann}}[^\circ\text{C}]/t_{\text{ann}}[\text{h}]$, whereas $t_{\text{ann}} = 0$ describes a thermal cycle without plateau, i.e., cooldown immediately after the peak temperature was reached.

4.2.1 Characterization of the ZnO:Al Layers in the as-deposited State

Before subjecting the ZnO:Al layers to different annealing sequences they were investigated in the as-deposited state. In particular, the influence of varying thickness was examined. The optical data of the samples in the as-deposited state are presented in fig. 4.1. As expected the absorption generally increases with thickness, thus narrowing the optical window of the ZnO:Al particularly in the NIR where the FCA takes place.

Figure 4.2 shows the electronic parameters n_e , μ and ρ derived from hall measurements as a function of the film thickness. The values for n_e and μ scale with film thickness, being $\approx 3.50 \text{ cm}^{-3} / 28 \frac{\text{cm}^2}{\text{Vs}}$ and $3.75 \text{ cm}^{-3} / 32.5 \frac{\text{cm}^2}{\text{Vs}}$ for the 358 and 692 nm sample, respectively¹⁸. However, the trend in n_e is very small and hence not reliable. It will not be discussed.

The evolution of μ with d_{film} can be understood as a bulk effect. It is often interpreted as a direct consequence of less grain boundary scattering due to increasing crystallite size and higher crystallinity with increasing thickness [148, 149]. For instance, Minami shows the evolution of μ together with the characteristic grain size (derived from quantitative XRD-

¹⁸The values for the 531 nm sample don't follow this trend. This is ascribed to a slightly lower substrate temperature during the deposition. The sample was prepared as first in the row. At presence, a preheating of the substrate carrier avoids this effect. Unfortunately, this was not yet implemented at the time these samples have been made. However, it will not affect the general findings presented in this section.

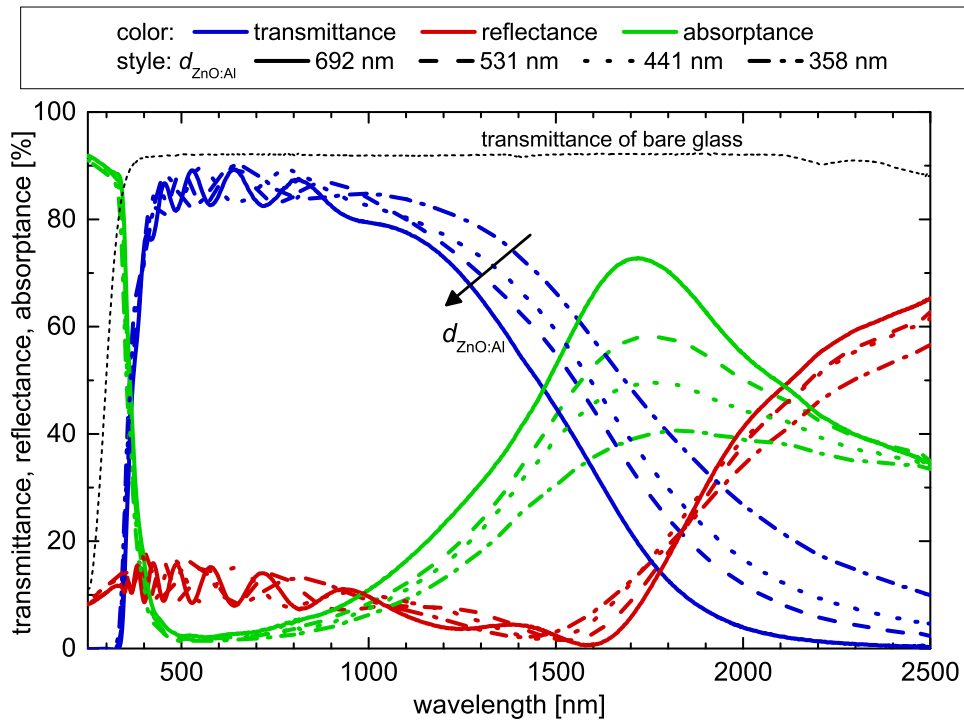


Figure 4.1: Transmittance, reflectance and absorptance of ZnO:Al films with different thickness on SiO_xN_y coated glass as a function of wavelength. The arrow indicates the narrowing of the optical window in the NIR for increasing thickness as the major effect with respect to solar cell application. Absorption was calculated according to eq. (2.23). For comparison, the transmittance of the bare glass substrate has been added to the plot (black, dashed line).

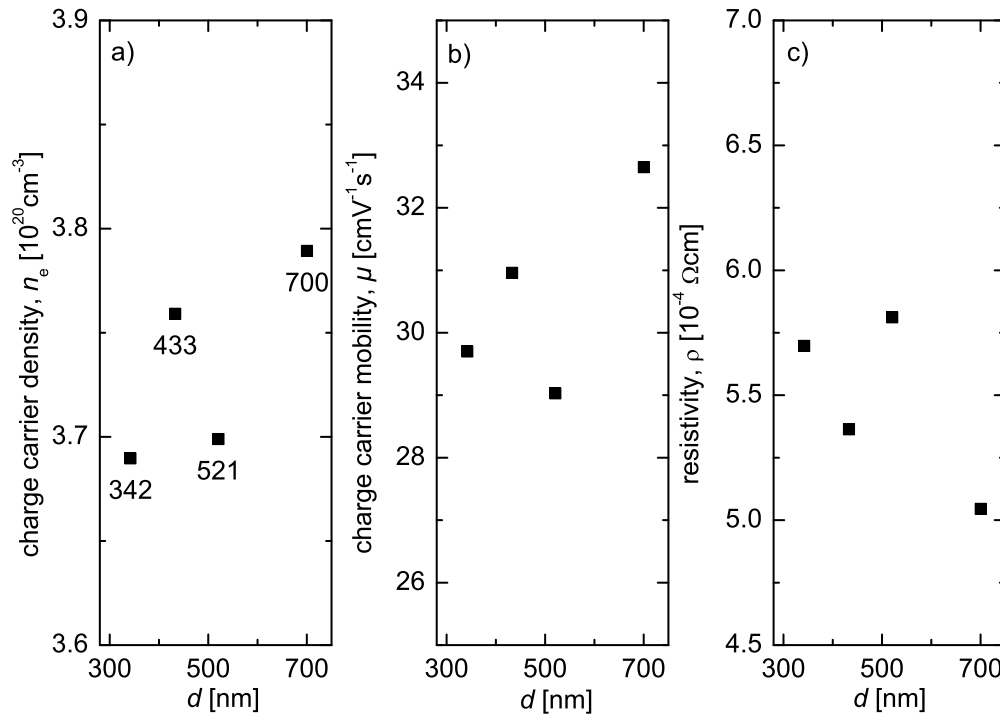


Figure 4.2: Electronic properties of ZnO:Al layers in the as-deposited state as a function of layer thickness.

analysis) with film thickness for PLD-grown ZnO:Al samples [148]. In her PhD thesis, Ding investigated this trend for LPCVD-grown ZnO and ZnO:B [39]. She also found a correlation of the Hall-mobility with thickness, i.e. grain size (derived from SEM images in this case).

In fig. 4.3 XRD-data, i.e. a $\theta - 2\theta$ scan, of a 360 and a 720 nm sample in the as-deposited state are presented together with a powder diffraction pattern of ZnO. For better comparison all data are normalized to the maximum intensity of the (002)-reflection. As can be seen by comparing to the powder diffraction pattern, both ZnO:Al films are predominantly $\langle 001 \rangle$ -oriented perpendicular to the film surface. This preferential orientation is well known for ZnO grown by sputtering on foreign substrates [9, 38, 128, 150–153]. The intensity ratio of the (103) to the (004) peak is higher for the 358 nm sample. This indicates a lower preferential $\langle 001 \rangle$ orientation for thinner films, which is also evident considering that all films originate from the disordered nucleation layer at the bottom of the ZnO:Al films. In other words, $\langle 001 \rangle$ oriented growth develops with increasing thickness. The extent to which this evolution is a real bulk effect or just stemming from less relative contribution of the disordered nucleation layer can not be distinguished by this simple comparison of the peak intensities.

The center position and the FWHM of the (002)-reflex is presented in fig. 4.4. The data was derived by fitting a pair of Pearson7 functions [154] to the $K\alpha$ doublet. A Gaussian centered at $2\theta \approx 35.8^\circ$ accounting for the unknown peak as well as a linear background have been included in the data fit. The position of the (002)-reflex increases with film thickness, but stays below that of the powder diffraction pattern ($2\theta = 34.435^\circ$; grey horizontal line in (a)). This could be interpreted as tensile stress along the [001]-direction which relaxes with increasing film thickness¹⁹. On the other hand, the FWHM increases with film thickness. The evolution of the electronic properties with growing film thickness (cf. fig. 4.2) seems to be contrary as increasing FWHM points at a somehow decreased crystalline quality. However, the range of variation in FWHM with film thickness is rather small and its validity is limited to the $\langle 001 \rangle$ -direction.

The thermal treatment leads to a nearly constant shift of the peak position to higher values. Thereby, the increase is stronger than the variation with film thickness found for the as-deposited samples, but again the values stay below that of the powder diffraction pattern. The FWHM clearly decreases, hence pointing to a better crystallinity as one would expect from the improvement in the electrical data. But, as before care needs to be taken when interpreting this correlation with respect to the constraints already discussed for the XRD data of the thickness series.

To conclude the investigation of the samples in the as-deposited state, the electronic properties of the ZnO:Al films tend to improve with film thickness. This can be understood by

¹⁹Note that the incorporation of Al leads to a widening of the ZnO host lattice [38], i.e., generally reduces the 2θ -positions of the reflexes compared to those of the intrinsic ZnO powder diffraction pattern.

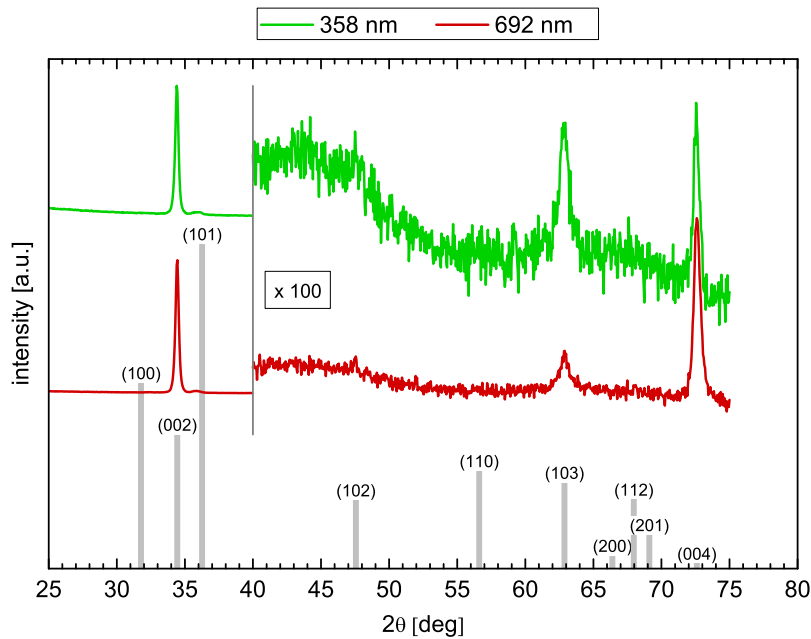


Figure 4.3: XRD data ($\theta - 2\theta$ spectra) of 358 and 692 nm thick ZnO:Al films on SiO_xN_y coated glass together with a powder diffraction pattern of ZnO. The reflexes of the powder diffraction pattern are labeled with the (hkl)-triplets of the corresponding crystallographic orientation. All data are normalized to the peak intensity of the (002)-reflex at $2\theta \approx 34.4^\circ$. For better reading the data are vertically offset and the film spectra are magnified by a factor of 100 for $2\theta > 40^\circ$.

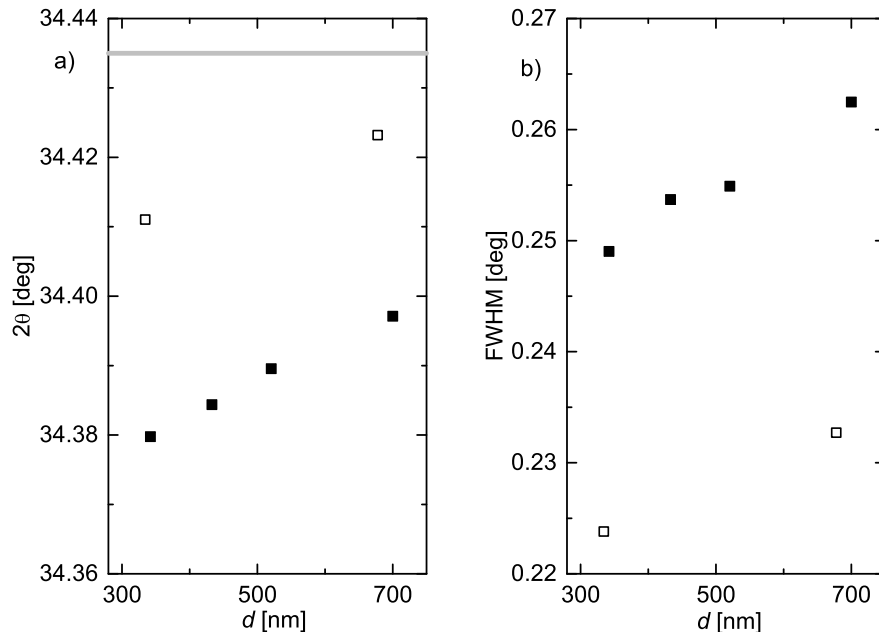


Figure 4.4: (a) 2θ position of the $\text{Cu-K}\alpha_1$ induced (002)-reflex and (b) the according full width at half maximum as a function of the ZnO:Al film thickness in the as-deposited state (full symbols). For the thinnest and thickest sample series data taken after a strong thermal treatment (550/0 thermal degradation followed by a 650/6 capped annealing) are also included (open symbols). The data was derived by fitting a pair of Pearson7 functions to the $\text{K}\alpha$ doublet. The grey horizontal line in (a) represents the (002)-position taken from the powder diffraction pattern already presented in fig. 4.3.

taking into account the existence of a highly disordered nucleation layer from which preferential $\langle 001 \rangle$ -oriented crystal growth emerges. As a consequence thinner samples exhibit a higher resistivity being around $6.3 \cdot 10^{-4} \Omega \text{cm}$ compared to $5.2 \cdot 10^{-4} \Omega \text{cm}$ for the 358 and 692 nm series, respectively. With respect to the changes of the electronic properties under different thermal treatments, the thickness dependent variation in the as-deposited state will only be of minor influence as we will see in the following.

4.2.2 Electronic Properties after Thermal Treatment

For most of the samples, the post deposition treatment started with a thermal degradation and was followed by the annealing under capping. The effect of the procedure on the electronic properties of the ZnO:Al films can be well summarized by regarding the mobility as a function of the charge carrier density. Such a plot is presented in fig. 4.5 including all variations of film thickness, treatment sequences and states. For clarity, the data of the as-deposited and thermally degraded state is limited to one representative sample per variation.

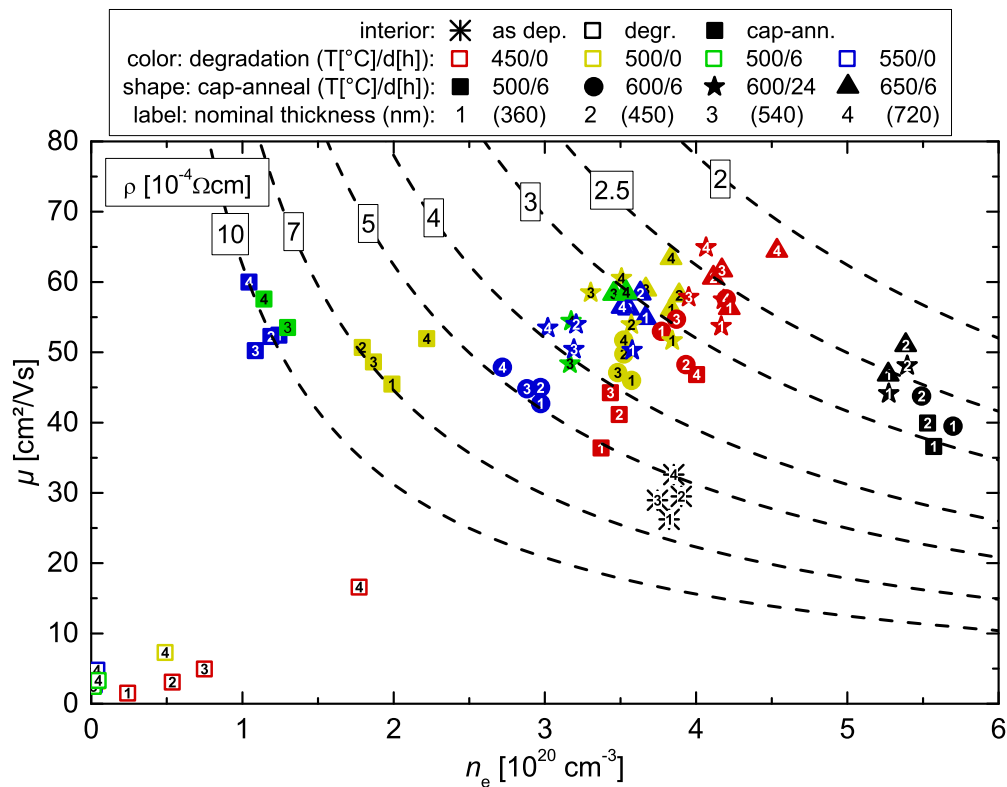


Figure 4.5: Mobility as a function of charge carrier density for the ZnO:Al films of different thickness in the as-deposited state (black asterisks) and after application of thermal degradation (open, colored symbols), cap-annealing (black, filled symbols) and 2-step annealing (filled, colored symbols). The numbers above the data points indicate the nominal film thickness (1, 2, 3 and 4 for 360, 450, 540 and 720 nm, respectively). The grey dashed lines represent lines of constant resistivity ranging from 2 to $10 \cdot 10^{-4} \Omega \text{cm}$ and labelled accordingly at the top of the graph.)

After thermal degradation, all samples exhibit lower mobility and reduced charge carrier density with respect to the as-deposited state. The degradation increases with higher treatment temperatures and is stronger for thinner samples. Comparing the data for $500^{\circ}\text{C}/6\text{ h}$ and $550^{\circ}\text{C}/0\text{ h}$ degradation, a lower annealing temperature, to a certain extent can be compensated by the presence of a plateau time. After strong thermal degradation the charge carrier density shows values as low as $1.43 \cdot 10^{18} \text{ cm}^{-3}$. This is a reduction of more than two orders of magnitude. The degradation of mobility seems to saturate at a certain intensity of the treatment and approaches values around $3 \frac{\text{cm}^2}{\text{Vs}}$, whereas higher intensities are needed for saturation with thicker samples. As a consequence, for some samples, the resistivity reaches values above $1 \Omega\text{cm}$ after thermal degradation. This corresponds to a sheet resistances above $10 \text{ k}\Omega$ (even for the thick samples). Thus, these samples can not be applied as front electrode in solar cells.

For the 360 and 450 nm series, cap-annealing was also applied without preceding thermal degradation (black, full symbols in fig. 4.5). These samples show an increase in charge carrier density by a factor of ≈ 1.5 accompanied by a higher mobility, which is exactly the opposite behavior to the thermal degradation²⁰. The slightly higher μ and n_e of the 450 compared to the 360 nm samples in the as-deposited state is still present after the cap-annealing²¹. A higher treatment intensity leads to higher mobilities (up to $51 \frac{\text{cm}^2}{\text{Vs}}$; corresponding to an increase of 40 %) accompanied by a slight reduction in the charge carrier density compared to low treatment intensity. As a result, the resistivity could be reduced by more than 50 % in all cases, reaching values below $2.5 \cdot 10^{-4} \Omega\text{cm}$ for the 450 nm samples at intensive treatments. This corresponds to $R_S < 5.6 \Omega$, which is well suited for cell application.

The last group of data represents the samples subjected to 2-step annealing (colored, full symbols in fig. 4.5), i.e. subsequent cap-annealing of the thermally degraded samples already discussed. With respect to the as-deposited state, the only general finding is a gain in mobility. For fixed cap-annealing conditions, the charge carrier density generally decreases with increasing intensity of the preceding thermal degradation. On the other hand, for fixed thermal degradation conditions, it increases for stronger cap-annealing treatment. Regarding the dependence of mobility on charge carrier density two characteristic sub-sets can be distinguished. The first, located at rather low values of $n_e = 1 \dots 2.2 \cdot 10^{20} \text{ cm}^{-3}$ comprises the treatment variations where the temperature applied during thermal degradation was higher or equal to that applied during cap-annealing. With respect to the different variations in thermal degradation it shows a slightly negative trend in μ with increasing n_e . Accordingly, the highest mobility of $\mu = 60 \frac{\text{cm}^2}{\text{Vs}}$ within this sub-set is reached for the rather low value of

²⁰Note the only difference between these two treatments is the presence of the 100 nm intrinsic a-Si:H capping layer in the case of cap-annealing. This clearly demonstrates the outstanding role of the capping.

²¹The only exception to this finding is the charge carrier density determined for the 360 nm sample after the $600^{\circ}\text{C}/6\text{ h}$ cap-annealing (black, full circle labeled with 1). The reason for this deviation from the general trend is not known.

$n_e = 1 \cdot 10^{20} \text{ cm}^{-3}$. Despite this remarkably high mobility (almost doubled with respect to the as-deposited state), due to the low charge carrier density the resulting conductivity is reduced by a factor of 0.5, hence being less attractive for solar cell application. However, these samples are highly interesting for investigation of the transport properties, as they lie on the lower edge of the mobility window limited by grain boundary scattering (cf. sec. 4.2.3).

Following this interpretation, those samples should exhibit a rather low density of acceptor-like defects at the grain boundaries as they still possess high μ . This is remarkable since the low n_e suggests high compensation of the Al_{Zn} -donors, i.e. the ZnO:Al is oxygen-rich. Oxidation of the Al during thermal degradation would also explain the phenomena but is very unlikely a dominating process since thermally induced reduction of Al-oxides during cap-annealing can be excluded as the reason for the recovery of n_e with respect to typical binding energies of Al-O. The coexistence of low defect density at the grain boundaries and oxygen-rich conditions within the grains points at different mechanisms related to the particular phenomenon. The reduction of grain boundary defects, either being already present in the as-deposited state or formed during thermal degradation, seems to be (partially) reversible already for $T_{\text{cap-ann.}} \leq T_{\text{th.deg.}}$. In contrast to that, the recovery of n_e seems to scale with the temperature applied during cap-annealing, whereas the achieved values are generally lower when the preceding thermal degradation was stronger.

The second sub-set of 2-step annealed samples accordingly comprises of variations with cap-annealing temperatures above those applied during thermal degradation. In contrast to the first sub-set, these data generally show a positive dependence of μ on n_e . This holds true for both increasing intensity of the cap-annealing and same thermal degradation as well as (with lower slope) decreasing intensity of the thermal degradation and fixed cap-annealing. Consequently, the highest mobilities and charge carrier densities within this group are achieved by combining the weakest thermal degradation and the strongest cap-annealing, reaching values of $64.5 \frac{\text{cm}^2}{\text{Vs}}$ and $4.4 \cdot 10^{20} \text{ cm}^{-3}$, respectively. Compared to the as-deposited state, this yields a reduction of the resistivity by almost 60 % to $2.2 \cdot 10^{-4} \Omega\text{cm}$. Besides this remarkable result it is also noteworthy that all samples of this sub-set exhibit an increase in conductivity.

4.2.3 Mechanism of Thermal Treatment

Based on the observation made on the influence of annealing on mobility and charge carrier density we propose the following model.

An as-deposited ZnO:Al exhibits a free charge carrier density resulting from intrinsic (i.e. V_{O} and Zn_i) and extrinsic (i.e. Al_{Zn}) n-doping. Part of those donors are compensated by acceptors (i.e. V_{Zn} and O_i) or remain in an inactive configuration (e.g. by formation of

Al-O complexes²²) [20]. According to first-principles calculation of the formation energies by Lany and Zunger [155] the compensation of donors is dominated by zinc vacancies. Whereas, Noh *et al.* showed that oxygen interstitials were the main reason for compensation in their experiments [156]. Therefore, the density of ionized impurities is always higher than the free carrier density (assuming predominantly Al_{Zn} donors, i.e. neglecting multiple charged donors). In other words the doping efficiency is not only limited by inactive donors but also by compensating acceptors.

The charge carrier density, n_e , can be increased by annealing, whereas the partial pressure of oxygen has to be kept as low as possible to prevent the formation of additional compensating acceptors and possibly also the elimination of existing donors. This can be realized, for instance, by capping the ZnO:Al films with a protective layer. In this work, an approximately 100 nm thick a-Si:H layer deposited by PECVD was used for that purpose. The subsequent annealing was carried out for up to $t_{\text{ann}} = 24$ h in a N₂-rich atmosphere at temperatures up to $T_{\text{ann}} = 650$ °C and at atmospheric pressure. As a result, the charge carrier density is generally improved. This can be explained by an activation or formation of donors and the elimination of compensating acceptor states. Additionally increasing carrier mobility was observed for most of the samples after capped annealing. Neglecting the influence of the grain boundary scattering (which is indeed a very rough assumption), the increased mobility can be understood as a consequence of reduced IIS. This would be a hint to eliminated compensating acceptor states being the dominant process during the capped annealing as this is the only way for reducing the density of ionized impurities while increasing n_e at the same time. Moreover, a thermal activation (i.e. reduction) of the relatively stable Al-O compounds is very unlikely. In the case of annealing without a protective capping layer, i.e. high oxygen partial pressure, n_e decreases usually accompanied by a reduced μ . The former is very likely due to the elimination of intrinsic donors as well as the formation of compensating acceptor states. The deactivation of Al-donors via oxidation also has to be considered. The decreased mobility is a consequence of the increased grain boundary scattering, i.e. a broadening of the depletion zone at the grain boundaries (in terms of the Seto-model).

4.2.4 Optical Properties after Thermal Treatment

Of course, all these changes in electronic properties that were observed in sec. 4.2.2 are closely related to changes in the optical properties of the ZnO:Al films (cf. sec. 2.1.5). To demonstrate this influence, the absorptance data of differently treated samples of similar thickness are presented in fig. 4.6. Compared to any annealed samples, the non-annealed one exhibits a remarkable absorptance tail in the sub band gap region ($h\nu = 3.7 \dots 2.7$ eV).

²²It is worth noting that the oxidation of an Al-atom after film growth generally implies the formation of oxygen vacancies, hence would have a reduced (or no) net effect on the free carrier density

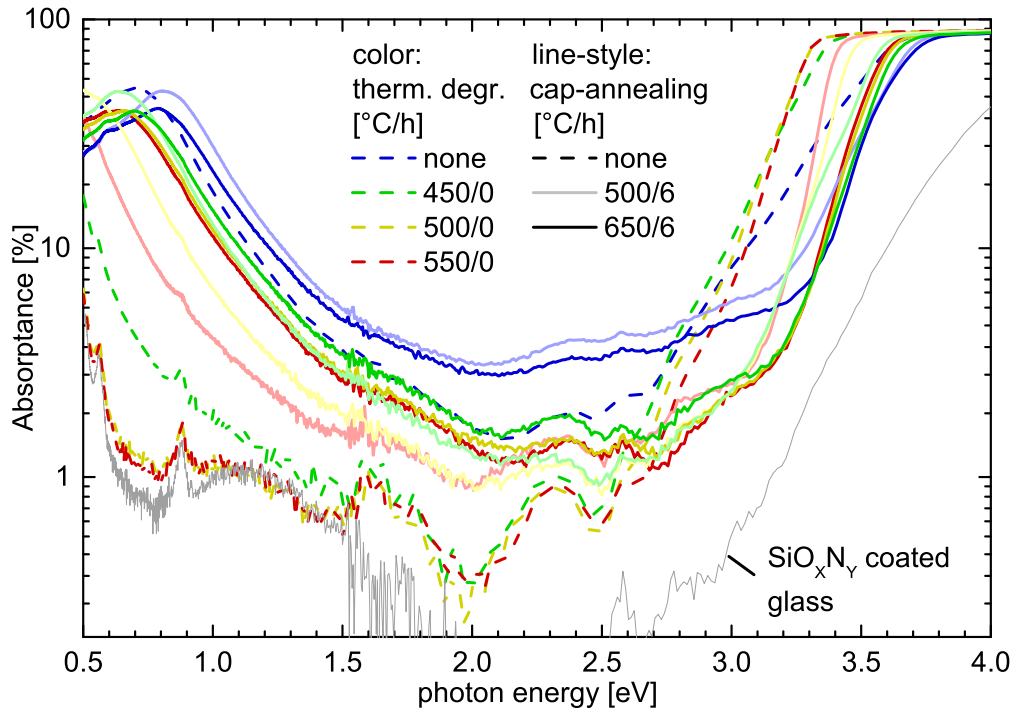


Figure 4.6: Absorbance of different ZnO:Al films on SiO_xN_y coated glass as a function of photon energy. The ZnO:Al film thickness for all samples shown ranges from 419 to 440 nm. The dashed lines represent values obtained after thermal degradation (if any). The solid lines show the absorbance after subsequent cap-annealing for 6h at 500 (light color) and 650 °C (dark color). The absorbance of a SiO_xN_y coated glass without ZnO:Al layer is added for reference.

The narrowing of this absorption tail upon any annealing is generally ascribed to healing of defects in the ZnO:Al. This is also observed for samples exclusively subjected to thermal degradation and is hence not related to the presence of a protective capping layer. The microscopic origin of this effect is still under investigation. Recent annealing experiments conducted in our group based on a variation of deposition temperature and the admixture of oxygen, nitrogen and hydrogen during ZnO:Al growth, and assisted by Raman spectroscopy lead to the assumption that healing of extended defects in the crystalline structure rather than of point defects related to doping is responsible for the narrowing of the absorption tails [157–159]. Moreover, it was found that these tails show an exponential decay. Following the URBACH formalism their width can be described by a distinct URBACH energy [160]. For more details on this particular topic refer to the work of Schönau [161].

Regarding the samples in the thermally degraded state (dashed lines) a decrease in free carrier absorption with increasing treatment temperature can be observed in the low energy part of the plot. This is qualitatively in accordance with the reduction of n_e observed experimentally by the HALL-effect measurements. For the samples thermally degraded at 500

and 550 °C there is no more significant FCA observable when compared to the data of the SiO_xN_y coated glass reference. This trend is also represented by the onset of the fundamental absorption edge, when coming from high energies. The decaying absorptance towards lower photon energies on the other hand is steeper for stronger thermal degradation. This difference is also present for the two samples degraded at 500 and 550 °C, which showed no observable difference in the carrier density related optical properties. Hence, this result supports the hypothesis, that the tailing is due to defects that are not related to the doping and that can be healed upon annealing. In the visual spectral region ($h\nu = 1.5 \dots 2.5 \text{ eV}$), all samples subjected exclusively to thermal degradation show a very similar low absorptance. The remaining features are related either to characteristic absorption peaks originating from the glass substrate ($h\nu = 0.5 \dots 0.6, 0.9, 2.6 \text{ eV}$, cf. fig. 3.1) or interference effects in the ZnO:Al film (pronounced oscillations for $h\nu = 1.5 \dots 2.5 \text{ eV}$)²³. Both features are also observable in the data of all other ZnO:Al films presented in fig. 4.6, but are more or less superimposed by FCA or sub band gap absorption.

The absorptance data for the samples subjected to thermal degradation and subsequent cap-annealing (i.e. 2-step annealing) demonstrate the (partial) recover of the charge carrier density, already observed by the HALL-effect measurements. Thereby a stronger preceding thermal degradation leads to lower charge carrier density, as indicated by lower FCA and a smaller band gap energy (again with respect to the onset of the decay in absorptance for decreasing photon energy) for a fixed cap-annealing procedure. A higher cap-annealing temperature on the other hand promotes the increase in n_e , hence FCA and band gap energy. The variations in the absorptance data due to different thermal degradation become smaller for stronger cap-annealing but qualitatively still remain. The narrowest slope at the band gap is observed for the strongest thermal degradation followed by the weakest cap-annealing. Note that samples from this treatment regime (i.e. $T_{\text{cap-ann.}} \leq T_{\text{th.-deg.}}$) had unusual trends in their electronic properties, i.e. high mobility at rather low charge carrier density (cf. fig. 4.5). For higher cap-annealing temperature the slope is not that narrow.

Apart from the vicinity of the band gap, all samples that were annealed without capping at some stage show a lower absorptance compared to the non-annealed sample. Noteworthy, two of these 2-step annealed samples exhibit a higher charge carrier density than the non-annealed ZnO:Al film. However, the higher mobility in these samples leads to a lower maximum value and a stronger decay of the FCA peak [162], overcompensating its shift towards higher photon energy. In contrast to that the ZnO:Al layers that were exclusively cap-annealed, show a higher absorptance away from the band gap compared to the

²³The presence of interferential effects in absorptance data obtained from separate measurements of transmittance and reflectance is commonly interpreted as an artifact due to imperfect repositioning of the sample in combination with non-uniform film properties. However, we would like to note that such effects can also be understood as a real phenomenon.

non-annealed sample. For the FCA, in the low energy part of the spectrum this can be explained by the strong increase in charge carrier density, which also leads to the high band gap energies obtained for these samples. It is noteworthy that these samples, in contrast to thermally degraded ones, show a reduction of the absorptance with increasing cap-annealing temperature. This is in accordance with the (slight) decrease in charge carrier density for stronger cap-annealing exclusively observed for this group of samples (solely cap-annealed). Additionally, these samples exhibit a pronounced absorptance in the visual part of the spectrum ($h\nu \approx 1.9 \dots 3.2 \text{ eV}$), whose magnitude scales with FCA, i.e. charge carrier density. Absorption in visual part of the spectrum is a known phenomenon for ZnO:Al being sputtered e.g. with oxygen deficiency (metal-rich) [163] or in an atmosphere containing residual gases like nitrogen [164]. However, in the present case the absorption is clearly a result of the cap-annealing. An incorporation of impurities, like nitrogen is very unlikely or should be even more pronounced for the thermal degradation step, which is carried out without capping layer. Since the charge carrier density is strongly increased for this group of samples, a relation to the high doping level is very likely. For instance, the formation of metallic complexes containing Zn and/or Al can be imagined. However, the origin of this additional absorption remains speculative and needs further investigation.

To evaluate the results with respect to application of the annealed ZnO:Al films as front electrode in solar cells, fig. 4.7 shows the absorptance and electronic properties for a compilation of reasonable samples including several ZnO:Al thicknesses and annealing procedures. The solid curves represent samples with similar sheet resistance ($R_S = 7.0 \dots 7.6 \Omega$), hence these samples are equivalent for cell application from an electrical point of view. All treated ones show a marked overall reduction in absorptance compared to the non-annealed reference. In the NIR, this is due to lower FCA thanks to either lower charge carrier density or film thickness (or both) and to increased mobility. The samples with higher charge carrier density and reduced thickness additionally show a broadening of the optical window in the band gap region. Finally, all these samples exhibit lower sub band gap absorption. Note that the sample that was exclusively cap-annealed indeed shows a higher absorptance away from the band gap edge compared to other treated samples. Nevertheless, with respect to the non-annealed ZnO:Al film, the absorptance is still reduced except for the region $\lambda = 470 \dots 620 \text{ nm}$ where a slight increase is observable.

All in all, these results demonstrate the potential benefit of the annealing procedure, since it enables a reduction in the parasitic absorption in ZnO:Al films applied as front electrode in solar cells, and hence an increase in the photo current density while at the same time the low sheet resistance can be conserved. The remaining data in fig. 4.7 (dotted and dashed line) demonstrates the versatility of ZnO:Al annealing. The sample represented by the dotted line shows a remarkably low sheet resistance ($R_S = 3.1 \Omega$, i.e. $\rho = 2.1 \cdot 10^{-4} \Omega\text{cm}$) while at the

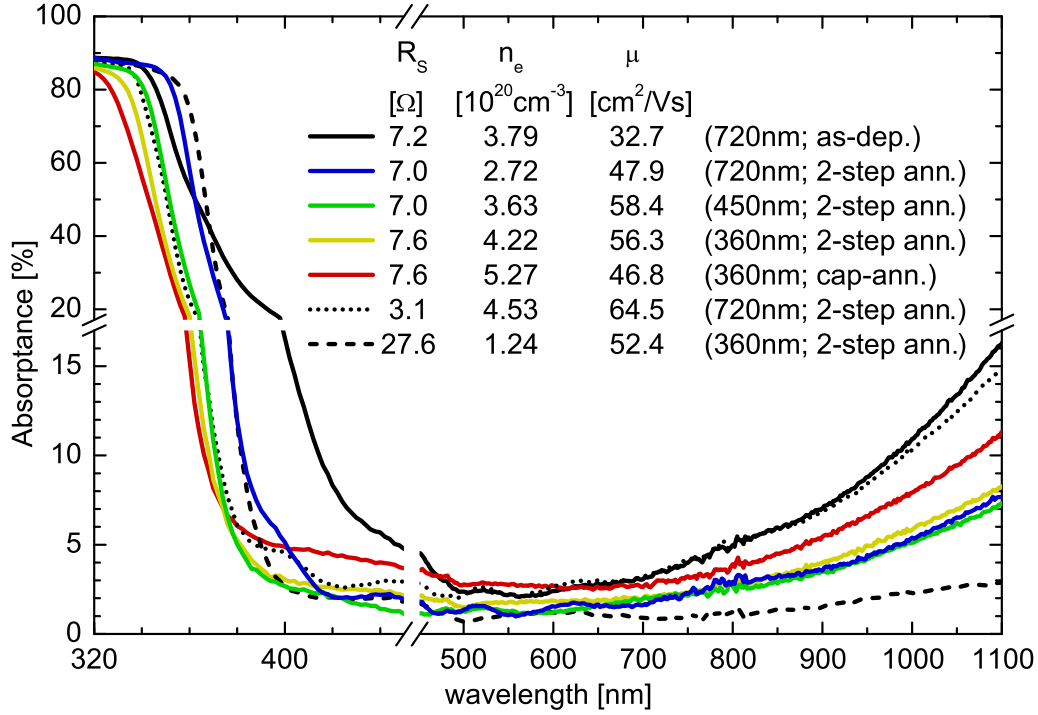


Figure 4.7: Absorbance of different ZnO:Al films on SiO_xN_y coated glass as a function of wavelength. The shown wavelength interval represents the region of interest with respect to light harvesting in Si-based solar cells. The solid lines represent samples with similar sheet resistance ($R_S = 7.0 \dots 7.6 \Omega$). The dashed and dotted lines show the absorbance of the sample with the lowest ($R_S = 3.1 \Omega$) and highest sheet resistance ($R_S = 27.6 \Omega$) after 2-step annealing. The particular values for R_S , n_e and μ as well as the nominal thickness and kind of treatment are included in the legend. Note that both axes are broken to emphasize the residual absorption in the optical window and the behavior in the vicinity of the band gap.

same time film thickness was maintained and short wavelength absorbance (for $\lambda < 500 \text{ nm}$) even reduced compared to the non-annealed reference sample. The sample represented by the dashed line on the other hand exhibits a very low FCA while possessing a sheet resistance of $R_S = 27.6 \Omega$ which is still reasonable for application as a front electrode in solar cells.

4.2.5 Technological Evaluation of the Results

In sec. 4.2.2/4.2.4 it was shown, that the annealing procedure provides the possibility to vary the opto-electronic properties of sputtered ZnO:Al films over a wide range. This creates the need to define a quantitative measure, i.e. a metric, of the opto-electronic film properties with respect to application of the ZnO:Al as front electrode in solar cells. Of course, this is not a new issue in the general context of TCOs. There are several ways to define a figure of merit (FoM) in order to rate a TCO's fitness. For instance the FoM proposed by Haacke ($\Phi_H = T^{10}/R_S$) [165] is often used. Refer to Barnes for a brief review of different FoMs in the context of transparent conductors in general [166]. In the following we will evaluate the data

presented in sec. 4.2.2/4.2.4 in terms of another widely used FoM, which was developed by Jain [167] and promoted by Gordon [168] as well as in terms of a current density equivalent expression accounting for the absorptive loss in a front TCO with respect to the particular (representative) *EQE* of the underlying cell technology [166].

Jain's figure of merit is defined as [167]

$$\Phi_J = \frac{\sigma}{\alpha} = - \left[R_S \ln \left(\frac{T}{1-R} \right) \right]^{-1}, \quad (4.1)$$

which is simply the ratio of conductivity and absorption coefficient. Both quantities, and thus Φ_J , are material properties and hence are not dependent on the TCO film thickness. This is a ideal assumption, as we have already discussed throughout this section. The right side of eq. (4.1) follows from the LAMBERT-BEER law, eq. (2.25). Moreover, by applying the DRUDE theory and accounting for FCA, as the only absorption mechanism, an upper limit of this FoM can be written as

$$\Phi_J(\omega) = \sqrt{\varepsilon_\infty} \varepsilon_0 c \left(\frac{m^* \mu}{e} \right)^2 \omega^2. \quad (4.2)$$

Note that there is no dependence on charge carrier density. Following this expression, the FoM exclusively depends on μ and m^* (i.e. the relaxation time, τ , cf. eq. (2.3)), and ε_∞ . This is an interesting result with respect to the annealing procedures, which generally tends to higher mobility, whereas the remaining two quantities do not allow much variation for a common TCO.

Despite both Φ_H and Φ_J being widely used, there is no general recommendation on the wavelength (range) that should be used to determine α . In literature, the α is often referred to the value at $\lambda = 550$ nm (sometimes averaged/smoothed to get rid of the interferential oscillation in T and R). Obviously, this would be an unsatisfying definition for our purpose. Thus, we will rely on the commonly used definition of solar weighted quantities:

$$T_{\text{solar}} = \frac{\int T(\lambda) \cdot E_{\text{STC}}(\lambda) d\lambda}{\int E_{\text{STC}}(\lambda) d\lambda}, \quad (4.3)$$

where $T(\lambda)$ is the measured transmittance of the TCO (on substrate) and E_{STC} the standardized solar spectrum (cf. sec. 3.2.4). Similarly, R_{solar} is calculated from $R(\lambda)$. As before, in the context of a-Si:H/ μ c-Si:H tandem cells the wavelength range between 300 and 1100 nm is an appropriate choice for the lower and upper integration limit, respectively.

Figure 4.8 shows the conductivity as a function of the solar weighted absorption coefficient, α_{solar} . The latter is calculated in accordance to eq. (2.25) by using T_{solar} and R_{solar} . It is noteworthy that this method attributes the overall absorption in the glass and the SiO_xN_y

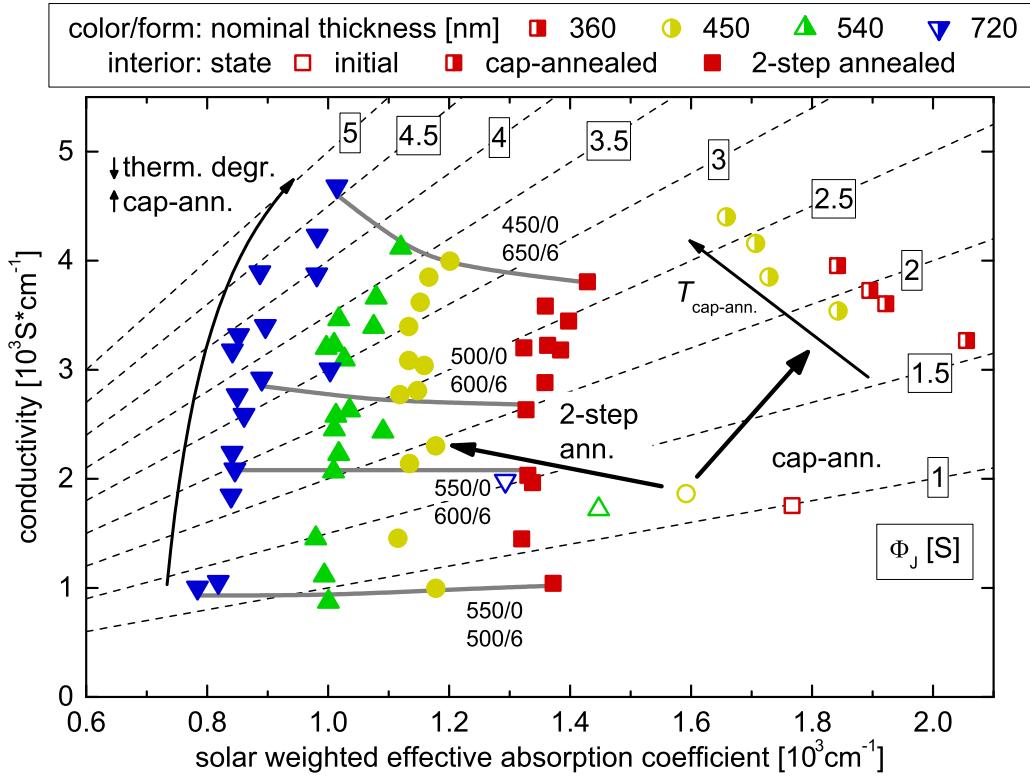


Figure 4.8: Conductivity (σ) as a function of solar weighted effective absorption coefficient, α_{solar} . The plot includes data of samples with different nominal ZnO:Al film thickness (symbol color) prior to annealing (open symbols), after cap-annealing (half right filled symbols) or after 2-step annealing (full symbols). The dashed lines are lines of constant Φ_J . The particular values of Φ_J are given in Siemens by the framed numbers. The arrows indicate the general trend in the treatment conditions. The grey lines are guides to the eye and connect data with same treatment conditions but different nominal ZnO:Al film thickness. The numbers indicate the particular treatment. The notation is [thermal degradation ($^{\circ}\text{C}/\text{h}$); cap-annealing ($^{\circ}\text{C}/\text{h}$)]. The absorption coefficient was calculated according to the right hand side of eq. (4.1) by inserting T_{solar} and R_{solar} (eq. (4.3)). The integration limits were set to 300 and 1100 nm.

and ZnO:Al layer exclusively to the ZnO:Al layer, which is why we denoted it as “effective”. It is hence an approximation only valid if the ZnO:Al absorption is much greater than that of the glass and SiO_xN_y . As can be seen, for instance, from fig. 4.6, this requirement is hardly fulfilled, particular for ZnO:Al films with rather low residual absorptance. That is why the data in fig. 4.8 shows this general pronounced shift to lower absorption coefficient with increasing ZnO:Al film thickness. In other words, the thickness dependence of the absorption coefficient and hence Φ_J is biased by the residual absorptance of the substrate. Therefore, fig. 4.8 is not wholly suited for comparison of the FoM of ZnO:Al films with different thickness. Note that this is only caused by the way α is calculated. Despite this constraint, the plot nicely demonstrates the general effects for the different annealing procedures.

Samples exclusively cap-annealed show higher absorption and conductivity compared to the initial state. For stronger annealing conditions, the increase in α_{solar} gets smaller while at

the same time σ evolves further. For the highest annealing temperature, there is almost no increase in solar weighted absorption compared to the initial state. With respect to Φ_J (according to eq. (4.1)) the cap-annealing procedure generally improves the ZnO:Al properties. The highest value is achieved for the strongest cap-annealing.

All samples subjected to 2-step annealing show a substantial reduction of the solar weighted absorption coefficient, which tends to be less for weaker thermal degradation/stronger cap-annealing. The conductivity on the other hand shows a distinct variation with treatment conditions. For strong thermal degradation followed by mild cap-annealing the conductivity falls below that of the initial state. Applying milder thermal degradation in conjunction with stronger cap-annealing leads to a remarkable improvement in Φ_J , being at best almost fivefold in the case of the 720 nm series. The value of Φ_J is predominantly controlled by the variation in conductivity. For higher values of σ , the improvement in Φ_J is more and more impeded by the slightly increasing α . Despite that, for all nominal thicknesses, the highest value of the FoM coincides with the highest conductivity, which is achieved for the weakest thermal degradation followed by the strongest cap-annealing. The 2-step annealing allows higher values of Φ_J compared to the samples exclusively cap-annealed. Strong thermal degradation followed by weak 2-step annealing on the other, hand can even lower the FoM and is hence inappropriate.

Restricting the treatments to those compatible to float glass, i.e. having $T_{\text{anneal}} \leq 500^\circ\text{C}$, still allows a noteworthy improvement in Φ_J . The FoM values after cap-annealing are less affected by this restriction, hence the best cap-annealing yields similar values for Φ_J compared to the best 2-step annealing procedure. However, the limitation to float glass compatibility noticeably reduces the benefit of ZnO:Al annealing.

To conclude, analyzing Jain's FoM, Φ_J , (cf. fig. 4.8, p. 64) allowed us to quantify the improvement of opto-electronic properties of ZnO:Al layers due to annealing. However, in terms of solar cell application, its value remains abstract to some extent. A more meaningful quantity in this context, is the absorption-related photo current loss [166], which will be introduced in the next paragraph.

The absorption related photo current loss is defined as [166]

$$J_{\text{loss}} = e \int EQE(\lambda) \cdot A_{\text{TCO}}(\lambda) \cdot \Phi_{\text{ph}}(\lambda) d\lambda = \int SR(\lambda) \cdot A_{\text{TCO}}(\lambda) \cdot E(\lambda) d\lambda. \quad (4.4)$$

Note the similarity to eq. (2.49), which is used to derive current densities from e.g. EQE values. Actually, J_{loss} should be interpreted as the loss in photo current density of a particular cell (i.e. particular EQE), which is implied by the absorption in the front TCO. For the calculations we used a fixed data set of EQE values, representing the general spectral distribution of the EQE for an a-Si:H/ $\mu\text{c-Si:H}$ solar cell. For the absorptance of the TCO, A_{TCO} , we use the

absorptance derived from applying eq. (2.23) to the measured transmittance and reflectance data of flat ZnO:Al layers on glass. It shall be noted, that in the original form of eq. (4.4) the term $(1 - T_{\text{TCO}})$ is used instead of A_{TCO} [166], but since the transmittance data of flat ZnO:Al layers exhibits interferential oscillations we felt that the use of the absorptance data is more reliable in our case. Like for the calculation of Φ_{J} , the absorption related data also contains the contributions coming from the glass and the SiO_xN_y . But this time, since the absorptance is used instead of the absorption coefficient, this does not lead to any artificial shift in the data. Moreover, from a technological point of view the absorption of the whole front substrates is indeed of interest. Note that for the calculation of J_{loss} the TCO film thickness is not needed.

Figure 4.9 presents J_{loss} for the same set of samples as shown in fig. 4.8 as a function of their sheet resistance. In the semi-logarithmic presentation used here, the data of the samples in initial state are situated on a straight line (indicated by the upper grey line). The

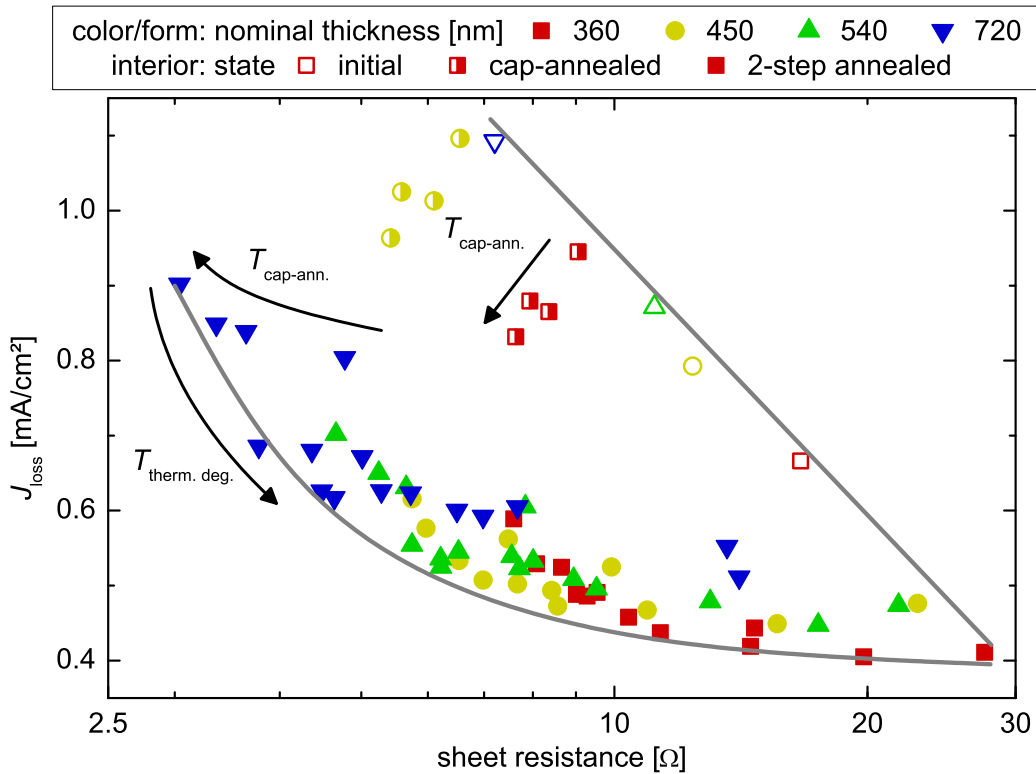


Figure 4.9: Solar cell weighted implied photo current density loss in an a-Si:H/ μc :Si-H tandem cell due to absorption in the front contact (J_{loss}) for annealed ZnO:Al films on glass as a function of their sheet resistance. The plot includes data of samples with different nominal ZnO:Al film thickness (symbol color) prior to annealing (open symbols), after cap-annealing (half right filled symbols) or after 2-step annealing (full symbols). The arrows indicate the general trend in the treatment conditions. The grey lines are guides to the eye and indicate the upper and lower boundary as observed from the presented data sets. Note the logarithmic scale applied to the horizontal axis. J_{loss} was calculated according to eq. (4.4). The measured *EQE* of a representative a-Si:H/ μc :Si-H tandem cell was used for the weighting.

cap-annealed samples show a tendency towards lower J_{loss} and R_{S} with increasing treatment temperature, which means an improvement in both conductivity and transparency, but the absorptive loss is higher than in the initial state. However, for the highest applied annealing temperature it is e.g. possible to achieve the sheet resistance of the 720 nm sample in its initial state with a lower J_{loss} for the thin cap-annealed sample.

The data of the 2-step annealed samples shows a pronounced lower boundary (indicated by the lower grey line), with decreasing J_{loss} for evolving sheet resistance. The thicker samples are generally arranged at lower values of the sheet resistance, but consequently exhibit a higher absorptive loss. For each particular thickness set all two-step annealing variations lead to a lower absorptive loss. In contrast to the samples exclusively subjected to cap-annealing, a higher cap-annealing temperature slightly increases the absorptive loss, while the sheet resistance again decreases. The intensity of the preceding thermal degradation basically shifts the data along the observed lower boundary. Thereby, stronger thermal degradation leads to higher R_{S} and lower J_{loss} (after subsequent cap-annealing).

From a technological point of view this presentation of the data is very convenient. If the target value of the sheet resistance is known, the best substrate/treatment combination can immediately be read from the graph. However, at this point it has to be mentioned, that the calculation of J_{loss} is a coarse approximation to the real situation within a solar cell. First we have a different optical situation. For instance the interface ZnO:Al/air is now a ZnO:Al/Si interface. Moreover, the ZnO:Al/Si surface is commonly textured in order to achieve good light coupling and trapping. This will lead to higher absorptance also in the ZnO:Al, particular in the long wavelength region, where the Si-absorbers are getting more and more transparent and the light path enhancement plays an important role. This will very likely lead to a distortion of the particular values for J_{loss} , but we believe that it will not affect the general trends shown in fig. 4.9. Concerning the absolute values of J_{loss} they consequently have to be understood as a lower limit for the real case.

4.3 Interdependence of Annealing and Texture Formation

As already pointed out in Section 2.2.3, when sputtered ZnO:Al is used as front-contact in a-Si:H/ μ c-Si:H based solar cells wet-chemical etching of the ZnO:Al in diluted HCl is the standard approach to introduce sufficient light trapping. The particular topography formation is known to be very sensitive on sputter conditions. Therefore, it is very likely that the annealing procedure also affects the topography formation when etching is carried out subsequently to annealing. This assumption is also supported by the findings of Berginski, who investigated a modification of the texture formation upon wet-chemical etching after vacuum annealing ($T \leq 500^{\circ}\text{C}$; without capping layer) in the case of RF-sputtered ZnO:Al [44].

In order to investigate this effect with respect to the annealing procedure applied in the present work three identical sets of ZnO:Al samples underwent annealing (if applied, both thermal degradation and cap-annealing at $500^\circ/6h$) and a texture etching (150 s/0.5 % HCl). Thereby, three different sequencings according to tab. 4.1 were applied. The ZnO:Al used for this study originates from a different industry partner and was processed in a non-reactive in-line DC magnetron sputtering system working with ceramic ZnO:Al₂O₃ tube targets (1 wt.% Al₂O₃) depositing on large area low iron float glass substrates. This particular ZnO:Al was optimized for high light trapping abilities and hence comprises a rather large scaled surface topography, which makes it ideal for this study, since even minor effects of the annealing on the texture formation can be easily detected.

Table 4.1: Particular process sequence for the different sets of samples

sample set	sequence		
	1 st	2 nd	3 rd
A (ref.)	texturing	n/a	n/a
B	thermal degradation	texturing	n/a
C	thermal degradation	cap-annealing	texturing

In fig. 4.10, tilted-view SEM images and a corresponding topographical AFM-scan of the textured ZnO:Al samples (150 s etch duration) are shown for each set of samples. Obviously, the same texturization procedure yields different topographies depending on the annealing state of the sample. Sample A (fig. 4.10 (a,d)) exhibits a dense arrangement of similarly shaped craters with rather smooth walls and well defined crater rims. Neighboring craters seem to share their crater rims, i.e. regarding the AFM-scan (d) the rims seem to form a network. In case of sample B (fig. 4.10 (b,e)) the craters are not that adjacent. Rather the surface consists of more or less independent craters and nearly flat regions in between. The particular shape of the craters is still similar to those of sample A, i.e. they also exhibit smooth walls, whereas their typical diameter seems to be smaller and shows higher fluctuation. In contrast to sample A, a reasonable amount of deep craters with steep walls could be found on sample B. From analyzing the AFM-scans it seems that some of those craters even reach the bottom of the ZnO:Al layer. On sample C (fig. 4.10 (c,f)) the craters formed upon etching appear very jagged. The whole texture is somehow disturbed and shows a porous character compared to sample A (and B). The average crater size is even smaller as for sample B and also shows a high fluctuation. For sample B few of the craters exhibit very steep walls and a shallow bottom, whereas those craters occur more frequently for sample C.

All these qualitative findings are well represented by a statistical analysis of the AFM-scans. Figure 4.11 shows the height distribution (a) and the inclination distribution (b) of the

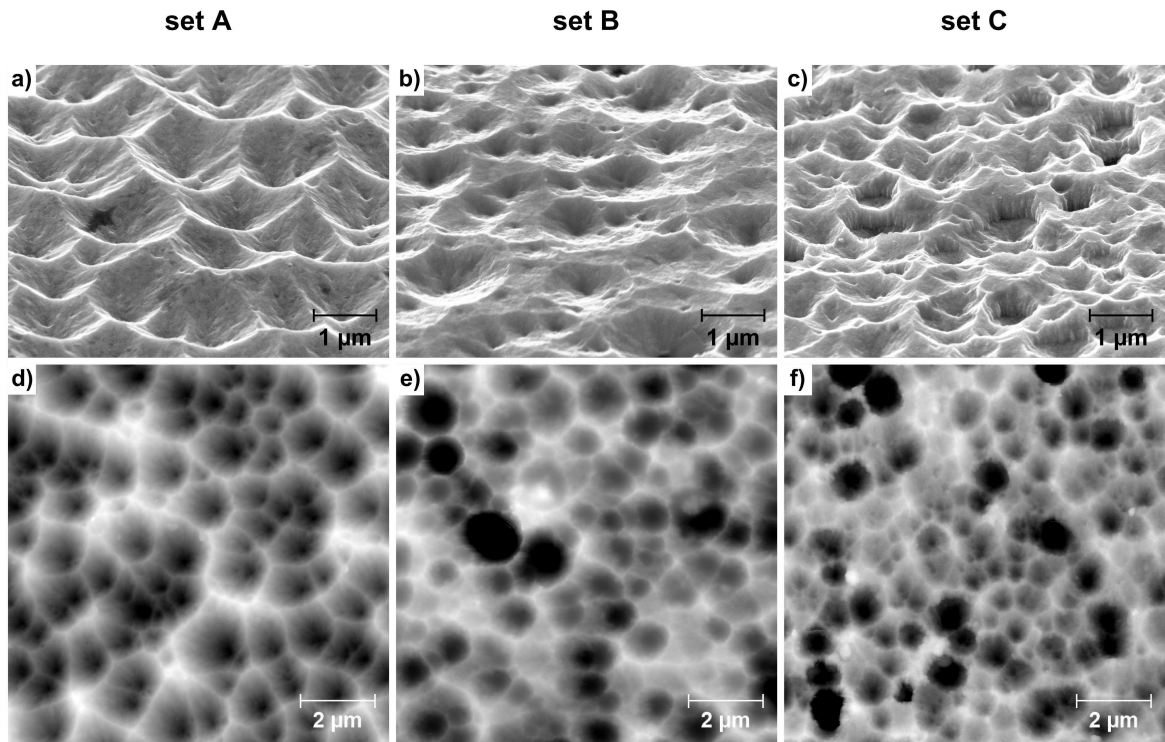


Figure 4.10: Tilted-view SEM images (a-c) and AFM topography scans (d-f) of annealed, textured ZnO:Al processed with sequence A (a,d), B (b, e) and C (c, f) according to tab. 4.1.

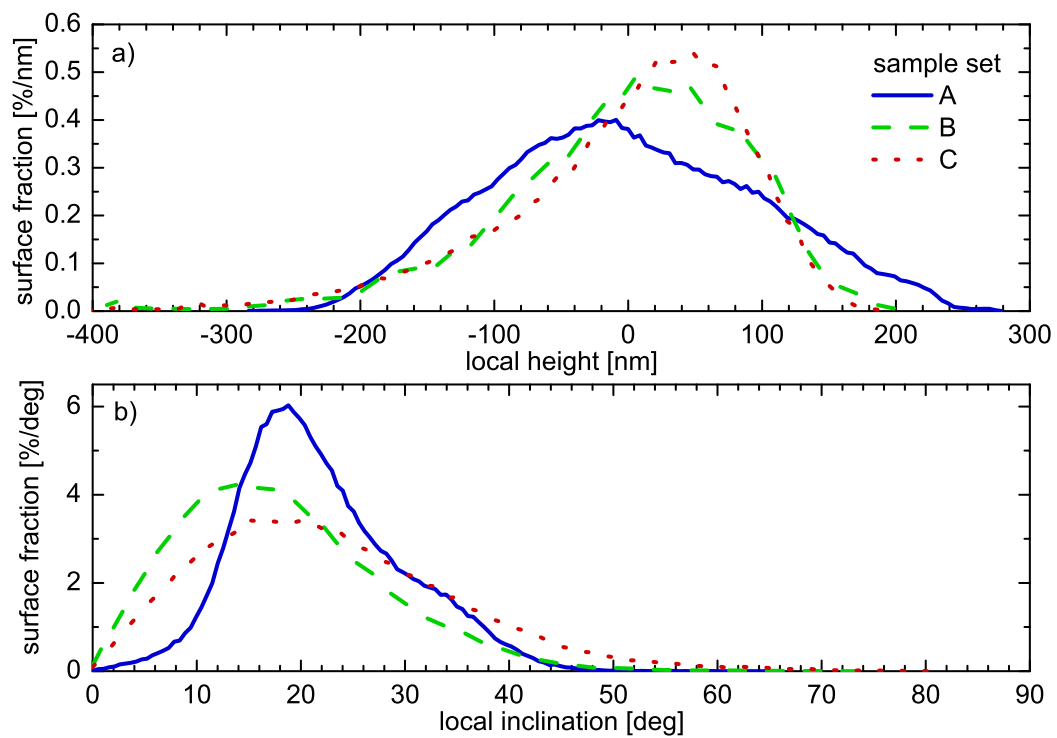


Figure 4.11: (a) Height and (b) inclination distribution of annealed, textured ZnO:Al processed with sequence A, B and C according to tab. 4.1.

AFM-scans presented in fig. 4.10 d) to f). Concerning the height distribution sample A shows a nearly symmetric curve, whereas the data of sample B and C have an obvious skew. They exhibit tailing towards small values and a rather steep drop towards large values, both more pronounced for sample C. The skew points at the somehow higher scatter in crater size, hence deepness, for sample B and C compared to sample A. Moreover, the data of sample B and C comprise a small peak at -0.38 and -0.32 μm , respectively. This is due to the few craters which are very likely reaching the base of the ZnO:Al film and hence have a flat bottom. Regarding the inclination distribution in fig. 4.11 b) sample A exhibits only a low amount of pixels with inclination below 10° . This is evident since there are effectively no flat regions in the surface of sample A (cf. fig. 4.10 a) and d)). Besides that, the data of sample A shows a well-defined maximum at around 19° followed by a quite steep drop towards higher angle. There is hardly any occurrence of inclinations above 50° for sample A. In contrast to sample A, sample B exhibits a high occurrence of inclinations below 10° , representing the presence of the flat regions visible in fig. 4.10 b). The data reaches a maximum at around 15° . Despite being hard to see in fig. 4.11 b), the occurrence of inclinations above 50° is one order of magnitude higher for sample B compared to sample A. This is ascribed to the few deep craters existing in sample B. Sample C shows the most shallow inclination distribution curve of all three samples. It exhibits an intermediated frequency for inclinations below 10° , shows a minor pronounced maximum at around 18° and clearly comprises the highest occurrence of inclinations above 50° . The latter is clearly linked with the rather steep crater walls for sample C.

With respect to application as front electrode for Si-based thin film solar cells, both the presence of virtually non-textured regions, like for sample B, as well as the existence of high inclination angles, like for sample C, should be avoided in order to introduce as much light trapping as possible and to ensure high-quality Si-growth, respectively.

Additional tests were applied to the industrial ZnO:Al presented in sec. 3.1.3, which qualitatively confirmed the aforementioned sequence related effects. Moreover, this ZnO:Al was applied to tandem solar cells after being 2-step annealed either before or after texture etching. The corresponding J - V data of representative a:Si:H/ μc -Si:H tandem cells is presented in tab. 4.2 together with those of a reference cell deposited on non-annealed, textured ZnO:Al. Though, both annealing sequences yield an improvement in J_{SC} ($+0.3$ mA/cm^2), sequence C leads to a detrimental reduction in V_{OC} and FF ²⁴. This provides evidence for the worse device-quality of the Si grown on the sharp texture formed by applying sequence C. The minor drop in V_{OC} and FF for cell D compared to the non-annealed reference A is not texture related and will be discussed in sec. 6.1.

²⁴Si-deposition for all cells presented in tab. 4.1 was done with a so-called substrate-on-carrier process. This causes the rather low FF even for the reference cell and top cell limited J_{SC} for all of those cells.

Table 4.2: J - V data of a:Si:H/ μ c-Si:H tandem cells deposited on wet-chemically textured, 2-step annealed ZnO:Al. The particular sequence of the ZnO:Al post deposition treatment is denoted in the first column.

sequence	J_{SC} [mA/cm ²]	V_{OC} [mV]	FF [%]	eff. [%]
texturing, 2-step ann. (D)	11.7	1401	67.3	11.0
2-step ann., texturing (C)	11.7	1243	62.5	9.1
texturing w/o ann. (A, ref.)	11.4	1413	69.4	11.2

To conclude, both thermal degradation as well as 2-step annealing affect the texture being formed during a subsequent wet-chemical etching²⁵. The particular topographic modifications have been evaluated as disadvantageous for cell application. This could be demonstrated by a sharp drop in V_{OC} and FF of tandem cells processed on ZnO:Al prepared according to sequence C in comparison to those of type D (and non-annealed reference cells, A). Consequently, the texturization of the ZnO:Al was always carried out prior to any annealing steps according to sequence D. This also provided the unique opportunity to modify the optoelectronic properties of a textured ZnO:Al over a wide range without affecting its particular surface topography. Note that this would be a big issue, also in the case of other textured TCO materials, if being realized by adapting the deposition process [44, 75, 169].

²⁵The influence of a separate cap-annealing in this context was not investigated here since its application was not in focus when these tests were conducted. However, it seems reasonable to assume a similar effect as found for sequence C.

5 Analysis of a Light Coupling related Artifact in *EQE* Data

Before we come to the application of annealed ZnO:Al to a-Si:H/ μ c-Si:H solar cells (sec. 6), a discrepancy observed in the photo current density as derived from *EQE* and *J-V* measurements is described and analyzed in this section.

5.1 Description of the Discrepancy

In the course of setting up our device fabrication and characterization here at PVcomB we early started recognizing a systematic discrepancy between the current densities as obtained from *EQE* and *J-V* measurements. As both measurement techniques are crucial for cell development this discrepancy deserved further investigation. After excluding many things related to the particular measurement setups itself, we started to focus on possible relations to our sample design (cf. sec. 3.1). Since the effect, which we identified as the root cause, particular its dependency on the light scattering within solar cells is closely related to some of the experimental results presented in this thesis, we decided to provide the results of these investigation here. As already pointed out in sec. 2.2, the short circuit current density of a tandem cell obtained from a *J-V* measurement should equal the lower (lowest) sub-cell photo current density, as obtained from *EQE* measurements. This effect is commonly referred as *current limitation*²⁶. A tandem cell can be bottom cell limited ($J_{\text{top}}/J_{\text{bot}} < 1$), top cell limited ($J_{\text{top}}/J_{\text{bot}} > 1$) or matched ($J_{\text{top}}/J_{\text{bot}} = 1$).

Figure 5.1 shows the current density determined by *EQE*, of the top and the bottom cell normalized to the corresponding short circuit current density obtained from *J-V* measurement, as a function of the current limitation. It comprises 174 datasets obtained from a-Si:H/ μ c-Si:H cells grown on different moderately textured TCOs over a period of roughly 10 months.

The current density obtained from *EQE* measurement is systematically underestimated, with respect to the *J-V* derived short circuit current density, by approximately 1.5 and 8.5 % for the top and the bottom cell, respectively, as can be noted for the respective limiting conditions. The difference in this deviation causes the offset of the matching point for *EQE*- and *J-V*-derived data.

5.2 Considerations on the Root Cause

In the *EQE* setup, the probe beam irradiates only a small spot of about $3 \times 3 \text{ mm}^2$ within the $10 \times 10 \text{ mm}^2$ -cells. This is a different situation with respect to the *J-V* measurement at

²⁶Strictly speaking J_{SC} can be slightly higher than the photo current density of the limiting cell. This is due to the fact that the limiting cell is driven in reverse bias to maintain the tandem device at short circuit conditions; a direct consequence of the electrical series connection of the sub-cells. However, for cells with reasonable performance and moderate current mismatch, this can be neglected.

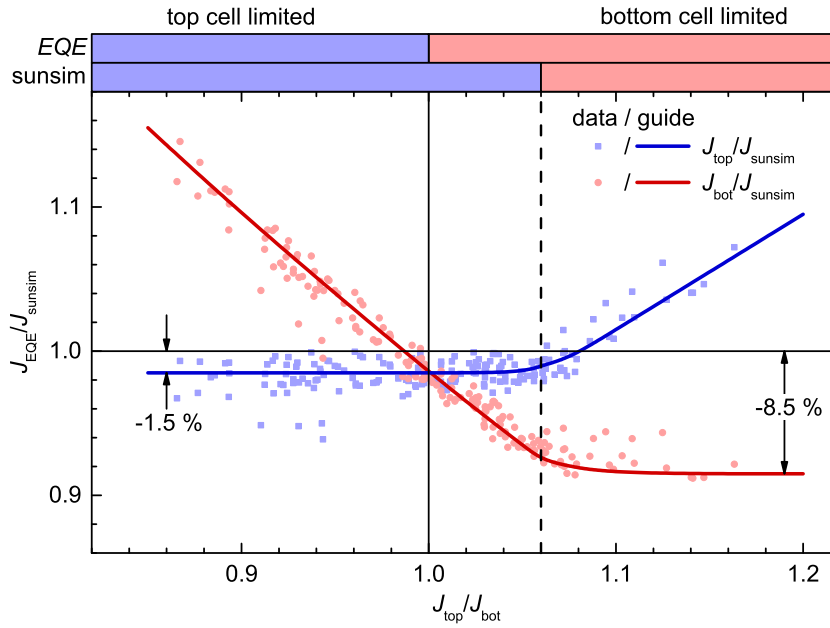


Figure 5.1: *EQE*-derived photo current density of the top and the bottom cell of a:Si-H/ μ c-Si:H tandem cells normalized to the short circuit current density obtained from *J-V* measurement as a function of the current limitation. The solid vertical line represents the matching point as obtained from the *EQE* data. The dashed vertical line indicates the matching point for the *J-V* measurement as implied by the onset of the slopes in the present data. The percentage values denote the approximate relative discrepancy of the *EQE*-derived photo current density for the top (left) and the bottom cell (right) with respect to the short circuit current density obtained from *J-V* measurement. Note, that cells with $FF < 68\%$ have been filtered out in order to limit the data to reasonably working cells. The blue and red lines are guides to the eye.

the solar simulator, where the whole $100 \times 100 \text{ mm}^2$ sample is illuminated (almost) over the full area. In fig. 5.2, the illumination scenario for the *EQE* measurement is illustrated in a schematic cross section of the cell. The drawing is not to scale. The lateral propagation of light within the thin layers can be neglected. As the cells commonly exhibit a textured TCO, part of the light is reflected to oblique angles. Due to the random topography not only the light transmitted to the Si, but also the diffusely reflected portion exhibits a continuous angular distribution. Hence, part of it traverses laterally within the rather thick front glass due to total internal reflection at the glass-air interface. This part of the light is trapped in the glass.

The remainder will be ordinarily reflected or transmitted according to FRESNEL's equations and hence also traverse laterally or contribute to the diffuse cell reflection, respectively. Assuming $n_{\text{glass}} = 1.5$, the critical angle for total internal reflection at the glass-air interface is $\varphi_{\text{crit.}} = 41.8^\circ$. Thus, for a glass thickness of 3.2 mm the light subjected to total internal reflection at least traverses $2 \times 3.2 \text{ mm} / \tan(\varphi_{\text{crit.}}) = 7.2 \text{ mm}$ before it reaches the glass/TCO interface again. As a consequence, a reasonable portion of the back-scattered light is absorbed in the Si outside the active cell area, where it does not contribute to the measured photo

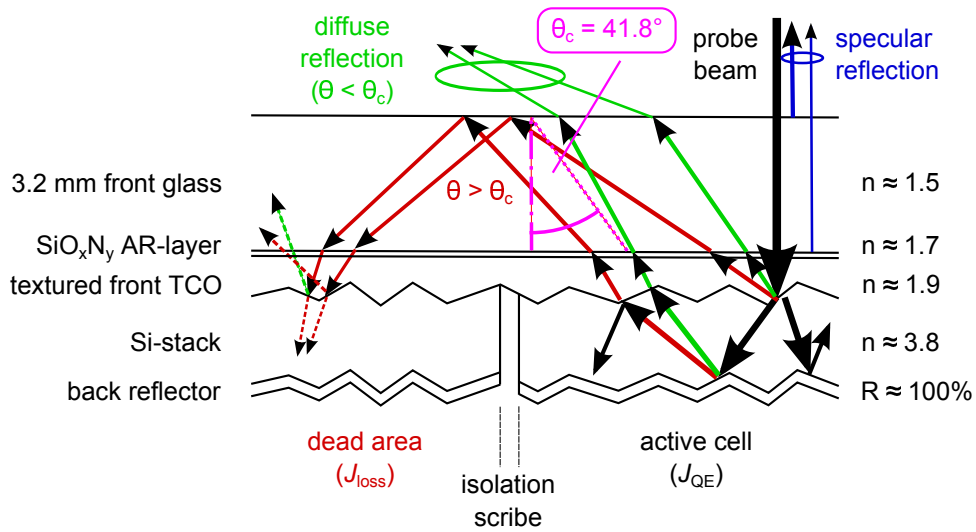


Figure 5.2: Illustration of the optical collection losses related to small spot illumination. The drawing shows a cell cross section including the isolation cut defining the cell area and the light paths relevant for the optical losses. Part of the light is reflected to oblique angles and, by multiple reflection, traverses laterally within the front glass before being partially absorbed in the Si-stack outside the active cell area, where it does not contribute to the measured photo current. This is accompanied by a diffuse cell reflection, whereas the reflection at the flat air/glass and glass/TCO interface leads to specular reflection.

current.

This effect can lead to a systematic underestimation of the photo current derived from the EQE measurement. In particular the use of rather thick front glass and the incorporation of strong light scattering, i.e. good light trapping, should promote losses in the determined photo current.

5.3 The Concentric Cell Experiment

To estimate the consequences of this effect, an experiment with concentric cells deposited onto a textured ZnO:Al, exhibiting rather strong light scattering abilities, was conducted. For this purpose, concentric square shaped cells with different dimensions were created on a $10 \times 10 \text{ cm}^2$ sample by laser scribing. The individual segments were subsequently electrically connected to each other between each EQE measurement. The resulting EQE data is presented in fig. 5.3 a) together with the corresponding AM1.5g current densities and the total cell absorptance. Figure 5.3 b) presents the corresponding relative differences in the summed EQE with respect to the data of the standard $1 \times 1 \text{ cm}^2$ cell. It also includes a sketch of the sample design. The measured EQE systematically increases with cell area throughout the whole wavelength range. With respect to spectral distribution, the relative gain (fig. 5.3 b)) remains almost constant for $\lambda < 700 \text{ nm}$ before it increases with wavelength until $\lambda \approx 800 \text{ nm}$ to reach a plateau again above that wavelength. According to the scenario depicted in fig. 5.2, the diffuse cell reflection should, to a certain extent, correlate with the

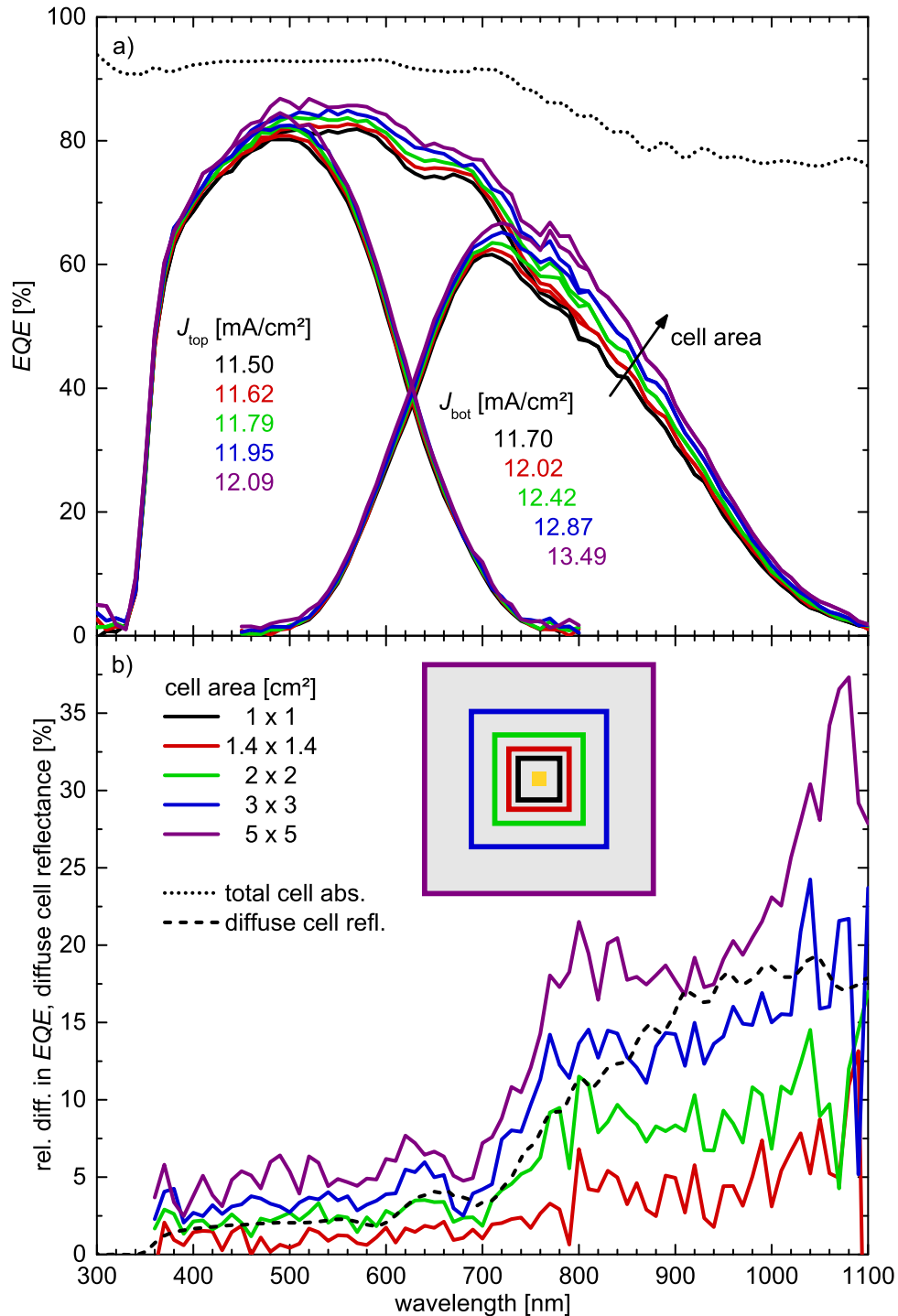


Figure 5.3: a) EQE of concentric a-Si:H/μc-Si-H tandem cells with different cell dimensions deposited onto a strongly light scattering textured ZnO:Al substrate. The numbers indicate the derived current densities. The font color corresponds to the curve color. The total cell absorptance (black dotted line) is also presented. b) Relative difference of the summed EQE with respect to the data of the 1 × 1 cm² standard-sized cell. The black dashed line shows the diffuse reflectance of the cell. The corresponding sample design is depicted by the concentric squares (roughly to scale). The line color matches the corresponding EQE data. The inner yellow square represents the monochromatic probe beam.

gain for larger cell areas. Therefore, the diffuse cell reflection was also added to fig. 5.3 b). Indeed, below $\lambda \approx 800$ nm the general trend with wavelength is very similar for the relative gain in EQE and the diffuse cell reflectance. The increase in relative EQE gain and diffuse reflection for $\lambda > 700$ nm is induced by the diminishing absorption in the Si for longer wavelengths, i.e., the light reflected at the back reflector is no longer fully absorbed in the Si and starts contributing to the light being diffusely back reflected to the glass-air interface. Above 800 nm, the diffuse reflection further increases, whereas the relative gain in EQE saturates due to the decreasing utilization of the laterally traversed light, i.e. reducing EQE .

As presented in fig. 5.4, the current density, J_{QE} , derived from the EQE data (eq. (2.49)), evolves with the cell area, whereas, in accordance with the relative gains in EQE , the increase is lower for the top cell compared to the bottom cell. For the biggest cell area (5×5 cm²) it amounts to 0.59 and 1.79 mA/cm², respectively. An asymptotic fit has been applied to the experimental data to estimate the saturation level of the increase in J_{QE} . The fit results suggest that for the top cell, the losses due to lateral light propagation are reasonably reduced for a cell size of 5×5 cm², whereas no significant saturation could be found for the bottom cell current density. However, due to the limited precision of the EQE measurement, especially for

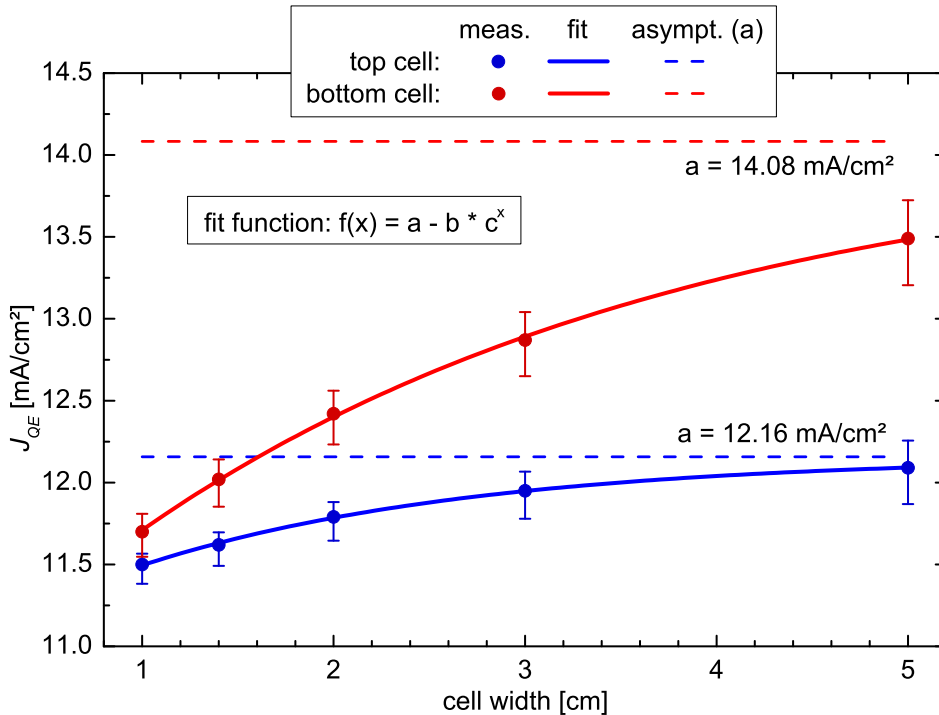


Figure 5.4: a) J_{QE} for the top cell (blue) and the bottom cell (red) of concentric a-Si:H/ μ c-Si:H tandem cells with different cell dimensions deposited onto a strongly light scattering textured ZnO:Al substrate as a function of cell width. The values were derived from the EQE data shown in fig. 5.3 a) (symbols) and fitted to an asymptotic function ($f(x) = a - b \cdot c^x$, full line). The asymptotic value, a , is represented by the dotted line.

the larger sized cells²⁷ the fit results, particularly the asymptotic value need to be interpreted with care.

Using large cell dimensions noticeably reduced the current density loss but is undesirable for both *EQE* measurement and *J-V* characterization, since the measurement noise scales with cell area and the resistive losses in the TCO would increase, respectively. Moreover, it is hard to quantify these losses with that method. A reduction of the glass thickness would also be beneficial, since the lateral propagation of light in the glass scales linearly with its thickness. But, from a practical point of view a reduction of the glass thickness is no option for many of the substrate types used at PVcomB.

5.4 The Large Area Setup

Another way to avoid the underestimation of photo current density is to use a large-area monochromatic probe beam. This is somehow analogous to using small spot probe beam and a large cell, whereas the problems of increasing measurement noise and resistive loss are avoided. Unfortunately, this can not be realized with a grating monochromator setup. Either the irradiance would be too low or the spectral line width too wide. Therefore, *QE* measurement setups with large-area illumination are usually fitted with several optical narrow band pass filters instead. Figure 5.5 shows the *EQE* data of $1 \times 1 \text{ cm}^2$ -sized a-Si:H/ $\mu\text{c-Si-H}$ tandem cells obtained with the previously described small spot setup and such a large area setup²⁸.

Four different front textures have been used for the cells. Without going into detail at this point, they exhibit significantly different surface morphologies: (i) a non-textured, (ii) a moderately textured and (iii) a strongly textured ZnO:Al film on planar glass, and (iv) a ZnO:Al coated textured glass substrate. Substrate (iii) exhibits the same texture as the ZnO:Al used as front contact for the concentric cell experiment described in sec. 5.3. The inset of fig. 5.5 shows the difference of the corresponding current densities ($J_{\text{QE}}^{\text{large}} - J_{\text{QE}}^{\text{small}}$) for the top cell and the bottom cell. Both values increase for stronger texture of the ZnO:Al, whereas the difference is generally higher for bottom cell current density. This finding proves the model for the lateral propagation of back-scattered light within the front glass: increasing texture leads to increasing light trapping both in the Si and in the glass.

The cell on textured glass shows the highest difference in J_{QE} of the top cell and also a rather large difference for the bottom cell. The reasons for that are not in focus for now, but will be discussed in a very similar context in sec. 6.5. The cell grown on the non-textured ZnO:Al exhibits strong oscillations visible in the *EQE* data of the small spot measurement

²⁷The precision was estimated to scale with the cell area. This is a sound assumption since the noise, i.e. the bias current, scales with the cell area.

²⁸For the large area measurements a home-built setup at IEK-5 Photoltaik, Forschungszentrum Jülich was used. The measurements were carried out by Christoph Zahren.

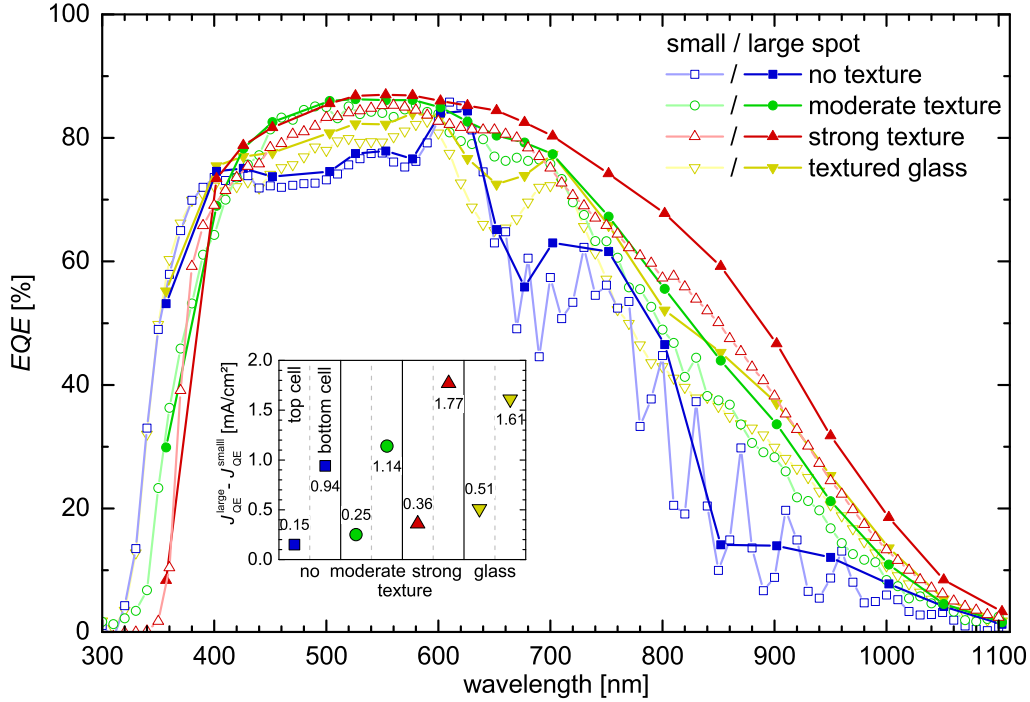


Figure 5.5: Summed EQE data of $1 \times 1 \text{ cm}^2$ -sized $a\text{-Si:H}/\mu\text{c-Si-H}$ tandem cells derived from a small beam (light lines, open symbols) and a large area (dark lines, full symbols) setup for different front textures: non (blue, \square \blacksquare), moderately (green, \bullet \circ) and strongly textured ZnO:Al (red, \triangle \blacktriangle) on planar glass, and ZnO:Al coated textured glass (yellow, ∇ \blacktriangledown). The symbols represent the sampling points. For the sake of clarity, the particular EQE data of the top cell and the bottom cell is not presented. The inset shows the absolute difference in the corresponding current density, $J_{QE}^{\text{large}} - J_{QE}^{\text{small}}$, for the top cell and the bottom cell, and the different front textures. The numbers next to the data points denote the values of the differences.

above $\lambda = 650 \text{ nm}$. They occur due to interference effects in the Si-stack. Anyhow, these oscillations are very likely also present for the large area irradiation, but can not be resolved by the system due to the limited number of sampling points, i.e. narrow band pass filters. Thus the value of the related J_{QE} are not that reliable, since the sampling points could by chance predominantly coincide either with the maxima or minima of the oscillations. The former seems to happen in the present case for $\lambda = 690 \dots 800 \text{ nm}$, which is why the difference in J_{QE} for the bottom cell on the non-textured ZnO:Al substrate is very likely overestimated. For the same reason (sparsely distributed sampling points) J_{QE} derived from the large area measurement is slightly underestimated at the short wavelength onset for all textures. Bearing this in mind, the differences in J_{QE} for the cells on the strongly textured ZnO:Al substrate match the gain achieved with the same ZnO:Al texture in the concentric cell experiment for going from $1 \times 1 \text{ cm}^2$ to $5 \times 5 \text{ cm}^2$ cell area.

The experiments demonstrated the presence of a systematic loss in the EQE determined

from $1 \times 1 \text{ cm}^2$ -sized cells with the available small spot setup. The effect could be related to lateral propagation of back-scattered light within the front glass. Hence, the loss scales to some extent with the light trapping ability of the front texture. For strong light scattering the losses in J_{QE} of an a-Si:H/ $\mu\text{c-Si:H}$ tandem cell amount to about 0.5 and 1.8 mA/cm² for the top cell and the bottom cell, respectively. Of course, the exact mechanism behind that phenomenon is much more complex and like for light trapping within the active layers, it is hard to predict the amount of loss (or gain) in terms of current density. In particular, a correlation with a coarse classification of the surface texture as made above is far from being universal. However, the four different textures used for the comparison of the small spot and the large area *EQE* setup are representative of the majority of the textures applied to cells in this thesis. Therefore, when discussing absolute *EQE* values or derived current densities we will refer to the results of these experiments²⁹.

²⁹Unless otherwise stated, there will be no corrections of any results.

6 Application of annealed ZnO:Al to a-Si:H/ μ c-Si:H Solar Cells

In sec. 4 the annealing of ZnO:Al layers was introduced as a versatile method to improve and tailor the opto-electronic properties of ZnO:Al layers. Besides a discussion of the different mechanism incorporated in terms of electronic transport and doping, the effect of different annealing procedures on the macroscopic film properties was also investigated. This section is dedicated to the utilization of annealed ZnO:Al as front electrode in a-Si:H/ μ c-Si:H based thin-film solar cells.

6.1 Annealing and the ZnO:Al/p-layer contact

The crucial role of the TCO/p-layer contact has been widely discussed for both Si-based thin-film [170–176] and hetero-junction [177–181] solar cells. At the interface a tunnel recombination junction between the n-type TCO and the p-type Si-layer is formed. For amorphous p-i-n cells and corresponding boron-doped a-SiC:H(p) layers grown onto SnO₂:F and ZnO:Al (or ZnO:Al coated SnO₂) the following investigations have been made by photo electron spectroscopy and cell preparation:

(i) The plasma used for p-layer deposition causes a hydrogen induced chemical reduction of the TCO. This is accompanied by the formation of SiO₂ at the TCO/p-layer interface, which is less pronounced for ZnO:Al. In the case of SnO₂:F the existence of reasonable amounts of elemental tin was observed, which leads to an increased parasitic absorption [182] and hence reduces the photo current density [183]. In contrast to that only small or no amounts of elemental zinc could be detected when ZnO:Al was exposed to the p-layer deposition or a pure hydrogen plasma, respectively. This is ascribed to the volatility of elemental zinc [170], but also to a high plasma stability of ZnO:Al with respect to SnO₂ [184]. Hence the high transmittance of the ZnO:Al is maintained upon cell deposition.

(ii) However, when ZnO:Al was used as front-electrode in combination with an a-SiC:H p-layer a reduction in FF and V_{OC} was observed. The effect was higher for lower deposition rates of the p-layer and vice versa, which was interpreted as a measure of hydrogen plasma impact on the ZnO:Al surface before being covered by the growing p-layer. This finding can be explained by the formation of hydrogen induced surface states leading to an electron accumulation layer and a downwards band bending at the ZnO:Al surface. This also yields a downwards bending of the bands in the p-layer and hence increases the width of the depletion zone, worsening the transport through the TCO/p-layer contact and as a consequence the FF and V_{OC} of the solar cell [183].

This issue can be overcome by introducing a μ c-Si:H buffer layer at the TCO/p-layer interface. Due to the higher doping-level and conductivity compared to a-Si:H or a-SiC:H the

depletion zone at the interface to ZnO:Al remains very narrow and the contact is thus less affected by the hydrogen induced downbending. As already explained in sec. 3.1.6 all cells used in this work make use of ZnO:Al front electrodes and a highly doped μ C-Si:H p-doped buffer layer. However, the ZnO:Al/p-layer contact remains a crucial interface, particular when the ZnO:Al was subjected to annealing procedures prior to cell deposition.

The cap-annealing as used in this work is adapted from solid phase crystallization of an e-beam evaporated a-Si precursor typically conducted at $T_{\text{ann}} = 600^\circ\text{C}$ for 24 hours in nitrogen atmosphere [12]. The ZnO:Al layer underneath was originally intended to be used as transparent electrode after crystallization and preparation of a poly-Si based thin-film cell [185]. Later on the impact of this process on a buried ZnO:Al/a-Si:H(n) interface was investigated by x-ray emission spectroscopy [173] and XPS [174, 175]. The formation of Si-O_x bonds at the expense of Zn-O was found, i.e. the ZnO:Al is chemically reduced at the interface. Furthermore, a redistribution of zinc and aluminum in the proximity of the interface was observed. To which extend this is related to the beneficial changes of the electronic bulk properties upon cap-annealing remains an open question. However, for our approach these findings point at a possible modification of the electronic properties at the ZnO:Al surface, which likely remains after the cap is removed, i.e. prior to cell deposition.

Before examining the effect of ZnO:Al annealing on cell performance the presence of a possible impact of the capping/decapping process by itself was investigated. To this end three nominally identical, textured ZnO:Al substrates were used as front electrodes in a-Si:H/ μ C-Si:H tandem cells. Prior to cell deposition sample A was exclusively exposed to the NF₃ plasma originally used to remove the 100 nm thick a-Si:H(i) capping layer. Sample B was capped and subsequently decapped in the regular manner, but without intermediate annealing. Sample C served as a non-treated reference. For all samples there was no additional treatment, i.e. no HCl-dip. Cell deposition was carried out a few days after this treatments, in particular the samples have been stored in air, which is also common for cell deposition on annealed ZnO:Al films. The corresponding J - V data, and the EQE and cell absorptance is presented in tab. 6.1 and fig. 6.1, respectively.

Generally, the data shows only minor differences between the samples. This is also valid when accounting for the J - V data of all 60 dot-cells measured per sample, i.e. there were no statistically significant differences. The slight variation in the EQE and $1-R$ data around 650 and 850 nm wavelength are likely due to small fluctuations in the surface morphology. However, plasma-related surface modifications would primarily affect small scaled features, which are linked to the short wavelength characteristic of the light distribution. Since the EQE as well as cell absorptance of all samples coincide for $\lambda < 600$ the plasma exposure can virtually be excluded as the reason for the slight differences at longer wavelength. More likely there is a small variation in the ZnO:Al deposition and/or texturing process. In summary

Table 6.1: J - V data of representative a:Si:H/ μ c-Si:H tandem cells deposited on wet-chemically textured ZnO:Al. Sample A was exclusively subjected to the NF_3 plasma originally used to remove the capping, i.e. no capping was applied, whereas sample B was capped and subsequently decapped in the original way, but without any annealing. Sample C serves as a reference and was kept untreated. All treatments were carried out prior to cell deposition.

sample	treatment	J_{SC} [mA/cm ²]	V_{OC} [mV]	FF [%]	eff. [%]
A	NF_3 plasma only	11.13	1413	73.2	11.5
B	capping/decapping	11.12	1415	73.3	11.5
C	none	11.11	1410	73.8	11.6

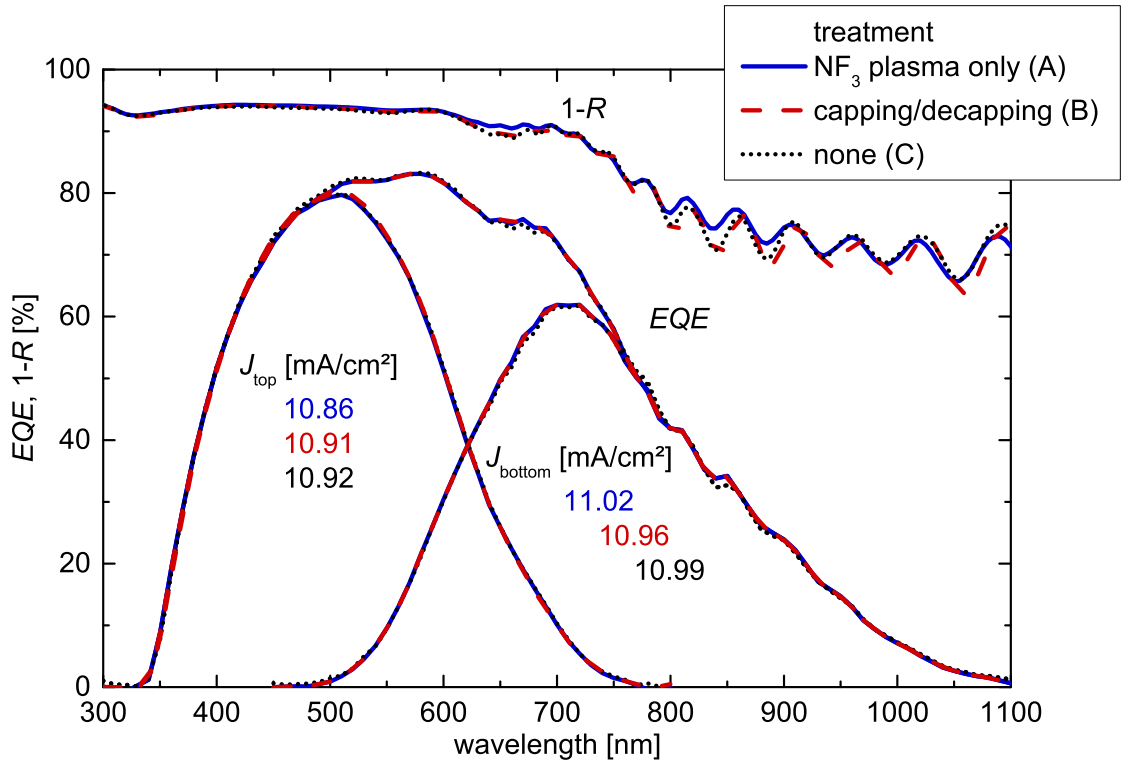


Figure 6.1: EQE and $1 - R$ data of representative a:Si:H/ μ c-Si:H tandem cells deposited on wet-chemically textured ZnO:Al. Sample A was exclusively subjected to the NF_3 plasma originally used to remove the capping, i.e. no capping was applied, whereas sample B was capped and subsequently decapped in the original way, but without any annealing. Sample C serves as a reference and was kept untreated. All treatments were carried out prior to cell deposition. The EQE derived photo current densities for the top and the bottom cell are also shown.

it is evident that there is no impact of the capping and/or decapping process on the cell performance. In a next experiment the effect of ZnO:Al annealing on the cell performance is investigated.

In tab. 6.2 the J - V data of a-Si:H/ μ C-Si:H tandem cells grown on 2-step annealed ZnO:Al are listed. After removing the a-Si:H(i)-capping sample B was subjected to a hydrogen plasma whereas sample C was immersed in 0.5% HCl for 5s. Sample A underwent no additional treatment and sample D comprises a non-annealed ZnO:Al layer added for reference. All samples have been wet-chemically surface textured (prior to annealing). The samples on annealed ZnO:Al (A to C) show an improvement in J_{SC} of 0.4 mA/cm² compared to sample D (non-annealed). This is a direct consequence of the intended suppression of parasitic absorption in the ZnO:Al.

However, a closer examination of the EQE and $1 - R$ data depicted in fig. 6.2 reveals some differences among the cells on annealed ZnO:Al not represented in the J - V data. The latter is ascribed to the short circuit current derived from J - V measurement being limited by the top cell in all cases(cf. sec. 3.2.4). Among the annealed samples the untreated one (A) shows the highest EQE for both top and bottom cell. The hydrogen plasma exposure clearly reduces the EQE virtually throughout the whole wavelength range, whereas its cell absorptance remains unchanged with respect to sample A. Thus, it exhibits an increased fraction of parasitic absorption. This is unexpected, since elemental zinc eventually formed should evaporate [170, 184, 186] and the accumulation of any other species is unlikely. A possible reason could be re-deposition of residual Si originating from the chamber walls of the PECVD reactor. Though, the chamber has been plasma-cleaned prior to the experiment, this can not be excluded. The HCl-dip on the other hand induces only small changes which can be observed in both EQE and $1 - R$, hence indicating minor modifications of the surface texture-related light-coupling(/-trapping) properties. This is plausible, since the dip etches the surface of the ZnO:Al. To further reduce such unwanted effects on the surface texture the HCl-dip was carried out in 0.1% HCl (10s) for future experiments.

Beside these optical differences the J - V data presented in tab. 6.2 also shows different electrical performance of the cells with respect to the treatment. Without any treatment after decapping (A) FF and V_{OC} are lower compared to the non-annealed reference (D). Both findings are even more pronounced after H-plasma exposure (B). This is somehow similar to the deteriorated FF and V_{OC} Kubon *et al.* found when switching from SnO₂ to ZnO:Al coated SnO₂ substrates [183]. However, remember that our samples already include a highly doped μ C-Si(p) buffer layer at the ZnO:Al/p-layer interface to mitigate this original issue. The effect of cap-annealing on the interfacial composition at the ZnO:Al/p-layer contact after removal of the original capping and deposition of the p-layer has not yet been investigated in such a detailed manner. Thus, the root cause for the deteriorated electrical performance in our cells

Table 6.2: J - V data of representative a:Si:H/ μ c-Si:H tandem cells deposited on wet-chemically textured ZnO:Al. Sample A to C comprise 2-step annealed ZnO:Al substrates, sample D serves as a reference grown on non-annealed ZnO:Al. After cap-removal sample A was left unchanged, sample B was exposed to a hydrogen plasma and sample C was immersed in 0.5% HCl for 5 s prior to cell deposition.

sample	treatment after decapping	J_{SC} [mA/cm ²]	V_{OC} [mV]	FF [%]	eff. [%]
A	none	11.8	1391	68.4	11.2
B	H-plasma	11.8	1380	65.1	10.6
C	HCl-dip	11.8	1434	71.1	12.1
D	reference	11.4	1413	70.6	11.4

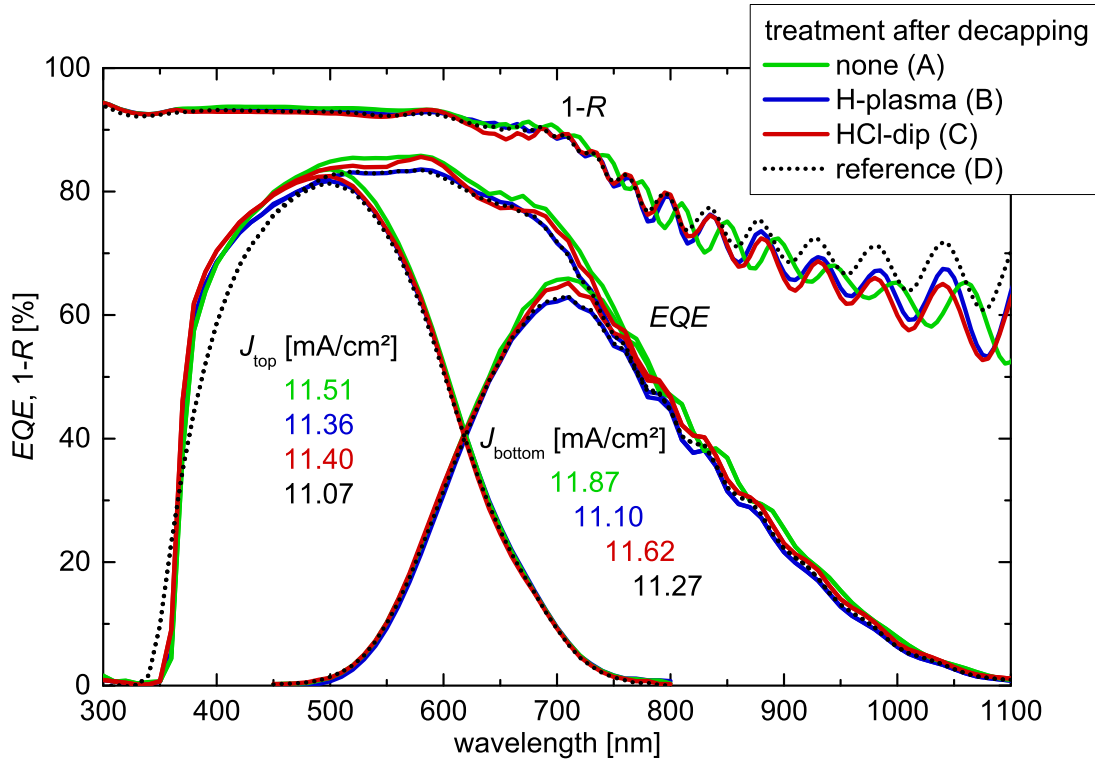


Figure 6.2: EQE and $1 - R$ data of representative a:Si:H/ μ c-Si:H tandem cells deposited on wet-chemically textured ZnO:Al. Sample A to C comprise 2-step annealed ZnO:Al substrates, sample D serves as a reference grown on non-annealed ZnO:Al. After cap-removal sample A was left unchanged, sample B was exposed to a hydrogen plasma and sample C was immersed in 0.5% HCl for 5 s prior to cell deposition. The EQE derived photo current densities for the top and the bottom cell are also shown.

remains subjected to speculation.

In both cases (A) and (B) the beneficial increase in short circuit current is overcompensated by the inferior electrical cell performance. The sample subjected to the HCl-dip (C) on the other hand even shows improved FF and V_{OC} compared to the non-annealed reference sample(D). First, this evidences that the bad electrical performance of sample (A) and (B) are no bulk effects of the ZnO:Al but very likely related to the ZnO:Al/p-layer interface. Moreover, the HCl-dip (except for its duration) is identical to the texturing step all samples, i.e. also sample D, have been subjected to. Hence, the improved FF and V_{OC} seems to be related to modifications in the ZnO:Al bulk upon annealing.

In summary these findings point at the cap-annealing step as the cause for the beneficial modifications of the ZnO:Al/p-layer contact. Moreover, this was observed for cells grown on both cap-annealed and 2-step annealed ZnO:Al exhibiting a significantly lower and higher carrier concentration (≈ 1.5 and $\approx 5 \cdot 10^{20} \text{ cm}^{-3}$), respectively, compared to the non-annealed state ($\approx 3 \cdot 10^{20} \text{ cm}^{-3}$). This again emphasizes an investigation of the electronic states at the interface between annealed ZnO:Al (with and without HCl-dip) and the μ C-Si:H(p) buffer layer.

6.2 Improving the opto-electronic Properties of conventional ZnO:Al Layers

The data presented in this section has already been published in ref. [187].

In sec. 4 the versatile opportunities of thermal treatments have been examined. For application to solar cells the first approach was to optimize the opto-electronic properties of conventional ZnO:Al films, i.e. texture-etched films with an as-deposited film thickness of $d \approx 800 \text{ nm}$ deposited on float glass. As these films originally have been designed to serve as front-electrode for a-Si:H/ μ C-Si:H tandem cells they already exhibit a sufficiently low sheet resistance ($R_S \approx 12 \Omega$) and a proper light trapping both after being texture-etched. Therefore, the strategy with these films is to maximize transparency while maintaining sheet resistance, i.e. resistivity.

This is achieved by maximizing the mobility and accordingly decreasing the charge carrier concentration (cf. eq. (2.9)). To this end texture etched industrial ZnO:Al films have been 2-step annealed. Both the thermal degradation and the subsequent cap-annealing were carried out at 500°C for 6 h. Recall that this is the maximum temperature applicable to the float glass. Table 6.3 shows the electronic properties of corresponding films, which were not subjected to the texture-etching in order to ease the opto-electronic characterization. The optical properties of these films are presented in fig. 6.3.

The thermal treatment shows the behavior already expected from the previously presented experiments. The first annealing without capping yields a degradation of both the charge

Table 6.3: Electronic properties, derived from Hall-measurements, of 816 nm thick, non-texturized industrial ZnO:Al for different annealing states.

annealing state	$n_{e,\text{Hall}}$ 10^{20} cm^{-3}	μ_{Hall} $\frac{\text{cm}^2}{\text{Vs}}$	ρ_{Hall} $10^{-4} \Omega\text{cm}$
as-deposited	3.14	30	6.6
thermally degraded	0.30	8.1	260
2-step annealed	1.42	60	7.3

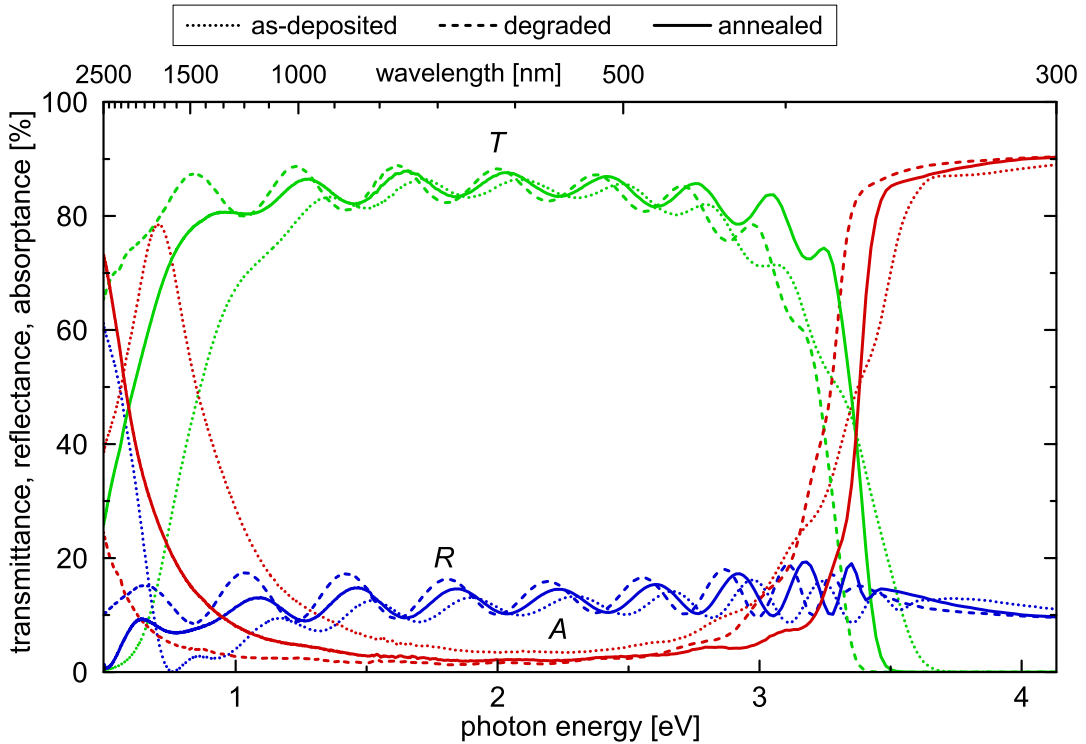


Figure 6.3: Transmittance T , reflectance R and absorbance A of 816 nm thick, non-texturized ZnO:Al layers on SiO_xN_y coated float glass for different annealing states as function of photon energy. A was calculated according to eq. (2.23)

carrier concentration and mobility whereas the subsequent second annealing under a-Si capping leads to an increase of the mobility (doubling from 30 to 60 $\frac{\text{cm}^2}{\text{Vs}}$) while the charge carrier concentration partially recovers with respect to the as-deposited state. As a consequence the resistivity of the ZnO:Al was maintained at $\rho \approx 7 \cdot 10^{-4} \Omega\text{cm}$ while its transparency was improved almost throughout the whole spectral range investigated. Only for photon energies $h\nu < 3.4\text{eV}$ the transparency is lower compared to the as-deposited state, which is due to the n_e related band gap shift dominated by the BURSTEIN-MOSS-effect (cf. sec. 2.1.5). For photon energies just below the ZnO:Al band gap the transparency increases due to curing of defect states whereas the reduced charge carrier density leads to an IR shift of the plasmonic absorption peak present in the NIR, hence increasing transparency. The reduction of the residual absorptance in the intermediate visual spectral range can be attributed to the latter two effects: The absorption at the band gap shows less tailing into the Vis and the peak of FCA is shifted further into the IR. Following from Drude-theory for constant charge carrier concentration a higher mobility leads to a decreased width and amplitude of the FCA peak. However, due to the simultaneous decrease in n_e and the related IR shift of the FCA peak in combination with the limited measurement range the FCA peak is not observable in the present case.

To evaluate how the annealing induced modification translate to solar cells, two identical sets of a-Si:H/ μ C-Si:H tandem cells have been prepared on equally texturized ZnO:Al samples in the as-deposited and 2-step annealed state. The whole thermal treatment was carried out after 75 s of texture etching in 0.5 wt.% HCl. The residual film thickness was approximately 650 nm yielding $R_S \approx 10.5$ and 12Ω for the as-deposited and 2-step annealed sample, respectively. Prior to Si-deposition another HCl-dip was applied to the annealed sample (cf. sec. 6.1).

The resulting external quantum efficiencies are presented in fig. 6.4 (a). For direct comparison the absorptance and transmittance of the corresponding non-textured ZnO:Al films (already presented in fig. 6.3 on a photon energy scale) are added in fig. 6.4 (b). Obviously the difference due to the 2-step annealing in *EQE* and cell reflectance coincide with those found for the corresponding ZnO:Al films. For the cell on annealed ZnO:Al (i) the UV onset of the *EQE* is slightly shifted to longer wavelength (band gap shift), (ii) the blue response is clearly increased (decreased sub band gap absorption), (iii) the *EQE* remains slightly higher in the Vis (lower residual absorptance) and (iv) the relative improvement in *EQE* again increases in the NIR (reduction of FCA). Since the ZnO:Al texture used here comprises a rather moderate light trapping (for the sake of high quality Si-growth) the latter is hard to see by eye. This observation is also supported by the reduced total cell absorption in the NIR for the cell on the annealed ZnO:Al, which generally indicates either less parasitic absorption in the ZnO:Al or a reduced light trapping. Both would lead to an increase of back reflected light out of the

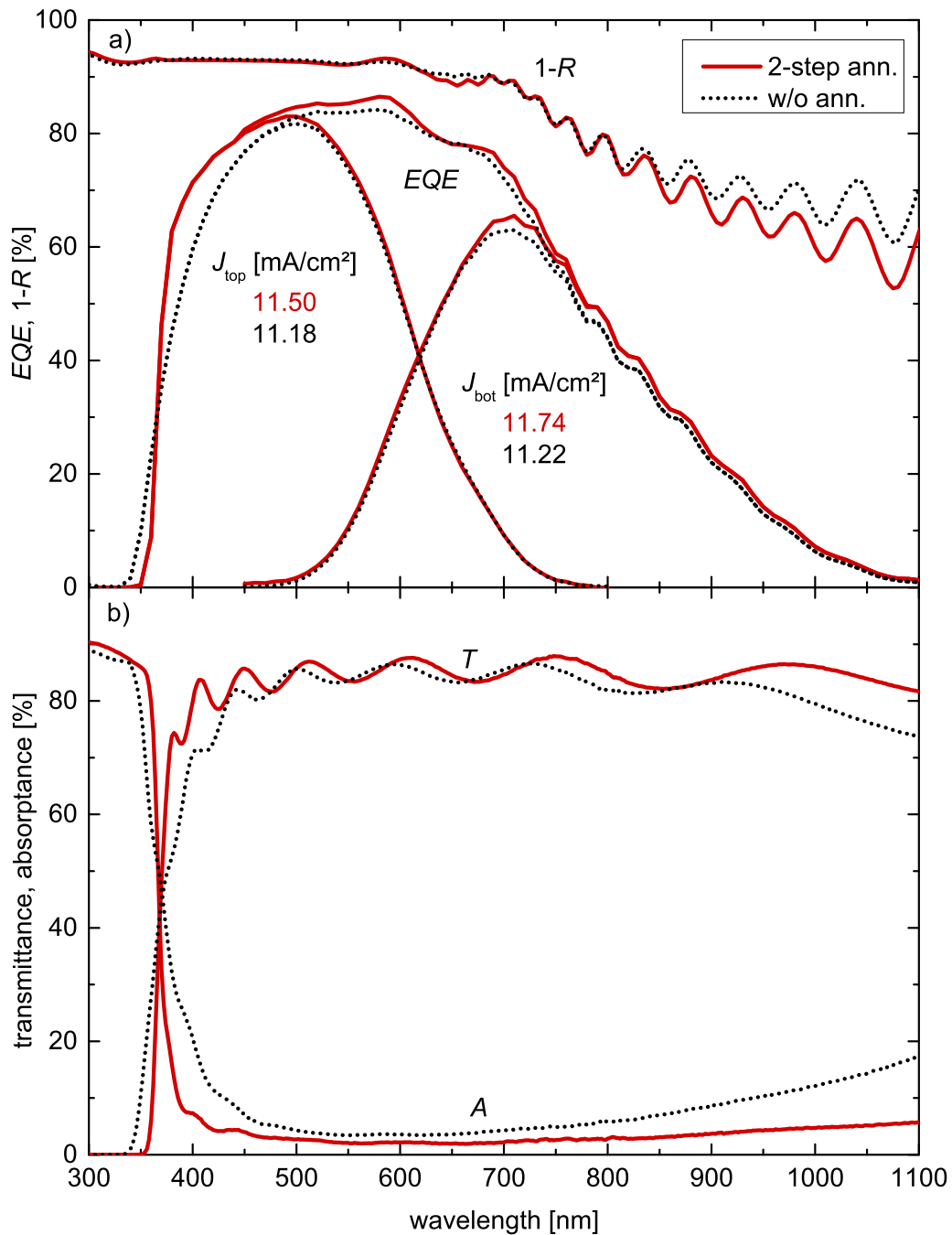


Figure 6.4: a) *EQE* and $1 - R$ of a:Si:H/ μ c-Si:H tandem cells on textured ZnO:Al in the as-deposited(dotted line) and 2-step annealed(solid line) state and b) transmittance T and absorbance A of the corresponding 816 nm thick, non-texturized ZnO:Al layers.

silicon for longer wavelength. However, the latter is very unlikely. First, the texturization for both ZnO:Al films was identical. Furthermore, less light trapping would lead to higher amplitudes of the Si-related NIR oscillations in $1 - R$ and EQE commonly accompanied by a phase shift and a slight reduction in their frequency. This becomes plausible by assuming the light trapping as a disturbance of the coherence for the Si-layer stack. The frequency reduction can be thought of as a consequence of decreased effective Si-thickness due to a lower average inclination angle. As none of those effects is observed here the reduced total cell absorptance is ascribed to reduced FCA. Referring to the EQE derived current densities, also presented in fig. 6.4, the 2-step annealing yields an improvement of 0.32 and 0.52 mA/cm² for the top and the bottom cell, respectively. This corresponds to a relative gain in total current density of 3.8 %.

The J - V data of the cells presented in fig. 6.4 are listed in tab. 6.4. As already found

Table 6.4: J - V parameters for cells on as-deposited and 2-step annealed, textured ZnO:Al films.

annealing	J_{SC}	V_{OC}	FF	η
state	mA/cm ⁻²	mV	%	%
as-deposited	11.44	1413	70.5	11.4
2-step annealed	11.85	1434	71.1	12.1

from the EQE results, the use of 2-step annealed ZnO:Al as front electrode leads to an increase in short circuit current density. Moreover, V_{OC} and FF improved by 21 mV and 0.6 %, respectively. The latter can be ascribed to higher current density mismatch of top and bottom cell for the cell on annealed ZnO:Al. From eq. (2.44) V_{OC} can be derived as a function of photo current (neglecting the contribution of finite R_p):

$$V_{OC} = \frac{nkT}{e} \ln \left(\frac{J_{ph}}{J_0} + 1 \right). \quad (6.1)$$

Thus, by assuming typical values of 10^{-11} and 10^{-6} mA/cm² for J_0 of an a-Si:H and μ C-Si:H cell [188] and further ascribing 900 mV and 513 mV to those cells, respectively, we get a photo current related increase of only about 2.3 mV for the V_{OC} of the present tandem cells due to annealing. Hence, the increase in V_{OC} observed experimentally can not be explained as a consequence of optical device improvement. A possible explanation for this effect was already discussed in sec. 6.1.

In conclusion the application of 2-step annealing to ready-made, textured ZnO:Al front electrodes resulted in an improved conversion efficiency of 12.1 %, for tandem cells grown on top, which is a relative gain of 6.1 %. This demonstrates the successful utilization of the annealing-induced benefits in the opto-electronic properties of ZnO:Al-layers for light

harvesting in a-Si:H/ μ c-Si:H tandem cells.

6.3 Thin, highly conductive ZnO:Al Electrodes

For the cells presented in sec. 6.2 the basic idea was to improve the transparency of a ready-made ZnO:Al film as much as possible while maintaining its sheet resistance. This was achieved by increasing the carrier mobility while reducing the carrier concentration accordingly. In this section the ZnO:Al layer thickness will be considered as an additional parameter. As demonstrated in sec. 4.2 the annealing can also be utilized to e.g. halve the thickness of a ZnO:Al layer while maintaining its sheet resistance. Recall that the annealing temperatures applied to achieve such a result are not applicable to float glasses (cf. tab. 3.1). However, even with this limitation there is plenty of room for improvement.

Among the remaining annealing treatments the most promising is a cap-annealing carried out at 500 °C/6 h without preceding thermal degradation. In spite of the increasing absorption coefficient related to such a treatment (cf. sec. 4.2) a reduction in film thickness should allow to compensate for this in terms of generated photo current density. Furthermore, it was the only remaining treatment that allows a reasonable increase in conductivity of the ZnO:Al layer. The annealing should allow to remarkably reduce the ZnO:Al layer thickness while the cell efficiency is at least maintained at a reasonably high level.

Figure 6.5 shows the EQE and $1 - R$ of two a-Si:H/ μ c-Si:H tandem cells. The initial film thickness and final sheet resistance of the ZnO:Al layers was about 550 nm/ 10Ω and 820 nm/ 11Ω for the thin cap-annealed and the standard ZnO:Al type, respectively. The EQE of the cell on thin annealed ZnO:Al shows a better blue response. Above $\lambda = 500$ nm the EQE data for both cells is rather similar. Compared to the cell on the standard ZnO:Al the total cell absorptance of the cell on thin annealed ZnO:Al shows some small oscillations with a rather large period and slightly lower values for $\lambda > 650$ nm. Since the EQE is not lower in this wavelength region, the latter indicates less parasitic absorption in the thin annealed ZnO:Al. A detailed discussion of such features is presented in sec. 6.5.3. For now it is sufficient to conclude that, beside the different blue response, there are only minor differences in the EQE of these two cells. As a result the photo current density of the cell on thin annealed ZnO:Al is slightly higher for both the top and bottom cell compared to the cell on standard ZnO:Al.

The $J-V$ data for these two cells before and after 168 h (1 week) of light soaking are presented in tab. 6.5. Like for the EQE and $1 - R$ data, there are only minor differences in the $J-V$ data of the two cells both initial and after light soaking. The only noteworthy difference is the slightly higher degradation in V_{OC} and FF found for the cell on the standard ZnO:Al electrode. Despite being small, the difference is statistically significant as it is also observed in the median of the 20 individual cells measured per ZnO:Al type. This could

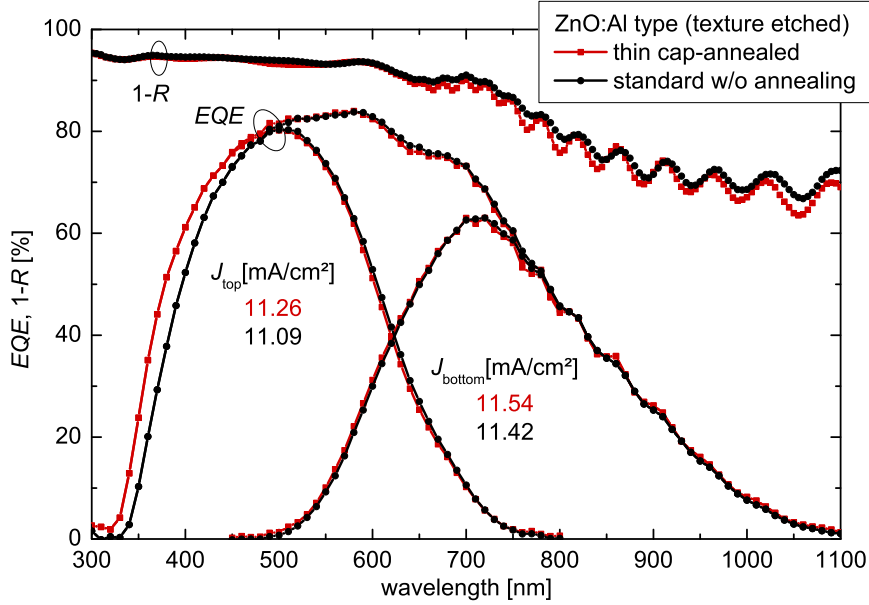


Figure 6.5: External quantum efficiency and total cell absorptance of an a-Si:H/ μ C-Si:H tandem cell on thin, textured, cap-annealed ZnO:Al (red line, squares) and on standard textured ZnO:Al (black line, circles). The *EQE* derived photo current densities for the top and the bottom cell are added to the plot. The font color corresponds to the particular line/symbol color.

Table 6.5: *J-V* parameters of an a-Si:H/ μ C-Si:H tandem cell on thin, textured, cap-annealed ZnO:Al and on standard textured ZnO:Al before/after 168 h of light soaking.

ZnO:Al	J_{SC}	V_{OC}	FF	η
type	mA/cm^{-2}	mV	%	%
thin cap-annealed	11.54/11.25	1405/1386	72.7/68.5	11.8/10.7
standard w/o annealing	11.31/11.05	1402/1373	72.8/67.5	11.5/10.2

be a hint on a slightly different surface topography of the two ZnO:Al types. For the FF it could also partially be related to the somewhat higher sheet resistance found for the standard ZnO:Al electrode. The former is very likely, as we will see in the next section.

The experiment showed, that thanks to the cap-annealing the as-grown ZnO:Al film thickness can be remarkably reduced, -33% in the present case, while the cell efficiency can be maintained at a reasonable level. Actually, there was even a slight improvement observed. Like in the previous section, where we improved the efficiency of cells by applying a 2-step annealing to one of two otherwise identical textured ZnO:Al electrodes, the present result again points at the benefit of the application of post-deposition ZnO:Al annealing. This time the benefit was in terms of a reduced ZnO:Al layer thickness. Hence, from an economical point of view this approach saves deposition time and reduces material consumption (provided that the annealing procedure can be realized in an economical manner on a large scale).

6.4 Limitations for textured ZnO:Al

Motivated by the good results achieved in a-Si:H/ μ c-Si:H tandem cells incorporating cap-annealing of thin, textured ZnO:Al substrates we tried to further reduce the thickness of the ZnO:Al layers while maintaining the cell efficiency. But in doing so we realized a severe limitation. Interestingly, it was not the sheet resistance, as one might expect, rather we found a limit in introducing an appropriate light trapping texture to the ZnO:Al surface upon wet-chemical etching.

As already discussed in sec. 4.2 the crystalline quality of sputtered ZnO:Al films evolves with film thickness originating from a nucleation layer with high disorder. This not only affects the electronic properties (already shown), but also the wet-chemical surface texture forming process. Figure 6.6 shows the height (a) and inclination distribution (b) as derived from statistical analysis of the particular AFM scans presented in (d-g) for wet-chemically textured ZnO:Al films on SiO_xN_y coated Corning glass; the haze is plotted in (c). The

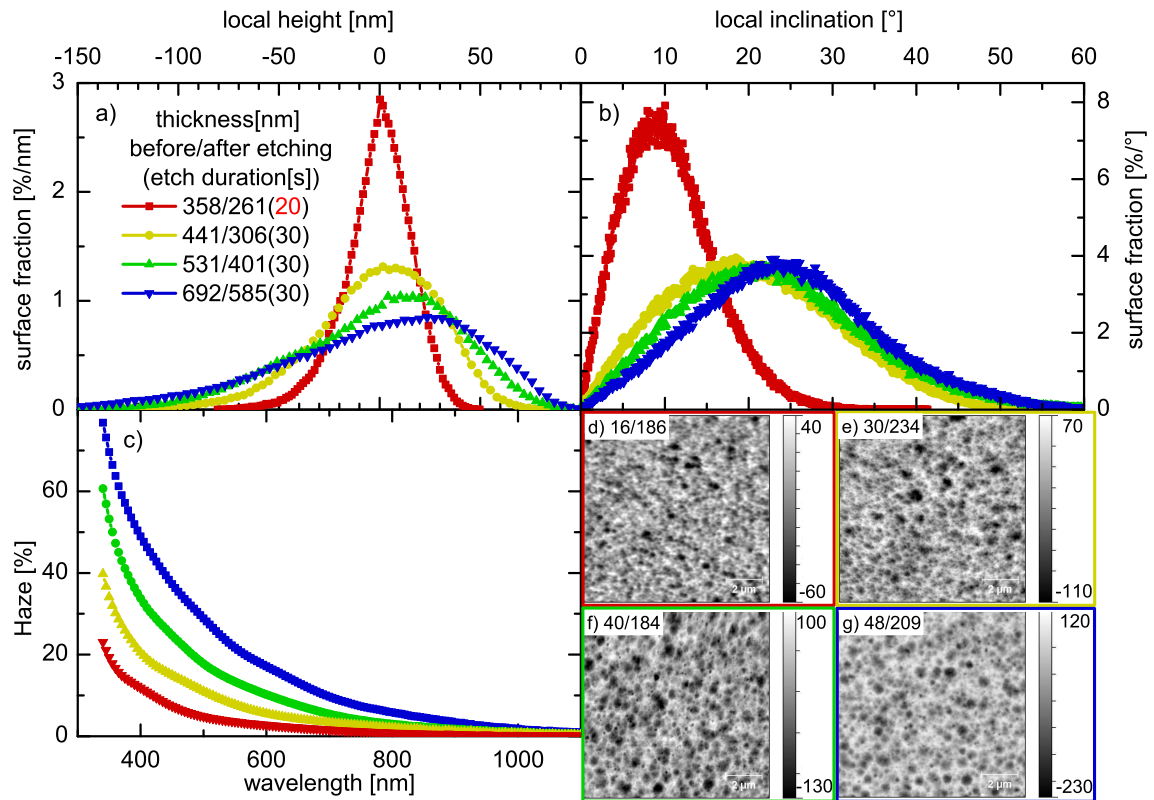


Figure 6.6: Statistical analysis of the surface topography of wet-chemically etched ZnO:Al films with different initial film thickness. (a) Local height distribution and (b) local inclination distribution as derived from the particular AFM-scans in (d-g), and (c) corresponding haze. The local height values are shifted relative to the particular mean value. The topographic scans in (d-g) are alphabetically arranged in ascending order with respect to the film thickness. The color of the frame corresponds to the line/symbol color. The inset numbers denote the particular RMS-roughness followed by the auto correlation length (both in nm). The numbers next to the false color scale represent its min/max values in nm. Note the different height scaling for different samples. The scan area was $10 \times 10 \mu\text{m}^2$.

samples had different initial ZnO:Al film thickness and originate from the sets, which were already used in the study presented in sec. 4.2. Since the induced surface texture hinders optical determination of the film thickness, it was derived from step profiler measurements instead, both before and after texturing. The wet-chemical etching was carried out in 0.5% HCl. The etch duration was originally set to 30 s. Since this led to inadequate sheet resistance as high as 54Ω for the sample set with the thinnest film thickness it was adapted to 20 s in this case. Regarding the statistical surface data presented in fig. 6.6 (a, b) both the height and the inclination show a broadening of the distribution with increasing film thickness. Moreover, the height distribution gets more asymmetric and ranges deeper. This asymmetry is typical (but not distinct) for the formation craters with no pronounced bottom area. The wider range of the height distribution for thicker films corresponds with the evolution of σ_{RMS} from 16 to 48 nm for the thinnest and thickest ZnO:Al film, respectively. The ACL on the other hand does not show any significant trend with film thickness, indicating similar lateral size of the predominant morphological features. This finding is also supported by the visual impression from the AFM scans: In all four images there are some distinct craters with an approximate diameter of 500 nm. The density (i.e. amount per area) of craters increases with film thickness, but their lateral size remains more or less constant. Besides those distinct deeper craters the remaining surface also shows reasonable roughness with more granular texture.

Following the etching model proposed by Hüpkes *et al.* [189] the formation of (crater-like) surface features is related to the compactness of the grain boundaries. The etching agent predominantly accesses disturbed grain boundaries. From these points of attack the distinct craters evolve with ongoing etching. In an initial survival of the fastest phase the craters grow in depth and diameter until they cover the whole surface. From this point on there is hardly any further evolution in the particular surface topography. As crystalline quality scales to a certain extent with ZnO:Al-film thickness, the density of attack points for the etching should increase for thinner ZnO:Al layers. Hence, the wet-chemical etching should generally yield smaller lateral feature size and reduced RMS-roughness. All these effects have indeed been observed by Owen [190] for ZnO:Al layers originating from a dynamic non-reactive RF magnetron sputter process incorporating ceramic ZnO targets with 1 wt.% Al_2O_3 . However, our ZnO:Al films differ in terms of this model. Apparently the density of attack points is not significantly affected by the initial film thickness, as indicated by the presence of laterally similar sized roughness features covering the full surface in all cases. Despite that, the RMS-roughness (but not the ACL) evolves with film thickness. This is again contrary to the above mentioned etching model. A possible explanation for this different behavior could be a generally lower compactness of our films. Following this assumption the grain boundaries are more exposed to the etch agent and the density of attack centers is rather high. This leads

to the generally observed roughness. The positions where craters are formed upon etching could be imagined as effective nano-holes allowing the etching agent to penetrate to a certain extent into the film. This assumption is supported by (i) a generally much smaller lateral feature size on etched ZnO:Al films, being around 400 nm in our case compared to 1...2 μm for those investigated by Hüpkes or Owen [189,190], hence pointing at the higher density of attack points and (ii) the observation of a moderate grain-like texture with lateral feature size around 50...100 nm modulated onto the apparent texture for our samples, indicating even higher density of attack points.

Irrespective of the microscopical origin the lower roughness of thinner ZnO:Al layers leads to a reduction of the haze throughout the whole wavelength range (fig. 6.6 c)). Since the general topography does not vary significantly between the samples, as indicated by similar ACL and visual impression of the AFM scans, the changes in haze should be a good qualitative measure for the changes in the light trapping ability of the ZnO:Al topography when implemented in solar cells.

Another effect connected to texture-etching of rather thin ZnO:Al layers is the higher relative increase in sheet resistance for the same removed layer thickness simply due to the larger ratio of removed to residual film thickness. As a consequence the target sheet resistance after texture etching is more sensitive to deviations in etch duration, i.e. the etching rate in terms of sheet resistance increases, making the etch process harder to control. This is further aggravated by the progressive deterioration of conductivity (cf. fig. 4.2, p. 52) and the increased etching rate observed for thinner ZnO:Al films at least for the material observed here. The latter being 3.57 and 4.85 nm/s for the thickest and thinnest sample presented in fig. 6.6, respectively.

All in all the introduction of light trapping via wet-chemical texturing of the ZnO:Al surface shows lacking effectiveness with decreasing (initial) ZnO:Al layer thickness. Thus, since the annealing procedure allows implementation of such thin ZnO:Al-layers in terms of opto-electronic properties (cf. sec. 4.2.24.2.4), the introduction of light trapping in a way circumventing ZnO:Al texturization would be very attractive.

6.5 Utilization of micro-textured Glass Substrates

The data presented in this section has partially already been published in ref. [191].

In sec. 6.4 the issue of deteriorated light trapping ability of thin, wet-chemically textured ZnO:Al films was presented. This finding led to the demand for alternative light trapping concepts. One of these concepts, among others (cf. sec. 2.2.4), is the incorporation of micro-textured glass substrates that will be presented in this section. The textured glass substrates have been realized and provided by *Berliner Glas*³⁰. The micro-texture is achieved by a multi-

³⁰Berliner Glas Surface Technology, Giengener Str. 16, 89428 Syrgenstein-Landshausen, Germany

step acid treatment based on classic inorganic fluorine chemistry. The texture is brought on to a conventional white glass ($d = 3.2$ mm) as presented in sec. 3.1.1. The process is carried out with batches of large glass sheets. It can hence easily be applied on an industrial scale. The details of the wet-chemical texturing are subjected to the intellectual property of *Berliner Glas* and can therefore not be published here.

First the surface topography and the growth as well as the opto-electronic properties of ZnO:Al layers on micro-textured glass will be discussed. Afterwards the implementation of thin, annealed ZnO:Al films on such substrates in a-Si:H/ μ c-Si:H tandem cells will be presented. The result are compared to reference devices incorporating the same ZnO:Al layer as well as conventionally rather thick, non-annealed, texture-etched ZnO:Al on planar glass. Thereby emphasis is placed on the light management in such devices.

The utilization of micro-textured glass basically changes the needs on the subsequently deposited ZnO:Al layer: Formation of an appropriate surface texture upon wet-chemical etching is no longer required. Thus, the ZnO:Al layer, i.e. its processing, can be further adapted with focus set to its opto-electronic properties. On the other hand the ZnO:Al growth on textured substrates could become an issue. However, in the following study the ZnO:Al deposition process was not varied. First, this allows better comparison of the different front texture systems and second, there was no need to adapt the process, since growth was reasonable well also on the rough glass substrate, as we will see in the following.

6.5.1 Surface morphology and ZnO:Al film growth

Figure 6.7 shows the surface topography of the micro-textured glass (a) without and (b) with ZnO:Al coating ($d \approx 260$ nm, non-texturized; incl. SiO_xN_y), and for reference (c) conventionally texture-etched ZnO:Al (already described as set A in sec. 4.3) with similar lateral feature size. The glass surface consists of well defined etching craters with a typical diameter around 800 nm. Additionally, some small plateaus (green marking) and grain- or particle-like regions (blue marking) can be observed. The former are very likely remaining portions of the original glass surface, which were not attacked by the glass texture etching due to some reason not known. Since the textured glass substrates have also undergone the cleaning process used for uncoated glasses (cf. sec. 3.1 the presence of loosely bound particles is very unlikely. Thus the grain-like features are very likely due to the glass texturing process. They did not constitute an issue throughout the whole cell processing. In fig. 6.7 (b) the blue marks exemplarily show regions where the ZnO:Al seems to cover such textures.

On the bare textured glass the particular craters have smooth walls and a bowl-like appearance. The latter is distinct compared to the texture-etched ZnO:Al, which shows commonly a rather V-shaped crater profile, as can also be seen from the line profiles depicted in fig. 6.8. As a consequence no distinct crater opening angle, like sometimes used as a

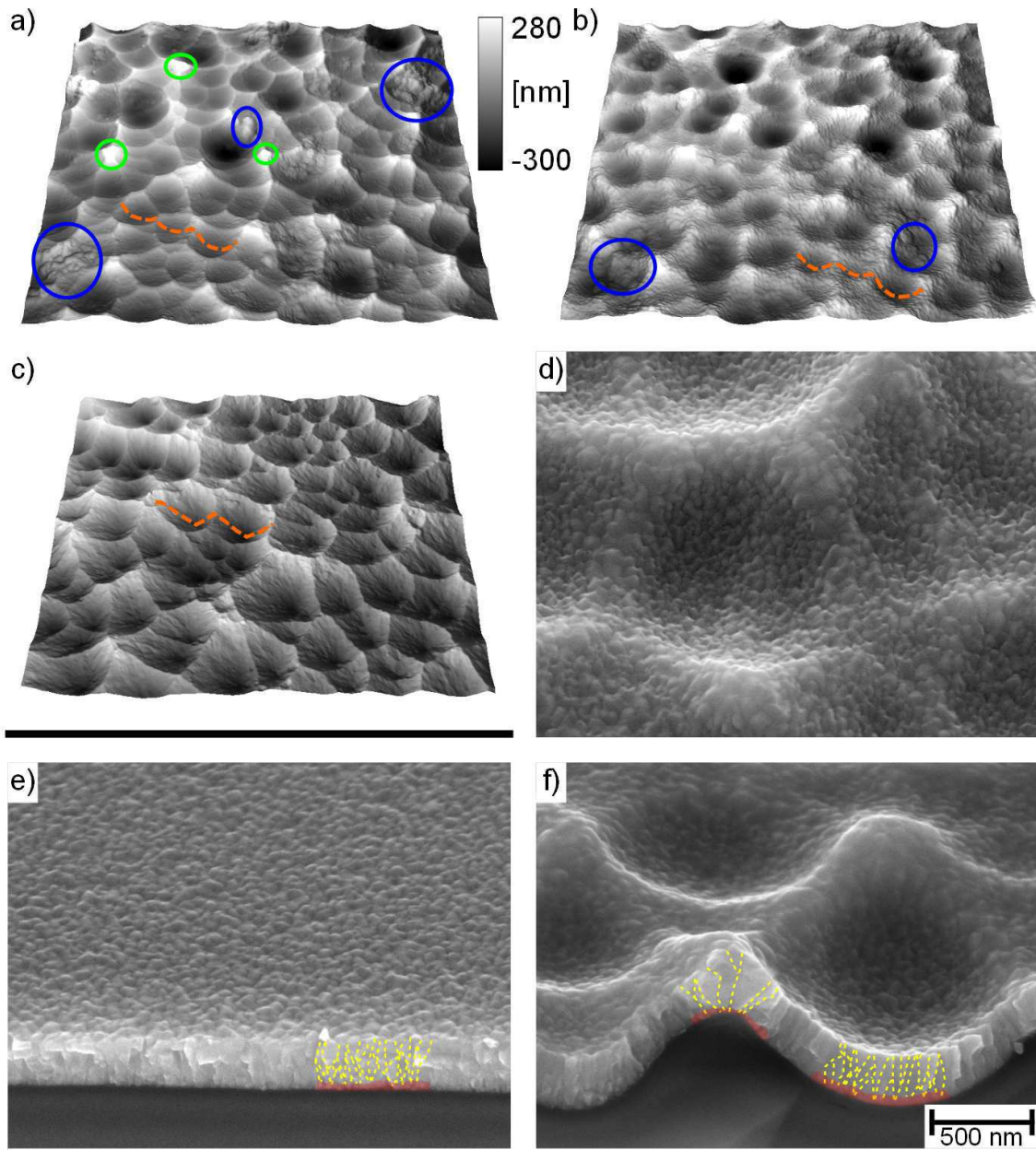


Figure 6.7: (a-c) Topographical AFM scans ($10 \times 10 \mu\text{m}$; 512×512 pixel) of the surface of micro-textured glass (a) without and (b) with ZnO:Al coating ($d \approx 260 \text{ nm}$, non-texturized; incl. SiO_xN_y), and for reference (c) conventionally texture-etched ZnO:Al (cf. sample set A in sec. 4.3). The scans are presented in a 3-D tilted view. The false color scale is identical for all three scans. The green, blue and orange markings indicate the position of residual plateaus, grain like textures (see text) and the line-profiles presented in fig. 6.8, respectively. (d-f) SEM images of the ZnO:Al-layers on micro-textured glass, (d) tilted top view and (f) tilted cross sectional as well as (e) tilted cross sectional view of the same ZnO:Al co-deposited on planar glass. All SEM images have the same magnification. The red shaded areas and yellow dashed lines indicate the nucleation layer and visible column boundaries, respectively (see text).

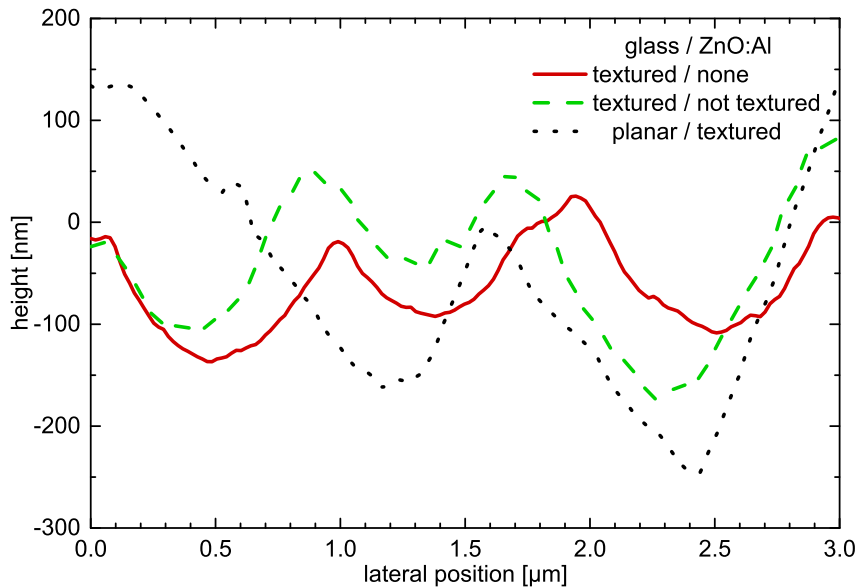


Figure 6.8: Line profile of the surface topography of micro-textured glass without (red solid line) and with ZnO:Al coating (green dashed line), and conventionally wet-chemically textured ZnO:Al on planar glass (black dotted line). The particular profiles were derived from the corresponding 2-D AFM-scans depicted in fig. 6.7 (indicated by the orange dashed lines).

derived property of textured TCOs, can be ascribed to these profiles. Compared to the textured ZnO:Al the apparent crater depth is lower for most of the craters on the textured glass. As can be seen from fig. 6.9 (a), this does neither lead to a narrowing of the height distribution nor to a reduction of σ_{RMS} , which is surprising at a first glance. The reason for this is of statistical nature and linked to the bowl-like crater form in combination with the presence of very few rather deep craters for the textured glass. The inclination distribution (b) on the other hand shows marked differences between those two: For the textured ZnO:Al a pronounced maximum is visible at an inclination of 19° , which shows a rather steep decay particular towards smaller angles. Most of the surface fraction belongs to the crater walls, which show a well defined inclination (V-shape) on the textured ZnO:Al. In contrast to this, there is no reasonably distinct inclination linked to the crater walls for the textured glass (bowl-shape). The presence of the ZnO:Al on top yields a moderate gain for higher values of the local heights and inclination for both at the expense of intermediate values. Due to the rather directional deposition characteristic of the sputter process and to shadowing effects during deposition the craters get indeed slightly narrower and effectively steeper, since the crater rims are subjected to a broadening. This can also be seen from comparing the corresponding profiles in fig. 6.8. Moreover, this should lead to a slight increase in crater depth, and hence σ_{RMS} . However, the increase observed from the experiment is hardly reliable from a statistical point of view.

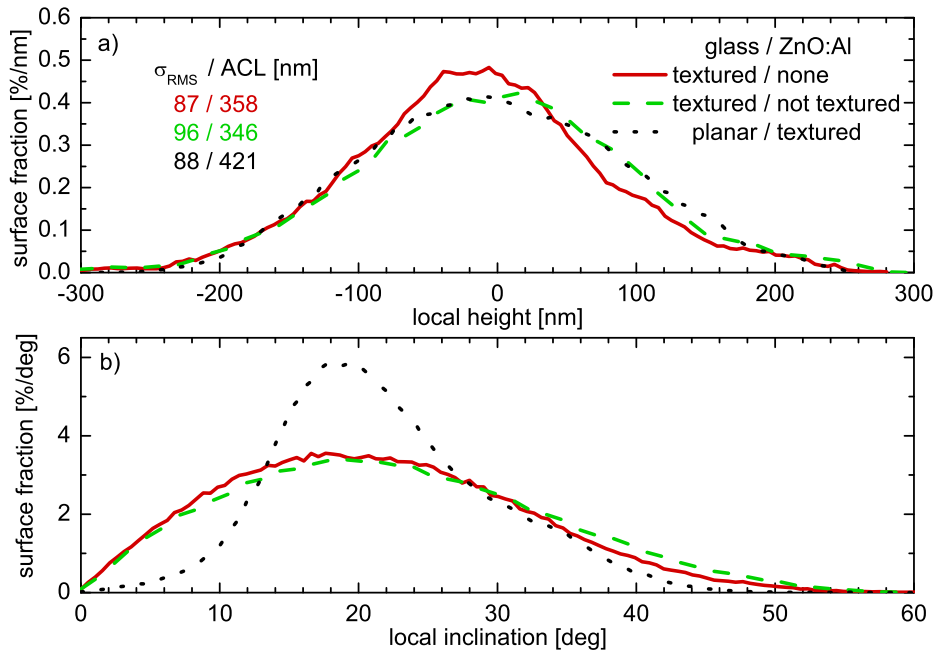


Figure 6.9: (a) Height and (b) inclination distribution for the surface topography of micro-textured glass without (red solid line) and with ZnO:Al coating (green dashed line), and conventionally wet-chemically textured ZnO:Al on planar glass (black dotted line). The data is derived from the corresponding AFM-scans presented in fig. 6.7. The local heights are given relative to the particular mean value. The values of the RMS-roughness (σ_{RMS} and auto correlation length (ACL) are added in (a). The font color corresponds to the line color.

The remaining sub-figures of Figure 6.7 (d-f) are dedicated to the ZnO:Al growth itself. They show SEM images of the as-deposited ZnO:Al films of about 260 nm thickness (including SiO_xN_y layer). All SEM images have the same magnification. Sub-figure (d) shows a tilted top view for growth on textured glass. A tilted cross sectional view is shown in (f) for this sample and (e) for the same ZnO:Al co-deposited on planar glass. Obviously, all films show an as-grown (non-intended) surface texture, which is common for sputtered, poly-crystalline ZnO:Al layers [9]. It comprises a rather small lateral feature size ($l \lesssim 100$ nm) and RMS-roughness ($\lesssim 5$ nm) not appropriate to introduce light scattering in the visible wavelength range (sub-wavelength sized), even in silicon with its high refractive index. The origin of this texture is well known and gets obvious from the cross sectional views in (e) and (f): After a certain film thickness the initially disorder growth (illustrated by the red shaded areas) turns in to a fiber textured growth regime. From there on the films show a predominantly columnar appearance (yellow dashed lines illustrate column boundaries) indicating the preferential [001]-directional crystalline orientation (cf. sec. 4.2.1). The top of each of those columns appears as one hill-like surface feature. Noticeable, the columns, as indicated by their visible boundaries do not represent a single crystal. Moreover, they typically consist of several crystals [192].

From sub-figures (d) and (f) it can be seen that the ZnO:Al layer nicely covers the micro-texture of the glass. The film thickness (normal to the local plane) increases from crater walls to valleys to rims (≈ 240 , 280 and $\lesssim 310$ nm, respectively); again a consequence of the predominantly directional deposition characteristic of the sputtering process³¹. The thickness of the film co-deposited on the planar glass (e) shows an intermediate value of ≈ 260 nm. This is in good accordance to the thickness of 268 nm as derived from step profiler measurements in this case.

Concerning the column orientation on the textured glass surface, it is apparently mainly determined by the local inclination of the substrate. The lateral column size follows the curvature of the surface, being larger at convex sites, i.e. the crater rims and slightly smaller at concave sites, i.e. the crater bottom, compared to non-curved sites, i.e. the crater walls. This effect is also well known and related to the growth mechanism of the ZnO:Al layer: After the nucleation process the columnar crystallites grow predominantly in (001)-directional orientation. Without any surface curvature neighboring columns just grow side by side and form a dense layer. For convex substrate curvature the crystallites need to expand laterally with growing film thickness in order to maintain a dense layer. In other words, the directional guidance normally experienced by neighboring crystallites is lost to a certain extent (scaling with the particular curvature). For concave curvature on the other hand neighboring columns increasingly compete with each other with evolving film thickness. This competition is generally accompanied by an increased crystal defect density. In extreme cases this can also lead to “hard” collision of growing crystallites leading to the formation of voids underneath.

A good experimental investigation and discussion of the growth of sputtered ZnO:Al on various, particular textured, model substrates can be found in the thesis of Greiner [47], particular in chapter 3. These experiments were conducted on ZnO:Al originating from a static, non-reactive RF-magnetron sputter process incorporating a ceramic ZnO target doped with 1 wt.% Al₂O₃. Despite the differing deposition technique, his findings support our observation concerning the growth of ZnO:Al layers on the textured substrate.

To conclude the observations of morphology and ZnO:Al growth, the micro-textured glass shows a crater-like topography with lateral crater dimensions and RMS-roughness similar to those of a specific conventionally texture-etched sputtered ZnO:Al, which is known to have very good light trapping properties in combination with an μ C-Si:H based absorber. Despite this similarity, the crater form is different; bowl-like for the glass and inverted cone like (V-shaped) for the ZnO:Al. This difference should be preferential for the material quality of silicon grown on top in order to realize a thin film solar cell (cf. sec. 2.2.3). The consequences of this difference for the light trapping in such devices will be discussed later.

³¹The film thicknesses given in parenthesis have been derived directly from the SEM image (corrected for the tilt).

ZnO:Al films grown on top of the textured glass form a dense layer with no obvious (visual) defects. The film thickness varies slightly for the different feature sites. The typical columnar growth was also observed. As expected, the columns are in principal aligned perpendicular to the local glass surface. This leads to a lateral size of the columns, being larger on top of the rims and slightly lower at the bottom of the craters.

6.5.2 Light scattering and opto-electronic properties of the ZnO:Al

The motivation for the incorporation of the micro-textured glass is the introduction of light trapping without the necessity to texture-etch the ZnO:Al layer. Therefore we will first briefly evaluate its light scattering ability in comparison to conventionally textured ZnO:Al layers on planar glass. Figure 6.10 shows haze and total transmittance of micro-textured glass with and without a ZnO:Al layer on top. The latter is the sample already presented in fig. 6.7

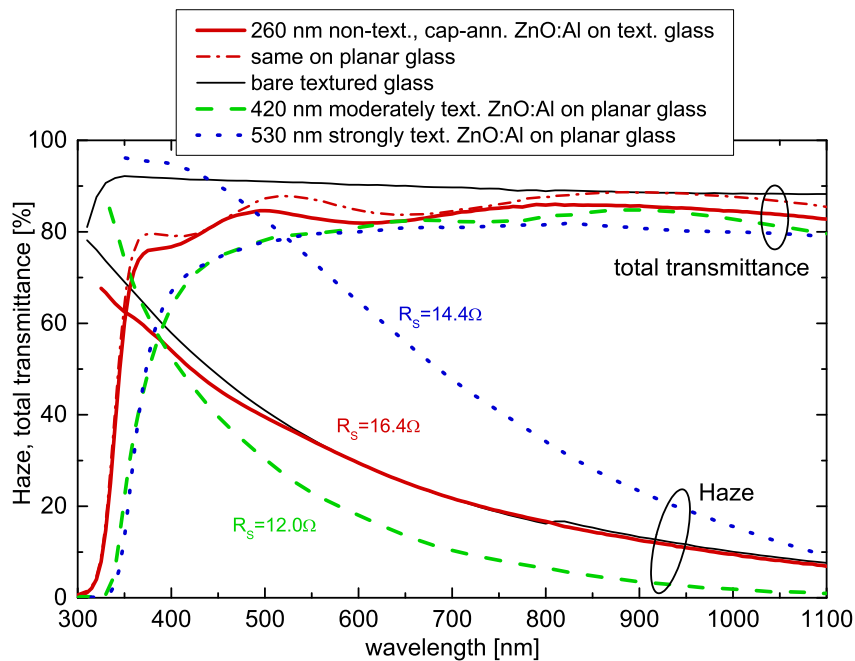


Figure 6.10: Haze and total transmittance of micro-textured glass and textured ZnO:Al layers on planar glass as a function of the wavelength. The plot includes the data for bare micro-textured glass (black line), the same coated with a 250 nm thick, non-texturized, cap-annealed (500 °C, 6 h) ZnO:Al layer (solid red line), the same ZnO:Al deposited on to planar glass (borofloat) and treated in the same manner (dash dotted red line), and a conventionally textured ZnO:Al layers on planar glass (white glass, dotted blue line). The topography of the particular samples has already been presented in fig. 6.7 (a), (b,d,f), (e) and (c), respectively. Additionally the plot shows the data of another conventionally texturized ZnO:Al layer on planar glass (dashed green line). This sample represents our standard front electrode. Despite the different thickness, the material is identical to that used for the coating of the micro-textured glass. The surface topography is very similar to that of the sample presented in fig. 6.6 (g). All samples containing a ZnO:Al layer also exhibit an intermediate SiO_xN_y layer. The value of the sheet resistance is also added to the plot for these samples.

(b,d,f), but after being subjected to a cap-annealing (500 °C, 6 h). The data is compared to those of the similarly textured ZnO:Al layer presented in fig. 6.7 and a thicker, textured, non-annealed version of the same ZnO:Al type used on the micro textured glass. The latter representing our standard front electrode.

The bare micro-textured glass shows a reasonable amount of haze with a decay towards longer wavelength, which is usually observed with such lateral feature dimensions. At the same time it exhibits the high transmittance of a typical white glass ($T \approx 92\%$) with a slight decrease towards longer wavelength. The latter is very likely related to higher absorptance, as the texture also introduces an internal light trapping within the glass itself.

The presence of the ZnO:Al layer (incl. SiO_xN_y) on top of the micro-texture does generally not affect the haze. Only for short wavelength ($\lambda < 550$ nm) a slight reduction can be observed. Compared to the two conventionally textured ZnO:Al layers on planar glass the haze obtained with the micro-textured glass is far below that of the textured ZnO:Al layer, which noteworthy comprises a similar lateral feature size and RMS-roughness (cf. fig. 6.7 and fig. 6.9 (a)), but outperforms that of our standard ZnO:Al front electrode. Both ZnO:Al-based textures show a stronger decay in haze towards longer wavelength. Thereby, the slope of the moderately textured sample shows a pronounced reduction with evolving wavelength, whereas that of the strongly textured ZnO:Al is rather constant. For $\lambda \gtrsim 400$ nm the haze is higher on the moderately textured standard ZnO:Al compared to the ZnO:Al coated micro-textured glass. For long wavelength on the other hand the latter approaches the curve of the strongly textured ZnO:Al surface.

The marked difference in haze for the strongly textured ZnO:Al and the micro-textured glass, which turned out to have a rather similar topography, at least in the commonly regarded quantities lateral feature size (or ACL) and σ_{RMS} (and even the height distribution itself) is one of the finest examples for the big influence of the actual shape of the topography on the light scattering properties of a surface topography. Furthermore, since both textures are obviously very different in terms of the resulting haze, the higher haze for the ZnO:Al based texture does not necessarily imply a better light trapping when implemented as front electrode in solar cells. This is vice versa also true for the rather low haze of the third, moderately textured standard ZnO:Al layer. We will come back to this circumstance in the course of this section.

Regarding the total transmittance of those three samples, thanks to the cap-annealing and the rather thin layer thickness the ZnO:Al coated micro-textured glass clearly outperforms the other two. The values for the sheet resistance of this three samples have also been added to the plot. Without concerning about the minor differences, which could be easily canceled out by adapting initial film thickness, etch duration or cap-annealing without changing the general optical differences shown here, all samples have a comparable sheet resistance reasonable for

application as front electrode in a-Si:H/ μ c-Si:H tandem solar cells.

To evaluate the impact of the micro-textured glass on the electronic properties of the ZnO:Al layers grown on top of that, a set of ZnO:Al films has been co-deposited on planar and micro-textured glass. The films are nominally identical to those introduced in fig. 6.7 (e) and (b,d,f), respectively. Table 6.6 shows the electronic properties for this samples after and before (in parenthesis) cap-annealing (500 °C/6 h) as derived from HALL-effect measurements. Since the determination of the ZnO:Al film thickness on micro textured glass is not straight forward, we will assume the film thickness to be equal to that measured for the film deposited on planar glass. Referring to the film thickness as derived from the SEM images (fig. 6.7 (e), (f)) this is a proper estimation. Note, that the determination of both μ_{Hall} and R_{S} does not depend on the film thickness.

Table 6.6: Electronic properties of thin ZnO:Al layers on micro-textured and planar glass. The values after/before cap-annealing are placed before/in the parenthesis, respectively. The cap-annealing was carried out at 500 °C for 6 h.

glass	$n_{\text{e,Hall}}$	μ_{Hall}	ρ_{Hall}	R_{S}	$d_{\text{ZnO:Al}}$
surface	10^{20} cm^{-3}	$\frac{\text{cm}^2}{\text{Vs}}$	$10^{-4} \Omega\text{cm}$	Ω	nm
textured	5.6(3.7)	23(26)	4.85(6.41)	19.5(25.6)	250*
planar	5.5(3.8)	32(29)	3.60(5.69)	14.5(22.7)	250

* The same thickness as determined for the samples on planar glass has been assumed for calculation.

The charge carrier density in the ZnO:Al is not significantly affected by the choice of the substrate both before and after cap-annealing. As expected from the results presented in sec. 4.2.2 it increases upon cap-annealing. The mobility on the other hand is initially slightly lower for the film on micro-textured glass and even decreases upon cap-annealing, whereas the film on planar glass shows the expected slight increase in mobility. With respect to resistivity (and sheet resistance) the drop in mobility is still overcompensated by the gain in charge carrier density but severely reduces the benefit of cap-annealing.

The lower mobility for the ZnO:Al layer grown on the micro-textured glass points at a higher density of defects affecting the electronic transport already in the initial state. The cap-annealing, despite introducing a higher charge carrier density, seems to be less efficient in terms of defect annealing. At this point it is noteworthy, that Greiners thesis [47] mentioned above is originally dedicated to investigations on the degradation of the electronic properties of ZnO(:Al) layers in a so called damp heat test; a specific accelerated aging test where the samples are exposed to an atmosphere with 85 % relative humidity and 85 °C ambient temperature.

This is particular an issue in the context of thin film solar cells realized in substrate

configuration, where the ZnO:Al front electrode is the uppermost layer in the stack and hence more exposed to environmental influences. Moreover, it was evidenced that the degradation is due to the disturbance of the ZnO:Al structure related to the growth on micro-textured substrates (*extended grain boundaries*), see also [193], like in our case. In the initial state the ZnO:Al layers showed only slightly lower conductivity, but after exposure to the damp heat environment a severe degradation particular in DC-, i.e., HALL-mobility was observed. The stability in this context was higher for thicker layers.

All in all there are a lot of analogies in the observations. This leads us to the assumption of similar root causes and indicates another trade-off; beside those like light trapping versus Si-growth or transmittance vs. conductivity etc.; that deserves attention when incorporating (micro)-textured substrates. Of course, to clarify the root cause of this effect needs further investigation, but is not in the focus at this point.

The important thing for now is to recall that the cap-annealing of the thin ZnO:Al layer grown on the micro textured glass still showed an improvement in conductivity. Furthermore, it still comprises the optical gains (reduced sub-band gap absorption, band-gap shift) already observed for films grown on planar glass.

6.5.3 Application to solar cells

In this section the micro-textured glass will be utilized as substrate in a-Si:H/ μ C-Si:H tandem cells (referred to as sample type A here). The results will be compared to those of cells grown on planar glass incorporating the same, thin, non-textured, cap-annealed ZnO:Al layer (sample type B) and a conventionally texture-etched, non-annealed (standard) ZnO:Al layer (sample type C). In a first part we will focus on the light management in these devices before the results of the overall cell performance will be presented in a second part.

Figure 6.11 shows the external quantum efficiency and the total cell absorptance for all three sample types. The short wavelength onset of the *EQE* is located at $\lambda \approx 320$ nm for sample A and B and at 340 nm for sample C. Moreover, the slope is steeper for the former two compared to the latter. Both differences are clearly related to the use of cap-annealed ZnO:Al, namely the band gap shift due to increased charge carrier density and the reduction of sub-band gap absorption, respectively. At a wavelength of ≈ 390 nm the *EQE* of sample A and B saturates rather abrupt at a value of about 72%, whereas the *EQE* of sample C increases further until it reaches a maximum of 85% at 490 nm. This differences seem to correspond with a drop in total cell absorptance for sample A and even more pronounced for sample B as soon as the ZnO:Al gets transparent, i.e. a reasonable *EQE* is detected for these cells.

In the further course the general trends in *EQE* and $1 - R$ coincide for each particular cell. The data for sample B shows some smooth oscillations and a prominent hump at $\lambda = 615$ nm

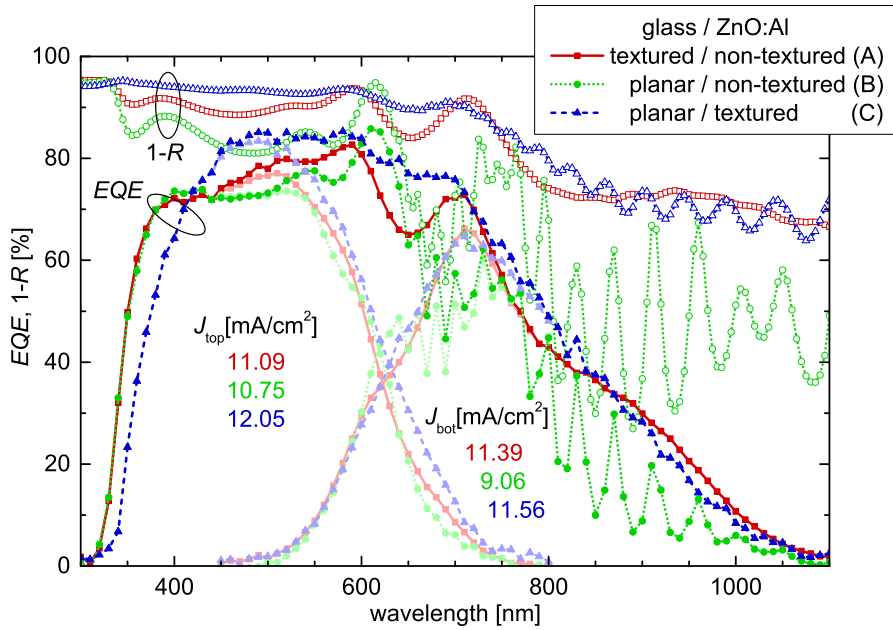


Figure 6.11: *EQE* and $1 - R$ of $a\text{-Si:H}/\mu\text{c-Si:H}$ tandem cells. The particular cells incorporate a 250 nm thick, cap-annealed (500 °C/6 h) ZnO:Al layer on micro-textured glass (red solid line, squares) and planar glass (green dotted line, circles) as well as our standard front-electrode consisting of a non-annealed, texture-etched ZnO:Al on planar glass (blue dashed line, triangles). The latter had a film thickness of 705 and ≈ 420 nm before and after texturing, respectively. For the sake of clarity the individual sub-cell *EQE* data is presented in pale colors. The *EQE* derived photo current densities for the top and the bottom cell are added to the plot. The font color corresponds to the particular line/symbol color.

followed by a deep minimum centered around 690 nm. Both features can also be observed, despite being less pronounced, for sample A and very gently for sample C. In both cases the features occur at slightly shorter wavelength, namely 590 and 650 nm for the hump and the minimum, respectively. In the long wavelength region ($\lambda > 640$ nm) the data for sample B is dominated by strong oscillation with a rather small period, again coinciding for *EQE* and $1 - R$. Both stays virtually below the corresponding data of the other two samples, only approaching those at the position of the maxima of the afore mentioned oscillation. The occurrence of such an oscillation; i.e. with a similar, small period; can also be observed in the data of sample C and (at least in $1 - R$) sample A. Since the amplitude is rather small in these cases, particular for sample A, it is hard to determine a starting wavelength.

Comparing the data for sample A and C, the afore mentioned hump and minimum could also be interpreted as zeroth order of a damped oscillation, which seems to be also present for sample B, but is masked due to superimposition of the marked small period oscillation in this case.

Finally, all these effects yield a lack in top cell current density, being 1 and 1.4 mA/cm² for sample A and B, respectively, compared to sample C. For the bottom cell the photo current density of sample A almost approaches that of sample C, whereas sample B exhibits a marked

deficiency. Recalling the under estimation of the photo current related to the particular small spot setup, also used for the *EQE* measurements presented in fig. 6.11, and especially the differences therein depending on the light trapping texture (cf. sec. 5, particular fig. 5.5, p. 78), the picture remains generally the same, but the bottom cell current of sample A even slightly outperforms that of sample C. However, the data derived from the small spot setup was favored, since its small step size ($\Delta\lambda = 10$ nm) is more appropriate to sample all the features observed and presented above.

To get an idea of the origin of the various features described above, the calculation of the *IQE* as well as the separation of total cell reflectance into its specular and diffuse component is very helpful. Figure 6.12 depicts those data for all three cells (A-C). Recall that the *IQE* represents the fraction of totally absorbed light which contributes to the collected photo current (cf. eq. (2.48)). A comparison of the large area and small spot setup derived *IQE* reveals that the offset of the curves visible in the small spot derived data below $\lambda \approx 700$ nm is mainly attributed to the artificial underestimation related to multiple reflection within the front glass (cf. sec. 5). Even the pronounced dip in the *IQE* for sample A at 650 nm is largely due to this artifact. Despite that, and the shift and steeper slope of the onset for sample A and B, related to the ZnO:Al annealing, the *IQE* data of all samples is rather similar. This evidences our assumption, that the remaining prominent differences found in *EQE* are mainly related to different reflective losses rather than different parasitic absorption.

Before we come to the specular and diffuse cell reflectance, we should reflect and conclude about some basic expectations: (i) A flat surface should only yield specular reflectance; (ii) A rough surface yields a certain fraction of diffuse reflectance; (iii) The light scattering ability of micro-textured surfaces decreases with evolving wavelength; (iv) The occurrence of interferential effects, detectable as oscillations in the reflectance, is related to multiple reflections within particular layers and requires a certain amount of coherence.

Now we will come to the reflectance data presented in fig. 6.12 (b). At a wavelength of 250 nm all samples exhibit a specular reflectance around 4.5% and virtually no diffuse reflection. At this point the ZnO:Al layer is highly absorptive and hence no light is transmitted beyond that layer. The observed specular reflectance originates mostly from the air/glass interface. Moreover, there can be no reasonable reflectance at the glass/SiO_xN_y and SiO_xN_y/ZnO:Al interface. Otherwise one should see a significantly higher value of R_{specular} for sample B and C as these interfaces are flat in these devices, in contrast to sample A. This evidences the effectiveness of the SiO_xN_y layer in serving as anti-reflective film.

With evolving wavelength the ZnO:Al film gets transparent rather abruptly as soon as its band gap wavelength is passed and additional features appear in the data for each sample: Sample A for the first time shows a diffuse reflectance comprising an oscillation. The specular reflectance of sample B shows an additional portion, which is very similar to the latter but

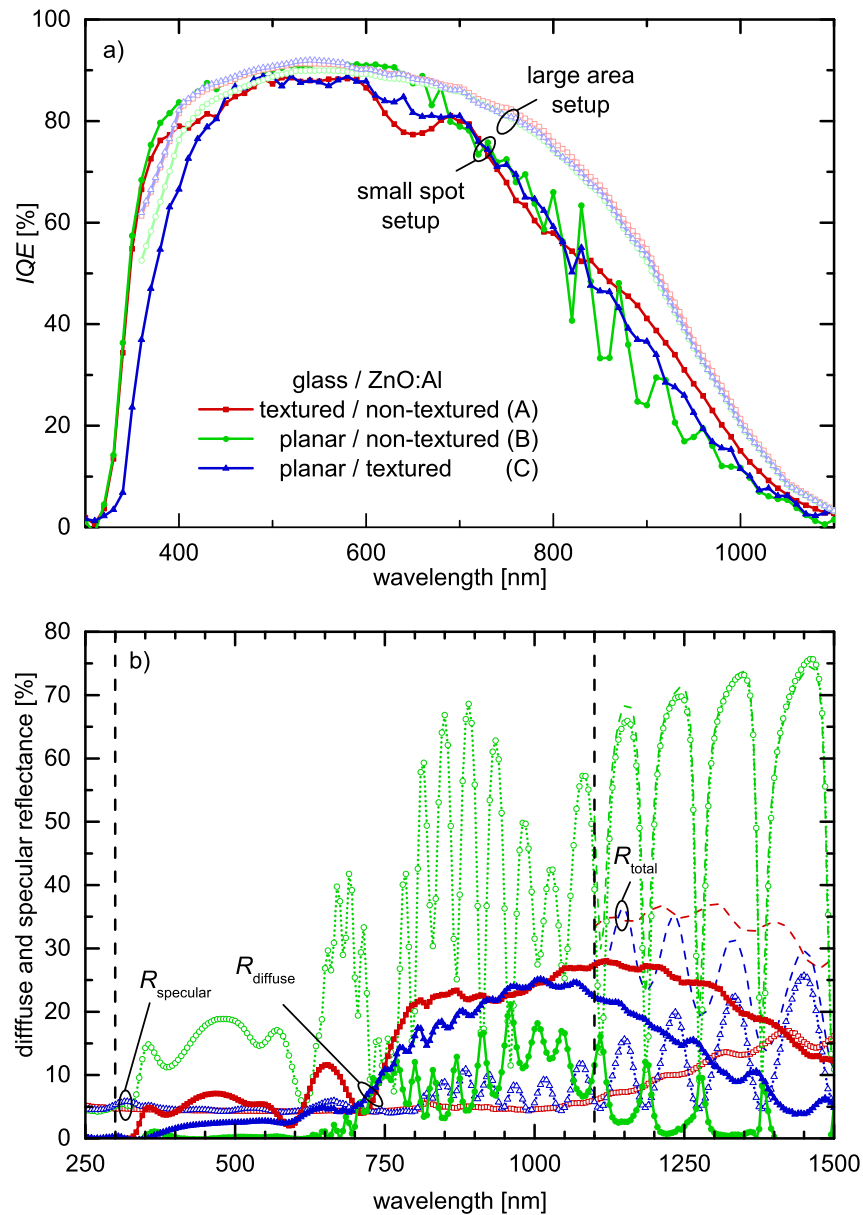


Figure 6.12: (a) IQE based on EQE as derived from the small spot (dark lines, full symbols) and the large area setup (pale lines, open symbols), and (b) diffuse (solid lines, full symbols) and specular (dotted lines, open symbols) reflectance of the a-Si:H/ μ c-Si:H tandem cells already presented in fig. 6.11. For wavelength above 1100 nm the corresponding total reflectance is also shown (dashed, lines). The particular cells incorporate a 250 nm thick, cap-annealed (500 °C/6 h) ZnO:Al layer on micro-textured glass (red line, squares) and planar glass (green line, circles) as well as our standard front-electrode consisting of a non-annealed, texture-etched ZnO:Al on planar glass (blue line, triangles). The latter had a film thickness of 705 and \approx 420 nm before and after texturing, respectively. Note the wider wavelength range of sub-figure (b) (indicated by the vertical dashed lines).

shows a bit higher level and amplitude. Sample C on the other hand only shows a gradual minor increase in R_{diffuse} , which exhibits no interferential features. All remaining quantities don't show any significant changes. Since the a-Si:H top cell absorber can be assumed as fully absorbing for $\lambda \lesssim 600$ nm, all these features are ascribed to the ZnO:Al layer, i.e. to interferences originating from reflections at the ZnO:Al/Si interface. This is further evidenced by the fact, that the distance in wavelength between adjacent extrema decreases for thicker ZnO:Al layer thickness for samples of type B (not shown).

The absence of oscillations and the low level of additional (diffuse) reflectance for sample C indicates an effective light scattering (less coherence) and light coupling (low R) of the texture-etched ZnO:Al surface, i.e. ZnO:Al/Si interface. Vice versa the presence of oscillations and the reasonable increase in R for sample A and B is an indicator for low light scattering and light coupling ability, respectively. For sample B this is less surprising, since it doesn't have any reasonable surface roughness. Sample A on the other hand exhibits a rather pronounced surface texture, but obviously this is neither providing reasonable light diffusion nor light coupling.

Note, that for sample A it was the diffuse reflection that did increase and showed interferential, hence coherent, effects whereas its specular reflectance was virtually not affected. This seems to be contradictory but is simply related to the somehow misleading notation of *diffuse* reflection in this particular context: Assuming, for simplicity, geometric light scattering (i.e. $2 \cdot ACL \gg \lambda$) the reflection at a reasonable tilted surface element would be completely specular. However, due to the tilt it won't be detected as being specular by our measurement setup (cf. sec. 3.2.2). Following this interpretation and regarding the particular surface topography of the micro-textured glass (cf. fig. 6.7 (b,d,f)), which sample A is representing, it seems to lack sufficiently small lateral features and would be hence indeed more geometric in terms of its light scattering regime for the short wavelength region compared to the texture of sample C (cf. e.g. fig. 6.6, p. 92). In other words, the reflected light is in fact redirected with respect to the specular direction by the texture of sample A, but it is not reasonably diffused, i.e. a reasonable fraction of the reflected intensity is arranged within a small angular distribution, and hence still allows interferential effects. This argumentation should also be supported by the fact, that the ZnO:Al layer in sample A, in contrast to sample C, still exhibits a rather conformal character. Despite being grown on a micro-textured surface, the ZnO:Al film itself shows only minor thickness variations (cf. fig. 6.7 (f)).

At a wavelength of around 600 nm the hump, followed by the minimum, was observed in cell absorptance and EQE (cf. fig. 6.11). Accordingly a minimum and a hump, respectively, is expected either in R_{specular} or R_{diffuse} or both. Like before, the features are solely occurring in R_{diffuse} for sample A and (more pronounced) in R_{specular} for sample B. For sample C the rather small feature can be related to both specular but mainly diffuse reflectance. The

appearance of those features can be ascribed to the back reflections from the intermediated reflector layer, like we will see in the course of this section, leading to more or less pronounced interference effects in the a-Si:H top cell.

For $\lambda > 620$ nm interference fringes with a rather small period start to appear in both $R_{diffuse}$ and (more pronounced) $R_{specular}$ for sample B. Moreover, this is the first time that sample B shows a reasonable amount of diffuse reflection. This wavelength position represents the point, where the light reflected at the back reflector escapes the cell for the first time. The oscillation is related to the $\mu\text{-Si:H}$ bottom cell and the period hence to its optical thickness. Due to the native roughness of the $\mu\text{-Si:H}$ surface, this reflection comprises a diffuse fraction. Apart from the oscillation the latter reaches a maximum around $\lambda = 1000$ nm and afterwards slowly decays to zero again. This indicates that the native $\mu\text{-Si:H}$ texture gets more and more inappropriate to scatter light with increasing wavelength. Also note the offset in position of the minima and maxima in the interference fringes between the specular and diffuse reflectance. They indicate a very slight optical path difference, i.e. a very low effective scattering angle of the diffuse portion. With evolving wavelength gradually more of the scattered light is detected within the acceptance cone of the specular measurement channel, and is hence artificially accounted as being specular (cf. sec. 3.2.2). This also explains the increasing asymmetric shape of the oscillations for longer wavelength.

A similar behavior can be observed for sample C: Above $\lambda \approx 700$ nm the diffuse reflectance increases with wavelength and starts containing oscillations with a rather moderate amplitude compared to sample B. It reaches a global maximum around 1100 nm before it gently decays. At $\lambda = 800$ nm the specular reflectance of sample C also starts to exhibit interference fringes, which's amplitude generally increases with wavelength. Despite that, the minima remain at values around $R_{specular} = 4.5\%$. The interpretation remains generally the same as for the planar sample B, but qualitatively the front texture present in sample C leads to stronger light scattering and a higher degree of incoherence, as indicated by the generally higher fraction of diffuse reflectance and the overall lower amplitudes of the interference fringes, respectively.

Following this argumentation sample A shows the strongest light scattering and highest incoherence of reflected light in the long wavelength range above 750 nm. It comprises only minor of these bottom cell related interferential features in both specular and diffuse reflectance. Moreover, it shows by far the highest diffuse reflectance, particular for $\lambda > 1050$ nm, whereas its $R_{specular}$ approximately follows that of sample C, apart from the oscillation observed mainly in the latter.

To answer the question whether the bad light coupling found for sample A can be related to the generally larger surface features compared to sample C, in fig. 6.13 we compare the EQE and $1 - R$ of sample A (grown on micro-textured glass) to that of an a-Si:H/ $\mu\text{-Si:H}$ tandem cell grown on the ZnO:Al type presented in fig. 6.7 (c), which has similar σ_{RMS} and

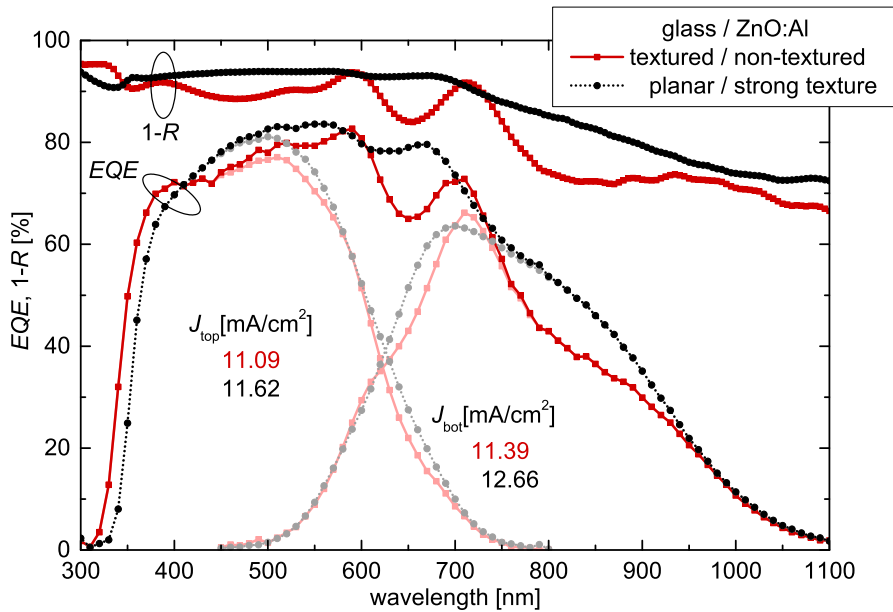


Figure 6.13: EQE and $1-R$ of the a-Si:H/ μ C-Si:H tandem cell already presented as sample A in fig. 6.11 (red solid line, squares) compared to those of a cell grown on a non-annealed, texture-etched ZnO:Al on planar glass (black dotted line, circles). The latter is of the same type as the one shown in fig. 6.7 (c) and hence comprises a similar topography in term of its surface statistic (see text there). For the sake of clarity the individual sub-cell EQE data is presented in pale colors. The EQE derived photo current densities for the top and the bottom cell are added to the plot. The font color corresponds to the particular line/symbol color.

ACL as sample A. Without going into detail the cell grown on the similarly textured ZnO:Al layer shows both excellent light coupling and light trapping. Therefore, it is evidenced that the bad light coupling found in the cell grown on micro-textured glass is not an issue of general feature size or depth. The bowl-like shape found for the micro-textured glass seems to be not appropriate in this sense.

Another explanation could be linked to the fact, that the texture in sample A is introduced via the glass/ZnO:Al interface instead the ZnO:Al/Si interface. An interesting hint to that can be derived from a recent publication by Meier *et. al* [115]. They used UV-nanoimprint lithography (cf. sec. 2.2.4) to transfer the surface topography of a sputter-etched ZnO:Al with rather large feature sizes (similar to that of the ZnO:Al presented in fig. 6.7 (c)) to a thin polymeric film on glass. The refractive index of this polymeric was very close to that of glass. Afterwards a 250 nm thick, virtually smooth ZnO:Al-layer was deposited onto the texture. Obviously, the sample setup is hence very similar to ours in the case of the samples on textured glass, despite the particular texture itself. Finally, they utilized these samples as substrates for p-i-n μ C-Si:H single junction solar cells and observed interferential features leading to reflective losses, like we did in sample A (and B). The key point is, that they did not observe any interferential oscillations in their reference sample grown on the original,

identically textured ZnO:Al.

This can not be explained by the different thickness of the ZnO:Al layer itself, since this would mainly just lead to a different wavelength period of the interferential oscillations (shorter for the thicker film). Hence, this demonstrates that the light coupling ability of a substrate is not solely related to the texture at the ZnO:Al/Si interface, but also on the particular layer setup underneath. Similar observation were also presented in a publication from the same group utilizing dry-etching processes to texture glass substrates [194]. In both publications the undesired effect was circumvented by implementing a ZnO:Al layer as thin as 60 nm, which simply shifts the interference fringes away from the optical window of the ZnO:Al. However, this of course significantly increases the sheet resistance of the ZnO:Al and hence leads to a severe resistive loss when utilized in solar cells.

This brings us to the point where we should discuss how light coupling can be achieved by texturing an interface. There are mainly three effects related to that: The first one is referred to as effective medium approach (EMA) originally based on a work by BRUGGEMAN [51]. It basically treats the roughness between two media as a graded transition of the particular refractive indices. The important restriction to that concept is the assumption, that the lateral feature size of the incorporated texture elements is sub-wavelength sized. Otherwise the texture would no longer serve as an effective index grading rather than simply introduce light scattering. In the case of Si with $n_{\text{Si}} \approx 4$ this limits the lateral feature size contributing to the EMA to $\lesssim 100 \dots 250$ nm depending on the wavelength regime. Therefore, it is rather unlikely, that the huge lack in light coupling found for sample A is exclusively related to EMA (see also [101]). The second effect takes place in the geometrical regime, i.e. when the typical lateral feature size is larger than the wavelength of the light. The portion of light that is (specular) reflected at an inclined surface element has a certain chance to imping the surface again at a neighboring surface element [195–197]. We will come back to this effect in sec. 6.6, where we make explicit use of it. For the situation discussed here, it could have some impact on the light coupling but is not believed to comprise a major contribution. The third effect yielding light coupling at a rough interface is of rather secondary nature and related to light scattering of the *reflected* light. This in general leads to total reflection for part of the back reflected light as we have already seen in sec. 5 (cf. fig. 5.2, p. 74). Actually, the phenomenon discussed there as an artificial loss in the *EQE*, when measured with the small spot setup, is in fact part of the light coupling mechanism discussed here.

Figure 6.14 depicts the different situation for the back-reflected light when utilizing textured glass compared to textured ZnO:Al. The scheme is a coarse geometrical approximation of a local situation, but it provides a plausible illustration for a possible reason of the worse light coupling when the texture is introduced at the glass/ZnO:Al interface instead of the ZnO:Al/Si interface, even when the same texture is utilized. For a real micro-texture the

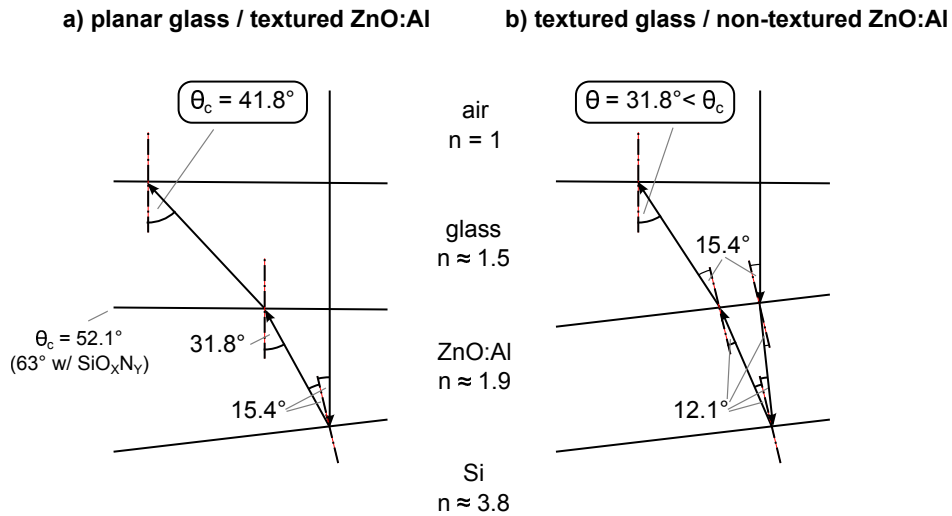


Figure 6.14: Schematic drawing indicating the impact of using textured glass on the retro-reflective light coupling. The values shown are based on geometrical optics and hence a coarse approximation. Depicted are analog situations for both the utilization of (a) textured ZnO:Al on planar glass and (b) textured glass coated with a uniform ZnO:Al film. The inclination of the particular “texture” is the same in (a) and (b) and was chosen as to fit the critical angle of total reflection at the air/glass interface in example (a). For larger “scattering” angles an analog situation would occur for total reflection at the ZnO/glass or the ZnO/SiO_xN_y and SiO_xN_y/glass interfaces as indicated by the additional critical angles given.

light is of course scattered, i.e. exhibits an angular distribution, and hence is only partially affected by the depicted situation.

Some of the above listed observation have substantial similarity with those made by Dominé for a-Si:H/ μ c-Si:H grown on differently textured and/or plasma-treated [198] LPCVD-grown ZnO:B layers [101]. Namely, he found (i) an overall increased total cell reflectance for longer plasma-treatment, i.e. nano-scaled smoothing, of the ZnO:B surface; and (ii) additionally the occurrence of interference fringes for $\lambda > 500$ nm if an intermediated reflector layer was incorporated. Both effects led to a reduction of the photo generated current density and scaled with the duration of the smoothing plasma-treatment. The latter (ii) also depended on the thickness of the IRL and could be attributed to the diffuse reflectance as obtained from additional experiments he carried out on glass/ZnO:B/a-Si:H stacks. The analogy in this problems gets even more pronounced if we follow the original description of Bailat on the modifications obtained on the ZnO:B surface topography due to the plasma-treatment. He stated, that “V-shaped valleys [...] turn into U-shaped valleys”. Hence this also supports the marked differences found in light coupling for the otherwise similar bowl-(U-) and inverted cone-(V-)like topography of the micro-textured glass and the strongly textured ZnO:Al, respectively (cf. fig. 6.7 (a-c) and fig. 6.13).

Moreover, Dominé observed a decreasing efficacy (gain in top cell current density) and efficiency (ratio of gain in top cell to loss in bottom cell current density) of the IRL with

increasing plasma-treatment time [101]. Both effects were present for all (non-zero) IRL thicknesses. The sensitivity of the IRL performance on the particular texture of the front TCO utilized in an a-Si:H/ μ c-Si:H tandem cell was also discussed in a publication from our group [99], which compared the IRL performance as a function of its thickness in cells grown on different TCOs, i.e. different textures, based on experiments and rigorous optical simulations. The outcome of both works can coarsely be summarized by a rule of thumb: Both the efficacy and efficiency of the IRL mainly rely on a good light trapping introduced by the front texture, particular in the wavelength region 500 to 700 nm, where the IRL is working. Otherwise the light reflected by the IRL is not efficiently trapped within the top cell and yields reflective and absorptive losses. The latter is ascribed to increased parasitic absorption. Moreover, the response to a variation of the IRL thickness is distinct for the different front textures, leading to different optimal IRL thickness in terms of top cell gain [99].

In the following we will have a closer look on the influence of the IRL in the context of our three substrate types. Figure 6.15 shows EQE and $1 - R$ (a,c,e) as well as IQE (b,d,f) of nominal identical a-Si:H/ μ c-Si:H tandem cells, comprising a different thickness of the intermediate reflector layer (none “0”, 20 and 60 nm) grown on the known three front texture/electrode configurations, A(a,b), B(c,d) and C(e,f). For $\lambda \lesssim 500$ nm all shown data is virtually identical for each cell type irrespective of the IRL thickness variation. This first demonstrates the good reproducibility of all processes and characterization techniques incorporated, and furthermore evidences that the light entering the top cell is indeed fully absorbed within a single pass in this wavelength regime, since it is not affected by the different optical situation behind the top cell. The general variations for the different cell structures due to the use of thin cap-annealed ZnO:Al for sample type A and B as well as the texture-/layer setup-related lack in light coupling in these two types, as discussed before, are apparently present.

Regarding the influence of the IRL, starting with sample C this time, with increasing d_{IRL} the falling and rising edge of the top and bottom cell EQE (e), respectively, is gradually shifted towards longer wavelength. This is exactly, what the IRL is intended for: shifting bottom cell into top cell current density. Besides that, the presence of the IRL has only minor effects on the summed EQE and $1 - R$: Above $\lambda = 500$ nm the interferential oscillations (already discussed) appear and are more pronounced for thicker IRLs. Note that also without the IRL a rather small oscillation can be seen. This is due to the bottom cell p-layer, which also contains a thin μ c-SiO_x:H-based sub-layer (with low refractive index), hence comprising also a small reflective effect. The IQE of these cells depicted in fig. 6.15 (f) reveals that the insertion of an IRL also leads to a small absorptive loss for $\lambda > 700$ nm. This has to be due to additional absorption of light in the IRL itself or in other layers not contributing to the photo current generation. The latter can be explained by a light trapping effect, e.g. within

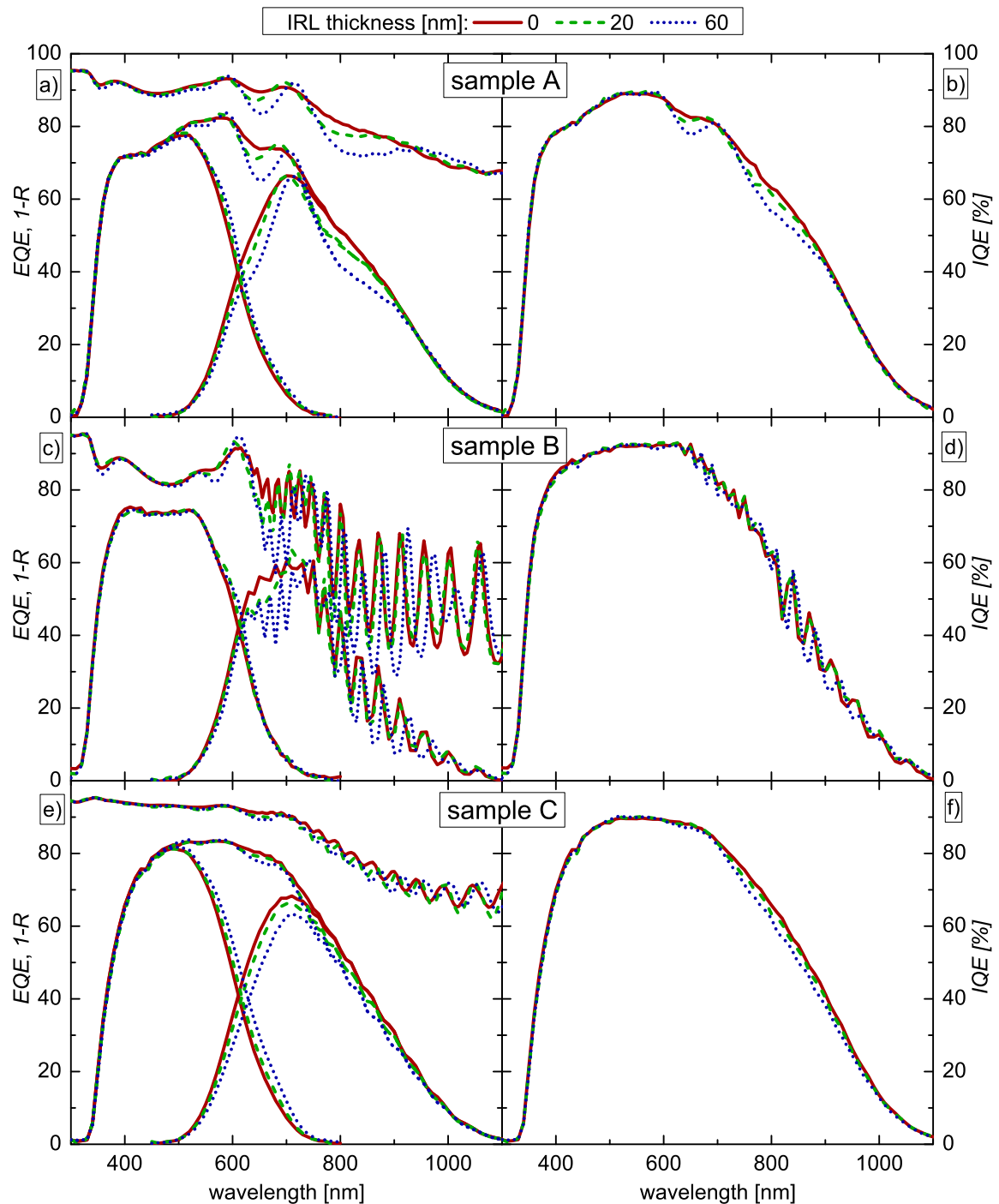


Figure 6.15: (a,c,e) EQE , $1 - R$ and (b,d,f) IQE for a-Si:H/ μ C-Si:H tandem cells with differing intermediate reflector layer thickness. The particular IRL thicknesses were “0”, i.e. no intended IRL (red solid line), 20 (green dashed line) and 60 nm (standard thickness, blue dotted line). The cells are grown on the known three front texture/electrode configurations used throughout this section, namely sample type A (a,b), B(c,d) and C(e,f). For the sake of clarity the curves for the summed EQE are not shown for sample B (c).

the top cell where this light can not be utilized rather than gets parasitically absorbed in the surrounding layers.

For the sample type B the implementation of the IRL shows almost no improvement of the top cell EQE , but at the same time clearly reduces that of the bottom cell. In other words: It fails its desired purpose. The latter is linked to strong interferential effects observable in EQE and $1 - R$ leading to severe reflective losses above $\lambda \approx 500$ nm. They are modulated onto the interference fringes originating from the interaction of the back reflector and the bottom cell. Therefore it is hard to quantify the differences, but the IQE of these cells (d) shows virtually no difference, hence indicating no changes in the fraction of parasitic absorption with respect to the totally absorbed light, irrespective of the particular IRL thickness.

The most obvious influence of the IRL is found for the cell type A (cf. fig. 6.15 (a)). Here, the interferences, again promoted by thicker IRL layers, can be clearly identified as oscillations, again for $\lambda > 500$ nm, ranging throughout the whole recorded spectral range (even up to 1500 nm; not shown). Since light with $\lambda \gtrsim 750$ nm can not be absorbed in the a-Si:H based top cell this constitutes an inherent loss. In spite of that, the IRL seems to shift at least some of the current density lost in the bottom cell to the top cell. The IQE of these cells (b) indicates that part of the EQE losses are due to parasitic absorption. From comparison with IQE data derived from the large area EQE measurement setup the dip observed around 650 nm can be ascribed to the artificial loss related to the small spot EQE measurement setup (cf. fig. 6.12). Note, that this does not affect the reflective portion of this loss. The bump between 700 and 900 nm on the other hand is a real absorptive loss.

The bar graph shown in fig. 6.16 allows a quantitative comparison of the changes introduced by the IRL in terms of the corresponding (implied) photo current densities. The interpretation of the particular bars is as follows: The IRL typically introduces a loss in bottom cell current density (total bar height), which either contributes to the gain in top cell current density (the intended purpose, blue fraction) or it is lost for photo current generation due to increased reflective (green fraction) and/or absorptive losses (red fraction).

The data reflects the qualitative assumption already made. For sample B the introduction of the IRL yields virtually no efficacy, i.e. the top cell current density is almost unaffected. The bottom cell current density on the other hand is significantly reduced mainly due to reflective losses. Both effects increase with IRL thickness. The absorptive losses are rather small.

For the cells of type A and C the changes in case of the 20 nm thick IRL are in effect identical. In contrast to type B cells roughly a third of the bottom cell current density loss is shifted to the top cell. The reflective loss is rather small and the absorptive one accounts approximately half of the bottom cell current density loss. In case of the IRL with 60 nm (standard) thickness bottom cell and absorptive loss are still similar for type A and C, but the

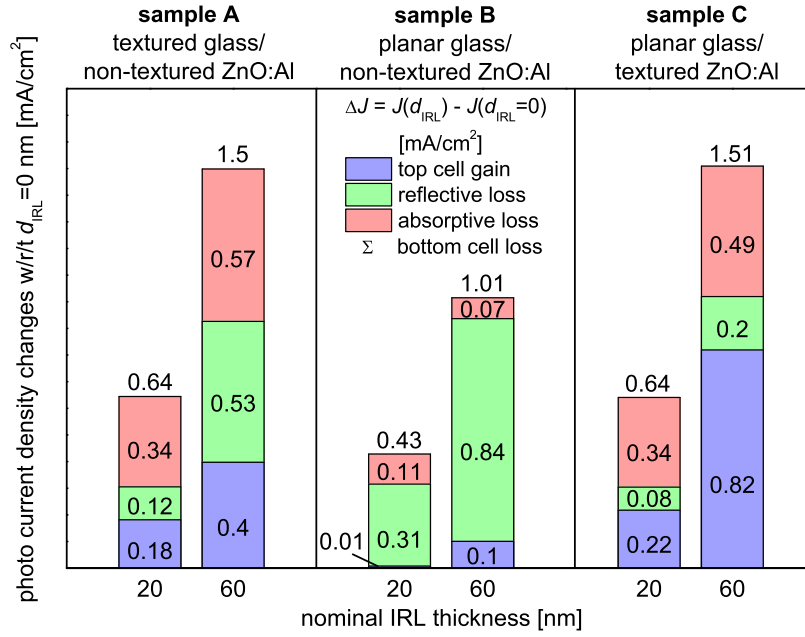


Figure 6.16: Quantitative analysis of optical changes introduced by the intermediate reflector layer for different front texture/electrode types expressed in terms of photo current density and with respect to the respective cell without an IRL. The particular data is derived from calculation of the corresponding current densities according to eq. (2.49). It is based on the average value of three co-deposited cells per sample type and IRL thickness variation. For calculating the reflective and absorptive loss the reflectance and $1 - EQE_{\text{summed}}$ was used, respectively, instead of an EQE and the integration was carried out between 300 and 1100 nm, which allows to express these losses as an respective implied photo current density ($J_{\text{refl.}}$ and $J_{\text{absorp.}}$) within this wavelength interval. Note that the graph only depicts the changes in the respective quantities, i.e. $J_i(d_{\text{IRL}}) - J_i(d_{\text{IRL}} = 0)$. The explicit values of the respective changes are added to the bars.

top cell gain is twice as high for sample type C compared to A. Consequently the reflective loss is higher for the latter. In terms of bottom cell loss the effect of the IRL is higher by a factor of about 1.5 for cells of type A and C compared to B.

However, since the intention of the IRL is not to reduce the bottom cell current density rather than to promote that of the top cell the major result is that our standard IRL is less effective in combination with the micro-textured glass samples compared to the textured ZnO:Al. In fact a similar loss of about 1.5 mA/cm^2 in bottom cell current density was converted in a gain of 0.4 and 0.8 mA/cm^2 in top cell current density for cell type A and C, respectively. For the samples comprising no intended front texture (B) the additional reflection introduced by the IRL also leads to a reduction of the bottom cell current density, but can virtually not be utilized for a gain in top cell current density. Rather the light is simply reflected out of the cell.

In total the IRL experiment confirmed the importance of the particular front texture for the efficiency of the IRL. If the front texture is not appropriate the IRL reflects light with long wavelength which inherently can not be utilized by an a-Si:H-based top cell due to its high

band gap. This can therefore be interpreted as insufficient light coupling to the bottom cell - *introduced by the IRL*. Moreover the light reflected at the intended wavelength region (around 500 to 700 nm) is not efficiently trapped within the top cell and hence also contributes to reflective losses. Like for the worse light coupling generally found for sample type A (and B) also these IRL-induced losses could be rather due to the particular front texture or the fact that it is introduced via the glass/ZnO:Al interface (cf. fig. 6.14) or both.

Concluding our observation concerning the light management in the different samples, sample B comprises bad light coupling and virtually no light trapping ability, which is both not surprising, since it contains no intended texture. Sample A also shows weak light coupling, but very good light trapping, at least in the long wavelength range, where the bottom cell is absorbing. Sample C on the other hand shows excellent light coupling abilities and reasonable light trapping throughout the whole wavelength range observed. Obviously the micro-textured glass setup in sample A is not appropriate to achieve good light coupling, especially in the short to mid wavelength range. The beneficial effect of an IRL used to swap light and hence generated photo current density from the bottom cell to the top cell is significantly lower for sample type A and particular B.

After having observed the optical cell performance for the different sample types we will now come to the J - V data of these cells. Figure 6.17 shows J_{SC} , V_{OC} , FF and η for sample type A, B and C and for different IRL thickness before and after 167 h (i.e. one week) of light soaking. Each variation is represented by a data set of 20 single 1 cm^2 -cells.

The J_{SC} data generally corresponds to the findings already made from the EQE analysis. Except for the cells of type B with the 60 nm thick IRL, the short circuit current density, at least in the initial state, is limited by the top cell. This is evidenced by a comparison to the photo current densities derived from EQE measurements conducted at the large area setup, which are presented in fig. 6.18. Hence, J_{SC} follows the top cell current density and increases with the IRL thickness in case of sample type A and C. On sample B the 60 nm IRL leads to bottom cell limitation which is why J_{SC} is reduced in this case. This is accompanied by a widening of the box which indicates higher (statistical) scattering in the current density provided by the bottom cell as compared to that of the top cell. This is not surprising, since the process regime needed for growing micro-crystalline silicon is generally more sensitive to deviations than that used for a-Si:H growth. Anyhow, the scattering still constitutes no issue. Due to the bottom cell limitation this particular cell also shows virtually no light induced degradation of J_{SC} , since only the a-Si:H based top cell shows a (noticeable) LID.

Regarding the initial V_{OC} the highest values were achieved for sample type B. No clear trend with the IRL variation could be observed in that case. The samples of type A on the other hand exhibit the lowest values in V_{OC} which increase with IRL incorporation/thickness, particular when going from 20 to 60 nm. The samples of type C show intermediate V_{OC} values.

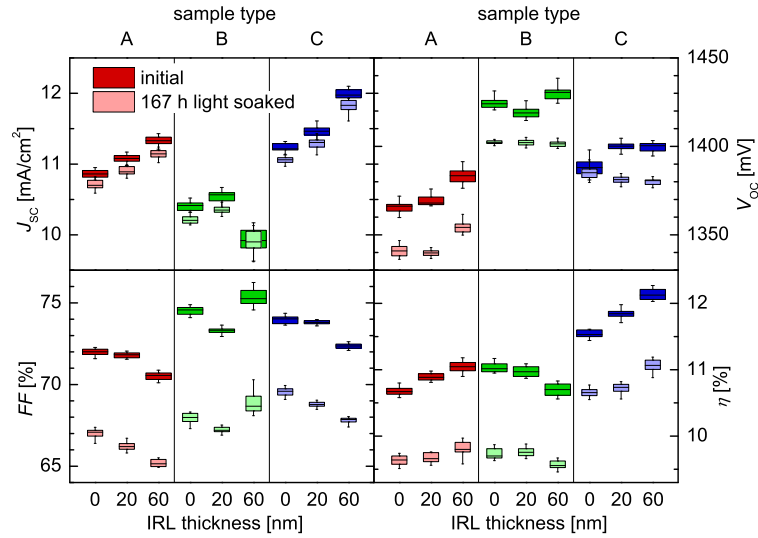


Figure 6.17: J - V data of a-Si:H/ μ C-Si:H tandem cells with different front texture/electrode types and varying IRL thickness before (dark color) and after (pale color) 1 week of light soaking. The sample types are the same as used throughout this section. Each data set consists of the data of 20 single 1 cm²-cells originating from one substrate. The data is presented in a box plot. The inner vertical line of the box represents the median value. The lower and upper edge indicates the 25th and 75th percentile, i.e. half of all data lies inside the box, and a quarter below and above. The lower/upper whisker shows the value of the outermost data point which is at maximum 1.5 times the box height below/above the lower/upper edge of the box, respectively. This presentation allows to easily get a visual impression of the statistical distribution of the data.

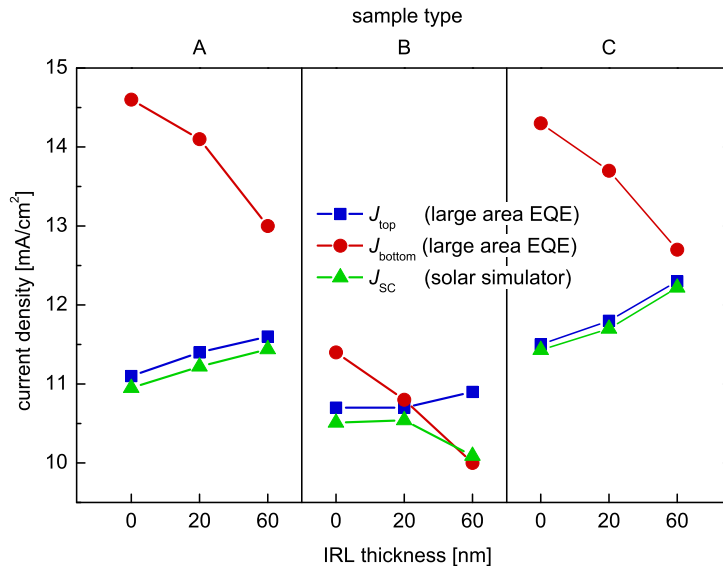


Figure 6.18: Photo current densities of a-Si:H/ μ C-Si:H tandem cells with different front texture/electrode types and varying IRL thickness as derived from J - V and EQE measurements. The particular cells incorporate a 250 nm thick, cap-annealed (500 °C/6 h) ZnO:Al layer on micro-textured glass (type A) and planar glass (type B) as well as our standard front-electrode consisting of a non-annealed, texture-etched ZnO:Al on planar glass (type C). The latter had a film thickness of 705 and \approx 420 nm before and after texturing, respectively. The EQE derived current densities are based on measurements conducted at the large area setup. The lines are guides to the eye.

Thereby, V_{OC} increases as soon as an IRL is implemented, but shows no further dependence on its particular thickness.

The generally different level of open circuit voltage obtained for the different sample types is mainly ascribed to the material quality of the grown silicon stacks (cf. sec. 2.2.3). On a flat substrate (sample B) the growth is virtually not affected, resulting in the best material quality and hence the highest values in V_{OC} . Consequently, the surface of the ZnO:Al coated micro-textured glass (sample A) seems to be less appropriate for high quality silicon growth compared to our standard textured ZnO:Al (sample C). Despite having rather similar distribution of the local surface inclination (compare fig. 6.6 (b) and fig. 6.9 (b)) the larger feature size and RMS-roughness observed for sample A very likely leads to severer disturbance, since it can not be so easily smeared out by the Si growth itself.

The tendency to higher values of V_{OC} with incorporation or increased thickness of the IRL found in sample C and A, respectively, can be explained by the so called *shunt quenching* effect [199] originating particular from the low in-plane conductivity of the IRL. This inhibits the undesired current drain introduced at local shunt paths, i.e. it more effectively isolates bad regions from good ones. So, if there are bad regions, like we assumed for sample C and particular A, the implementation of the IRL reduces the losses occurring due to those and V_{OC} hence increases. Unfortunately, V_{OC} also tends to show stronger LID when an IRL is used. This leads to even lower open circuit voltages, at least in the case of sample C, when an IRL is used. The reasons for that are not known, but Kirner already pointed out, that the LID of the cell efficiency correlates with the inverse slope of the J - V curve around the open circuit point [107]. This quantity has the dimension of a resistance (per area), is referred to as R_{OC} and can be interpreted as an indicator for the series resistance within the device. Indeed, a gradual increase in R_{OC} can be observed for all cell types with increasing IRL thickness (not shown).

The interpretation of the FF of a tandem cell is not straight forward, as it is always biased by the current matching situation between top and bottom cell. Thereby the FF is commonly lowest when the cell is matched and increases gradually with current mismatching. The latter is usually more pronounced for bottom cell limitation. A nice demonstration and explanation of this effect can for instance be found in ref. [200]. Recalling the particular current matching situation as presented in fig. 6.18 one can conclude, that the FF for sample B is generally on a high level and the variation follows the matching situation. The latter can also be stated for sample A and C. But, the level of the FF is slightly lower for sample C compared to sample B and lowest for sample A, despite being strongly top cell limited irrespective of the IRL thickness. Therefore, beside this matching related trends the comparison of FF between different sample types corresponds to the trend already observed in V_{OC} . This is less surprising, since the FF is also a very sensitive indicator for the electrical device quality.

Moreover, the differences in sheet resistance of the ZnO:Al layers used as front electrode are influencing the FF . The highest sheet resistance was observed for sample A ($R_S \approx 18.3 \Omega$). The values for sample B and C were about 15.8 and 11 Ω , respectively. From our experience this could easily account for a reduction in FF of about 2%. The LID of the FF is slightly higher/lower for sample type B/C compared to A, respectively, but this is not of importance for the general trends observed.

It shall be noted, that another explanation for the worse FF and V_{OC} found for sample A compared to C could be a significantly larger surface area per device area. This would increase the relative contribution of interface recombination and hence reduce the device quality. From the AFM data presented in fig. 6.6 (g) and fig. 6.7 (b) (representative for type C) the surface area factor, i.e. the ratio of surface area to scan area, was determined for sample A and B to be 1.126 and 1.137, respectively. Obviously, the values are very close to each other, which is why we exclude this effect as a reasonable cause for the differences found.

All the differences found in the J - V data finally yield an efficiency of 11/9.8% (initial/light soaked) for sample type A, and 12.2/11.1% for sample type C. Thus, the reasonable high efficiency achieved on our standard texture-etched ZnO:Al electrode on planar glass (type C) could not be reached by the cells incorporating the thin cap-annealed ZnO:Al grown on the micro-textured glass. The reasons for that have been clearly identified: Roughly half of the difference is due to the lower J_{SC} and hence related to the light management issues discussed. The remainder of the difference is due to the lower FF and V_{OC} found for sample type A. Thereby, the loss in FF is very likely related to the higher sheet resistance of the ZnO:Al layer used there. It shall be noted again, that this can probably be circumvented by applying slightly thicker ZnO:Al layers. The shortfall in V_{OC} is interpreted as a direct consequence of the differences in the particular texture of the substrates, leading to variations in the device quality of the Si. Note, that in spite of the shortfalls in light coupling the cells on micro-textured glass had the highest bottom cell current densities among all sample types, irrespective of the IRL variation. This points at the good light trapping properties provided by this texture in the long wavelength region, where it is needed the most.

6.6 Application of a textured Front Cover

In this section the effect of a regularly textured transparent polymeric sheet applied to the front side of the glass is presented. The particular textured sheets are of the commercial type *MaxRay Crystal* and were provided by *SolarExcel* (now with *DSM*), the manufacturer of the product. There is a recent publication on the application of this particular front texture to a-Si:H/ μ c-Si:H based solar cells [197] (see also ref. [200]). However, we think that we can provide valuable additional results and considerations to this work.

In contrast to all light management textures discussed so far, this particular product

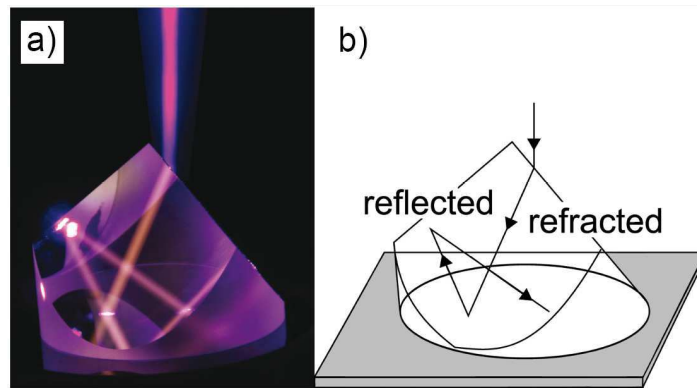


Figure 6.19: (a) Photograph of a model of a surface element of the textured front cover situated on a Si-wafer and illuminated by a purple laser beam. (b) a simplified schematic drawing of the situation presented in (a). See text for further description. Figure taken from ref. [200].

comprises a *regular texture* and exhibits a lateral feature size on the millimeter scale. The latter in particular allows the application of geometric optics. The polymeric itself has a refractive index rather similar to that of glass and exhibits a comparably low absorption throughout the whole wavelength range relevant for our cells, i.e. 350...1100 nm. To ensure proper optical coupling, the sheet was adhesively attached to the (non-coated) front side of individual $100 \times 100 \text{ mm}^2$ -sized samples by means of a drop of de-ionized water.

According to Ulbrich *et al.* [197] the texture provides two beneficial effects: (i) it reduces the reflection at the air/polymeric (former air/glass) interface by allowing the reflected part of the light to hit the surface a second time. It follows from FRESNEL'S equations that this reflection accounts for about 4%. Hence this is the upper limit of reduction in reflective losses that can be achieved by this mechanism. (ii) The texture has a retro-reflecting effect that actually introduces an additional light trapping at the polymeric/air interface. This is illustrated in fig. 6.19. Sub-figure (a) depicts a photograph of a model of a single surface element of the texture. It is placed on a Si-wafer. A purple laser beam impinging on the surface demonstrates the general working principle of the texture: The incident beam is refracted at the air/polymeric interface and reflected at the polymeric/Si interface. When it reaches the polymeric/air interface again, it is subjected to total reflection and hence can not escape the texture at this point. Therefore, these textures are also referred as *retro-reflector*. For clarity fig. 6.19 (b) provides a schematic drawing of this situation.

In a real solar cell, comprising internal textures (like a textured TCO surface) this effect is generally restricted to only a non-unity portion of the back reflected light. However, as we have demonstrated in the course of the last section it is exactly this retro-reflective effect that could significantly mitigate the light management issues observed for a-Si:H/ $\mu\text{c-Si:H}$ tandem cells incorporating thin cap-annealed, non-textured ZnO:Al grown on these particular micro-textured (and planar) glass substrates.

Before we present our results, we again would like to emphasize that a comprehensive investigation for the interaction of this particular front texture with Si-based thin-film cells is already provided by Ulbrich *et al.* [197,197]. But, first there was no application to cells grown on micro-textured glass comprising thin, non-textured TCO layers; and second we would like to contribute an interesting finding related to the analysis of diffuse and specular cell reflectance in that context.

In the following the textured front cover was applied to the cells presented in the IRL thickness variation in sec. 6.5.3. As the incorporation of the front cover significantly promotes lateral propagation of light within the glass substrate, we had to rely on the large area setup to obtain reliable *EQE* measurements. Figure 6.20 exemplarily shows the *EQE* and $1 - R$ for the cell on micro textured glass (sample type A), comprising the thin, cap-annealed, non-texture ZnO:Al and a 60 nm thick IRL. For comparison the curve for $1 - R_{\text{diffuse}}$ (cf. fig. 6.12) for the measurement without textured front cover was added. The front cover significantly reduces the reflective losses. Thereby, the diffuse reflectance obtained for the uncovered sample reasonably resembles the total reflectance obtained with the cover. This evidences, that the textured cover suppresses virtually the whole specular reflectance. Recall, that the specular reflectance found for this sample type (A) below $\lambda = 1100$ nm was exclusively due to the primary reflection at the air/glass interface. This, on the other hand, means that beside this primary anti-reflective effect there is no noticeable gain by the retro-reflective effect with these samples. This is also evidenced by the coincidence of the corresponding *IQE* curves, which are shown in fig. 6.21. The gradually lower *IQE* for $\lambda < 560$ nm found for the covered cell compared to the uncovered one is interpreted as a higher fraction of parasitic absorption in the top cell p-layer. This and the slight shift of the position of the IRL related oscillation observable in $1 - R$ indicates that a redirection of the incident light compared to the uncovered cell indeed takes place, but obviously does not increase the cell absorptance. To date we found no reasonable explanation for this behavior.

The improvement in current density upon application of the front cover accounts 0.4 mA/cm^2 ($\approx 3.2\%$) for both the top and the bottom cell. This is in good accordance to the reduction of the primary (specular) reflection ($\approx 4.5\%$) obtained by applying the textured front cover. Note that part of the gain in total cell absorptance also contributes to an increase in parasitic absorption (i.e. the *IQE* was virtually not affected).

Figure 6.22 summarizes the *EQE* derived photo current densities for all cell types (A-C) and IRL configurations (0, 20 and 60 nm). For sample type A the gain in photo current density by applying the front texture seems to be limited to the reduction of the primary reflection at the air/glass interface, irrespective of the IRL thickness. In the case of sample type C the gain in top cell current is generally slightly higher as compared to sample type A. For 60 nm IRL thickness the improvement in bottom cell current density upon application of

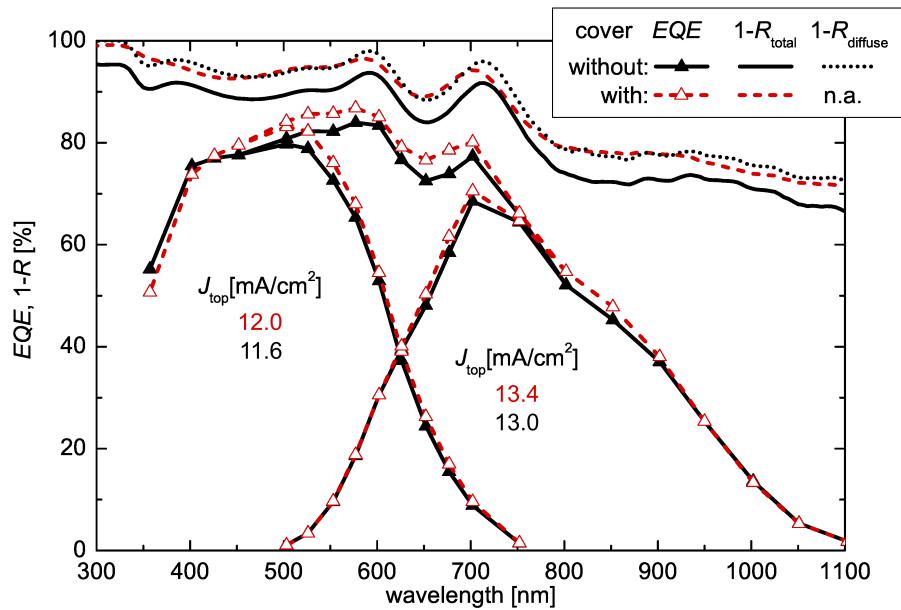


Figure 6.20: *EQE* (obtained at the large area setup) and $1 - R$ of the a-Si:H/ μ c-Si:H tandem cell (60 nm IRL thickness) already presented as sample A in fig. 6.11 without (black solid lines, full symbols) and with (red dashed lines, open symbols) textured front cover attached to the glass. For the measurement without textured front cover the data for $1 - R_{\text{diffuse}}$ is also shown (black dotted line). The *EQE* derived photo current densities for the top and the bottom cell are added to the plot. The font color corresponds to the particular line/symbol color.

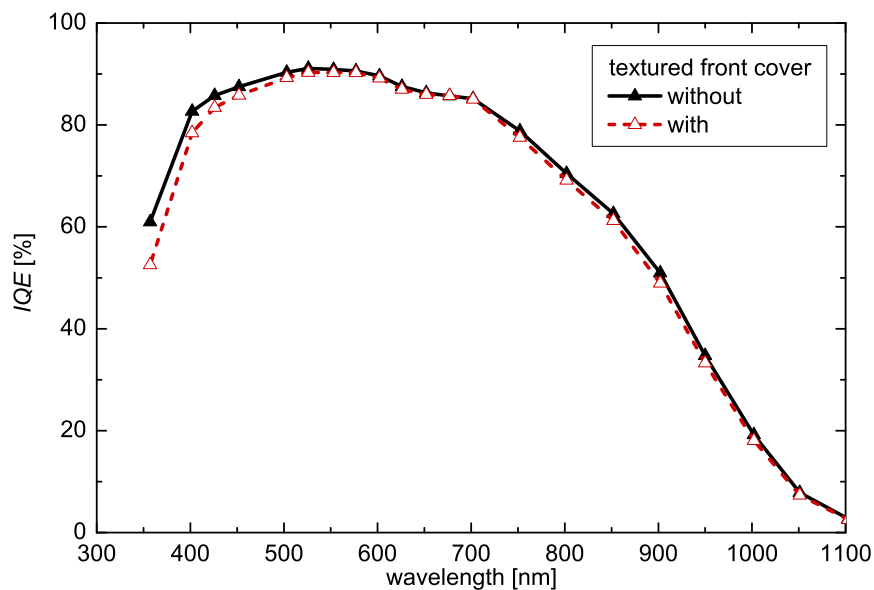


Figure 6.21: Internal quantum efficiency of the a-Si:H/ μ c-Si:H tandem cell already presented in fig. 6.20 without (black solid lines, full symbols) and with (red dashed lines, open symbols) textured front cover attached to the glass.

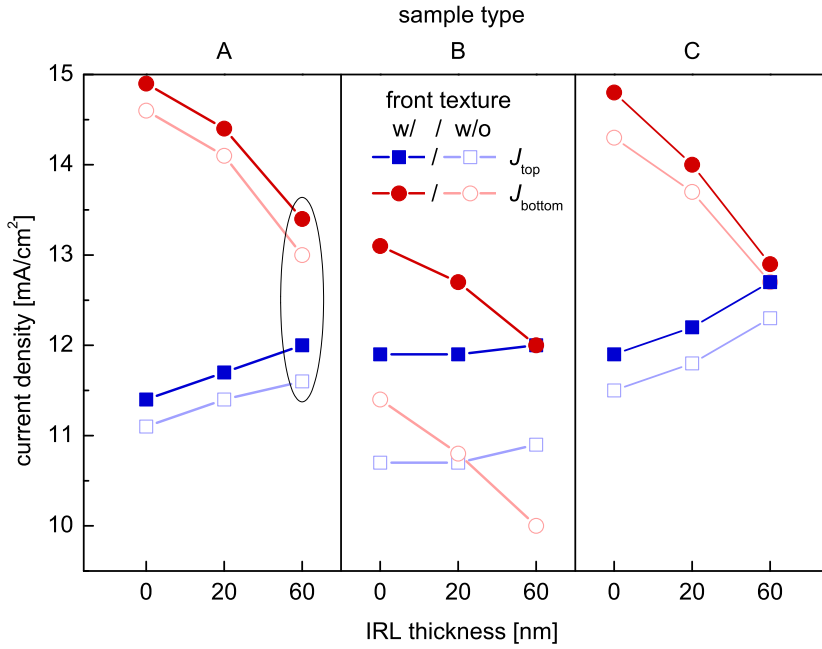


Figure 6.22: Photo current densities of a-Si:H/ μ c-Si:H tandem cells with different front texture/electrode types and varying IRL thickness as derived from J - V and EQE measurements. The particular cells incorporate a 250 nm thick, cap-annealed (500 °C/6 h) ZnO:Al layer on micro-textured glass (type A) and planar glass (type B) as well as our standard front-electrode consisting of a non-annealed, texture-etched ZnO:Al on planar glass (type C). The latter had a film thickness of 705 and \approx 420 nm before and after texturing, respectively. The data obtained without front texture (pale colors, open symbols) was already presented in fig. 6.18. The black oval marks the sample presented in fig. 6.20. The current densities are based on EQE measurements conducted at the large area setup. The lines are guides to the eye.

the front texture is similar to that observed for sample A and slightly increases for thinner IRLs.

Compared to sample A and C, sample B shows a remarkable gain in photo current density when the front texture is applied. This clearly demonstrates the added value of the retro-reflective light trapping effect provided by the front texture. In fact this was already demonstrated by Ulbrich *et al.*, but we would like to emphasize the remarkable level in photo current density reached with this texture: For a cell without any IRL a summed photo current density of 25 mA/cm² was achieved in an a-Si:H/ μ c-Si:H tandem cell *without any intended internal light scattering*.

Moreover, recall the superior electric performance observed for this cell type, despite having a front electrode consisting of only 250 nm thin (cap-annealed) ZnO:Al. Finally we obtained a median (over 20 cells) cell efficiency of 12.2/10.9 % (initial/after 168 h of light soaking) for these cells. For comparison the respective values for sample A and C were 11.3/10.1 % and 12.4/11.3 %, respectively.

To summarize the experiments with the millimeter-sized regular front texture, we generally observed an efficient suppression of the primary reflection at the air/glass interface

due to the geometrical anti-reflective effect of the texture. Comparing the results for cells on planar (B) and textured ZnO:Al (C) electrodes on planar glass we saw that the retro-reflective light trapping effect provided by the front texture strongly depends on the presence of an additional internal light scattering texture: If there is no internal texture (sample B) the front texture clearly provides light trapping, but if a reasonable light trapping is already provided by internal textures no additional improvement could be obtained by the texture. These findings nicely confirm the results of Ulbrich *et al.* [197, 200].

Moreover the separate measurement of diffuse and specular cell reflectance without front texture allowed us to directly evidence the different working principle of the AR- and the retro-reflecting-effect.

For the cells on the micro-textured glass substrates we could not observe any other benefit than the AR-effect. This is a bit surprising, since these samples, like those on planar glass and contrary to those on textured ZnO:Al, showed an insufficient light coupling. However, for these samples this shortfall could not be mitigated by the front texture. The reasons for that remain open questions.

For the flat cells (type B) the improvement due to the front texture yielded remarkable absolute values for the summed photo current density (25 mA/cm^2) and thanks to the flat interfaces also a reasonably high (median) efficiency of 12.2/10.9% (initial/after 168 h of light soaking). This (i) demonstrated the impressive light management capability of the particular front texture, (ii) showed that it is possible to achieve high cell efficiencies with ZnO:Al front electrodes as thin as 250 nm and (iii) nicely indicated the potential that lies in the attempt to introduce light management while circumventing layer growth on rough substrates (see e.g. [201]).

7 Achievements in Si-based Thin-film Cells and Modules

This section is dedicated to a brief overview on the achievements of Si-based thin-film cells and modules at PVcomB. Thereby, we will focus on the contribution of utilizing annealed ZnO:Al layers as front contact.

7.1 High Efficiency Tandem Cells and Modules

This section presents the results of the a-Si:H/ μ c-Si:H tandem devices, with the highest stabilized efficiency among all particular tandem devices made at PVcomB so far. Most of the results were already published in ref. [136].

The device types are as follows: (i) a *single cell* with an area of $1 \times 1 \text{ cm}^2$, like those used throughout this thesis up to here, (ii) a *mini module* with $10 \times 10 \text{ cm}^2$ total size comprising 12 monolithically interconnected single cells arranged on an *aperture area* of 63.4 cm^2 . The cell width was optimized for a minimal total loss with respect to ohmic losses in the front electrode and optical losses in the interconnect region, which is not contributing to cell performance (“dead area”). This resulted in a cell width of 6.6 mm including the $\approx 130 \mu\text{m}$ wide interconnect region (see ref. [120] for further information). (iii) The last device type, named *full size module*, had a total size of $30 \times 30 \text{ cm}^2$. It is actually just an up-scaled version of the mini module design, i.e. the number of single cells was increased from 12 to 41 and there length was adapted to fit the larger substrate size, resulting in an aperture area of 757.7 cm^2 . The width of the cells and the interconnect was left unchanged.

Besides the different layout, all three devices were processed in the same manner. Compared to our standard device, these devices had a thicker bottom cell i-layer ($2.8 \mu\text{m}$ instead of $2.2 \mu\text{m}$) and were processed on 2-step annealed ZnO:Al. Figure 7.1 shows (a) the *EQE* and (b) *J-V* curves of the single cell after 995 h of light soaking with textured front cover (cf. sec. 6.6) attached to the front glass. The *J-V* data for the same cell prior to light soaking is also shown in (b). The *EQE* measurement was conducted at the large area setup (cf. sec. 5.4). The according *J-V* parameters are listed in tab. 7.1 together with those of the mini module and the full size module. The efficiency of this particular cell after light soaking was also confirmed by an accredited laboratory (*ISE CalLab*, Germany). The *J-V* measurement of the full-size module was done in a different solar simulator (customized by *h.a.l.m. elektronik* Germany), which is suited for larger device dimensions.

Compared to some of the highest confirmed efficiency values reported so far for a-Si:H/ μ c-Si:H cells and modules (see e.g. ref. [202]) the values achieved with our devices are remarkable.

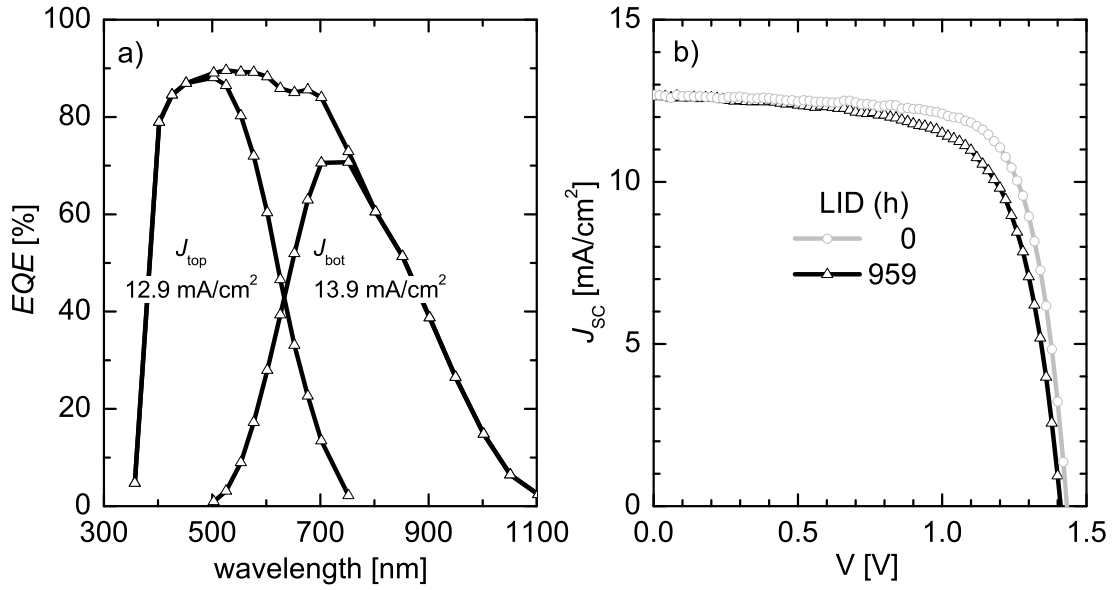


Figure 7.1: (a) External quantum efficiency and (b) J - V curve of the a-Si:H/ μ c-Si:H tandem cell with the highest stabilized efficiency among all cells made at PVcomB so far. The cell was subjected to light soaking for 995 h. The J - V curve of the same cell prior to light soaking is also added to (b) (grey line, circles). Compared to our standard device this cell had a thicker bottom cell i-layer ($2.8 \mu\text{m}$ instead of $2.2 \mu\text{m}$). It comprises a 2-step annealed ZnO:Al layer as front contact. The EQE derived photo current densities for the top and the bottom cell are added to the plot. The EQE measurement was conducted at the large area setup (cf. sec. 5.4) after light soaking.

Table 7.1: J - V parameters of the particular a-Si:H/ μ c-Si:H tandem devices with the highest stabilized efficiency among all devices made at PVcomB so far. The data for the particular device types single cell, mini module and full-size module is listed before and after light soaking for several weeks.

device	LID	J_{SC}	V_{OC}	FF	η
type	h	mA/cm^{-2}	mV	%	%
single cell	0	12.7	1432	73.2	13.3
(1 cm^2 active area)	995	12.6	1411	67.8	12.1
mini module , 12 cells	0	12.3	1425	72.8	12.8
(63.4 cm^2 aperture area)	939	12.1	1414	68.0	11.6
full-size module , 41 cells	0	11.8	1443	71.3	12.2
(757.7 cm^2 aperture area)	454	11.6	1412	64.5	10.6

7.2 Mini Modules on very thin, cap-annealed ZnO:Al layers

In sec. 6.5 we have presented the utilization of micro-textured glass substrates in combination with thin, cap-annealed ZnO:Al layer as an alternative front contact system. It turned out that this particular combination had a shortfall in terms of light coupling resulting in only

moderate cell performance. However, in the framework of his Master thesis [120] Welker used these substrates in a study based on mini modules. The question was, how far the transparency-sheet resistance trade-off can be pushed towards high transparency and sheet resistance, i.e. thin ZnO:Al layers, when an adaption of the cell width to the particular situation is used to mitigate the resistive loss.

The series is based on a thickness variation of cap-annealed ZnO:Al layers. The cell width (w) of a-Si:H/ μ c-Si:H tandem mini modules was adapted to the particular sheet resistance of the incorporated ZnO:Al layer. The width of the interconnect was kept constant at 180 μ m. Note that this experiment is based on an older version of our device. It comprises a 270 nm/1750 nm top and bottom cell i-layer thickness, a different top cell p-layer stack, which showed a higher parasitic absorptance and a thinner IRL (45 nm) processed with slightly different gas flow ratios. This is just mentioned in order to explain the generally lower efficiency level found for this series.

Table 7.2 lists the main results of this experiment. The reduced ZnO:Al layer thickness did not lead to a reduction in efficiency. This is first of all due to the cap-annealing, but also due to a mitigation of the resistive losses by decreasing the cell width. An efficiency above 10% was achieved with a ZnO:Al layer of only \approx 100 nm thickness for an adapted monolithically interconnected module design. For further details refer to the Master thesis of Welker [120].

Table 7.2: ZnO:Al layer properties, cell width and J - V parameters of single cells for a-Si:H/ μ c-Si:H tandem mini modules on micro-textured glass. The ZnO:Al layer thickness was determined by a step profiler. The J - V data relates to representative individual cells of a mini module. All J - V data is given with respect to the aperture cell area, i.e. includes the area loss due to the interconnect.

ZnO:Al treatment	d nm	R_S Ω	w mm	J_{SC} mA/cm ⁻²	V_{OC} mV	FF %	η %
cap-annealed	103	39.3	4.3	10.3	1386	72.6	10.4
cap-annealed	240	14.0	6.0	10.4	1381	73.8	10.6
initial (reference)	476	11.6	6.4	10.3	1370	73.5	10.4

8 Conclusions and Outlook

The aim of this thesis was to utilize the annealing-induced improvements in the opto-electronic properties of ZnO:Al layers in a-Si:H/ μ c-Si:H based solar cells. From previous material investigations a beneficial effect of ZnO:Al cap-annealing on cell performance was anticipated, but could not be demonstrated yet.

We successfully transferred the annealing procedure to our equipment and scaled it from small sample sizes to our standard substrate size of $300 \times 300 \text{ mm}^2$. This included the PECVD processes used for capping and decapping the samples, as well as the annealing of the ZnO:Al layers itself (sec. 3.1.5). At this time, the experiments were based on ZnO:Al layers provided by an industry partner. Later on, we extended the application to our in-house deposited ZnO:Al layers. This was an important step, since it allowed us to use the ZnO:Al layer thickness as an additional parameter for optimization.

In sec. 4.2 we conducted a systematic study on the influence of post deposition annealing on the opto-electronic properties of ZnO:Al layers. The study was based on variation of the ZnO:Al layer thickness (about 340 to 700 nm), as well as the temperatures and durations for both annealing steps, namely thermal degradation and subsequent cap-annealing. The use of Corning glass, in this case, allowed us to apply annealing temperatures up to $650 \text{ }^\circ\text{C}$.

The key findings of this study concerning the electronic properties were as follows:

- The cap-annealing, with or without preceding thermal degradation, generally resulted in an increased charge carrier mobility of up to $65 \frac{\text{cm}^2}{\text{Vs}}$ ($33 \frac{\text{cm}^2}{\text{Vs}}$ initial).
- Variations in the particular annealing temperatures and durations allowed a tuning of charge carrier density over a wide range (1 to $5.7 \cdot 10^{20} \text{ cm}^{-3}$).
- The lowest achieved resistivity was $2.1 \cdot 10^{-4} \Omega\text{cm}$ ($5.0 \cdot 10^{-4} \Omega\text{cm}$ initial), which is a remarkable value for a TCO, in particular for a DC-magnetron sputtered ZnO:Al grown on glass substrate. For this particular layer, this was accompanied by a reduced absorption throughout the whole observed wavelength range from 250 to 2500 nm.
- A reduction of the ZnO:Al layer thickness showed no significant influence in terms of the relative changes in mobility and charge carrier density upon annealing.
- An interesting exception to this was a higher stability against thermal degradation observed for thicker ZnO:Al films.

All these changes were realized in a *post-deposition* treatment and are not related to fundamental changes in the extended crystal structure. Therefore, ZnO:Al annealing also provides an experimental tool for investigation of the electronic transport in such layers.

Section 4.2.4 was dedicated to annealing-related changes in the optical properties of the ZnO:Al layers. Beside the well understood shift of the fundamental absorption edge (charge carrier density) and the variation in the free carrier absorption (charge carrier density and mobility), we also identified the reduction of a sub-band gap absorption, which was initially present in all films. The root cause for this sub-band gap absorption and its suppression upon annealing is yet not fully understood, but subjected to current investigations in our institute.

For samples that were exclusively cap-annealed we observed an additional absorption in the visible spectral range. This seems to relate to the high charge carrier density found for these samples. But, to date we found no explanation that could support this hypothesis.

Compared to a 700 nm thick ZnO:Al layer in the initial state, the application of the annealing procedure allowed, for instance,

- to decrease the sheet resistance from 7.2 to 3.1 Ω , while the thickness was kept constant and the absorptive losses still slightly decreased,
- to halve the layer thickness while the sheet resistance was maintained and the absorptive losses reasonably decreased,
- to strongly decrease the absorptive losses while the film thickness and the sheet resistance were kept constant.

A large variety in applied treatments and film thickness was also discussed in the context of a figure of merit and an implied photo current density loss. This allowed a more convenient interpretation of the data, in particular with respect to application of such layers in solar cells.

In sec. 4.3 the relation between annealing and wet-chemical surface texturing of the ZnO:Al layers was examined. When any annealing was carried out prior to the texture etching, the particular texture obtained was changed. From statistical surface analysis we could identify these changes as unfavorable both in terms of light scattering (flat regions) as well as high quality silicon growth (steep features). The latter was evidenced by a deterioration observed in V_{OC} and FF for cells grown on such substrates. Therefore, we decided to do the annealing generally after texture formation (if applied).

Another important question was addressed in sec. 6.1. From literature it was known, that the ZnO:Al/p-layer contact is a critical interface in a-Si:H based cells. It turned out that cells grown on 2-step annealed ZnO:Al layers directly after the capping was removed experienced a severe reduction in V_{OC} and FF . Additional experiments could exclude the capping/decapping procedure itself as a possible reason for this observation. This leads us to the assumption, that the effects Wimmer *et al.* observed [174,175] at the buried ZnO:Al/Si interface upon annealing remain to some extent even after the cap has been removed. Hence it has to be attributed to the annealing. When the ZnO:Al layers were shortly dipped in

diluted HCl the deterioration vanished and V_{OC} showed even an improvement compared to cells grown on non-annealed ZnO:Al layers. This is a hint to both a modification of the ZnO:Al surface and the bulk upon annealing. Based on this observation we included a HCl dip prior to cell deposition in our process.

The experiment presented in sec. 6.2, for the first time revealed the potential of this technique when applied in solar cells. A 2-step annealing was used to double the mobility and at the same time decrease the charge carrier density of a conventional ZnO:Al layer. This resulted in an improved cell efficiency of 12.1 % (11.4 % without annealing).

Section 6.3 addressed the question, to which extend the improved opto-electronic properties of ZnO-Al layers upon annealing can be used to allow a reduction of their thickness while, at least, maintaining cell efficiency on the reference level. We showed, that the ZnO:Al-layer thickness could be reduced from 820 nm to 550 nm without any loss in efficiency, by applying a cap-annealing to the thinner ZnO:Al film.

When we further reduced the ZnO:Al layer thickness, we experienced a limitation in the texture formation process. We were no longer able to obtain an appropriate light scattering texture by wet-chemical etching of the ZnO-Al layers. The opto-electronic properties of such thin ZnO:Al layers, on the other hand, were still suited for cell application.

To overcome this issue, we focused on the introduction of light scattering by utilizing micro-textured glass. In sec. 6.5.1 the surface topography of the particular micro-textured glass was evaluated and compared to that of a textured ZnO:Al, known to show good light scattering abilities. We observed similar RMS-roughness and lateral feature size, but different feature shape. The micro-textured glass exhibits bowl-like craters, whereas the reference ZnO:Al showed a V-shaped crater profile.

The ZnO:Al growth on top of the micro-textured glass yielded good film quality as examined by microscopical investigation and electronic transport measurements. Only a slight reduction in mobility could be observed. The light scattering properties of these textures, as observed by haze measurements, also turned out to be good.

Upon cap-annealing, the ≈ 250 nm thick ZnO:Al layers grown on micro textured glass still showed a significant improvement in conductivity, but in contrast to the films deposited on planar glass, the charge carrier mobility for the first time decreased. Obviously, the micro textured glass influenced the structural and electronic properties of the ZnO:Al layers. This point deserves further investigation.

In sec. 6.5.3 we implemented micro-textured glass coated with thin, cap-annealed ZnO:Al layers as front contact in a-Si:H/ μ c-Si:H cells and found high reflective losses comparable to those observed for cells on planar front electrodes. Observation of the diffuse and specular cell reflectance and comparison to different front electrode structures indicated that these losses to a certain extent are related to the rather conformal character of the thin ZnO:Al layer

in combination with the bowl-shaped surface topography, leading to noticeable interferential effects. An analog effect occurs in the top cell, this time with the reflection from the IRL. This was evidenced from variations in the IRL thickness, that led to changes in the intensity of some of those interferential effects. In consequence mainly the top cell current density is lacking from this effects, whereas the front texture seems to be able to introduce a good light trapping within the bottom cell.

Concerning the J - V data of these cells on micro-textured glass, the device quality of the Si-growth seems to suffer from the textured substrate, as indicated by lower values of V_{OC} compared to cells grown on standard texture-etched ZnO:Al layers.

In sec. 6.6 we investigate the application of a millimeter-sized, regular texture to the air/glass interface. This textures are known to exhibit a retro-reflecting effect that can be used to mitigate reflective losses from internal interfaces in a-Si:H/ μ c-Si:H cells. Beside the direct anti-reflective effect of this texture, we could not observe any benefit from applying it to cells on micro-textured glass. The reason for that is not clear and deserves further investigation.

For a-Si:H/ μ c-Si:H cells on planar front electrodes, on the other hand, there was a huge improvement in current density upon applying the front texture. With that, we were able to achieve an efficiency of 12.2/10.9 % (before/after 168 h of light soaking) on a planar front electrode comprising a 250 nm thick, cap-annealed ZnO:Al layer.

In sec. 7 we showed two exemplary routes for the successful application of annealed ZnO:Al films as electrodes in a-Si:H/ μ c-Si:H tandem cells. One route is dedicated to high efficiency devices and utilizes a 2-step annealing to reduce the parasitic absorption in the ZnO:Al layer. The other route is based on maximizing the conductivity to allow for very thin ZnO:Al films.

References

- [1] R. C. Chittick, J. H. Alexander, and H. F. Sterling, *Journal of The Electrochemical Society* **116**, 77 (1969).
- [2] W. Spear and P. Le Comber, *Solid State Communications* **17**, 1193 (1975).
- [3] W. Spear and P. Le Comber, *Philosophical Magazine* **33**, 935 (1976).
- [4] D. Carlson, C. Wronski, J. Pankove, P. Zanzucchi, and D. Staebler, *RCA Review* **38**, 211 (1977).
- [5] A. V. Shah et al., *Progress in Photovoltaics: Research and Applications* **12**, 113 (2004).
- [6] D. Redfield, *Applied Physics Letters* **25**, 647 (1974).
- [7] T. Tiedje, B. Abeles, J. M. Cebulka, and J. Pelz, *Applied Physics Letters* **42**, 712 (1983).
- [8] H. Deckman, C. Wronski, H. Witzke, and E. Yablonovitch, *Applied Physics Letters* **42**, 968 (1983).
- [9] O. Kluth et al., *Thin Solid Films* **351**, 247 (1999).
- [10] A. Löffl et al., *Solid State Phenomena* **67-8**, 277 (1999).
- [11] M. Berginski et al., *Journal of Applied Physics* **101**, 074903 (2007).
- [12] K. Y. Lee et al., *Applied Physics Letters* **91**, 241911 (2007).
- [13] F. Ruske et al., *Journal of Applied Physics* **107**, 013708 (2010).
- [14] M. Wimmer, F. Ruske, S. Scherf, and B. Rech, *Thin Solid Films* **520**, 4203 (2012).
- [15] J. Bass, 1.2.2 Pure metal resistivities from $T = 10 - 15$ K till melting point, in *Landolt-Börnstein - Group III Condensed Matter*, edited by K.-H. Hellwege and J. L. Olsen, volume 15a, SpringerMaterials - The Landolt-Börnstein Database, 2014.
- [16] G. J. Exarhos and X.-D. Zhou, *Thin Solid Films* **515**, 7025 (2007).
- [17] H. Agura, A. Suzuki, T. Matsushita, T. Aoki, and M. Okuda, *Thin Solid Films* **445**, 263 (2003).
- [18] K. Ellmer and A. Klein, *Transparent Conductive Zinc Oxide*, volume 104 of *Springer series in material Science*, chapter 1, Springer Berlin Heidelberg New York, 2008.
- [19] K. Ellmer, *Journal of Physics D: Applied Physics* **34**, 3097 (2001).
- [20] C. Agashe et al., *Journal of Applied Physics* **95**, 1911 (2004).
- [21] B. Szyszka, *Vakuum in Forschung und Praxis* **13**, 38 (2001).
- [22] T. Minami, H. Nanto, and S. Takata, *Applied Physics Letters* **41**, 958 (1982).
- [23] T. Minami, H. Nanto, S. Shooji, and S. Takata, *Thin Solid Films* **111**, 167 (1984).
- [24] T. Minami, *MRS Bulletin* **25**, 38 (2000).
- [25] E. Mollwo, *Zeitschrift für Physik* **138**, 478 (1954).
- [26] C. Van De Walle, *Physical Review B* **85**, 1012 (2000).

- [27] N. Mott, Proceedings of the Royal Society of London. Series A: Mathematical and Physical Sciences **382**, 1 (1982).
- [28] P. Drude, Annalen der Physik **306**, 566 (1900).
- [29] D. C. Look et al., Physical Review B **84**, 115202 (2011).
- [30] T. Minami, S. Suzuki, and T. Miyata, Electrical conduction mechanism of highly transparent and conductive ZnO thin films, in *Materials Research Society Symposium - Proceedings*, volume 666, pages F131–F137, 2001.
- [31] K. Chopra, S. Major, and D. Pandya, Thin Solid Films **102**, 1 (1983).
- [32] H. Brooks, Advances in Electronics and Electron Physics **7**, 85 (1955).
- [33] R. Dingle, Philosophical Magazine Series 7 **46**, 831 (1955).
- [34] E. Conwell and V. F. Weisskopf, Physical Review **77**, 388 (1950).
- [35] T. Pisarkiewicz, K. Zakrzewska, and E. Leja, Thin Solid Films **174**, 217 (1989).
- [36] J. Seto, Journal of Applied Physics **46**, 5247 (1975).
- [37] K. Ellmer and R. Mientus, Thin Solid Films **516**, 4620 (2008).
- [38] F. Ruske, *Magnetronspütern von hochleitfähigen ZnO:Al-Schichten für die Photovoltaik*, PhD thesis, Fraunhofer IST Braunschweig, 2008.
- [39] L. Ding, *Low-Pressure Chemical Vapor Deposited Zinc Oxide Films: Toward Decoupled Opto-Electrical and Morphological Properties for More Efficient Electrodes*, PhD thesis, École polytechnique fédérale de Lausanne, 2013.
- [40] S. Myong et al., Solar Energy Materials and Solar Cells **91**, 1269 (2007).
- [41] J. Steinhauser, S. Fay, N. Oliveira, E. Vallat-Sauvain, and C. Ballif, Applied Physics Letters **90**, 142107 (2007).
- [42] J. Steinhauser et al., Physica Status Solidi A **205**, 1983 (2008).
- [43] B. E. Sernelius, K. F. Berggren, Z. C. Jin, I. Hamberg, and C. G. Granqvist, Physical Review B **37**, 10244 (1988).
- [44] M. Berginski, *Lichtstreuende Oberflächen, Schichten und Schichtsysteme zur Verbesserung der Lichteinkopplung in Silizium-Dünnschichtsolarzellen*, PhD thesis, RWTH Aachen, 2007.
- [45] A. Pflug, V. Sittinger, F. Ruske, B. Szyszka, and G. Dittmar, Thin Solid Films **455-456**, 201 (2004).
- [46] Z.-C. Jin, I. Hamberg, and C. Granqvist, Journal of Applied Physics **64**, 5117 (1988).
- [47] D. Greiner, *Ursache der Leitfähigkeitsabnahme nach künstlicher Alterung in feuchter Wärme bei hochdotierten Zinkoxid-Schichten für die Dünnschichtfotovoltaik*, PhD thesis, FU Berlin, 2010.
- [48] J. Leng, J. Opsal, H. Chu, M. Senko, and D. Aspnes, Thin Solid Films **313-314**, 132 (1998).
- [49] I. Hamberg and C. G. Granqvist, Journal of Applied Physics **60**, R123 (1986).

- [50] E. Gerlach, *Journal of Physics C: Solid State Physics* **19**, 4585 (1986).
- [51] D. A. G. Bruggeman, *Annalen der Physik* **416**, 636 (1935).
- [52] S. Gall and B. Rech, *Solar Energy Materials and Solar Cells* **119**, 306 (2013).
- [53] C. Becker et al., *Solar Energy Materials and Solar Cells* **119**, 112 (2013).
- [54] S. Varlamov et al., *Solar Energy Materials and Solar Cells* **119**, 246 (2013).
- [55] F. Meillaud, A. Shah, C. Droz, E. Vallat-Sauvain, and C. Miazza, *Solar Energy Materials and Solar Cells* **90**, 2952 (2006).
- [56] J. Meier et al., On the way towards high efficiency thin film silicon solar cells by the "micromorph" concept, in *Materials Research Society Symposium - Proceedings*, volume 420, pages 3–14, 1996.
- [57] S. M. Sze, *Physics of Semiconductor Devices*, John Wiley & Sons, Inc., 2nd edition, 1981.
- [58] A. Poruba et al., *Journal of Applied Physics* **88**, 148 (2000).
- [59] N. Beck et al., Optical and electrical properties of undoped microcrystalline silicon deposited by the VHF-GD with different dilutions of silane in hydrogen, in *Materials Research Society Symposium - Proceedings*, volume 452, pages 761–766, 1997.
- [60] R. A. Street, *Hydrogenated amorphous silicon*, Cambridge solid state science series, Cambridge University Press, 1991.
- [61] J. Tauc, R. Grigorovici, and A. Vancu, *Physica Status Solidi B* **15**, 627 (1966).
- [62] D. L. Staebler and C. R. Wronski, *Applied Physics Letters* **31**, 292 (1977).
- [63] M. Stutzmann, W. B. Jackson, and C. C. Tsai, *Physical Review B* **32**, 23 (1985).
- [64] M. J. Powell and S. C. Deane, *Physical Review B* **48**, 10815 (1993).
- [65] H. M. Branz, *Physical Review B* **59**, 5498 (1999).
- [66] H. Fritzsche, *Annual Review of Materials Research* **31**, 47 (2001).
- [67] A. H. M. Smets, W. M. M. Kessels, and M. C. M. van de Sanden, *Applied Physics Letters* **82**, 1547 (2003).
- [68] M. Fehr et al., *Physical Review B* **84**, 245203 (2011).
- [69] J. Melskens et al., *IEEE Journal of Photovoltaics* **3**, 65 (2013).
- [70] O. Vetterl et al., *Solar Energy Materials and Solar Cells* **62**, 97 (2000).
- [71] A. Shah, *Thin-Film Silicon Solar Cells*, chapter 4, page 207, EPFL Press, 1st edition, 2010.
- [72] R. S. Crandall, *Journal of Applied Physics* **54**, 7176 (1983).
- [73] J. Merten et al., *IEEE Transactions on Electron Devices* **45**, 423 (1998).
- [74] J. Müller, B. Rech, J. Springer, and M. Vanecek, *Solar Energy* **77**, 917 (2004).
- [75] S. Fay et al., *Solar Energy Materials and Solar Cells* **90**, 2960 (2006).

- [76] S. Hegedus, W. Buchanan, X. Liu, and R. Gordon, Effect of textured tin oxide and zinc oxide substrates on the current generation in amorphous silicon solar cells, in *Conference Record of the IEEE Photovoltaic Specialists Conference*, pages 1129–1132, 1996.
- [77] J. Krc et al., *Thin Solid Films* **518**, 3054 (2010).
- [78] O. Kluth et al., *Thin Solid Films* **442**, 80 (2003).
- [79] S. Fay, U. Kroll, C. Bucher, E. Vallat-Sauvain, and A. Shah, *Solar Energy Materials and Solar Cells* **86**, 385 (2005).
- [80] S. Fay, J. Steinhauser, S. Nicolay, and C. Ballif, *Thin Solid Films* **518**, 2961 (2010).
- [81] S. Nicolay, M. Despeisse, F.-J. Haug, and C. Ballif, *Solar Energy Materials and Solar Cells* **95**, 1031 (2011).
- [82] S. Nicolay et al., *Solar Energy Materials and Solar Cells* **105**, 46 (2012).
- [83] H. Liang and R. Gordon, *Journal of Materials Science* **42**, 6388 (2007).
- [84] D. Sheel et al., *Thin Solid Films* **517**, 3061 (2009).
- [85] Y. Nasuno, M. Kondo, and A. Matsuda, *Japanese Journal of Applied Physics, Part 2: Letters & Express Letters* **40**, L303 (2001).
- [86] H. B. T. Li, R. H. Franken, J. K. Rath, and R. E. I. Schropp, *Solar Energy Materials and Solar Cells* **93**, 338 (2009).
- [87] M. Despeisse et al., *Physica Status Solidi A* **208**, 1863 (2011).
- [88] C. K. Carniglia, *Optical Engineering* **18**, 182104 (1979).
- [89] O. Isabella, J. Krc, and M. Zeman, *Applied Physics Letters* **97**, 101106 (2010).
- [90] H. Stiebig et al., Light trapping in thin-film silicon solar cells by nano-textured interfaces, in *Proceedings of SPIE - The International Society for Optical Engineering*, volume 6197, page 619701, 2006.
- [91] C. Rockstuhl et al., *Optics Express* **18**, A335 (2010).
- [92] M. Zeman, R. A. C. M. M. van Swaaij, J. W. Metselaar, and R. E. I. Schropp, *Journal of Applied Physics* **88**, 6436 (2000).
- [93] J. Krc, M. Zeman, O. Kluth, F. Smole, and M. Topic, *Thin Solid Films* **426**, 296 (2003).
- [94] D. Dominé, F. J. Haug, C. Battaglia, and C. Ballif, *Journal of Applied Physics* **107**, 044504 (2010).
- [95] N. Sahraei, K. Forberich, S. Venkataraj, A. Aberle, and M. Peters, *Optics Express* **22**, A53 (2014).
- [96] C. Rockstuhl, F. Lederer, K. Bittkau, and R. Carius, *Applied Physics Letters* **91**, 171104 (2007).
- [97] D. Lockau et al., Rigorous optical simulation of light management in crystalline silicon thin film solar cells with rough interface textures, in *Proceedings of SPIE - The International Society for Optical Engineering*, volume 7933, page 79330M, 2011.

- [98] M. Hammerschmidt et al., FEM-based optical modeling of silicon thin-film tandem solar cells with randomly textured interfaces in 3D, in *Proceedings of SPIE - The International Society for Optical Engineering*, volume 8620, page 86201H, 2013.
- [99] S. Kirner et al., *IEEE Journal of Photovoltaics* **4**, 10 (2014).
- [100] E. Yablonovitch and G. Cody, *IEEE Transactions on Electron Devices* **29**, 300 (1982).
- [101] D. Dominé, *The role of front electrodes and intermediate reflectors in the optoelectronic properties of high-efficiency micromorph solar cells*, PhD thesis, École polytechnique fédérale de Lausanne, 2009.
- [102] T. Tiedje, E. Yablonovitch, G. Cody, and B. Brooks, *IEEE Transactions on Electron Devices* **31**, 711 (1984).
- [103] M. Berginski et al., *Solar Energy Materials and Solar Cells* **92**, 1037 (2008).
- [104] P. Cuony et al., *Advanced Materials* **24**, 1182 (2012).
- [105] P. Cuony et al., *Applied Physics Letters* **97**, 213502 (2010).
- [106] K. Yamamoto et al., *Solar Energy Materials and Solar Cells* **74**, 449 (2002).
- [107] S. Kirner, *Development of Wide Band Gap Materials for Thin Film Silicon Solar Cells*, PhD thesis, TU Berlin, 2013.
- [108] S. Kirner et al., *Physica Status Solidi C* **9**, 2145 (2012).
- [109] N. Borrelli, D. Hall, G. Kohnke, and S. Marjanovic, Textured superstrates for photovoltaics, 2011, US Patent App. 12/955,126.
- [110] J. Steinhauser et al., *Thin Solid Films* **520**, 1218 (2011).
- [111] H. Tan et al., *Applied Physics Letters* **103**, (2013).
- [112] N. Sahraei, S. Venkataraj, A. Aberle, and M. Peters, Optimum feature size of randomly textured glass substrates for maximum scattering inside thin-film silicon solar cells, in *Proceedings of SPIE - The International Society for Optical Engineering*, volume 8981, page 89811D, 2014.
- [113] A. Bessonov et al., *Solar Energy Materials and Solar Cells* **95**, 2886 (2011).
- [114] C. Battaglia et al., *Nano Letters* **11**, 661 (2011).
- [115] M. Meier et al., *Progress in Photovoltaics: Research and Applications* **22**, 1226 (2014).
- [116] J. Bailat et al., Recent Developments of High-Efficiency Micromorph® Tandem Solar Cells in KAI-M PECVD Reactors, in *Proceedings of the 25th European Photovoltaic Solar Energy Conference and Exhibition / 5th World Conference on Photovoltaic Energy Conversion*, 2010.
- [117] S. Jäger, B. Szyszka, J. Szczyrbowski, and G. Bräuer, *Surface and Coatings Technology* **98**, 1304 (1998).
- [118] B. Szyszka, *Thin Solid Films* **351**, 164 (1999).
- [119] M. Ruske, G. Bräuer, J. Pistner, J. Szczyrbowski, and M. Weigert, *Thin Solid Films* **351**, 158 (1999).

- [120] F. Welker, A systematic study of opto-electric properties of annealed zno:al for application in high efficiency a-si/ μ c-si based solar modules, Master thesis, TU Berlin, 2014.
- [121] O. Gabriel, S. Kirner, M. Klick, B. Stannowski, and R. Schlatmann, *European Physical Journal Photovoltaics* **5**, 55202 (2014).
- [122] S. Kirner, O. Gabriel, B. Stannowski, B. Rech, and R. Schlatmann, *Applied Physics Letters* **102**, 051906 (2013).
- [123] M. Rohde et al., *Thin Solid Films* **558**, 337 (2014).
- [124] K. Schwanitz et al., *Solar Energy Materials and Solar Cells* **105**, 187 (2012).
- [125] J. Springer et al., *Journal of Applied Physics* **95**, 1427 (2004).
- [126] L. J. van der Pauw, *Philips Research Reports* **13**, 1 (1958).
- [127] L. J. van der Pauw, *Philips Technical Review* **20**, 220 (1958).
- [128] M. Wimmer, *Thermische Nachbehandlung von aluminiumdotiertem Zinkoxid und die Silizium/Zinkoxid-Grenzfläche*, PhD thesis, TU Berlin, 2011.
- [129] <http://www.nist.gov/pml/div683/hall.cfm>, retrieved at June 27th 2014.
- [130] <http://gwyddion.net/>, retrieved at June 27th 2014.
- [131] International Standard IEC 60904-3 ed2.0: Photovoltaic devices - Part 3: Measurement principles for terrestrial photovoltaic (PV) solar devices with reference spectral irradiance data (International Electrotechnical Commission), 2008.
- [132] International Standard IEC 60904-9 ed2.0: Photovoltaic devices - Part 9: Solar simulator performance requirements (International Electrotechnical Commission), 2007.
- [133] T. Hänel, *Spannungs- und intensitätsabhängige spektrale Empfindlichkeit von poly-Si Dünnschichtsolarzellen*, Diploma thesis, HTW (former FHTW) Berlin, 2008.
- [134] M. Pravettoni, R. Galleano, A. Virtuani, H. Müllejjans, and E. D. Dunlop, *Measurement Science and Technology* **22**, 045902 (2011).
- [135] A. Shah and M. Python, *Thin-Film Silicon Solar Cells*, chapter 5, pages 255–264, EPFL Press, 1st edition, 2010.
- [136] B. Stannowski et al., *Solar Energy Materials and Solar Cells* **119**, 196 (2013).
- [137] M. Heckmann, *Reversible und irreversible Degradation in a-Si:H Solarzelle*, Master thesis, TU Berlin, 2012.
- [138] C. Lennon, R. Kodama, Y. Chang, S. Sivananthan, and M. Deshpande, *Journal of Vacuum Science and Technology B: Microelectronics and Nanometer Structures* **27**, 1641 (2009).
- [139] S. Ghosh, A. Sarkar, S. Bhattacharya, S. Chaudhuri, and A. Pal, *Journal of Crystal Growth* **108**, 534 (1991).
- [140] J. Chang, W. Lin, and M. Hon, *Applied Surface Science* **183**, 18 (2001).
- [141] B. Du Ahn et al., *Journal of Crystal Growth* **309**, 128 (2007).

- [142] X. Yu et al., *Thin Solid Films* **483**, 296 (2005).
- [143] Y. Igasaki, M. Ishikawa, and G. Shimaoka, *Applied Surface Science* **33-34**, 926 (1988).
- [144] T. Minami, T. Miyata, and T. Yamamoto, *Journal of Vacuum Science and Technology A: Vacuum, Surfaces and Films* **17**, 1822 (1999).
- [145] S. Takata, T. Minami, and H. Nanto, *Thin Solid Films* **135**, 183 (1986).
- [146] M. Berginski et al., Zno films with tailored material properties for highly efficient thin-film silicon solar modules, in *Proceedings of the 21st European Photovoltaic Solar Energy Conference and Exhibition*, pages 1539–1545, WIP-Renewable Energies, 2006.
- [147] M. Roczen, *Elektrische und optische Charakterisierung von temperaturstabilem ZnO:Al als transparente leitfähige Oxidschicht für Dünnschichtsolarzellen*, Diploma thesis, HU Berlin, 2009.
- [148] T. Minami, *Semiconductor Science and Technology* **20**, S35 (2005).
- [149] T. Yamada, H. Makino, N. Yamamoto, and T. Yamamoto, *Journal of Applied Physics* **107**, 123534 (2010).
- [150] S. B. Krupanidhi and M. Sayer, *Journal of Applied Physics* **56**, 3308 (1984).
- [151] S. Takada, *Journal of Applied Physics* **73**, 4739 (1993).
- [152] L.-J. Meng and M. dos Santos, *Thin Solid Films* **250**, 26 (1994).
- [153] E. Bachari, G. Baud, S. B. Amor, and M. Jacquet, *Thin Solid Films* **348**, 165 (1999).
- [154] S. K. Gupta, *Journal of Applied Crystallography* **31**, 474 (1998).
- [155] S. Lany and A. Zunger, *Physical Review Letters* **98**, 045501 (2007).
- [156] J. H. Noh et al., *Journal of Applied Physics* **104**, 073706 (2008).
- [157] S. Schönau, F. Ruske, S. Neubert, and B. Rech, *Applied Physics Letters* **103**, 192108 (2013).
- [158] S. Schönau, F. Ruske, S. Neubert, and B. Rech, *Physica Status Solidi C* **11**, 1468–1471 (2014).
- [159] F. Ruske et al., Material properties of high-mobility TCOs and application to solar cells, in *Proceedings of SPIE - The International Society for Optical Engineering*, volume 8987, page 898723, 2014.
- [160] F. Urbach, *Physical Review* **92**, 1324 (1953).
- [161] S. Schönau, to be published, PhD thesis.
- [162] T. J. Coutts, D. L. Young, and T. A. Gessert, *Handbook of Transparent Conductors*, chapter 3, Springer, 2010.
- [163] B. Szyszka, *Transparent Conductive Zinc Oxide*, volume 104 of *Springer series in material Science*, chapter 5, Springer Berlin Heidelberg New York, 2008.
- [164] J. Wang et al., *Thin Solid Films* **515**, 8780 (2007).
- [165] G. Haacke, *Journal of Applied Physics* **47**, 4086 (1976).
- [166] T. M. Barnes et al., *Advanced Energy Materials* **2**, 353 (2012).

- [167] V. K. Jain and A. P. Kulshreshtha, *Solar Energy Materials* **4**, 151 (1981).
- [168] R. G. Gordon, *MRS Bulletin* **25**, 52 (2000).
- [169] M. Boccard, P. Cuony, C. Battaglia, M. Despeisse, and C. Ballif, *Physica Status Solidi - Rapid Research Letters* **4**, 326 (2010).
- [170] E. Böhmer, F. Siebke, and H. Wagner, *Fresenius' Journal of Analytical Chemistry* **358**, 210 (1997).
- [171] H. Stiebig et al., *Solar Energy Materials and Solar Cells* **48**, 351 (1997).
- [172] F.-J. Haug et al., *Progress in Photovoltaics: Research and Applications* **20**, 727 (2012).
- [173] M. Bär et al., *Applied Physics Letters* **97**, (2010).
- [174] M. Wimmer et al., *Applied Physics Letters* **99**, 152104 (2011).
- [175] M. Wimmer et al., *Journal of Electron Spectroscopy and Related Phenomena* **190**, 309 (2013).
- [176] D. Gerlach et al., *Applied Physics Letters* **103**, 023903 (2013).
- [177] F. Einsele, P. Rostan, M. Schubert, and U. Rau, *Journal of Applied Physics* **102**, 094507 (2007).
- [178] A. Kanevce and W. Metzger, *Journal of Applied Physics* **105**, 094507 (2009).
- [179] M. Bivour, C. Reichel, M. Hermle, and S. Glunz, *Solar Energy Materials and Solar Cells* **106**, 11 (2012).
- [180] R. Rößler, C. Leendertz, L. Korte, N. Mingirulli, and B. Rech, *Journal of Applied Physics* **113**, 144513 (2013).
- [181] R. Rößler, *Transparente leitfähige Oxide (TCO) in Silizium-Heterostruktursolarzellen: Elektronische Eigenschaften des TCO/a-Si:H Kontakts*, PhD thesis, TU Berlin, 2013.
- [182] H. Schade, Z. E. Smith, J. Thomas III, and A. Catalano, *Thin Solid Films* **117**, 149 (1984).
- [183] M. Kubon et al., *Solar Energy Materials and Solar Cells* **41-42**, 485 (1996).
- [184] H. Wanka, E. Lotter, and M. Schubert, Characterization and optimization of the TCO/a-Si:H(B) interface for solar cells by in-situ ellipsometry and SIMS/XPS depth profiling, in *Materials Research Society Symposium - Proceedings*, volume 336, pages 657–662, 1994.
- [185] C. Becker et al., *Journal of Applied Physics* **106**, 084506 (2009).
- [186] R. Schaeffler and H. Schock, High mobility ZnO:Al thin films grown by reactive DC magnetron sputtering, in *Conference Record of the IEEE Photovoltaic Specialists Conference*, pages 1026–1030, 1993.
- [187] S. Neubert et al., *Progress in Photovoltaics: Research and Applications* **22**, 1285 (2014).
- [188] T. Repmann, *Stapelsolarzellen aus amorphem und mikrokristallinem Silizium*, PhD thesis, RWTH Aachen, 2003.
- [189] J. Hüpkens, J. Owen, S. Pust, and E. Bunte, *ChemPhysChem* **13**, 66 (2012).

-
- [190] J. I. Owen, *Growth, Etching, and Stability of Sputtered ZnO:Al for Thin-Film Silicon Solar Cells*, PhD thesis, RWTH Aachen, 2011.
- [191] S. Neubert et al., *Physica Status Solidi - Rapid Research Letters* **8**, 44 (2014).
- [192] I. Sieber et al., *Thin Solid Films* **330**, 108 (1998).
- [193] D. Greiner, N. Papathanasiou, A. Pflug, F. Ruske, and R. Klenk, *Thin Solid Films* **517**, 2291 (2009).
- [194] W. Zhang et al., *Energy Procedia* **44**, 151 (2014).
- [195] P. Campbell and M. Green, *Journal of Applied Physics* **62**, 243 (1987).
- [196] J. Escarré et al., *Solar Energy Materials and Solar Cells* **98**, 185 (2012).
- [197] C. Ulbrich, A. Gerber, K. Hermans, A. Lambertz, and U. Rau, *Progress in Photovoltaics: Research and Applications* **21**, 1672 (2013).
- [198] J. Bailat et al., High-efficiency p-i-n microcrystalline and micromorph thin film silicon solar cells deposited on LPCVD ZnO coated glass substrates, in *Conference Record of the 2006 IEEE 4th World Conference on Photovoltaic Energy Conversion, Vols 1 and 2*, pages 1533–1536, 2006.
- [199] M. Despeisse et al., *Applied Physics Letters* **96**, 073507 (2010).
- [200] C. Ulbrich, *Spectral and directional dependence of light-trapping in solar cells*, PhD thesis, RWTH Aachen, 2011.
- [201] K. Söderström, G. Bugnon, F. J. Haug, S. Nicolay, and C. Ballif, *Solar Energy Materials and Solar Cells* **101**, 193 (2012).
- [202] A. Shah, E. Moulin, and C. Ballif, *Solar Energy Materials and Solar Cells* **119**, 311 (2013).

List of Publications

Related to this Thesis

S. Neubert, S. Ring, F. Welker, S. Götzendörfer, F. Ruske, B. Stannowski, R. Schlatmann and B. Rech, *Very thin, highly-conductive ZnO: Al front electrode on textured glass as substrate for thin-film silicon solar cells*, Physica Status Solidi - Rapid Research Letters **8**, 44-47 (2014).

S. Neubert, M. Wimmer, F. Ruske, S. Calnan, O. Gabriel, B. Stannowski, R. Schlatmann and B. Rech, *Improved conversion efficiency of a-Si: H/ μ c-Si: H thin-film solar cells by using annealed Al-doped zinc oxide as front electrode material*, Progress in Photovoltaics: Research and Applications **22**, 1285-1291 (2014).

F. Ruske, S. Schönau, S. Ring, S. Neubert, B. Stannowski, V. Sittinger, S. Götzendörfer and B. Rech, *Material properties of high-mobility TCOs and application to solar cells*, Proceedings of SPIE - The International Society for Optical Engineering, 8987 (2014).

B. Stannowski, F. Ruske, S. Neubert, S. Schönau, S. Ring, S. Calnan, M. Wimmer, O. Gabriel, B. Szyszka, B. Rech and R. Schlatmann, *Potential of high-mobility sputtered zinc oxide as front contact for high efficiency thin film silicon solar cells*, Thin Solid Films **555**, 138-142 (2014).

B. Stannowski, O. Gabriel, S. Calnan, T. Frijnts, A. Heidelberg, S. Neubert, S. Kirner, S. Ring, M. Zelt, B. Rau, J.-H. Zollondz, H. Bloess, R. Schlatmann and B. Rech, *Achievements and challenges in thin film silicon module production*, Solar Energy Materials and Solar Cells **119**, 196-203 (2013).

S. Schönau, F. Ruske, S. Neubert and B. Rech, *Annealing related changes in near-edge absorption and structural properties of Al-doped ZnO thin films*, Physica Status Solidi C **11** (9-10), 1468-1471 (2014).

S. Schönau, F. Ruske, S. Neubert and B. Rech, *Analysis of Urbach-like absorption tails in thermally treated ZnO:Al thin films*, Applied Physics Letters **103**, 192108 (2013).

S. Schönau, F. Ruske, S. Neubert and B. Rech, *Investigation of band tailing in sputtered ZnO:Al thin films regarding structural properties and impurities*, MRS Proceedings, 1699 (2014).

F. Ruske, R. Röfler, M. Wimmer, S. Schönau, S. Kämpfer, M. Hendrichs, S. Neubert, L. Korte and B. Rech, *ZnO:Al with tuned properties for photovoltaic applications: Thin layers and high mobility material*, Proceedings of SPIE - The International Society for Optical Engineering, 8626 (2013).

Other Publications

M. Rohde, M. Zelt, O. Gabriel, S. Neubert, S. Kirner, D. Severin, T. Stolley, B. Rau, B. Stannowski and R. Schlatmann, *Plasma enhanced chemical vapor deposition process optimization for thin film silicon tandem junction solar cells*, Thin Solid Films **558**, 337-343 (2014).

S. Ring, S. Neubert, F. Ruske, B. Stannowski, F. Fink and R. Schlatmann, *Direct pulsed laser interference texturing for light trapping in a-Si:H/ μ c-Si:H tandem solar cells*, Proceedings of SPIE - The International Society for Optical Engineering, 9140 (2014).

- S. Ring, S. Neubert, C. Schultz, S. S. Schmidt, F. Ruske, B. Stannowski, F. Fink and R. Schlatmann, *Light trapping for a-Si:H/ μ c-Si:H tandem solar cells using direct pulsed laser interference texturing*, Physica Status Solidi - Rapid Research Letters **9**, 36-40 (2015).
- S. Kirner, M. Hammerschmidt, C. Schwanke, D. Lockau, S. Calnan, T. Frijnts, S. Neubert, A. Schopke, F. Schmidt, J.-H. Zollondz, A. Heidelberg, B. Stannowski, B. Rech and R. Schlatmann, *Implications of TCO topography on intermediate reflector design for a-si/ μ c-si tandem solar cells-experiments and rigorous optical simulations*, IEEE Journal of Photovoltaics **4**, 10-15 (2014).
- S. Kirner, S. Calnan, O. Gabriel, S. Neubert, M. Zelt, B. Stannowski, B. Rech and R. Schlatmann, *An improved silicon-oxide-based intermediate-reflector for micromorph solar cells*, Physica Status Solidi (C) **9**, 2145-2148 (2012).
- S. Calnan, S. Neubert, C. Nock, O. Gabriel, M. Rohde, F. Ruske, B. Stannowski and R. Schlatmann, *Detailed comparison of transparent front contacts for thin film silicon solar cells*, Conference Record of the IEEE Photovoltaic Specialists Conference, 579-584 (2011).
- S. Albrecht, B. Grootenk, S. Neubert, S. Roland, J. Wördenweber, M. Meier, R. Schlatmann, A. Gordijn and D. Neher, *Efficient hybrid inorganic/organic tandem solar cells with tailored recombination contacts*, Solar Energy Materials and Solar Cells **127**, 157-162 (2014).
- S. Roland, S. Neubert, S. Albrecht, B. Stannowski, M. Seger, A. Facchetti, R. Schlatmann, B. Rech and D. Neher, *Hybrid Organic/Inorganic Thin Film Multi-Junction Solar Cells approaching exceeding 11% Power Conversion Efficiency*, Advanced Materials Communication **27**, 1262-1267 (2015).
- S. Ring, S. Neubert, B. Stannowski, *a-Si/ μ c-Si module performance dependence on homogeneity: A study using I-V panel mapping*, Proceedings of the 25th EUPVSEC, Valencia (2010).
- A. Schulze, B. Hüttel, S. Neubert, B. Hund, J. Luschitz, T. Patzlaff, *2D-Analysis of Thin-Film Modules*, Proceedings of the 25th EUPVSEC, Valencia (2010).

Acknowledgements

These lines are dedicated to those who contributed to this work.

First I would like to thank Prof. Dr. Bernd Rech for supervising this thesis and the inspiring feedback he always had.

I am also very grateful to Prof. Dr. Rutger Schlatmann who initially gave me the chance to do my PhD at the PVcomB.

My sincere thanks to Prof. Dr. Christophe Ballif and Prof. Dr. Mario Dähne for kindly accepting to report on this thesis.

Special thanks go to Dr. Bernd Stannowski for the continuous guidance, support, confidence and friendship you provided to me since my very first days in the exciting world of Si-based thin-film PV. Working with you was always a pleasure to me.

Dr. Florian Ruske is acknowledged for his everlasting willingness to share his profound expertise on ZnO. Thank you too for the introduction to RIG-VM, the SEM measurements and the many fruitful discussions we had.

I would also like to thank Dr. Sven Ring. You always lent an ear to my problems. I learned a lot about optics from you. I would also like to thank you for your constructive criticism, your refreshing way to tackle problems and finally for being a friend.

I am very grateful to Dr. Sonya Calnan, who provided a warm welcome for me in my first days at PVcomB. Thank you for introducing me to many characterization techniques, for spending hours together at the AFM and XRD, for sharing your inexhaustible collection of literature with me, and for providing your good proficiency in English whenever it was needed.

Onno Gabriel is acknowledged for introducing me to plasma physics and diagnostic, for having many fruitful discussions on PECVD deposition and of course for your invaluable contribution to simplifying our daily life by providing such cool data management tools, like PDVisA and PEAVi indeed are (Mr. Big Data!)

In this context Tim Henkel also deserves my acknowledgement. I have never before met a programmer with such a short response time and fine nose for the needs of his “clients”.

Dr. Simon Kirner I would like to thank for the many fruitful discussions we had and of course for providing such a nicely reflecting, low absorbing, highly conducting intermediate reflector layer. It is a honor for me that I shared a desk with the very first person of PVcomB that successfully graduated. Katrin Frank, Manuel Hartig, Matthias Zelt and Christof Schultz are acknowledged for always providing excellent substrates, contacts, absorbers and laser patterns, respectively.

I would like to thank Karolina Mack, Tobias Hänel and Daniel Kubsch for lovely caring of all these measurement tools.

Dr. Björn Rau is acknowledged for his efforts to keep the whole equipment always running.

Thanks go to Martin Rohde, who taught me how to operate the AKT (in normal mode and beyond). Thank you also for providing the amazing triple-p-layer. I really miss your inspiring terminology (Hummel-clean).

I would also thank Florian Welker and Steffi Schönau for working along with me in the field of ZnO:Al annealing. Your work contributed a lot to this thesis.

Annett Gerch is acknowledged for managing all the administration related to travelling, publishing, purchasing etc.

I am grateful to Christoph Zahren and Wilfried Reetz from Forschungszentrum Jülich for carrying out the *EQE* measurements at the large area setup. Dr. Carolin Ulbrich is acknowledged for organizing my short stay in Jülich and for caring about me during that time

Dr. Sonya Calnan, Dr. Sven Ring, Dr. Florian Ruske and Dr. Bernd Stannowski also deserve a special thank for reviewing and proof reading of the manuscript of this thesis.

I also would like to thank the whole team at PVcomB. I always enjoyed the warm and inspiring atmosphere at PVcomB. Please, keep this alive.

My family and friends deserve my acknowledgement for their support during all this time.

Very special thanks go to my girlfriend, Christiane, who had so much patience, always believed in me and supported me a lot. I apologize for the extra load that you and Max often had to manage.

My son, Max, is acknowledged for being the way he is.

